

Spectroscopic Studies of the Electronic Structure in Layered Cuprates and Ruthenates

THÈSE N° 7893 (2017)

PRÉSENTÉE LE 7 SEPTEMBRE 2017
À LA FACULTÉ DES SCIENCES DE BASE
LABORATOIRE DE MAGNÉTISME QUANTIQUE
PROGRAMME DOCTORAL EN PHYSIQUE

ÉCOLE POLYTECHNIQUE FÉDÉRALE DE LAUSANNE

POUR L'OBTENTION DU GRADE DE DOCTEUR ÈS SCIENCES

PAR

Claudia Giuseppina FATUZZO

acceptée sur proposition du jury:

Prof. V. Savona, président du jury
Prof. H. M. Rønnow, Prof. J. J. Chang, directeurs de thèse
Dr M. Cuoco, rapporteur
Dr C. Monney, rapporteur
Prof. L. Forró, rapporteur



ÉCOLE POLYTECHNIQUE
FÉDÉRALE DE LAUSANNE

Suisse
2017

‘ “What makes the desert beautiful,”
said the little prince,
“is that *somewhere it hides a well...*” ’

— Antoine de Saint-Exupéry
The Little Prince

Abstract

In materials where electrons interact strongly, a number of exotic and exciting phenomena arise. The mechanisms at the base of many of these phenomena remain debated, as strongly correlated electron physics represents one of the biggest challenges for modern condensed matter physics. Transition metal oxides are a class of strongly correlated systems which exhibit a multitude of physical properties, among which unconventional superconductivity, incommensurate charge and spin ordering, partial anisotropic gapping, strange metallicity, colossal magnetoresistance, multiferroicity, antiferromagnetic Mott insulation, *etc.*. These properties are often observed in close vicinity, when pressure, temperature or chemical composition are varied. As a consequence, it is challenging to disentangle not only their origin, but also their effects on the elementary excitations of the system. In this thesis, high quality single crystals of copper and ruthenium based transition metal oxides (cuprate and ruthenate compounds) were investigated with synchrotron-based spectroscopic techniques.

Our angle resolved photoemission spectroscopy (ARPES) studies focused on the normal state of cuprates, at hole content varying from under- to over-doping. First, the low energy single particle excitations in overdoped cuprates were verified to fulfill the mathematical conditions for Landau Fermi quasiparticles. In a second study, the evolution of the spectral gap was followed as function of doping and temperature, across the charge order, pseudogap and strange metal phases of a cuprate compound, $\text{La}_{1.6-x}\text{Nd}_{0.4}\text{Sr}_x\text{CuO}_4$. This systematic study allowed the identification of an optimal doping regime for the investigation of the pseudogap physics in cuprates.

The orbital structure of single layer ruthenates was explored combining X-ray absorption and resonant inelastic X-ray spectroscopies (XAS and RIXS). Since spectroscopies at the L absorption edge of $4d$ materials are challenged by insufficient energy resolution, we performed our studies at the oxygen K edge, in the soft X-ray energy range. By exploiting the strong orbital hybridization between the oxygen $2p$ and the ruthenium $4d$ states, we obtained high resolution experimental access to the $4d$ electron properties. The results were interpreted through a simple model Hamiltonian, with analytic solutions that provide a consistent description of the low energy features observed.

Key words: cuprates, ruthenates, strong correlations, RIXS, ARPES, XAS, pseudogap, strange metal, spin orbit coupling, crystal field.

Sommario

Le teorie dei solidi sviluppate nel secolo scorso, che descrivono con successo la fisica di semiconduttori e metalli convenzionali, sono basate sull'ipotesi che le interazioni tra gli elettroni all'interno di un cristallo possano essere considerate alla stregua di un potenziale efficace. In materiali fortemente correlati, le interazioni tra elettroni devono essere trattate esplicitamente così che il problema ad N corpi (con N dell'ordine di 10^{23}) non può essere semplificato. Dalle forti correlazioni elettroniche emerge una serie di fenomeni esotici ed interessanti, la cui origine rimane controversa. I materiali fortemente correlati rimangono infatti una delle maggiori sfide della moderna fisica della materia condensata.

Gli ossidi dei metalli di transizione rappresentano una particolare classe di materiali fortemente correlati, ed esibiscono una moltitudine di sorprendenti proprietà fisiche, che spesso emergono in estrema vicinanza, quando si modifica la pressione, la temperatura o la composizione chimica. Di conseguenza, risulta estremamente complicato distinguere non solo le relative origini, ma perfino gli effetti di ciascuna sulle eccitazioni elementari del sistema. In questo lavoro di tesi, cristalli di ossidi di transizione a base di rame e di rutenio (denominati cuprati e rutenati) sono stati esplorati tramite tecniche spettroscopiche di sincrotrone.

I nostri studi tramite spettroscopia di photoemissione risolta in angolo (ARPES) si sono concentrati sullo studio dello stato normale dei cuprati, con diverso contenuto di droganti di tipo p . Nella prima parte, abbiamo verificato che le eccitazioni a bassa energia di cuprati sovra-drogati soddisfano le condizioni matematiche per la definizione delle quasi-particelle di Landau Fermi. Successivamente, abbiamo seguito l'evoluzione della gap di particella singola al variare di temperatura e drogaggio, attraverso le fasi di ordine di carica, pseudogap e metallicità non convenzionale del cuprato $\text{La}_{1.6-x}\text{Nd}_{0.4}\text{Sr}_x\text{CuO}_4$. Sulla base di questo studio sistematico è stato identificato un regime di drogaggio ideale per lo studio della misteriosa fase pseudogap dei cuprati.

La struttura orbitale di rutenati a layer singolo è stata esplorata tramite raggi X, in uno studio combinato di spettroscopia di assorbimento (XAS) e di risonanza inelastica (RIXS). Vista la scarsa risoluzione in energia alla risonanza di assorbimento della soglia L del rutenio, i composti sono stati studiati alla soglia K dell'ossigeno. Sfruttando l'ibridazione tra gli orbitali $2p$ dell'ossigeno e i $4d$ del rutenio, è stato possibile studiare questi ultimi con alta risoluzione in energia. I risultati ottenuti sono stati interpretati tramite un modello semplificato, le cui soluzioni analitiche producono una descrizione consistente delle eccitazioni osservate.

Contents

Abstract (English/Italiano)	i
List of figures	vii
List of tables	ix
1 Introduction	1
Outline of the manuscript	3
2 Experimental methods	5
2.1 Angle resolved photoemission spectroscopy - ARPES	6
2.1.1 The photoelectric effect	6
2.1.2 The three steps model	8
2.1.3 Electron analyzer	14
2.1.4 Experimental conditions and coordinate transformation	15
2.1.5 ARPES data normalization	17
2.2 Resonant Inelastic X-ray Spectroscopy - RIXS	21
2.2.1 Physical process	21
2.2.2 X-ray Absorption Spectroscopy - XAS	24
2.2.3 Dispersion in energy loss	27
2.2.4 Dispersion in incident energy	30
2.2.5 Dispersion in momentum	31
3 Normal state fermiology of cuprates	33
3.1 Self-energy and quasiparticle renormalization effects	35
3.1.1 Fermi surface of $\text{La}_{1.77}\text{Sr}_{0.23}\text{CuO}_4$	36
3.1.2 Analysis of nodal ARPES spectra	36
3.1.3 Spectral function model	40
3.1.4 Kramers-Kronig consistency	44
3.1.5 Summary of results	46
3.2 Single particle spectral gap evolution, from underdoped to overdoped regime .	50
3.2.1 ARPES spectra	51
3.2.2 Analysis	53
3.2.3 Discussion	64

Contents

3.2.4	Summary of results	66
4	Orbital structure of single-layer ruthenates	69
4.1	Experimental conditions	71
4.1.1	Choice of the absorption resonance	72
4.1.2	Orbital tuning	72
4.2	XAS results	75
4.2.1	O K-edge absorption spectra of Ca_2RuO_4	75
4.2.2	O-K edge absorption spectra of Sr_2RuO_4	78
4.2.3	Estimation of crystal field splitting	80
4.2.4	Self-absorption	81
4.2.5	Estimation of orbital occupancy	82
4.3	RIXS results	85
4.3.1	Momentum transferred along the sample surface	85
4.3.2	Dependence on incident energy	86
4.3.3	Dependence on incident angle	92
4.4	Model	96
4.4.1	Model application	99
4.5	Summary of Results	101
5	Conclusions	105
A	Additional information	107
A.1	XAS: data normalization	109
A.2	XAS: fit of LH spectra	111
A.3	RIXS: momentum transfer	113
A.4	RIXS: energy loss vs out-coming energy	115
A.5	RIXS: direct comparison of apical and planar spectra	117
A.6	Solution of model Hamiltonian	119
A.6.1	Definitions and useful relations	119
A.6.2	Proof of $\mathbf{L}_z^2 = \langle \mathbf{L}_z \rangle^2$	122
A.6.3	Spin orbit coupling	125
A.6.4	Solution	126
A.6.5	Summary	128
B	Other published results	129
	Hallmarks of Hunds coupling in Mott insulator Ca_2RuO_4	130
	Damped spin-excitations in $\text{La}_{2-x}\text{Sr}_x\text{CuO}_4$	137
	Acknowledgements	147
	Bibliography	164
	Curriculum Vitae	165

List of Figures

2.1	Photoemission energy conservation	7
2.2	Photoemission process	7
2.3	Free electron final state model	13
2.4	SCIENTA analyzer	15
2.5	Laboratory coordinate system	16
2.6	Manipulator rotational angles	16
2.7	ARPES data normalization	18
2.8	Extraction of the Fermi level and experimental resolution	19
2.9	RIXS process	22
2.10	RIXS accessible excitations	22
2.11	Dependence of the absorption edges energy on the atomic number	25
2.12	RIXS spectrometer	27
2.13	Raw RIXS spectrum	28
2.14	Calibration of RIXS spectra	29
2.15	Scattering geometry	32
3.1	Cuprates phase diagram	33
3.2	$\text{La}_{2-x}\text{Sr}_x\text{CuO}_4$ phase diagram	37
3.3	Anisotropy of Σ''	37
3.4	Nodal ARPES spectra of $\text{La}_{1.77}\text{Sr}_{0.23}\text{CuO}_4$ and selected distribution curves	39
3.5	Landau quasi-particle linewidth	40
3.6	Landau quasi-particle dispersion	43
3.7	Landau quasi-particle amplitude	43
3.8	Doping dependence of the single particle gap and charge order strength in $\text{La}_{2-x}\text{Ba}_x\text{CuO}_4$	50
3.9	$\text{La}_{1.6-x}\text{Nd}_{0.4}\text{Sr}_x\text{CuO}_4$ phase diagram in the low doping region	51
3.10	Samples of $\text{La}_{1.6-x}\text{Nd}_{0.4}\text{Sr}_x\text{CuO}_4$ ARPES spectra	52
3.11	Intrinsic lineshape	54
3.12	Symmetrization of energy distribution curves	55
3.13	Effect of finite experimental resolution	56
3.14	Effect of finite experimental resolution on gapped Lorentzian curves	58
3.15	Influence of the scattering rate	59

List of Figures

3.16 Evolution of the Symmetrized spectra with composition, Fermi surface angle and temperature	60
3.17 Spectral weight loss <i>vs</i> transfer	62
3.18 Correlation between spectral gap and scattering rate	64
4.1 Ca_2RuO_4 to Sr_2RuO_4 phase diagram	69
4.2 Ruthenate sample	71
4.3 XAS geometry	71
4.4 Degeneracy lifting	73
4.5 Selection of p orbital	74
4.6 $\text{O}2p\text{-Ru}4d$ hybridization	74
4.7 Selective tuning of XAS sensitivity	75
4.8 Full range O K-edge XAS on Ca_2RuO_4	77
4.9 XAS angle dependence Ca_2RuO_4	77
4.10 Full range O K-edge XAS on Sr_2RuO_4	79
4.11 XAS angle dependence Sr_2RuO_4	79
4.12 $\text{Ca}_{2-x}\text{Sr}_x\text{RuO}_4$ XAS from literature	80
4.13 TFY vs TEY	82
4.14 XAS fit LV	83
4.15 XAS fit results	84
4.16 RIXS incident energy dependence on Ca_2RuO_4	88
4.17 RIXS incident energy dependence on Sr_2RuO_4	89
4.18 LH RIXS incident energy dependence on Ca_2RuO_4	90
4.19 LV RIXS incident energy dependence on Sr_2RuO_4	91
4.20 Comparison of the energy scale of the RIXS excitations and XAS features	93
4.21 RIXS dependence on transferred momentum	94
4.22 Zoom at low energy loss of RIXS dependence on transferred momentum	95
4.23 Expected occupation ratio of \mathcal{H} eigenstates	97
4.24 Analytical solution of \mathcal{H}	100
4.25 Interpretation of low energy RIXS features	102
A.1 XAS data normalization	109
A.2 XAS fit LH	111
A.3 RIXS geometry	113
A.4 Orthorhombic and tetragonal unit cell	114
A.5 Comparison of RIXS spectra plotted versus out-coming energy or energy loss	115
A.6 Comparison of RIXS spectra at the apical and planar resonances for Ca_2RuO_4 and Sr_2RuO_4	117

List of Tables

4.1	Crystal field splitting evaluation	81
4.2	Absorption tuning	86
4.3	Recapitulation of the excitations observed in RIXS spectra and their relative intensity	93
4.4	Summary of results from the XAS-RIXS combined study on $(\text{Ca,Sr})_2\text{RuO}_4$	103

1 Introduction

‘T.T.T.

Put up in a place
where it's easy to see
the cryptic admonishment
T. T. T.

When you feel how depressingly
slowly you climb,
it's well to remember that
Things Take Time!

— Piet Hein

Macroscopic properties of materials are intimately connected with their microscopic electronic structure, which is determined by the mixing of the valence orbitals. An important role is played by the symmetry of these orbitals as well as their size. When one compares the inter-atomic distance D with the valence orbital radius R , two contrasting regimes can be identified. If the orbitals extend over neighboring atomic sites ($D \ll R$), the large overlap of orbitals originating from different atoms causes the electrons to lose their atomic identity. This is the case of s and p valence orbitals. The bands originated from these orbitals are generally broad and valence electrons can be treated as independent single particles, described by Bloch wavefunctions within the tight-binding model. This approach successfully describes the physics of conventional metals, insulators and semiconductors. Conversely, if the valence orbitals of different atomic sites have little overlap ($D \gg R$), the valence electrons retain their atomic character and produce narrow bands. In this case, strong electron-electron interactions take place and

to gain an accurate microscopic description requires solving of a many body problem. The d and f orbitals fall into this category and mean field approaches fail to describe their physics [1].

A clear example of this failure is demonstrated by those compounds expected to behave like band metals but which are found to be insulators, with an anti-ferromagnetic ground state. These materials are called Mott insulators. Within the the Mott-Hubbard model [2, 3], the origin of these gaps, referred to as Mott gaps, can be ascribed to a strong on-site Coulomb repulsion, U , which opposes charge fluctuations. If the Coulomb repulsion is larger than the orbital bandwidth, the valence band is split into a lower and an upper Hubbard band, separated by a gap of size given by U , typically of a few eV. Charge fluctuations may occur not only between two adjacent transition metal sites, but can involve a ligand, typically oxygen. The energy necessary to introduce a hole into the ligand band is the charge-transfer gap Δ . The ratio between U and Δ determines the size of the gap in these materials, classified as Mott-Hubbard or Charge-transfer insulators according to which energy scales determines the energy of the lowest possible charge excitation [4].

Transition metal oxides are a class of strongly correlated materials that exhibit a variety of surprising physical phenomena, such as multiferroicity, giant magnetoresistance or unconventional superconductivity, which are not predicted by either the tight-binding or the Mott-Hubbard models [1, 5, 6, 7]. These phenomena often arise in close vicinity to each other and to Mott insulation, when temperature, doping or pressure is modified. Therefore, it is evident that to capture the physics of these materials it is not sufficient to consider their orbital degrees of freedom alone, but charge, lattice, and spin should be also taken into account. As a result of this complexity, strongly correlated electron systems represent a challenging puzzle for modern solid state physics, and progress has been largely driven by experimental discoveries. The techniques successfully applied to this field rely on different probes, such as neutron and X-ray scattering, transport measurements, scanning tunneling microscopy, *etc.*. Angle resolved photoemission (ARPES) and resonant inelastic scattering (RIXS) are two powerful spectroscopic techniques which grant direct access to the electronic structure of the investigated materials.

In this thesis, two classes of transition metal oxides have been targeted, that of cuprates and ruthenates. The valence electrons in these compounds originate from the $3d$ orbitals in the case of cuprates, and the $4d$ ones in the case of ruthenates. The occupancy of these states is very different in the two cases, with a single hole found in the cuprates $3d$ orbitals. In the case of ruthenates, four electrons are expected to occupy the valence states originating from the $4d$ states. Furthermore, the spin orbit coupling is expected to be stronger in the $4d$ subshell than in the $3d$ one. Both these families of materials exhibit strong correlations and a variety of ground states. In particular, Mott insulation and unconventional superconductivity are found among both cuprates and ruthenates. It is not clear however if, across these families, the Mott gap has a common origin, or if the superconducting state, whose underlying mechanism is unknown, has the same symmetry. In fact, the superconducting gap of cuprates

has a d wave symmetry, but Sr_2RuO_4 has been proposed to be a p wave superconductor [8]. Furthermore, in cuprates, the Mott gap is opened in the half filled e_g single band by strong Coulomb interaction. In Ca_2RuO_4 , the 4 electrons in the $4d$ orbitals produce a $2/3$ occupancy in the $4d-t_{2g}$ substates, separated from the e_g states by the crystal field interaction. Since the crystal field acts differently on the different $d-t_{2g}$ states, namely it has opposite effects on the d_{xy} orbital, at planar character, and on the $d_{xz,yz}$ ones, at out of plane character. It is a matter of debate whether the d_{xy} orbital is stabilized at deeper energy by the crystal field, so that it is not involved in the origin of the upper and lower Hubbard bands [9, 10] or if the spin-orbit mixes the planar and out of plane orbitals and the Mott gap opens in an orbital dependent manner [11, 12].

Open questions in the physics of strongly correlated systems also exist regarding their normal state, outside the superconducting phase. In the so called strange, or bad, metal phase, gapless excitations do not follow the Drude-Sommerfeld model and low temperature resistivity does not scale with the temperature square. A strange metal phase is observed in cuprates, ruthenates, iron-based superconductors and heavy fermion systems (compounds with valence bands originating from f orbitals). Not only is a microscopic description for elementary excitations in strange metals missing, it is also not clear whether all strange metals originate from the same mechanism. Strongly correlated system also exhibit a mysterious pseudogap phase, where gapless excitations are found only in some region of momentum space and low temperature resistivity deviates from the temperature square law observed in conventional metals. A pseudogap phase is observed in underdoped cuprates and has been reported in surface doped iridates compounds [13]. The discussion on whether the pseudogap acts a precursor to unconventional superconductivity, or is in competition with it, is complicated by the observation of charge order, in the same region of the cuprates phase diagram [14, 15, 16, 17, 18].

To investigate the role of electron correlations, structural distortions, orbital and spin-orbital interactions, the elementary electronic excitations in these families have been studied via ARPES and RIXS, as function of chemical composition and/or temperature.

Outline of the manuscript

This manuscript is structured as follows. The experimental methods employed are outlined in **chapter 2**: angle resolved photoemission spectroscopy (ARPES, **2.1**) and resonant inelastic X-ray scattering (RIXS, **2.2**). The structure of the following sections follows the temporal development of the research performed.

First, the results obtained on cuprates are discussed, in **chapter 3**. **Section 3.1** is devoted to a careful analysis of the low energy excitations in the strange metal phase of cuprates. To conduct this study, high resolution ARPES data on $\text{La}_{1.77}\text{Sr}_{0.23}\text{CuO}_4$ are self-consistently analyzed in their momentum and energy evolution, with the aim of verifying the fulfillment of the math-

Chapter 1. Introduction

ematical conditions for Landau-Fermi quasiparticles. Next, the evolution of the ARPES spectra was systematically studied in the normal state of the cuprate system $\text{La}_{1.6-x}\text{Nd}_{0.4}\text{Sr}_x\text{CuO}_4$, described in **section 3.2**. In this section, the single particle spectral gap is estimated at various values of temperature and/or doping. Varying these parameters causes this system to exhibit different phenomena, such as charge order, pseudogap and strange metallicity. The scope of these experiments was to investigate the ARPES signatures of these different phases, which are universally displayed by cuprates.

Chapter 4 is devoted the RIXS investigation of $(\text{Ca,Sr})_2\text{RuO}_4$. The dependence on experimental geometry and incoming light polarization of the X-ray absorption spectroscopy (XAS) spectra was exploited to identify the energy scales of the states of d orbital origin. The identification of the absorption resonances was used to tune the photon energy to employ in the RIXS process. The low energy features in the RIXS spectra of both materials were interpreted within a simple model Hamiltonian with analytical solutions. This study focused on the effects of spin-orbit interaction and structural distortions on the electronic properties of strongly correlated systems.

Additional information on the methods or models employed can be found in the **appendix A**, at the end of the thesis. In **appendix B** are reproduced other published works to which the author contributed.

2 Experimental methods

In this chapter are described the techniques adopted in the studies presented in this manuscript, namely angle resolved photoemission spectroscopy (ARPES) and resonant inelastic X-ray scattering (RIXS). As will be discussed in the following sections, ARPES is a photon-in electron-out spectroscopy, while RIXS is a photon-in photon-out spectroscopy. Both these techniques require a monochromatic photon source and tremendously benefit from the high brilliance of third generation synchrotrons, such as for example the Swiss Light Source of the Paul Scherrer institute. Furthermore, the experimental impact of these spectroscopies has been enhanced by recent advances in technology, such as the tremendous improvements in crystal growing and ultra-high vacuum techniques, together with the developments of high resolution electron analyzers in the case of ARPES [19, 20] and high resolution Soft X-ray spectrometers for RIXS [21].

The aim of this chapter is to provide the reader with the necessary information to follow the experimental discussions, presented in sections 3 and 4. With this scope in mind, the occasional practical examples specifically refer to the materials and experimental set-ups employed in the experiments. More general and complete descriptions of the ARPES and RIXS techniques can be found in references [22, 23, 24] and [25, 26, 27], respectively, while information about synchrotron radiation can be found in reference [28]. All analysis presented in this thesis have been performed using MatLab commercial software, mostly via custom-made scripts.

2.1 Angle resolved photoemission spectroscopy - ARPES

2.1.1 The photoelectric effect

Angle resolved photoemission spectroscopy is a powerful technique, which gives direct access to the momentum and energy properties of electronic single particle excitations in a material. The photoelectric effect, discovered in 1887 [29] and explained in 1905 [30], manifests as the emission of electrons from a material illuminated with light of sufficient energy. As a result of the optical absorption, an electron escapes the material (photoelectron) and leaves behind an empty state (photohole). The energy threshold for the process coincides with the energy that electrons have to spend to escape the material, referred to as the work function W of the material, see figure 2.1. Energy and momentum conservation laws link the photoelectron state to that of the photohole, allowing direct experimental access to the electronic structure of solids. To extract meaningful information both in energy and momentum, the investigated samples should be single crystals appropriately aligned.

The emission process is illustrated in figure 2.2. A monochromatic photon beam of energy $h\nu$ is incident on the sample surface and a photoelectron is emitted, with energy E_{kin} and momentum $\mathbf{p} = \mathbf{p}_{//} + \mathbf{p}_{\perp}$ (components along the sample surface and its normal). We assume that the sample is oriented with a, b and c axis co-aligned with the x, y and z axis. Notice that the photoelectrons escape in all directions but are measured within a finite acceptance angle, defined by the detector geometry. Energy conservation law implies:

$$h\nu - E_B = E_{kin} + W, \quad (2.1)$$

where E_B indicates the binding energy of the electron before photon absorption (with $E_B=0$ at the Fermi level). Therefore for the modulus of the momentum:

$$p = \sqrt{2m_e E_{kin}}, \quad (2.2)$$

with m_e being the free electron mass.

Along the surface normal, the transitional symmetry is broken and \mathbf{p}_{\perp} is not conserved. However, for the component parallel to the sample surface, we can write:

$$p_{//} = \sqrt{2m_e E_{kin}} \sin \theta. \quad (2.3)$$

Since the photon momentum $\mathbf{k}_{h\nu}$ is typically negligible at the photon energies (5-500 eV) typically employed in ARPES experimentsⁱ, from momentum conservation we find:

$$\mathbf{k}_{//}^i + \mathbf{k}_{h\nu, //} \simeq \mathbf{k}_{//}^i = \mathbf{k}_{//}^f; \quad (2.4)$$

ⁱat $h\nu = 55$ eV for example, $k_{h\nu} \sim 0.004$ Å, corresponding to less than 1 per cent of the typical Brillouin zone of cuprates.

2.1. Angle resolved photoemission spectroscopy - ARPES

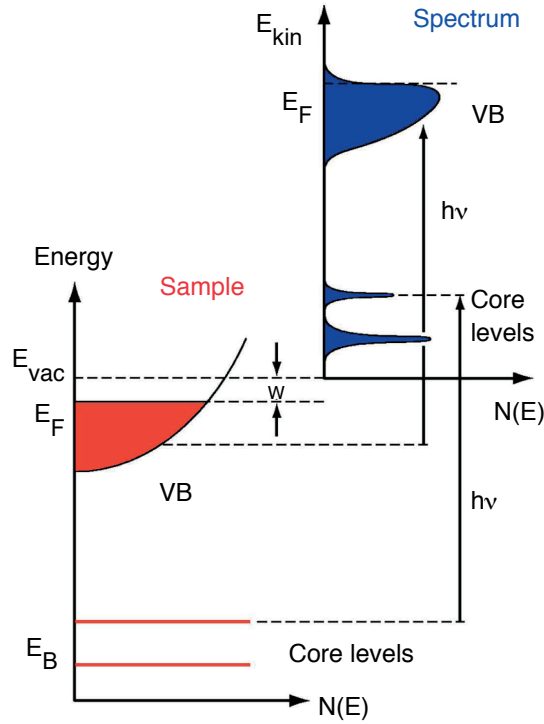


Figure 2.1 – **Photoemission energy conservation** | Within the sample, the Fermi level corresponds to zero binding energy. Once escaped, the kinetic energy of the photoelectron E_{kin} refers to the vacuum level $E_{vac}=E_F+W$ as the zero-energy level, where W indicates the work function of the sample. Adapted from reference [22].

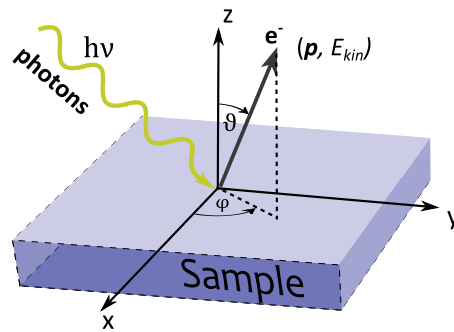


Figure 2.2 – **Photoemission process** | A monochromatic photon beam of (sufficient) energy $h\nu$ causes the emission of electrons of energy E_{kin} and momentum \mathbf{p} , directed in all directions. The direction along which photoelectrons are measured is identified by the polar angle θ and the azimuthal angle ϕ . From reference [31]

Chapter 2. Experimental methods

hence:

$$\mathbf{k}_{//} = \frac{\mathbf{p}_{//}}{\hbar} = \frac{\sqrt{2m_e E_{kin}}}{\hbar} \sin \theta (\cos \phi \hat{\mathbf{x}} + \sin \phi \hat{\mathbf{y}}), \quad (2.5)$$

where $\mathbf{k}_{//}$ is the electron crystal momentum, along the sample surface, in the extended zone scheme ⁱⁱ.

Equations 2.1 and 2.5 are at the basis of angle resolved photoemission spectroscopy. In quasi-2D materials, the dispersion along z can be neglected and the electronic dispersion relation $E(\mathbf{k}) \simeq E(\mathbf{k}_{//})$ can be evaluated without knowledge of \mathbf{k}_{\perp} ⁱⁱⁱ. In the following sections, a more detailed treatment is presented, which allows the derivation of a formal description of the ARPES intensity.

2.1.2 The three steps model

In the previous section, we have made the implicit assumption that the electrons within the material do not react to the presence of the photohole (non-interacting electron picture). However, photoemission is a many body process, in which the incident radiation causes emission of an electron from an interacting N -electron system, which evolves from the initial state Ψ_i^N to a final state Ψ_f^N . The process probability $w_{i \rightarrow f}$ can be approximated, within the lowest-order perturbation theory, by the Fermi golden rule:

$$w_{i \rightarrow f} = \frac{2\pi}{\hbar} |\langle \Psi_f^N | \mathcal{H}_{int} | \Psi_i^N \rangle|^2 \delta(E_f^N - E_i^N - \hbar\nu), \quad (2.6)$$

where $E_{f,i}^N$ are the initial and final energies of the N -electron system, and \mathcal{H}_{int} is the electron-photon interaction. In the Coulomb gauge and within the dipole approximation, $\mathcal{H}_{int} = i\hbar \frac{e}{m_e c} \mathbf{A} \cdot \nabla$ [23], with \mathbf{A} vector potential of the electromagnetic field, e electric charge of the electron and c speed of light.

To proceed, it is necessary to model the initial and final states wavefunction of the N -electron systems. The most widely adopted approach relies on the phenomenological three step model, which leads to a clear and intuitive picture of the photoemission process [22]. Within this phenomenological approach, the photoemission process is broken down in three independent steps:

1. optical excitation of an electron in the bulk;
2. transport of the excited electron from the bulk to the surface;

ⁱⁱTo obtain the crystal momentum in the reduced zone, is sufficient to subtract the corresponding reciprocal lattice vector \mathbf{G} .

ⁱⁱⁱIn the case of cuprates, their layered structure as well as the strong resistivity anisotropy (which, in the normal state, is two order of magnitude larger out of plane than in plane [32]) suggest a weak out of plane dispersion, which is neglected within the work presented in this thesis.

3. escape of the photoelectron through the surface into vacuum.

The photoemission intensity is then given by the product of the single steps probabilities, derived in the following sections.

2.1.2.1 Optical excitation

The first step in the photoemission process is the optical transition of an electron into an excited state, into the bulk. To evaluate the probability of the transition, we can refer to equation 2.6, with the sole difference that in the final states all electrons are still within the crystal. For photoelectrons with high kinetic energy, the transition can be treated within the sudden approximation, which assumes instantaneous removal of the excited electron ^{iv}.

Within the sudden approximation, the wavefunctions of the initial and final states can be factorized:

$$\Psi_{i,f}^N = \mathcal{A}_P \phi_{i,f}^{\mathbf{k}} \Psi_{i,f}^{N-1}, \quad (2.7)$$

where \mathcal{A}_P is an anti-symmetrization operator which ensures $\Psi_{i,f}^N$ satisfies Pauli exclusion principle and $\phi_{i,f}$ is the wavefunction of the electron of momentum \mathbf{k} , before and after absorption of the photon. The N-1 electron wavefunction $\Psi_i^{N-1} = c_{\mathbf{k}} \Psi_i^N$ ($c_{\mathbf{k}}$ annihilation operator) describes a ionized state, which is not a eigenstate of the system. The ensemble of the N-1 electrons can collectively be treated as a single particle of charge $+e$, the photohole. The final wavefunction of this ensemble Ψ_f^{N-1} will fall on one of the eigenstates of the excited system: $\Psi_f^{N-1} = \Psi_m^{N-1}$, of eigenenergy E_m^{N-1} . The probability of the optical excitation process is then given by the sum over all possible excited states and the initial and final energies can be written as: $E_i^N = E_i^{N-1} - E_i^{\mathbf{k}}$, $E_f^N = E_m^{N-1} + E_f^{\mathbf{k}}$, where $E_{i,f}^{\mathbf{k}}$ is the energy of the electron with wavefunction $\phi_{i,f}^{\mathbf{k}}$, within the material^v.

With this modelization for $\Psi_{i,f}^N$, the transition element in equation 2.6 can be split into a single and a collective part:

$$\begin{aligned} \langle \Psi_f^N | \mathcal{H}_{int} | \Psi_i^N \rangle &= \langle \phi_f^{\mathbf{k}} \Psi_m^{N-1} | \mathcal{A}_P^\dagger \mathcal{H}_{int} \mathcal{A}_P | \phi_i^{\mathbf{k}} \Psi_i^{N-1} \rangle = \\ &= \langle \phi_f^{\mathbf{k}} | \mathcal{H}_{int} | \phi_i^{\mathbf{k}} \rangle \langle \Psi_m^{N-1} | \Psi_i^{N-1} \rangle, \end{aligned} \quad (2.8)$$

where we used the fact that \mathcal{A}_P commutes with all Hermitian operators and is unitary^{vi}, and that, within the approximations adopted, \mathcal{H}_{int} operates only on the single particle part of the wavefunction. The term $\langle \phi_f^{\mathbf{k}} | \mathcal{H}_{int} | \phi_i^{\mathbf{k}} \rangle \equiv \mathcal{M}_{i \rightarrow f}^{\mathbf{k}}$ represents the one-electron dipole matrix

^{iv}In the case of cuprates, the sudden approximation is found appropriate already at kinetic energies of ~20 eV [22].

^vNotice that the energy E_i^{N-1} is higher than E_i^N , since the removal of an electron leaves the ensemble into a ionized state.

^{vi} $\mathcal{A}_P^\dagger \mathcal{A}_P$ gives the identity operator.

Chapter 2. Experimental methods

element while $\langle \Psi_m^{N-1} | \Psi_i^{N-1} \rangle$ gives the overlap integral of the remaining N-1 electron ensemble. Considering all possible final and initial states, for the photoemission intensity, function of \mathbf{k} and $E_{kin} = E_f^{\mathbf{k}}$, we have:

$$\mathcal{I}(E_{kin}, \mathbf{k}) \propto \sum_{i,f} w_{i \rightarrow f} \propto \sum_{i,f} |\mathcal{M}_{i \rightarrow f}^{\mathbf{k}}|^2 \sum_m |c_{i \rightarrow m}|^2 \delta(E_{kin} + E_m^{N-1} - E_i^N - h\nu), \quad (2.9)$$

where $|c_{i \rightarrow m}|^2$ gives the probability that after the sudden removal of the photoelectron the remaining N-1 electrons ensemble, initially in state Ψ_i^{N-1} will be left in state Ψ_m^{N-1} .

In the non-interacting particle picture, it is assumed that Ψ_i^{N-1} corresponds to one of the possible final states Ψ_m^{N-1} , so that $\sum_m |c_{\bar{m} \rightarrow m}|^2 = \delta_{m, \bar{m}}$ ^{vii}. The ARPES intensity, within this overly simplified picture, is then proportional to the delta function $\delta(E_{kin} + E_i^{\mathbf{k}} - h\nu)$, provided $\mathcal{M}_{i \rightarrow f}^{\mathbf{k}} \neq 0$. A more reasonable assumption is that the electron removal considerably affects the potential of the system, so that Ψ_i^{N-1} does not coincide with any of the excited eigenstates and $|c_{i \rightarrow m}|^2$ gives a finite contribution over many values of m . The ARPES intensity will then not have a delta profile, but will show a main line corresponding to the state with maximum overlap and several satellite lines, according to how many of the m states are created in the photoemission process [23].

At this point is useful to refer to the one-electron removal spectral function:

$$\mathcal{A}^-(\omega, \mathbf{k}) = \sum_m \langle \Psi_m^{N-1} | c_{\mathbf{k}} | \Psi_i^N \rangle \delta(\omega - E_m^{N-1} + E_i^N), \quad (2.10)$$

which gives the probability of removing an electron of momentum \mathbf{k} and energy ω from the N electrons system described by Ψ_i^N . Taking into account that $\Psi_i^{N-1} = c_{\mathbf{k}} \Psi_i^N$, and posing $\omega = E_{kin} - h\nu$, the photoemission intensity is proportional to the removal spectral function:

$$\mathcal{I}^-(\omega, \mathbf{k}) \propto \sum_{i,f} |\mathcal{M}_{i \rightarrow f}^{\mathbf{k}}|^2 \mathcal{A}^-(\omega, \mathbf{k}). \quad (2.11)$$

Analogously, the inverse photoemission process is proportional to the addition spectral function, $\mathcal{I}^+(\omega, \mathbf{k}) \propto \mathcal{A}^+(\omega, \mathbf{k})$ while the single particle spectral function is given by the sum of the two:

$$\mathcal{A}(\omega, \mathbf{k}) = \mathcal{A}^-(\omega, \mathbf{k}) + \mathcal{A}^+(\omega, \mathbf{k}). \quad (2.12)$$

The single particle spectral function contains information about physical quantities relevant for the electronic systems, such as mass renormalization due to correlations, lifetime of the

^{vii}Kronecker delta: $\delta_{m, \bar{m}} = 1$ if $m = \bar{m}$, 0 otherwise.

excitations, *ect.* $\mathcal{A}(\omega, \mathbf{k})$ is formally defined in its relation to the particle's Green function:

$$\begin{aligned}\mathcal{G}(\omega, \mathbf{k}) &= \mathcal{G}'(\omega, \mathbf{k}) + i\mathcal{G}''(\omega, \mathbf{k}); \\ \mathcal{A}(\omega, \mathbf{k}) &= \frac{-1}{\pi} \mathcal{G}''(\omega, \mathbf{k}).\end{aligned}\tag{2.13}$$

Since the Green function is a linear response function, causality dictates that its real and imaginary part are linked through the Kramers Kronig relations.

2.1.2.2 Transport to the surface, escape into vacuum and detection

Once the photoelectron is excited, within the material, it needs to travel to the surface (second step). This step can be described in terms of an effective mean free path. We need to evaluate the probability that the excited electron reaches the surface without losing information in energy or momentum, i.e. without undergoing scattering events. The scattered electrons, labeled as secondary, contribute to a momentum independent background.

The intensity of the primary photoelectrons scales with a factor $e^{-x/\lambda_{f-p}}$, where x is the distance from the location of excitation and λ_{f-p} is the electronic mean free path. λ_{f-p} has been shown to follow a universal curve as function of the electronic kinetic energy [33]. At the energies relevant for the work presented in this thesis^{viii}, $\lambda_{f-p} \sim 10 \text{ \AA}$. Since photoelectrons excited deeper into the material are scattered before reaching the surface, λ_{f-p} is referred to as the electronic escape depth. This implies that ARPES is a surface sensitive technique that can only probe a few atomic planes. In the soft X-ray regime ($h\nu > 200 \text{ eV}$) the electronic escape depth increases, improving bulk sensitivity.

The third and last step concerns the escape of the photoelectron, which can be described as the probability for the electron to be transmitted through the surface. To escape, the excited electrons have to overcome the material work function W , the energy difference between the Fermi level of the material and the vacuum level E_{vac} , see figure 2.1. The transmission probability T is a function of the momentum of the photoelectrons and the potential step to overcome W . For electrons directed along the surface normal, if $E_{kin} \gg W^{\text{ix}}$, $T \simeq 1$.

In order to escape, the emerging photoelectron loses part of its kinetic energy. If inside the material the photoelectron had kinetic energy E_{kin}^{int} , once escaped into vacuum its kinetic energy values $E_{kin}^{vac} = E_{kin}^{int} - W$. The need to overcome a potential barrier (W), puts a limit into the angles at which the excited photoelectrons can approach the surface and be able to escape. To illustrate this effect, it is useful to refer to the free electron final state model, illustrated in panel 2.3(a). Within this model, the excited photoelectron is assumed to follow the free electrons parabolic dispersion, with the bottom of the parabola given by E_0 , a constant *a priori*

^{viii}To optimize matrix element effects in the cuprates compounds investigated in this thesis, it is convenient to use an incoming photon beam of $h\nu \simeq 55 \text{ eV}$, which corresponds to a photoelectron kinetic energy of $\sim 50 \text{ eV}$.

^{ix}Typical values of W vary between 4 and 6 eV.

Chapter 2. Experimental methods

unknown. The kinetic energy of the photoelectron is measured from E_0 .

The momenta of the photoelectron inside and outside the material, $\mathbf{k}^{int,vac}$ see panel 2.3(b), are separated in their component along the sample surface and along the out of plane direction:

$$\mathbf{k}^{int,vac} = \mathbf{k}_{//}^{int,vac} + \mathbf{k}_{\perp}^{int,vac}. \quad (2.14)$$

The potential barrier V_0 is given by the difference between the vacuum level E_{vac} and E_0 and puts a lower limit into \mathbf{k}_{\perp}^{int} . To be able to escape, the out of plane component of the photoelectron momentum, within the material, must satisfy:

$$\hbar \mathbf{k}_{\perp}^{int} \geq \sqrt{2m_e V_0}. \quad (2.15)$$

Once escaped into vacuum, the photoelectrons reach the electron analyzer, described in section 2.1.3, without further interactions. The sample and the analyzer are kept in ultra high vacuum, with typical pressure below $0.7 \cdot 10^{-10}$ mbar. Entering into the detector changes again the kinetic energy, as a consequence of the contact potential (generated between the sample and the detector). Since the sample and the detector are in electric contact, their Fermi levels E_F align and the contact potential is given by $W - W^{det}$, with W^{det} work function of the detector. The detected kinetic energy is then given by:

$$E_{kin}^{det} = E_{kin}^{vac} + (W - W^{det}) = \hbar\nu - E_B - W^{det}; \quad (2.16)$$

with $E_B = \hbar\nu - E_{kin}^{int}$ binding energy of the photoelectron (*i.e.* energy level occupied prior excitation). Since the detector work function is known (typically, $W^{det} \approx 4.5$ eV), the binding energy can be evaluated. Experimentally, is it convenient to simply measure the kinetic energy corresponding to the Fermi level of the sample, E_{kin}^F , for example by recording photoemission spectra from polycrystalline metals in thermal and electric contact with the sample. The excitation energy $\omega = -E_B$ is the determined as the difference between the detected energy E_{kin}^{det} and the energy corresponding to the Fermi step, E_{kin}^F . This procedure is illustrated in section 2.1.5.

The effect of crossing the surface on the photoelectron momentum, is illustrated in panel 2.3(b). Within the free electron final state model, the momenta inside and outside the material have moduli:

$$\begin{aligned} k^{int} &= \frac{1}{\hbar} \sqrt{2m_e (E_{kin}^{int} - E_0)}; \\ k^{vac} &= \frac{1}{\hbar} \sqrt{2m_e (E_{kin}^{vac} - E_{vac})}. \end{aligned} \quad (2.17)$$

The momentum of the photoelectron is not modified by the optical excitation, *i.e.* $\mathbf{k} = \mathbf{k}^{int}$.

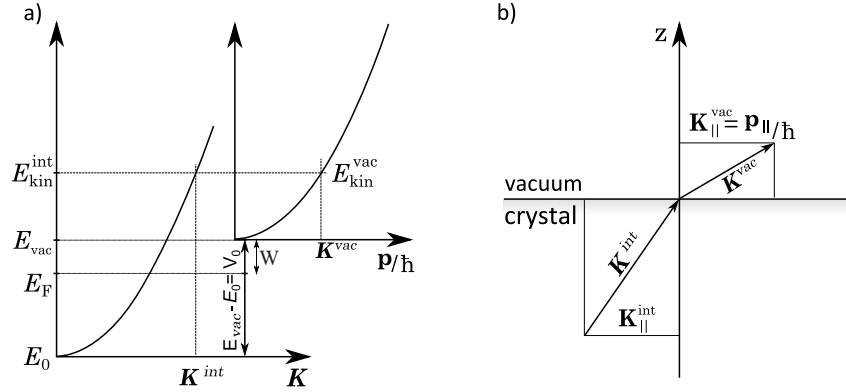


Figure 2.3 – **Free electron final state model and momentum discontinuity** a) Within the free electron final state model, the barrier to overcome for the escape of the photoelectrons is given by $V_0 = E_{vac} - E_0$, where E_0 is the bottom of the parabolic free electron dispersion. Once escaped, the photoelectron energy and momentum are modified, with $E_{kin}^{vac} = E_{kin}^{int} - V_0$. b) Crossing the sample surface breaks the translational invariance, in the direction normal to the surface. As a consequence, the momentum is conserved only in its component parallel to the surface. Adapted from reference [31].

As discussed in section 2.1.1, only the in-plane component of the photoelectron momentum is conserved in the process and the detection of the photoelectron as function of the outgoing angles θ and ϕ , see figure 2.2, directly probes $\mathbf{k}_{||} = \mathbf{k}_{||}^{vac} = \mathbf{k}^{det}$, see equation 2.5. An expression for the modulus of the out of plane momentum component can be derived, within the free electron final state model:

$$\begin{aligned} k_{\perp} &= \sqrt{k^2 - k_{||}^2} = \frac{1}{\hbar} \sqrt{2m_e (E_{kin}^{int} - E_0) - \hbar^2 k_{||}^2} = \frac{1}{\hbar} \sqrt{2m_e (E_{kin}^{det} + V_0) - \hbar^2 k_{||}^2} \\ &= \frac{1}{\hbar} \sqrt{2m_e (\hbar\nu - E_B - W^{det} + V_0) - \hbar^2 k_{||}^2}, \end{aligned} \quad (2.18)$$

in the extended zone representation. Notice that k_{\perp} can be indirectly probed by varying the energy of the incident photons, although its value ultimately depends on the unknown inner potential $V_0 = E_{vac} - E_0$.

2.1.2.3 Final equations

To conclude, we summarize the photoemission relations derived within the three steps model and adopting the sudden approximation and the free electron final state model.

The relation between the detected photoelectron energy and the energy level occupied before excitation, E_B , is given by:

$$E_B = \hbar\nu - E_{kin}^{det} - W^{det}. \quad (2.19)$$

For the photoelectron momentum, we have derived:

$$\begin{aligned}\mathbf{k}_{//} &= \frac{\sqrt{2m_e E_{kin}^{det}}}{\hbar} \sin \theta (\cos \phi \hat{\mathbf{x}} + \sin \phi \hat{\mathbf{y}}); \\ \mathbf{k}_{\perp} &= \frac{1}{\hbar} \sqrt{2m_e (\hbar\nu - E_B - W^{det} + V_0) - \hbar^2 k_{//}^2} \hat{\mathbf{z}}.\end{aligned}\tag{2.20}$$

The fact that direct photoemission only probes the occupied states can be taken into account by including, in the expression of the ARPES intensity, the Fermi Dirac distribution:

$$\mathcal{F}^D(\omega, T) = \left(1 + e^{\omega/(K_B T)}\right)^{-1},\tag{2.21}$$

where $\omega = -E_B$ is the excitation energy, K_B the Boltzmann constant and the Fermi level correspond to zero energy. The sample temperature T can be varied during the experiment and is usually measured by thermocouples. The ARPES intensity re-writes:

$$\mathcal{I}(\omega, \mathbf{k}) = \mathcal{I}_0(\omega, \mathbf{k}, \nu, \mathbf{A}) \bullet \mathcal{A}(\omega, \mathbf{k}) \bullet \mathcal{F}^D(\omega, T),\tag{2.22}$$

where $\mathcal{I}_0(\omega, \mathbf{k}, \nu, \mathbf{A})$ is proportional to the matrix element, which depends on the photoelectron momentum and energy, as well as the energy and polarization of the incident photon beam. The ability to directly probe the single particle spectral function $\mathcal{A}(\omega, \mathbf{k})$, modulated by matrix elements, is a unique characteristic of the ARPES technique.

2.1.3 Electron analyzer

There exists different kind of electron analyzers that can be employed in ARPES experiment [23]. The ARPES data presented in this manuscript have been acquired through a SCIENTA analyzer [19, 20] (specifically, SES2002 or R4000), whose main characteristics are illustrated in figure 2.4. At the core of the SCIENTA electron analyzers lies the electron deflector: an hemispherical capacitor with internal and external radii R_1 and R_2 . The potential difference between the two concentric hemispheres, ΔV , determines the pass energy $E_{pass} = e\Delta V \frac{R_1 R_2}{R_1^2 - R_2^2}$. Only electrons entering the capacitor (at the entrance slit) with kinetic energy close to E_{pass} can reach the detector.

Since the resolution in energy is proportional to E_{pass} , it is convenient to reduce the velocity of the photoelectrons, before they reach the capacitor entrance slit. This operation is performed, without changing the absolute spread in the photoelectrons speed, by multielement electrostatic lens, placed between the sample and the entrance slit. The detectors of SCIENTA analyzers are two-dimensional and position sensitive. The electrons are spread by the capacitor along the $x(y)$ detector direction, as a function of the direction (energy) with which they arrive at the entrance slit. As a result, multiple energies are measured at various momenta at the same time: each ARPES measure yields a 2D intensity map, recorded as n

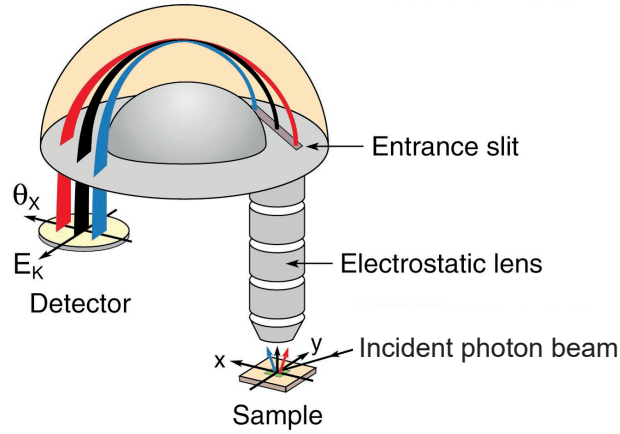


Figure 2.4 – **SCIENTA analyzer** | The photoelectrons are emitted in all directions but collected within a limited solid angle. In the first stage, multielements electrostatics lens decelerate the photoelectrons to match the acceptance energy, E_{pass} of the hemispherical capacitor. Only those electrons reaching the entrance slits with kinetic energy within a defined range around E_{pass} will reach the 2D detector plate. The electrons disperse according to the direction of entry along the detector x axis, Θ_x in the figure, and the energy of entry along the y axis, E_k . Adapted from reference [22].

energy distribution curves, where n is the number of detector channels (spread along the detector x direction, thus corresponding to different values of the photoelectron emission angle).

Similar hemispherical deflection analyzers are the SPECS PHOIBOS analyzers. Time of flight analyzers can also be employed, if the photon source has an appropriate time structure.

2.1.4 Experimental conditions and coordinate transformation

The ARPES data discussed in this thesis have been collected on single layered lanthanum-based cuprates, using SCIENTA SES2002 or R4000 analyzers (angle resolution <0.2 deg, energy resolution <10 meV), at the Swiss Light Source of the Paul Scherrer Institute, on the Surface and Interface Spectroscopy (SIS) beam line [34]. To optimize matrix elements effects, which are material specific, the energy of the incident photon beam was set to 55 eV, and all data were recorded in the second Brillouin zone, but presented in the equivalent points in the first zone, for convenience and clarity of display. Furthermore, the incident photon beam was circularly polarized.

The experiments were performed on high quality single crystals of $\text{La}_{2-x}\text{Sr}_x\text{CuO}_4$ and $\text{La}_{1.6-x}\text{Nd}_{0.4}\text{Sr}_x\text{CuO}_4$, grown by the traveling zone method. After alignment via Laue diffraction, sample of area $\sim 1 \text{ mm}^2$, were mounted on a polycrystalline copper sample holder with the c axis directed along the surface normal of both the sample and the holder. To ensure thermal and electric

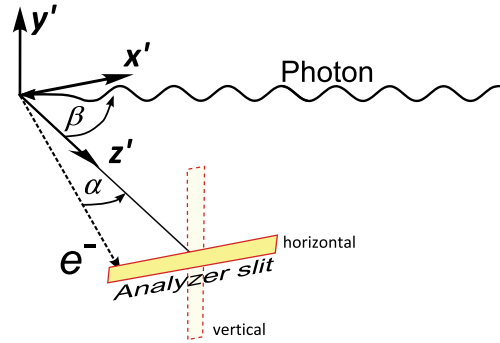


Figure 2.5 – **Laboratory coordinate system** | Adapted from reference [31].

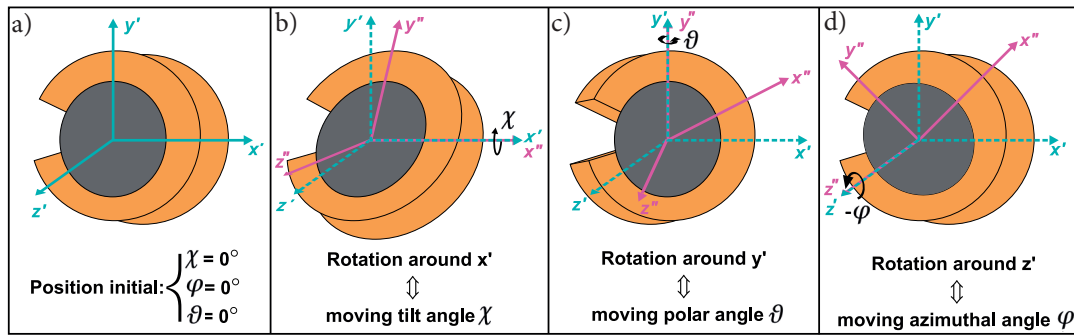


Figure 2.6 – **Manipulator rotational angles** | The gray area indicates the place where the sample holder is inserted. The copper belt around it keeps the holder in position and moves together with it. Prior rotation, the coordinate system of the sample holder overlaps with that of the laboratory, panel (a). Panels (b-d) illustrate the rotation around each of the axis of the laboratory frame. Adapted from reference [31].

contact, a vacuum compatible conductive silver epoxy was employed to fix the samples on the sample holders. To perform the experiment, the sample holder is mounted into the beam line manipulator, which is kept under ultra-high vacuum conditions. To expose fresh, atomically clean surfaces, the samples were cleaved *in-situ*, at pressure $\sim 0.5 \cdot 10^{-10}$ mbar, using a top-post technique or a specially designed cleaving tool [35].

The SIS beamline is equipped with a CARVING manipulator, which has six degrees of freedom. The position of the sample can be translated along and rotated around three axis, fixed in the laboratory frame, x' , y' and z' . As sketched in figure 2.5, z' points to the center of the analyzer and together with x' identifies the mirror plane, defined as the plane where lie both the incident photon momentum and the momentum of the detected photoelectron. The y' direction is orthogonal to the mirror plane. The angle between the direction of the incoming photon beam and the center of the analyzer slit, β , is fixed to 45 deg at the SIS endstation.

2.1. Angle resolved photoemission spectroscopy - ARPES

The ability to rotate the sample around 3 orthogonal axis allows to explore a wide portion of the Brillouin zone within the same experiment. As described in the previous section, the detector measures the photoelectron momentum along the detector axis Θ_x . In the laboratory coordinate system the measured momentum, of modulus k , is given by:

$$\mathbf{k}_{\Theta_x} = k(-\sin \alpha \hat{\mathbf{s}} + \cos \alpha \hat{\mathbf{z}}'); \quad (2.23)$$

where α is the angle between the photoelectron direction and z' and $\hat{\mathbf{s}}$ is a unitary vector whose direction depends on the direction of the analyzer slit. If the slit lies in the mirror plane, it is called horizontal and $\hat{\mathbf{s}}$ corresponds to $\hat{\mathbf{x}}'$. If the slit is perpendicular to the mirror plane, it is called vertical and $\hat{\mathbf{s}} = \hat{\mathbf{y}}'$.

We now want to convert the measured momentum to the sample coordinate system. To do so, it is convenient to refer to the coordinate system of the sample holder, defined as x'', y'' and z'' . We define χ , ϑ and φ the angles of rotation around x', y' and z' , see figure 2.6. To express \mathbf{k}_{Θ_x} into the sample holder coordinate system is sufficient to consider the three, independent, rotation matrices \mathcal{R}_χ , \mathcal{R}_ϑ and \mathcal{R}_φ :

$$\mathbf{k}'' = \mathcal{R}_\chi \mathcal{R}_\vartheta \mathcal{R}_\varphi \mathbf{k}_{\Theta_x}; \quad (2.24)$$

with:

$$\mathcal{R}_\chi = \begin{pmatrix} 1 & 0 & 0 \\ 0 & \cos \chi & \sin \chi \\ 0 & -\sin \chi & \cos \chi \end{pmatrix}; \quad \mathcal{R}_\vartheta = \begin{pmatrix} \cos \vartheta & 0 & -\sin \vartheta \\ 0 & 1 & 0 \\ \sin \vartheta & 0 & \cos \vartheta \end{pmatrix}; \quad \mathcal{R}_\varphi = \begin{pmatrix} \cos \varphi & -\sin \varphi & 0 \\ \sin \varphi & \cos \varphi & 0 \\ 0 & 0 & 1 \end{pmatrix}. \quad (2.25)$$

A misalignment between the a axis of the sample and x'' corresponds to an offset value for the angle φ . Given the angle γ between the c axis of the sample and z'' , we can express the momentum in the sample coordinate system:

$$\mathbf{k} = \begin{pmatrix} \cos \beta & -\sin \beta & 0 \\ \sin \beta & \cos \beta & 0 \\ 0 & 0 & 1 \end{pmatrix} \begin{pmatrix} \cos \gamma & 0 & -\sin \gamma \\ 0 & 1 & 0 \\ \sin \gamma & 0 & \cos \gamma \end{pmatrix} \begin{pmatrix} \cos \beta & \sin \beta & 0 \\ -\sin \beta & \cos \beta & 0 \\ 0 & 0 & 1 \end{pmatrix} \mathbf{k}''. \quad (2.26)$$

2.1.5 ARPES data normalization

To account for differences in the channel efficiency, accurately determine the kinetic energy corresponding to the Fermi level, and estimate the experimental resolution, 2D ARPES intensity maps are collected on the sample and on a polycrystalline metal reference (typically gold, copper or platinum), in thermal and electric contact with the sample.

In panel 2.7(a) is presented a raw ARPES map recorded on polycrystalline copper, kept at 22 K. ARPES data from a polycrystalline metal should have energy dependence given by the

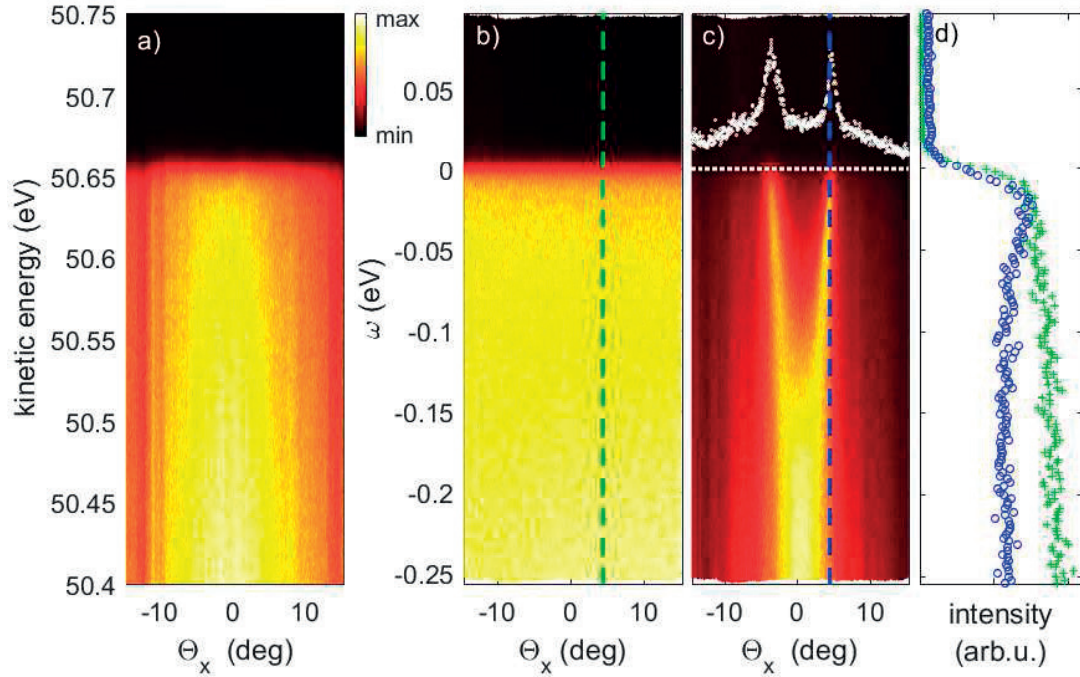


Figure 2.7 – **ARPES data normalization** | a) Raw ARPES intensity map recorded on polycrystalline copper at 22 K, as function of the kinetic energy and the detector angle Θ_x . b) Same map, normalized for the channels efficiency and plotted versus excitation energy $\omega = E_F$ -kinetic energy. The vertical green dashed line indicates at what detector angle was extracted the energy distribution curve shown in panel (d) with green crosses. c) Normalized ARPES intensity map recorded on a sample of $\text{La}_{1.4}\text{Nd}_{0.4}\text{Sr}_{0.2}\text{CuO}_4$, in thermal and electric contact with the polycrystalline copper. The horizontal white dashed line indicates the Fermi level. White dots illustrate the momentum distribution curve at the Fermi level, from which the Fermi momenta can be extracted. The vertical blue dashed line indicates at what detector angle was extracted the energy distribution curve shown in panel (d) in blue open dots. In panels (b) and (c), the intensity across the detector channels is normalized to the integrated intensity of the raw copper data, shown in panel (a). d) Example of energy distribution curves, extracted from panels (b,c).

Fermi Dirac distribution (plus a background due to secondary electrons) and no momentum dispersion. Indeed, the energy distribution curve at each detector channel shows the expected step function profile, see the green crosses curve in panel 2.7(d), but the intensity is not constant across the channels, due to different channel efficiencies. To correct for this effect, the intensity at each detector channel is integrated over the kinetic energy. By dividing the measured ARPES intensity over the raw copper integrated intensity, at each channel, the influence of the channel efficiency is removed, as shown in panel 2.7(b).

To go from the detected kinetic energy to the excitation energy, it is sufficient to evaluate

2.1. Angle resolved photoemission spectroscopy - ARPES

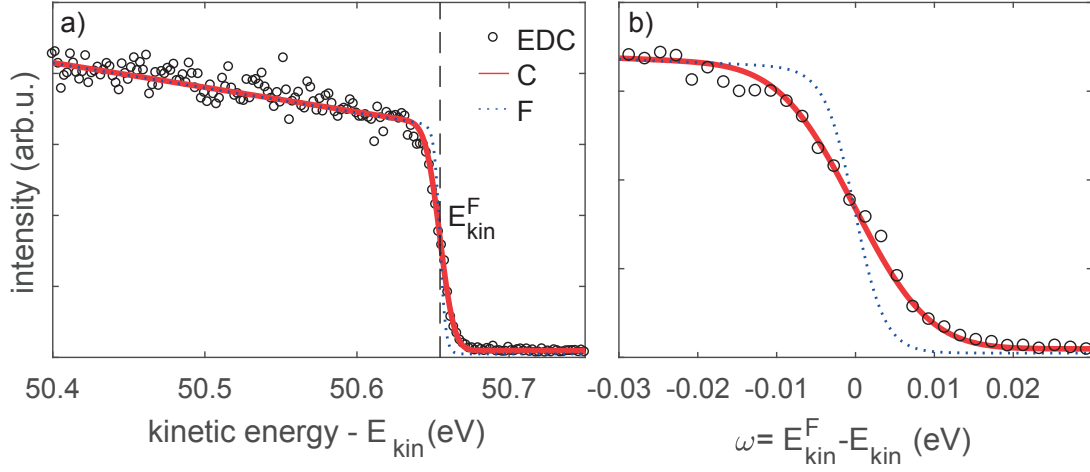


Figure 2.8 – **Extraction of the Fermi level and experimental resolution** | Open dots indicate the ARPES intensity measured on polycrystalline copper, at a certain detector angle (energy distribution curve, EDC). The red line is a fit to the convoluted Fermi Dirac distribution (C), where the value of the temperature was fixed to that measured on the metal (22 K). The unconvoluted Fermi Dirac function is indicated by the blue dotted line (F). The vertical dashed line indicates the extracted value of E_{kin}^F .

what kinetic energy corresponds to photoelectrons excited from the Fermi level, E_{kin}^F . In the case presented in panel 2.7(a), it corresponds to ~ 50.65 eV (incident photon energy was fixed at 55 eV). It is often critical to estimate the value of E_{kin}^F with the highest precision possible (for example if in presence of small gaps). The simplest way to do so, is to fit the energy distribution curve recorded on polycrystalline copper to the Fermi Dirac distribution, at temperatures fixed to the value measured on the metal (typically by thermocouples). To account for the presence of secondary electrons, a linear slope was added to the Fermi Dirac distribution, while finite resolution effects are included by Gaussian convolution. From this fit, illustrated in panel 2.8(a) by a red solid line, the position of the Fermi level and the standard deviation of the Gaussian convolution are extracted, at each channel. The blue dotted line in panels 2.8(a,b) indicates the same function lineshape, without finite resolution effects (without Gaussian convolution the width is only determined by thermal broadening). The Gaussian standard deviation extracted from the convoluted fit represents the effective experimental resolution, which in the studies presented in this thesis varied between 6 and 9 meV. Once E_{kin}^F has been extracted, the detected kinetic energy can be converted to the excitation energy $\omega = E_{kin}^F - E_{kin}$, as illustrated in 2.8(b) in a smaller energy range around E_{kin}^F , to better compare the convoluted and unconvoluted Fermi functions.

An example of normalized ARPES spectra is shown in panel 2.7(c). Routinely, the recorded 2D ARPES intensity maps are analyzed separately in their dependence on momentum and on energy. Momentum distribution curves are extracted at constant excitation energy ω and give the ARPES intensity as function of the photoelectron momentum. The white dotted curve

in panel 2.7(c) is an example of momentum distribution curve, extracted at the Fermi level ($\omega = 0$). In the given example, the spectral weight at $\omega=0$ follows the profile of two Lorentzian curves, over a smooth background. The momenta corresponding to the peaks of the momentum distribution curve at the Fermi level (MDC_F) are defined the Fermi momenta, \mathbf{k}_F .

Energy distribution curves are extracted at a given value of momentum and yield the ARPES intensity as function of the excitation energy. Notice that the energy distribution curve extracted at \mathbf{k}_F (EDC_F) peaks at the Fermi level only in absence of a spectral gap. In panel 2.7(d), the sample EDC_F is compared to the energy distribution curve recorded on copper, in the same channel. By comparing to the Fermi step extracted from polycrystalline copper, it appears that the EDC_F peaks at energies deeper than the Fermi level, while low energy spectral weight seems suppressed, indicating the presence of a spectral gap. In these case, one refers to \mathbf{k}_F as the underlying Fermi momentum.

2.2 Resonant Inelastic X-ray Spectroscopy - RIXS

2.2.1 Physical process

Resonant inelastic X-ray spectroscopy (RIXS) is an extremely versatile spectroscopic technique which probes charge-neutral excitations. In fact, contrarily to photoemission, X-ray scattering does not change the total charge of the target. The RIXS process is a second order process in which the investigated sample absorbs and re-emits highly energetic photons, as depicted in figure 2.9. The optical absorption process contains information about the unoccupied states within the sample and represents an independent investigation tool, X-ray absorption spectroscopy (XAS), which is discussed in section 2.2.2. Resonant inelastic X-ray spectroscopy relies on the ability to resolve the energy of the re-emitted photons, which allows a direct insight into the system excitations. Typically, in a RIXS experiment the samples are first investigated by XAS to accurately identify the system absorption resonances, which are then used to resonantly excite the system.

A monochromatic X-ray photon beam is directed towards the sample, which is initially in equilibrium. The energy of the in-coming beam, $h\nu_{in}$ - in the soft or hard X-ray energy range -, is set to an absorption resonance of the sample, to enhance the cross section of the process. It is important to note that by selecting a specific absorption edge, one controls in which chemical element the optical absorption occurs. Furthermore, the symmetry of the initial state can determine the symmetry of the unoccupied energy level to which the core electron is promoted. These aspects of the absorption process are discussed in section 2.2.2. In the course of a RIXS experiment, one varies $h\nu_{in}$ around the chosen resonance value (typically within ~ 1 eV), to investigate the in- and off-resonance effects.

The system is pushed far from equilibrium, in an intermediate state which is highly unstable due to the presence of a deep core hole. In order to relax, the core hole needs to be filled and the excess energy can be released back in the form of a photon (radiative relaxation). The energy of the re-emitted photon, $h\nu_{out}$, depends on the details of the relaxation event. If the highly-excited electron created by the absorption process falls back into the core level, the system will return to the initial state and the energy of the out-coming photon will be the same as the incident one: $h\nu_{out} = h\nu_{in}$. In this case, the overall process can be regarded as an elastic scattering event. However, any electron can fall into the core hole, so that the photon emerging from the scattering event will have energy $h\nu_{out} \leq h\nu_{in}$. The energy lost in this inelastic process is directly related to the energy difference between the initial and the final states.

Figure 2.10 summarizes the most common excitations that can be accessed via the resonant inelastic process described in this section. The most significant limitation in the observation of the various excitations is the energy resolution, particularly for those falling at low energy loss, where they may merge with the elastic peak.

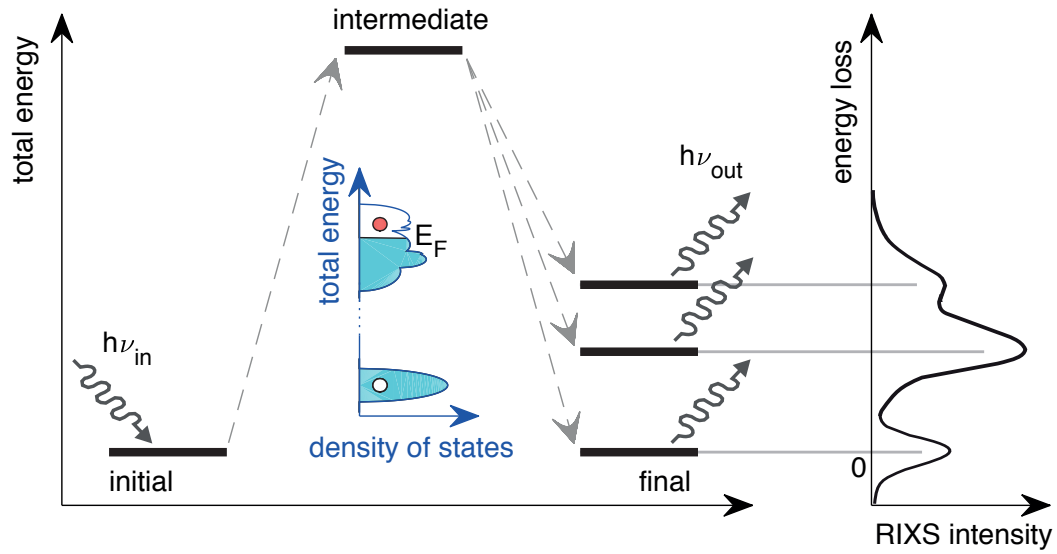


Figure 2.9 – **schematic depiction of the RIXS process** | The absorption of the incoming photons of energy $h\nu_{in}$ brings the system from equilibrium (initial state) to a high energy intermediate state, depicted in the central sketch. In this strongly out of equilibrium state, a core electron is promoted to an unoccupied state above the Fermi level, E_F - and leaves behind a core hole. Many channels can be available for the system to relax into a less out of equilibrium state, in which the core hole is filled and a photon of energy $h\nu_{out}$ is emitted. The energy lost by the out coming photons, $h\nu_{in} - h\nu_{out}$, is in direct correspondence with the energy of the final state.

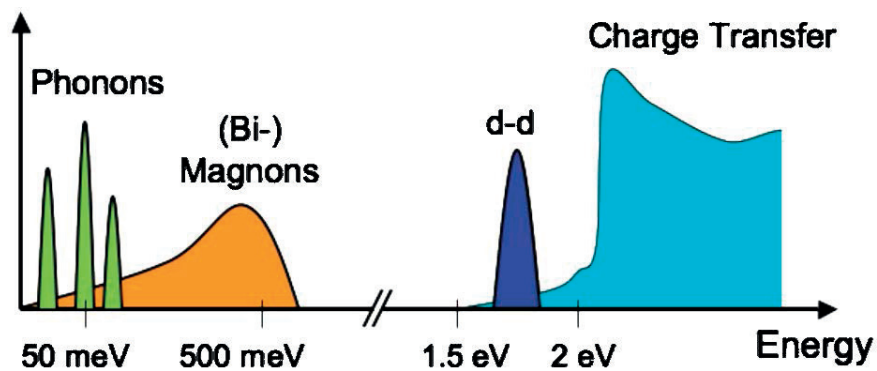


Figure 2.10 – **Excitations accessible by RIXS** | Indicative energy scale of the different excitations accessible by RIXS [25].

2.2.1.1 RIXS cross section

While optical absorption is a first order process, to derive the cross section for the RIXS process the Fermi golden rule should be expanded up to the second order:

$$w_{i \rightarrow f} = \frac{2\pi}{\hbar} \left| \langle f | \mathcal{H}_{int} | i \rangle + \sum_n \frac{\langle f | \mathcal{H}_{int} | n \rangle \langle n | \mathcal{H}_{int} | i \rangle}{E_i + \hbar\nu_{in} - E_n} \right|^2 \delta(E_f + \hbar\nu_{out} - (E_i + \hbar\nu_{in})), \quad (2.27)$$

where $|n\rangle$ indicates the intermediate state of energy E_n , $\hbar\nu_{in}$ the incident photon energy, $\hbar\nu_{out}$ the energy of the re-emitted photons and $|i, f\rangle$ the initial and final states of energies $E_{i,f}$. The direct transition from the initial to the final state represents the non-resonant inelastic scattering and is dominant at generic values of $\hbar\nu_{in}$. If however the incident energy is set to an absorption resonance ($\hbar\nu_{in} \simeq E_n - E_i$), the second term, describing resonant inelastic scattering, diverges and the first term can be neglected.

Resonant inelastic scattering is the result of two first order transitions, happening in sequence (resulting therefore in a second order process), from $|i\rangle$ to $|n\rangle$ and from $|n\rangle$ to $|f\rangle$. To take into account the finite lifetime τ of the intermediate state (the core hole relaxes within femtoseconds), the intermediate energy is considered a complex number, with imaginary part equal to the broadening $\Gamma = \hbar/\tau$.

Resonant scattering can in principle occur both via a magnetic and a non-magnetic term. However, the magnetic term has been shown [25] to be weaker^x. If the interaction between the radiation and the electron spin is neglected, the Hamiltonian connecting each of the first order transitions can be described, within the dipole approximation, by $i\hbar \frac{e}{m_e c} \mathbf{A} \cdot \nabla$, as already discussed within the three step model of ARPES (section 2.1.2).

Within these approximations, the RIXS cross section is described by the Kramers-Heisenberg equation:

$$\mathcal{F}(\nu_{in}, \nu_{out}) \propto \sum_f \left| \sum_n \frac{\langle f | \mathcal{D}^* | n \rangle \langle n | \mathcal{D} | i \rangle}{E_i + \hbar\nu_{in} - E_n - i\Gamma} \right|^2 \delta(E_f + \hbar\nu_{out} - (E_i + \hbar\nu_{in})), \quad (2.28)$$

with $\mathcal{D} = \epsilon \cdot \mathbf{r}$ the dipole absorption operator, $\mathcal{D}^* = \epsilon^* \cdot \mathbf{r}$ the dipole emission operator and ϵ the polarization of the absorbed/emitted photon.

The (coherent) sum over the intermediate state index n , accounts for the eventuality that the process involves more than one intermediate state, as long as their energy difference is smaller than Γ (this possibility is a consequence of the finite lifetime of the core hole). The (incoherent) sum over the final state index f describes the scattering contributions due to different final states and explains the versatility of RIXS. The final state can display excitations

^x10 to 100 times smaller than the non-magnetic term, in the soft X-ray range [36].

of different origins (lattice, magnetic, electronic, *etc.*), which are reflected in the RIXS intensity. The elastic process, corresponding to Thompson scattering, corresponds to the case $f=i$ and contains important information about the charge density of the system. The delta function enforces energy conservation. A complete derivation of the Kramers-Heisenberg equation can be found in references [25, 26, 27].

2.2.2 X-ray Absorption Spectroscopy - XAS

X-ray absorption spectroscopy is a well established experimental technique extensively employed in chemistry, solid state physics and material science for the investigation of molecules, gases, liquids and solids [37, 38, 39]. As discussed for the photoelectric process, when photons carrying sufficient energy are incident on a material, their energy can be absorbed by a bound electron, which is promoted to a previously unoccupied state (within the material), see inset of figure 2.9. In other words, the absorption process coincides with step one of the three step model of photoemission, optical excitation. A very important difference however is that, in the case of X-ray absorption, the state of origin of the excited electron is not in the material valence band but in the deep core levels, which retain a strong atomic character and have a well defined binding energy E_B . In fact, the optical absorption matrix elements allow a fine tuning of the electron initial and final states, as explained in the following.

As a consequence of the absorption process, the intensity I_0 of the beam incident on a sample of thickness t is reduced according to Beer's law [39]:

$$I_T(t) = I_0 e^{-\mu(\nu_{in})t}, \quad (2.29)$$

where $\mu(\nu_{in})$ is the material specific absorption coefficient, which strongly depends on the incident photon frequency, and I_T is the intensity of the transmitted X-ray beam. By varying the energy of the incident photon beam, $\mu(\nu_{in})$ can be determined by measuring the intensity of the incident and transmitted beams. Over wide energy ranges, μ is a smooth function of the incoming energy $h\nu_{in}$:

$$\mu(\nu_{in}) \sim \frac{\rho Z^4}{A(h\nu_{in})^3}, \quad (2.30)$$

where ρ is the sample density and Z and A are the atomic number and mass of the chemical element responsible for the absorption. Starting from low energies and increasing $h\nu_{in}$, a new absorption channel becomes available when the photon energy matches the binding energy of a core electron, which causes a sharp increase of the absorption coefficient. Further increase of the incoming energy results in a lower value of $\mu(\nu_{in})$, according to equation 2.30, until a new absorption resonance is matched and $\mu(\nu)$ exhibits a corresponding steep increase.

The energies corresponding to the discontinuities in $\mu(\nu_{in})$ are referred to as "absorption

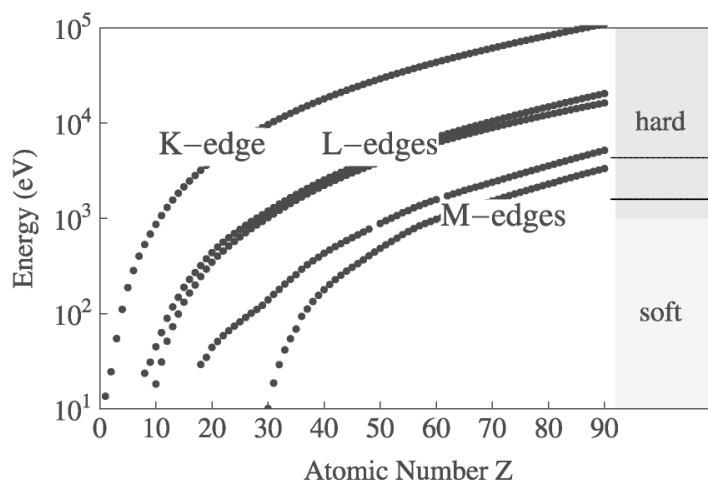


Figure 2.11 – **Dependence on the atomic number Z of the energy of K, L and M absorption edges** | For L and M edges, the highest and lowest energies are shown, corresponding to $L_{1,3}$ (where the core levels involved are within the $2s, 2p^{3/2}$ subshells), and $M_{1,5}$ ($3s, 3d^{5/2}$). The horizontal lines between the hard and soft X-ray energy ranges indicate the energies of 1.5 and 4 KeV. Adapted from reference [25].

edges". These edges occur at the binding energies of all core levels, and are classified according to the main quantum number n of the specific core level involved in the absorption: if the photon energy is absorbed by electrons in the first shell ($n=1$), the relative edge is labeled "K", the second shell corresponds to "L" absorption edges, the third to "M" and so on. Since the core levels retain a strong atomic character, the energy corresponding to each edge is only slightly influenced by a different chemical environment and varies, for each element, roughly as Z^2 , see figure 2.11. The incoming photon energy can therefore be set to a specific resonance, and contributions to the absorption from other elements or other core levels can be treated as a continuous background, see appendix A.1.

Another consequence of the strong atomic character of core levels is the fact that, at each edge, the initial state of the X-ray absorption process has a well defined symmetry. The quantum mechanical optical selection rules therefore place strong constraints on the symmetry of the final state. For example, the K-edge corresponds to the promotion of a $1s$ electron into unoccupied valence orbitals with a strong p character (electric dipole allowed transitions must correspond to a final state with orbital momentum ℓ increased or decreased by a quantum, $\Delta\ell = \pm 1$). Notice that the final state of the absorption process coincides with the RIXS intermediate state.

In conclusion, XAS is a chemical selective spectroscopy, sensitive to the unoccupied density of states as well as the symmetry of the unoccupied states. These characteristics make XAS a suitable probe of the local electronic structure, oxidation state as well as chemical coordination of specific elements within virtually any compound [37, 38, 40].

2.2.2.1 Total fluorescence yield and total electron yield

The absorption coefficient $\mu(v_{in})$ can be directly measured in transmission mode, which requires homogenous sample of thickness in the μm range. Such an experimental configuration is however unpractical, especially when the same sample is to be investigated via RIXS (which does not operate in transmission but rather reflection). A more convenient investigation method relies, similarly to the RIXS technique, on the relaxation of the core hole created in the absorption process. The core hole is filled within $\sim 10^{-15}$ seconds (in the femtoseconds timescale) after optical absorption, by an electron in the valence band of the system. The energy released by the electron which fills the core hole can be released in the form of a photon (radiative relaxation) or can be absorbed by another valence electron (Auger relaxation), which will transit into some unoccupied state within the material and may eventually escape into vacuum. Indirect XAS measures are operated in fluorescent yield mode or electron yield mode, according to which decay products (emitted photons or electrons) are measured.

As a result of the optical absorption and Auger relaxation, photoelectrons, secondary electrons and Auger electrons can escape the sample into vacuum. The samples are routinely grounded so that the emitted electrons (whose number is proportional to the number of absorbed photons) are replaced and the Fermi level of the system is not affected by the process (such a precaution is also adopted in photoemission experiments). In total electron yield (TEY) mode, one measures the current flowing from the ground to the sample, which preserves charge neutrality and is ultimately proportional to the absorbed intensity.

In total fluorescence yield (TFY) mode, photons emitted in the radiative relaxation of the core hole are collected by a detector with a finite angular acceptance. The detector does not resolve the photon energy and can be a photodiode, a channel electron multiplier or a microchannel plane detector. Therefore, in TFY mode out-coming photons are integrated over a finite solid angle and a broad range of photon energies. In other words, the TFY intensity at a certain incident energy $h\nu_{in}$ corresponds to the RIXS intensity at the same incident energy, non resolved in energy or angular dependence of the emitted photons. In the following section it is illustrated how the energy of the emitted photons is resolved by a RIXS spectrometer.

The escape depth of X-ray photons is larger than that of electrons, so that the TEY is more surface sensitive than the TFY. However, TFY can be influenced by self-absorption, *i.e.* the photon emitted in the radiative relaxation process can be re-absorbed by the sample. Self-absorption, if present, is influenced by the experimental geometry (since the probability of self-absorption increases with the sample thickness traversed to escape). Therefore, the lack of geometrical influences on the measured TFY spectra indicates little to no influence from self-absorption. It is good practice to compare the TEY and TFY signals, to evaluate whether the measured profile is affected by systematic errors, due to surface effects or self-absorption.

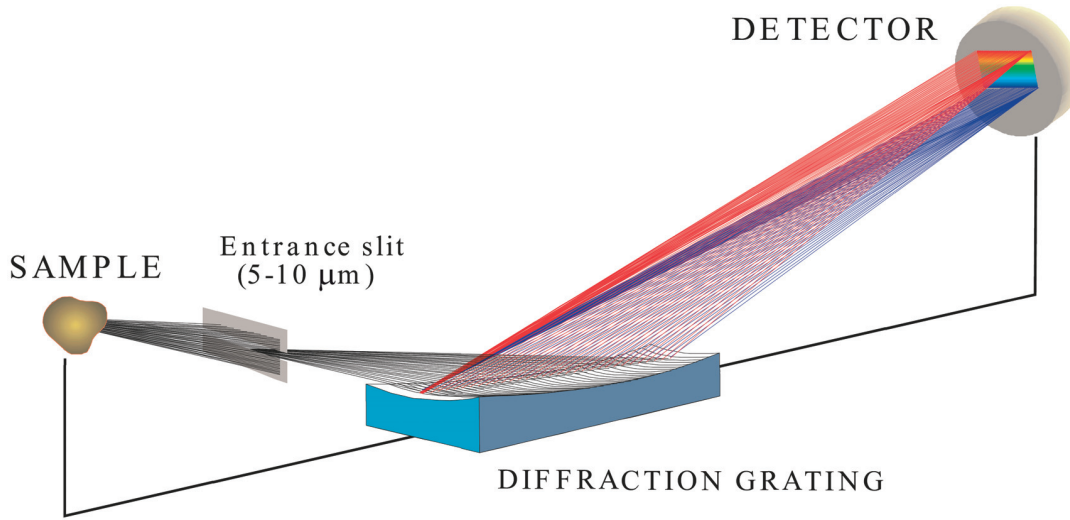


Figure 2.12 – **schematic depiction of a RIXS spectrometer**| The photon beam scattered by the sample is masked by an entrance slit, to select a well defined angle of incidence on the diffraction grating. The grating disperses the polychromatic beam according to the wavelength of its components: photons of different energies hit the detector at different heights. In this way one gains direct experimental access to the energy distribution of the scattered beam [adapted from [36]].

2.2.3 Dispersion in energy loss

Figure 2.12 illustrates the experimental realization of a RIXS spectrometer. The highly excited sample relaxes radiatively and emits x-ray photons in a large solid angle. The position of the detector defines the direction of measure and an entrance slits reduces the angular distribution of the out-coming polychromatic beam. The resolution in energy is obtained through diffraction, which disperses the beam, with photons of different energies scattered in different directions. The height of the detector determines the energy range to be measured (typically $\approx 5\text{-}15\text{ eV}$ around the central value), and needs to be adjusted when the energy of the in-coming monochromatic beam is changed by more than $\approx 10\text{ eV}$ (for example if different absorption edges are explored).

At a synchrotron, monochromatic photon beams of sufficient intensity can be obtained in a wide range of energies. For the diffraction to be effective, the spacing of the diffractometer has to be in the same order of magnitude as the photon wavelength. This is the same mechanism employed to select a specific energy from the Bremsstrahlung emission of the relativistic electrons circling in the synchrotron ring. Hard X-ray photons have wavelength in the order of the Angstrom ($\lambda \approx 1\text{-}3\text{ \AA}$ for $h\nu \approx 4\text{--}15\text{ KeV}$), and efficient diffraction can be obtained from crystals. The longer wavelength of soft X-ray photons well adapts to the groove spacing in grating monochromators, but only for $h\nu \leq 1.5\text{ KeV}$ ($\lambda \geq 8\text{ \AA}$).

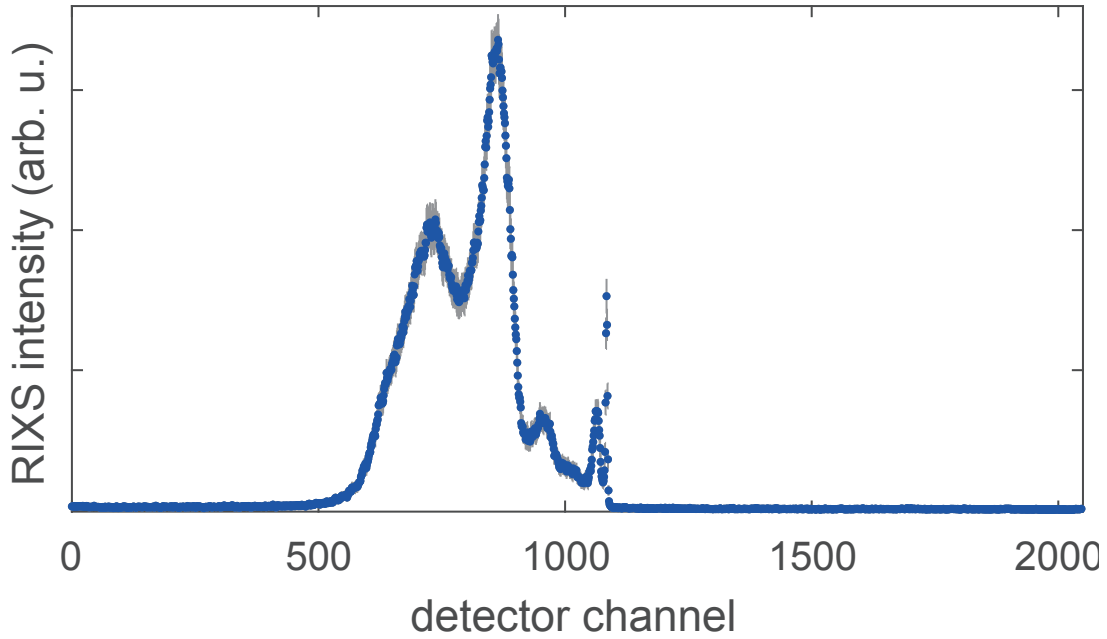


Figure 2.13 – **Raw RIXS spectrum** | taken on Ca_2RuO_4 with incident energy of 529.9 eV and linear horizontal polarization (parallel to the scattering plane). Gray bars indicate the uncertainties.

Figure 2.13 shows an example of RIXS spectrum as recorded by the detector at the high resolution ADRESS beamline of the Swiss Light Source, which operates in the soft X-ray energy range and employs plane diffraction gratings. Each of the detector channels corresponds to a specific photon energy, and is numbered with increasing energy. The energy difference between 2 adjacent channels is equal to 17.5 meV. As explained earlier, the energy of the central channel is not known *a priori* (but changes with the height of the detector). Figure 2.14 illustrates the energy calibration procedure.

The value of $h\nu_{in}$ puts an upper limit to the values of $h\nu_{out}$ that can be recorded, with $h\nu_{out}=h\nu_{in}$ for elastic events. Therefore by fitting the elastic peak (excitation observed at the highest detector channel) to a Gaussian, one can extract the channel corresponding to the energy value of $h\nu_{in}$:

$$F_{el}(x) = Ie^{-\frac{(x-c)^2}{2\sigma^2}} \quad (2.31)$$

With x = detector channel, c center of the elastic resonance of intensity I and full width at half maximum (FWHM) given by $2\sqrt{2\ln 2}\sigma$.

The center of the Gaussian is the channel corresponding to the value of the in-coming energy, while the FWHM gives an estimate of the experimental energy resolution.

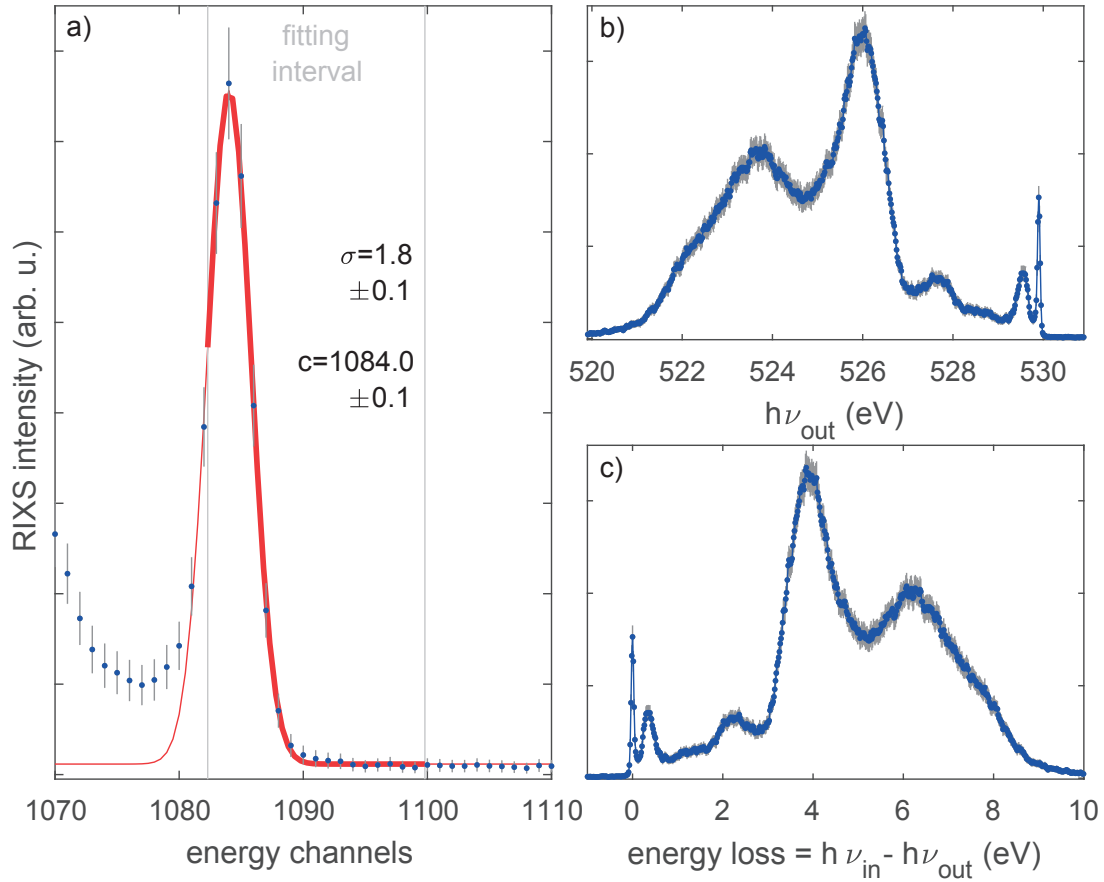


Figure 2.14 – **Calibration procedure of a RIXS spectrum** | taken on Ca_2RuO_4 with incident energy of $h\nu_{in} = 529.9$ eV and linear horizontal polarization. A) The red solid line is a Gaussian fit of the elastic peak. The values extracted for the center, c and the standard deviation, σ , are indicated in the figure. The fit is plotted in a thicker line within the region of fit (marked by the gray vertical lines), which is restricted to just after the peak on the left side, to avoid broadening due to possible contributions from low energy excitations (see figure 2.10). The full width at half maximum (FWHM), $\approx 2.35 \cdot \sigma$, gives an estimate on the energy resolution of the experiment, the position of the center of the elastic peak. b,c) calibrated spectrum, is a function of the energy of the out-coming beam, $h\nu_{out}$, or of the energy loss $= h\nu_{in} - h\nu_{out}$.

If the elastic peak on the sample is suppressed or there are low energy excitations partially or totally covering it, it is useful to take a reference on amorphous carbon (it is sufficient to apply some carbon tape next to the sample, at approximately the same height as the sample surface). The carbon tape reference in RIXS can be thought of as equivalent to the polycrystalline metal reference in ARPES. In fact, the elastic signal recorded on the carbon tape is also useful to derive the energy resolution, since its width is not affected by low energy features.

As illustrated in figure 2.10, a wide range of excitations are probed by the RIXS process, and,

on the sample, the presence of some very low energy loss features cannot be excluded. These would fall very close to the elastic peak of the sample, and could broaden its profile, on the lower energy side. For this reason the Gaussian fit is restricted to just after the peak, as indicated by the thicker red line in panel 2.14(a). In the case of the example, the agreement between the fit of the elastic peak and the data remains satisfying in a larger range, indicating absence of excitations at very low energies. It is important to check that the width extracted is equal, within a few percent, to that obtained from coplanar amorphous carbon.

Once the center of the elastic peak has been determined, the channels of the detector can be converted to the corresponding value in energy. The calibrated spectrum is shown in panels 2.14(b,c), where the intensity of the RIXS signal is plotted versus the value of $h\nu_{out}$, panel 2.14(b), or that of the energy loss $= h\nu_{in} - h\nu_{out}$, panel 2.14(c).

2.2.4 Dispersion in incident energy

Varying the energy of the monochromatic incident beam enables us to follow the evolution of the observed feature as function of incident energy. This possibility proves particularly useful in the identification of Raman-like vs fluorescent-like excitations, as explained below and shown for a practical example in appendix A.4.

The absorption of the in-coming photon brings the system strongly out of equilibrium, since it involves the assimilation of an enormous amount of energy (in the order of 100 eV or more, compared to typical energy scales of the order of the eV, or less). To return into a more stable state, many relaxation channels are available to the system. This situation is illustrated in figure 2.9. These channels can be classified according to their dependence on the energy of the incident or scattered photon.

Relaxation through a Raman channel leaves the system into a final state of well defined energy ΔE_R . As a consequence, varying the amount of incident energy results in a parallel change in the amount of energy released, since the system cannot retain more energy than ΔE_R . Fluorescence on the other hand is observed if, in the final state, the system can accommodate a wide range of energies (*i.e.* the final state belongs to a continuum of states). In this situation, the amount of energy released in the relaxation does not correlate with the amount of energy supplied to the system. A higher (or lower) incident photon energy does not affect the energy of the re-emitted photon, but rather the amount of energy retained by the system. In other words, varying the incident photon energy $h\nu_{in}$, Raman-like excitations manifest themselves at constant energy loss $= \Delta E_R$, while the energy loss related to fluorescent processes depends linearly on the incident energy, since in this case is $h\nu_{out}$ to remain constant.

Excitations of Raman character are for example the excitation of collective modes (photon, plasmon, magnon, *ect.*) or the effective transfer of an electron between valence orbitals with small band widths ($d - d$ excitations). If the bandwidth extends over a significant range of

energies, as is the case of oxygen states for example, the relaxation process assumes a fluorescent character. A common fluorescent excitation observed in transition metal oxides is charge transfer. To discuss the nature of this excitation is convenient to refer to a practical example.

Lets consider the case of oxygen K edge absorption resonance in the ruthenates. If we limit ourselves to the RuO_2 planes and consider the $4d$ ruthenium orbitals and the $2p$ oxygen ones. The total number of electrons occupying $\text{O}2p\text{-Ru}4d$ the valence states are 16, of which 12 are mostly localized around the strongly electronegative oxygen atoms and 4 spending most of their time near the ruthenium ones.

The excitation of a $1s$ oxygen core electron into the $\text{O}2p\text{-Ru}4d$ states causes a redistribution of the charge. In the strongly out of equilibrium intermediate state, there is an extra electron into the $\text{O}2p\text{-Ru}4d$ valence states which has to be (mostly) localized around the ruthenium atom. Notice that in a purely ionic model the $\text{O}1s \rightarrow \text{O}2p$ transition would be prohibited, since there would be no states available for the core electron to transit to.

In the final state, the core hole is filled and there are again 16 electrons in the $\text{O}2p\text{-Ru}4d$ states. Charge transfer occurs if the final charge distribution features 5 electrons, instead of the initial 4, mostly delocalized around the ruthenium nucleus, with a hole left in the oxygen states. Since the oxygen valence band extends over a wide range of energies^{xi}, in this final configuration the system can retain a similarly wide range of energies, which explains the observed fluorescent character of this relaxation channel. As a final remark, it is worth to mention that a redistribution of charges is energetically expensive, and it occurs at energy loss larger than 2 eV - as illustrated in figure 2.10.

2.2.5 Dispersion in momentum

In this section we discuss the conservation of momentum in the RIXS process, which gives access to the momentum dispersion of the observed excitations. For simplicity, we consider only the elastic case, where the in-coming and out-coming photons have same energy. The error introduced in this fashion is negligible, since an energy difference of 10 eV only changes the photon momentum by $\sim 5 \cdot 10^{-3} \text{ \AA}^{-1}$, and we operated in the soft X-ray regime where photons carry a momentum of the order of 10^{-1} \AA^{-1} ^{xii}.

In figure 2.15 the elastic scattering geometry is depicted for two case: specular condition in panel 2.15(a), and general in panel 2.15(b). The incident and scattered beams have momentum \mathbf{K}_{in} and \mathbf{K}_{out} , respectively, with $|\mathbf{K}_{\text{in}}|=|\mathbf{K}_{\text{out}}|=K$ (elastic process). The scattering angle α between \mathbf{K}_{in} and \mathbf{K}_{out} is generally fixed within each experiment (but can be varied upon necessity, by rotating the RIXS spectrometer). In our case it was fixed to $\alpha=50^\circ$, by the experi-

^{xi}The oxygen K absorption edge exhibits significant intensity from ~ 529 eV to 550 eV and more, see section 4.2.

^{xii}More specifically, our in-coming beam had energies varying between ~ 527 eV and ~ 531 eV, corresponding to a wavelength of $\sim 23.4 \text{ \AA}$ and a momentum of $\sim 0.268 \text{ \AA}^{-1}$.

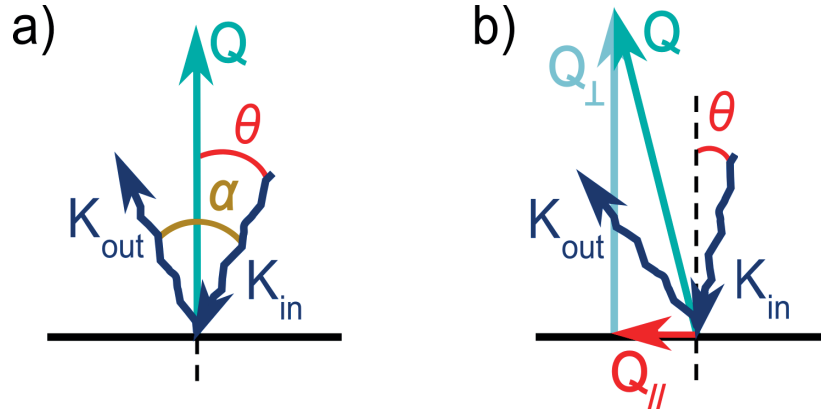


Figure 2.15 – **Scattering geometry of the elastic process** | θ is the angle between the normal to the sample surface and the momentum of the incident beam, \mathbf{K}_{in} . The scattering angle, α , is fixed by the direction of incidence and the direction of the RIXS spectrometer, which collects the out-coming beam of momentum \mathbf{K}_{out} . In the process, the momentum $\mathbf{Q} = \mathbf{K}_{out} - \mathbf{K}_{in}$ is transferred to the crystal. (a) \mathbf{Q} is perfectly orthogonal to the sample for $\theta = \alpha/2$, corresponding to the specular condition and enhancement of the elastic signal. (b) At all other values of θ , \mathbf{Q} has both an orthogonal and in-plane component, \mathbf{Q}_{\perp} and \mathbf{Q}_{\parallel} .

mental set up. θ is the angle between the normal to the sample surface and \mathbf{K}_{in} .

The scattering process involves the transfer of momentum $\mathbf{Q} = \mathbf{K}_{out} - \mathbf{K}_{in}$ to the sample, with direction defined by the bisector to α and modulus:

$$|\mathbf{Q}| = |\mathbf{K}_{out} - \mathbf{K}_{in}| = 2K \cos \frac{\alpha}{2} = 2 \frac{2\pi}{12.4} h\nu \cos(25^\circ) \simeq 0.92 \cdot h\nu \text{ \AA}^{-1} \quad (2.32)$$

In the case of $\alpha=50^\circ$ and with the photon energy expressed in KeV. In the case of the data presented in section 4.3, $h\nu \simeq 530 \text{ eV}$ and $|\mathbf{Q}| \simeq 0.49 \text{ \AA}^{-1}$. In the case of 2D, or quasi-2D systems, the quantity of interest however is the projection of \mathbf{Q} on the sample surface, which depends on the incident angle θ :

$$\begin{aligned} \mathbf{Q} &= \mathbf{Q}_{\perp} + \mathbf{Q}_{\parallel} = q_{\perp} \hat{\mathbf{e}}_{\perp} + q_{\parallel} \hat{\mathbf{e}}_{\parallel} \\ q_{\perp} &= |\mathbf{Q}| \cos \left(\frac{\alpha}{2} - \theta \right) \simeq 0.92 \cos(25^\circ - \theta) \cdot h\nu \text{ \AA}^{-1} \\ q_{\parallel} &= |\mathbf{Q}| \sin \left(\frac{\alpha}{2} - \theta \right) \simeq 0.92 \sin(25^\circ - \theta) \cdot h\nu \text{ \AA}^{-1} \end{aligned} \quad (2.33)$$

The specular condition is realized for $\theta = \alpha/2$, see panel 2.15(a). In this case, the momentum transferred to the sample is perpendicular to the sample surface: $\mathbf{Q} = q_{\perp} \hat{\mathbf{e}}_{\perp}$. For all other values of θ , the scattering process involves a momentum transfer along the plane of the sample, as shown in panel 2.15(b). Through this mechanism, the energy vs momentum dispersion of the observed excitations can be accessed.

3 Normal state fermiology of cuprates

Among transition metal oxides, cuprates are probably the most investigated compounds [22, 42, 43, 44]. These materials in fact exhibit a number of fascinating and unsolved physical phenomena, such as unconventional superconductivity, anti-ferromagnetic insulation, spin and charge modulation, anisotropic partial gapping and strange metallicity.

As illustrated in figure 3.1, these phenomena generally occur in close vicinity, when varying the composition and/or temperature, so that the relation connecting the one to the other is not evident. In fact, strongly correlated systems have a tendency for avalanches, where one electron instability triggers or facilitates another. To understand these phenomena therefore one should distinguish the driving mechanism from the secondary effects, which proves

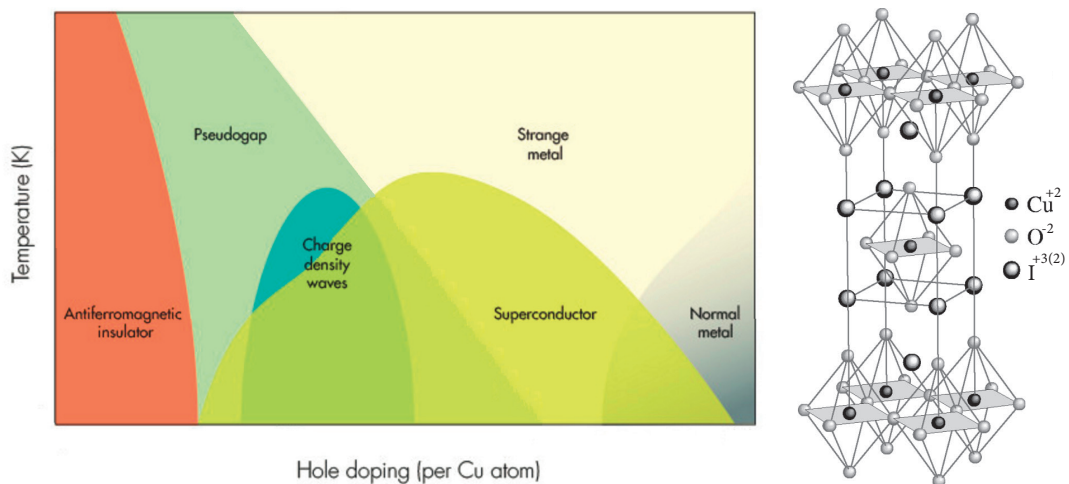


Figure 3.1 – **Cuprates phase diagram** | as function of temperature and hole doping. Adapted from reference [41]. The inset on the right shows the crystal structure of single layered cuprates, with indication of the valence states of each element. Substitution of interstitial elements at valence state +3, I^{+3} , with others at valence state +2, I^{+2} , corresponds to hole-doping the system. Adapted from reference [22].

extremely challenging.

The observation of the pseudogap, charge order, and superconductivity in the same region of the phase diagram triggers questions about their origin as well as relation. Do they arise as competing mechanism, or are they precursor to each other? Moving towards the right extrema in the phase diagram, one finds the strange metal phase, with gapless excitations that do not follow the Drude-Sommerfeld model and whose microscopic description is still missing.

The compounds employed for our study have a single-layered perovskite crystal structure, composed by a single layer of oxygen octahedra enclosing a copper atom and separated by interstitial elements, indicated as I, at valence states +3 or +2 (for example lanthanum, strontium, barium, europium or neodymium), see inset of figure 3.1. The hole content is given by the amount of I^{+2} atoms present in the crystal, per copper atom. Optimally doping corresponds to the maximum in the superconducting transition temperature, while crystals with a smaller (higher) hole content are called under(over)-doped.

In this section we will present our angle resolved photoemission spectroscopy results on the physics of the normal state of cuprates, outside of the superconducting phase. In particular, we will focus on the properties of low energy excitations in the strange metal phase, on the over-doped side of the phase diagram (section 3.1) and in the charge order and pseudo gap phases, found in the underdoped side (section 3.2).

3.1 Self-energy and quasiparticle renormalization effects

This section is devoted to a discussion on the nature of low energy nodal excitations in overdoped cuprates. The notion of "quasi-particle" underlies modern understanding of many condensed matter problems [45]. Electrons in solids are well known examples: the crystalline potential affects their physical description and they exhibit a different dispersion than in vacuum. The effects of the periodic potential can be accounted for by a mass normalization [46]. An *effective mass* is thus assigned to the electrons, which are consequently described as quasi-particles.

When the electronic interactions cannot be neglected, as happens in strongly correlated materials, a further mass normalization occurs to include these effects, and the quasi-particles are said to be "dressed" by the correlations. The effective mass assigned to the electronic quasi-particles as a result of the crystalline periodic potential only (in absence of electronic correlations) is called "bare-mass", m_b . The dispersion that the quasi-particles would follow in this case is called bare-band ε_b , as opposed to the experimentally observed renormalized dispersion ε_k .

It is useful to describe the quasi-particles in terms of their self-energy, $\Sigma = \Sigma' + i\Sigma''$. While the imaginary part of the self energy Σ'' describes the lifetime of the quasi-particles, the real part Σ' determines their renormalized mass m^* . In particular, for electrons (or holes) in strongly correlated materials such as the cuprates, the renormalized mass m^* is generally given by $m_b/m^* = Z\hat{Z}$, where $Z = (1 - \frac{\partial \Sigma'}{\partial \omega})^{-1}$ and $\hat{Z} = 1 + (m_b/\hbar^2 k_F) \partial \Sigma'(k, 0)/\partial k$ [47], with ω , k excitation energy and momentum and k_F Fermi momentum. If the self energy is momentum independent, the quasi-particle mass is given by $m^* = m_b/Z$, where Z indicates the quasi-particle residue: $Z^{-1} \equiv 1 - \frac{\partial \Sigma'}{\partial \omega}$

We provided an ARPES proof, published in reference [48], that the self energy of low energy excitations in the strange-metal phase of cuprates satisfies the mathematical conditions for Landau Fermi liquid quasi-particles [49, 50, 51], namely:

1. $\Sigma'' \propto \omega^2$
2. $-Z \bullet \Sigma'' < |\omega|$

For convenience, in this discussion the excitation energy ω is defined positive.

Generally, both Z and Σ are functions of the bare-band velocity $v_b = \frac{\partial \varepsilon_b}{\partial k}$, which is not experimentally accessible. Because of the difficulty in the determination of Σ and v_b [52], the exact nature had not yet been proved by ARPES, although the Landau quasi-particle terminology has been widely used to describe these excitations. This task was made possible by the availability of high quality nodal spectra of $\text{La}_{1.77}\text{Sr}_{0.23}\text{CuO}_4$, recorded as part of the detailed Fermi surface study performed by J. Chang, M. Månsson, S. Pailh  s, T. Claesson, O. J. Lipscombe,

S. M. Hayden, L. Patthey, O. Tjernberg and J. Mesot - published in reference [53] and briefly summarized in section 3.1.1. The analysis of the nodal spectra is presented in section 3.1.2, and the results are discussed in sections 3.1.3 and 3.1.4 and summarized in section 3.1.5.

3.1.1 Fermi surface of $\text{La}_{1.77}\text{Sr}_{0.23}\text{CuO}_4$

The scope of this section is to outline the main results of the Fermi surface study to which belongs the ARPES data used for our proof.

J. Chang *et al.* [53] used angle resolved photo emission to determine the Fermi surface of $\text{La}_{1.77}\text{Sr}_{0.23}\text{CuO}_4$ and extract the imaginary part of the self energy, Σ'' . The ARPES study was performed out of the superconducting phase, into the strange-metal state of the system. Gapless excitations were observed across the full Fermi surface, illustrated in the top left inset of figure 3.2.

Interestingly, the self energy dependence on the excitations energy ω was found to be highly anisotropic. Around the Fermi level, Σ'' would exhibit a quadratic dependence on ω in ARPES data taken along the Brillouin zone diagonal (nodal direction, corresponding to a Fermi surface angle $\phi \simeq 45^\circ$), and a linear dependence (not compatible with Fermi liquid quasi-particles) in data taken along the main Brillouin zone axis (anti-nodal direction, $\phi \simeq 0^\circ/90^\circ$).

Furthermore, at a given Fermi surface angle ϕ , a cut off energy value ω_c was identified, with $\Sigma'' \propto \omega$ for $\omega > \omega_c$. The value of ω_c , which defines the energy interval in which $\Sigma'' \propto \omega^2$ (compatible with Landau quasi-particle), undergoes a gradual evolution with the Fermi surface angle ϕ , as documented in figure 3.3.

3.1.2 Analysis of nodal ARPES spectra

Studying the Fermi surface of $\text{La}_{1.77}\text{Sr}_{0.23}\text{CuO}_4$, J. Chang *et al.* [53] have found arcs of Fermi-liquid-compatible quasi-particles (at excitation energy < 200 meV), separated by gapless non-Fermi liquid excitationsⁱ. The subsequent analysis presented in this and the following sections aimed at an experimental proof of the Fermi-liquid nature of the nodal low energy excitations.

The nodal ARPES data is presented in figure 3.4. Panel 3.4(a) displays the ARPES intensity $\mathcal{I}(\omega, k)$, recorded along the cut shown in the inset of panel 3.4(c), as function of the excitation energy ω and momentum $k - k_F$, where k_F indicates the Fermi momentum. The momentum distribution curves (MDCs) shown in panel 3.4(b) represent the ARPES intensity $\mathcal{I}(\bar{\omega}, k)$ as function of the momentum, at constant excitation energy $\bar{\omega}$ as indicated. The Fermi momentum k_F is extracted from the MDC at the Fermi energy, corresponding to $\omega = 0$ (see section 2.1). The energy distribution curves (EDCs) shown in panel 3.4(c), on the other hand, indicate

ⁱIn the pseudo gap phase a similar anisotropy is observed, but in that case the gapless excitations found in the so-called Fermi arcs are separated by gapped excitations.

3.1. Self-energy and quasiparticle renormalization effects

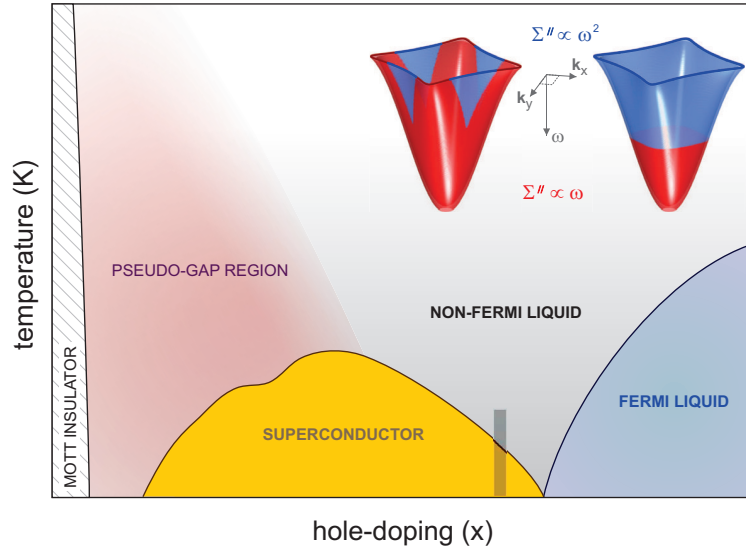


Figure 3.2 – **$\text{La}_{2-x}\text{Sr}_x\text{CuO}_4$ phase diagram** | and Fermi surface at hole content $x=0.23$, indicated by the vertical bar. The system evolves from a Mott insulator, for $x=0$, to a Fermi metal, for $x=2$. At intermediate values of x , the system exhibits a pseudogap phase and a superconducting ground state. In a strongly correlated Fermi liquid, the imaginary part of the self energy is expected to scale with the excitation energy squared, $\Sigma'' \propto \omega^2$, as illustrated in the top left inset. J. Chang *et al.* [53] report a breakdown of the Fermi liquid description in the Fermi surface of $\text{La}_{1.77}\text{Sr}_{0.23}\text{CuO}_4$, illustrated by the top left inset. Blue indicates an observed self energy compatible with Fermi liquid quasi-particles, red a non-Fermi liquid behavior ($\text{Im}\Sigma'' \propto \omega$). Adapted from reference [53].

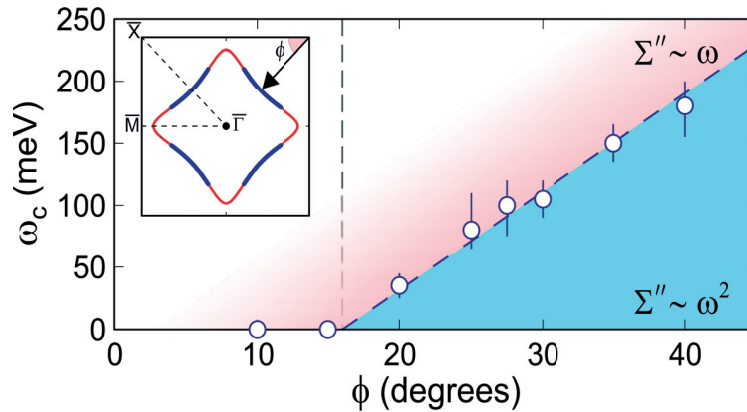


Figure 3.3 – **Anisotropy of Σ''** | Fermi liquid cutoff energy ω_c as function of the Fermi surface angle ϕ . Blue indicates an observed self energy compatible with Fermi liquid quasi-particles ($\Sigma'' \propto \omega^2$), red a non-Fermi liquid behavior ($\Sigma'' \propto \omega$). Adapted from reference [53].

the ARPES intensity $\mathcal{I}(\omega, \bar{k})$ as function of the excitation energy, for constant values of the momentum $\bar{k} - k_F$ as indicated. Note that an ω -dependent background was subtracted to the EDCs. The background was estimated from an EDC at momentum $k - k_F = 0.089\text{\AA}$, away from the dispersive features [53, 54], indicated by the vertical dashed line in panel 3.4(a). To double-check the background removal, EDCs at $k > k_F$ are shown in open circles at the bottom of panel 3.4(c). The same background was subtracted to all EDCs, but only those taken at $k > k_F$ appear featureless. Solid lines in panel 3.4(b) are fits to a Lorentzian function (equation 3.1), while the solid lines in panel 3.4(c) display the ω dependence of the ARPES intensity function derived in the following, which consistently describes both MDCs and EDCs, see equation 3.15.

We start our discussion with the momentum dependence of the ARPES intensity at constant excitation energy, *i.e.* the momentum distribution. The MDCs lineshape consists of symmetric peaks on constant background that can be empirically modeled by a Lorentzian function:

$$\mathcal{I}(\bar{\omega}, k) \equiv I_0 \frac{\Gamma}{(k - \bar{k})^2 + \Gamma^2} + C_{BG} \quad (3.1)$$

where Γ is the Lorentzian width (half width at half maximum), \bar{k} the peak position, I_0 the peak intensity and C_{BG} a constant background. From fitting of MDCs taken at different value of $\bar{\omega}$ to equation 3.1, the excitation dispersion $\varepsilon_k = f(\bar{k})$ can be extracted. At low excitation energy, this analysis yields a linear dispersion:

$$\varepsilon_k \simeq v_F(k - k_F) \quad (3.2)$$

with slope given by the Fermi velocity $v_F = 1.62(2) \text{ eV\AA}$ - in agreement with values previously derived on $\text{La}_{2-x}\text{Sr}_x\text{CuO}_4$ [55, 56].

The Lorentzian width Γ extracted is reproduced in figure 3.5, for the two cuts indicated by the color-coded bars in the top left inset, as a function of the excitation energy squared, ω^2 , and as a function of ω in the lower right inset. Γ is found to follow a quadratic law for $\omega < \omega_c = 0.18 \pm 0.02 \text{ eV}$, and a linear one for $\omega > \omega_c$. In the quadratic range:

$$\Gamma \simeq \Gamma(0) + \eta\omega^2 \quad (3.3)$$

with $\eta = 3.14(4) \text{ eV}^{-2}\text{\AA}^{-1}$ and $\Gamma(0) = 0.0117(1) \text{ \AA}^{-1}$ ⁱⁱ.

To obtain a consistent description of the EDC lineshape, we need to model the spectral function $\mathcal{A}(\omega, k)$, detailed in the following section.

ⁱⁱReported values of the elastic scattering $\Gamma(0)$ in $\text{La}_{2-x}\text{Sr}_x\text{CuO}_4$ are typically higher [56, 57]. Since impurity scattering contribute to the elastic scattering [58], lower values of $\Gamma(0)$ could indicate higher sample purity.

3.1. Self-energy and quasiparticle renormalization effects

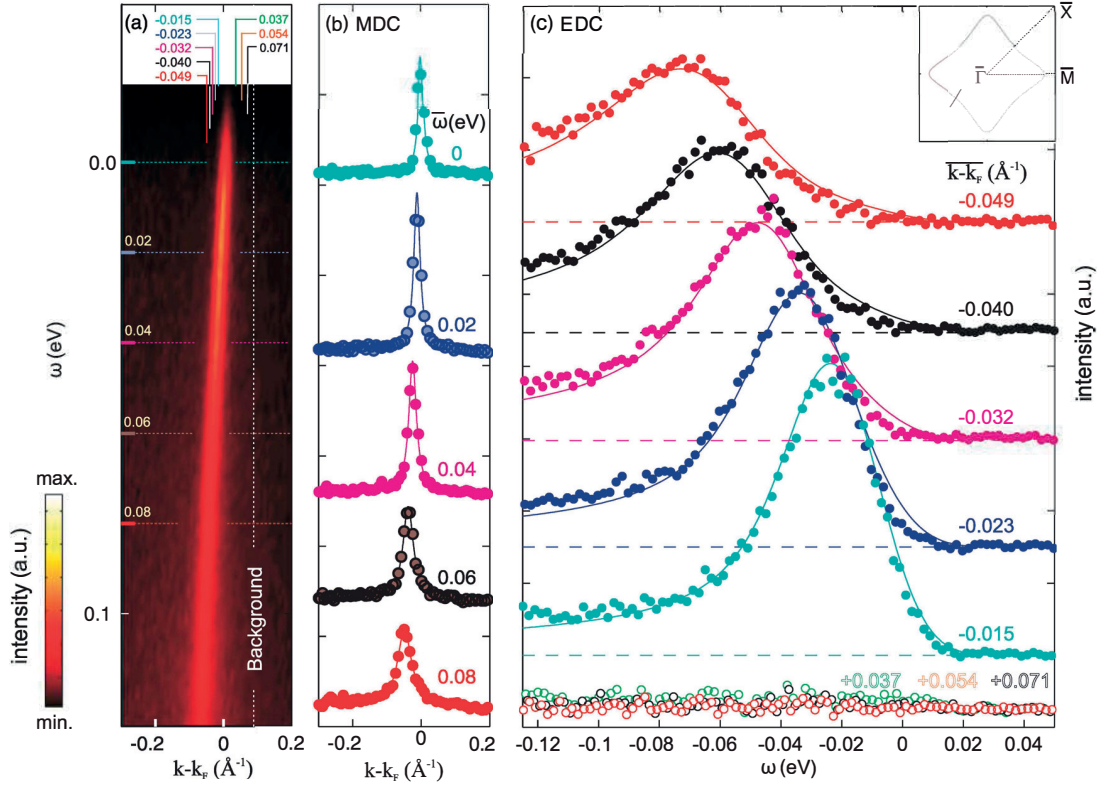


Figure 3.4 – **Nodal ARPES spectra and selected distribution curves** | recorded on cleaved [35] samples of over-doped $\text{La}_{2-x}\text{Sr}_x\text{CuO}_4$ ($x = 0.23$), at $T = 15$ K with 55 eV incident photon energy and circular polarization. The experiment was performed at the surface and interface spectroscopy beam line of the Swiss Light Source (SLS, Paul Scherrer Institute, Switzerland), under ultra-high vacuum conditions ($p \sim 10^{-11}$ mbar) [53]. a) ARPES intensity, indicated by the colorbar, displayed versus momentum $k - k_F$ (horizontal) and excitation energy ω (vertical). Color-coded horizontal and vertical bars indicate at which value of ω or $k - k_F$ where extracted the curves reproduced in panels (b,c), respectively. The vertical white dashed line indicates the ω dependent background, subtracted to the curves displayed in panel (c). b) Momentum distribution curves (MDCs) of the spectra shown in (a), at constant $\bar{\omega}$ as indicated. Solid lines are Lorentzian fits to the data. c) Energy distribution curves (EDCs) recorded at momenta $\bar{k} - k_F$ as indicated. An ω dependent background, taken at momentum $k - k_F = 0.089 \text{ \AA}^{-1}$, was removed from the EDCs. The horizontal dashed lines indicate zero net intensity (after the background removal) for the corresponding EDC. Note that curves taken at $k > k_F$ appear featureless. Solid lines display the ω -dependence of equation 3.15, convoluted with the instrumental resolution ($\sigma_{exp} = 9 \text{ meV}$). The Fermi surface of $\text{La}_{1.77}\text{Sr}_{0.23}\text{CuO}_4$ [53] is shown in the inset, with the black bar indicating the cut along which the ARPES spectra were recorded. The curves in panels (b) and (c) were arbitrarily shifted to improve visibility. Adapted from reference [48].

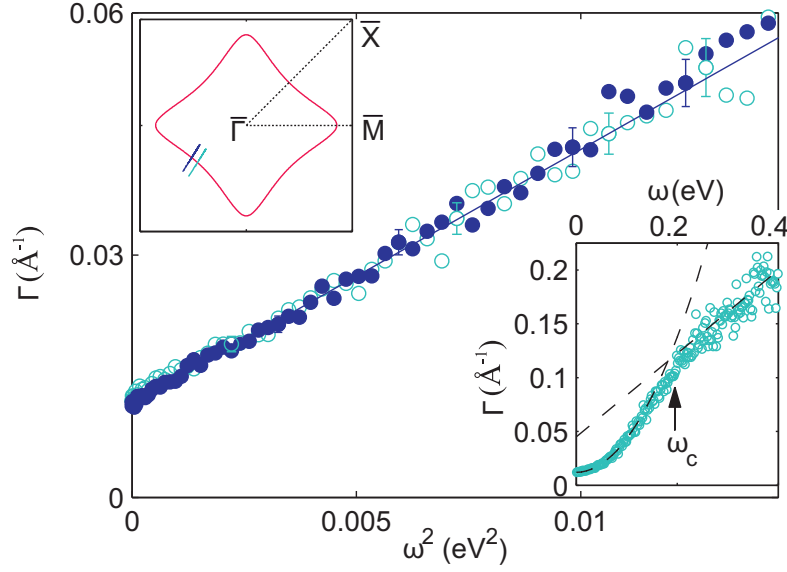


Figure 3.5 – **Low energy excitation linewidth** | extracted from the fits of the momentum distribution curves (MDCs) of ARPES spectra taken along the two cuts illustrated by the bars in the top left inset. The linewidth Γ is plotted versus the excitation energies squared (ω^2). Bottom right inset shows Γ vs ω . The arrow indicates the energy ω_c at which the ω -dependence of Γ changes from quadratic to \sim linear. Adapted from reference [48].

3.1.3 Spectral function model

As discussed in section 2.1, the photoemission intensity $\mathcal{I} = \mathcal{I}(\omega, k)$ can be modeled, within the three step model [22], by the spectral function $\mathcal{A}(\omega, k)$ times the Fermi-Dirac distribution at temperature T , $\mathcal{F}^D(\omega, T)$, modulated by a matrix element $\mathcal{M}(\omega, k)$:

$$\mathcal{I}(\omega, k) \simeq \mathcal{A}(\omega, k) \cdot \mathcal{F}^D(\omega, T) \cdot \mathcal{M}(\omega, k). \quad (3.4)$$

Since the gapless excitation were found to be compatible with the Fermi liquid description only for energies smaller than a cut off value of $\omega_c \leq \sim 180$ meV [53], we focuses our analysis in this energy range. Furthermore, from panels 3.4(a,b) we observe that the excitations disperse over a momentum interval smaller than 0.1 \AA^{-1} , corresponding to less than 10 percent of the Brillouin zone ($\frac{2\pi}{a} \sim 1.1 \text{ \AA}^{-1}$, with $a \approx 3.35 \text{ \AA}$ size of the tetragonal unit cell [59]).

Matrix elements typically vary weakly as a function of (ω, k) , and can be assumed to be \sim constant in the range considered ($\omega < 0.2 \text{ eV}$, $|k - k_F| < 0.1 \text{ \AA}^{-1}$). Under this assumption, $\mathcal{I}(\omega, k)$ directly probes the occupied part of the spectral function:

$$\mathcal{I}(\omega, k) \propto \mathcal{A}(\omega, k) \cdot \mathcal{F}^D(\omega, T). \quad (3.5)$$

3.1. Self-energy and quasiparticle renormalization effects

We separate the spectral function into coherent and incoherent contributions [22]:

$$\mathcal{A}(\omega, k) = \mathcal{A}_{coh}(\omega, k) + \mathcal{A}_{incoh}(\omega, k). \quad (3.6)$$

Sharp dispersing features are associated to $\mathcal{A}_{coh}(\omega, k)$, while diffuse featureless spectral weight is associated with the incoherent part of the spectral function. In the energy range of interest, coherent features dominates and we neglect $\mathcal{A}_{incoh}(\omega, k)$.

For the coherent part we write:

$$\mathcal{A}_{coh}(\omega, k) = \frac{-1}{\pi} \frac{\Sigma''(\omega, k)}{(\omega - \Sigma'(\omega, k) - \varepsilon_b)^2 + \Sigma''(\omega, k)^2} \quad (3.7)$$

where ε_b represents the bare band (*a priori* unknown) and the self energy Σ must obey $|\Sigma'| \gg |\Sigma''|$ [60].

We assume ε_b to follow a linear dispersion: $\varepsilon_b \simeq v_b(k - k_F)$. The observed, renormalized, band ε_k extracted from the fit of low energy MDCs to equation 3.1 is compared to the estimated ε_b in figure 3.6. Since the renormalized band follows a linear momentum dependence, it is reasonable to assume a linear dependence for the bare band ε_b . In fact, the bare band velocity $v_b \equiv \frac{\partial \varepsilon_b}{\partial k}$ is expected to be larger than the observed Fermi velocity v_F (LDA calculations for example estimate $v_b \simeq 3.5 \text{ eV\AA}$ [61]) so that, in the limited energy interval considered here ($\omega < 0.2 \text{ eV}$), eventual curvature effects can be neglected. In the inset of 3.6 the observed dispersion is reproduced in a larger energy interval and one can notice the change in slope around $\omega \sim 80 \text{ meV}$, known as the cuprates nodal kink and consistent with previous reports [53, 62, 63, 64, 65].

Furthermore, we assume that, within the interval of interest, the momentum dependence of the self-energy can be neglected: $\Sigma(k, \omega) \equiv \Sigma(\omega)$. This assumption is only justified locally, as Σ appears to vary strongly with the Fermi surface angle ϕ , as reported in figure 3.3 [53]. However, in the vicinity of the nodal direction ($\phi \sim 45 \text{ deg}$) the anisotropy of the self energy can be disregarded. This assumption is supported by the observations made of the two nodal cuts indicated in the top left inset of figure 3.5. Both the linewidth (figure 3.5) and the band velocity (figure 3.6) extracted from the MDCs analysis superpose for the two cuts, in the low excitation energy range considered. Even the Lorentzian intensities are found to be equivalent, as testified by figure 3.7. Moreover, a dependence on k of Σ would cause an asymmetry in the MDC intensity $\mathcal{I}(\tilde{\omega}, k)$. The symmetric lineshape of the MDCs (see panel 3.4(b)) therefore provides an additional argument in support of a (locally) momentum independent self energy.

Assuming the linearity of ε_b and the momentum independence of Σ allows to re-write the expression for the coherent part of the spectral weight:

$$\mathcal{A}_{coh}(\omega, k) \simeq \frac{-1}{\pi} \frac{\Sigma''(\omega)}{[\omega - \Sigma'(\omega) - v_b(k - k_F)]^2 + \Sigma''(\omega)^2}. \quad (3.8)$$

Chapter 3. Normal state fermiology of cuprates

Posing $(k - k_F) = \bar{k}$ and considering that energy over velocity has the dimension of the momentum, $\frac{\omega - \Sigma'(\omega)}{v_b} \equiv k$, the coherent part of the spectral weight assumes, in its dependence to k , the form of a Lorentzian function peaked around \bar{k} with half width at half maximum given by $\Sigma''(\omega) / v_b$:

$$\mathcal{A}_{coh}(\omega, k) \simeq \frac{-1}{\pi} \frac{1}{v_b} \frac{\frac{\Sigma''(\omega)}{v_b}}{(k - \bar{k})^2 + \left(\frac{\Sigma''(\omega)}{v_b}\right)^2}. \quad (3.9)$$

In other words, we have found a direct relation between $\mathcal{A}_{coh}(\omega, k)$ and the empirical parametrization of the MDCs intensity given in equation 3.1. From these considerations, we can extract an explicit expression for the imaginary part of the self energy:

$$-\frac{\Sigma''(\omega)}{v_b} \equiv \Gamma \quad \Rightarrow \quad \Sigma''(\omega) \equiv -v_b \bullet \Gamma = -v_b \eta \omega^2. \quad (3.10)$$

Therefore, $\Sigma''(\omega) \propto \omega^2$, compatibly with Landau Fermi quasi-particles.

To verify the fulfillment of the second mathematical condition, we need to evaluate the quasi-particle residue, $Z^{-1} \equiv 1 - \frac{\partial \Sigma'}{\partial \omega}$. Enforcing the self energy to be Kramers-Kronig consistent leads to a linear dependence on ω for the real part, $\Sigma'(\omega) \propto \omega$, and specifically:

$$\Sigma'(\omega) \equiv -\gamma \omega, \quad (3.11)$$

derived in the next section. From this expression of Σ' we can easily derive:

$$Z^{-1} \equiv 1 - \frac{\partial \Sigma'(\omega)}{\partial \omega} = 1 + \gamma \quad \Rightarrow \quad Z \equiv \frac{1}{1 + \gamma}. \quad (3.12)$$

And the coherent spectral function transforms, from equation 3.8, into:

$$\begin{aligned} \mathcal{A}_{coh}(\omega, k) &\simeq \frac{1}{\pi} \frac{v_b \Gamma}{[(1 + \gamma)\omega - v_b \bar{k}]^2 + v_b^2 \Gamma^2} = \\ &= \frac{1}{\pi} \frac{1}{1 + \gamma} \frac{\frac{v_b}{1 + \gamma} \Gamma}{\left(\omega - \frac{v_b}{1 + \gamma} \bar{k}\right)^2 + \frac{v_b^2}{(1 + \gamma)^2} \Gamma^2}; \end{aligned} \quad (3.13)$$

where we used $\bar{k} \equiv (k - k_F)$ and equations 3.10 and 3.11. In this form, the ω dependence of $\mathcal{A}_{coh}(\omega, k)$ is highlighted. As a function of the excitation energy, the coherent spectral weight assumes the shape of a Lorentzian peaked at $\frac{v_b}{1 + \gamma} \bar{k}$. Comparing to the momentum dependence, a consistent description of the ARPES intensity is found by imposing $\frac{v_b}{1 + \gamma} = v_F$, which implies:

$$\begin{aligned} Z &= \frac{v_F}{v_b}; \\ \mathcal{A}_{coh}(\omega, \bar{k}) &\simeq \frac{1}{\pi} Z \frac{v_F \Gamma}{(\omega - v_F \bar{k})^2 + v_F^2 \Gamma^2}. \end{aligned} \quad (3.14)$$

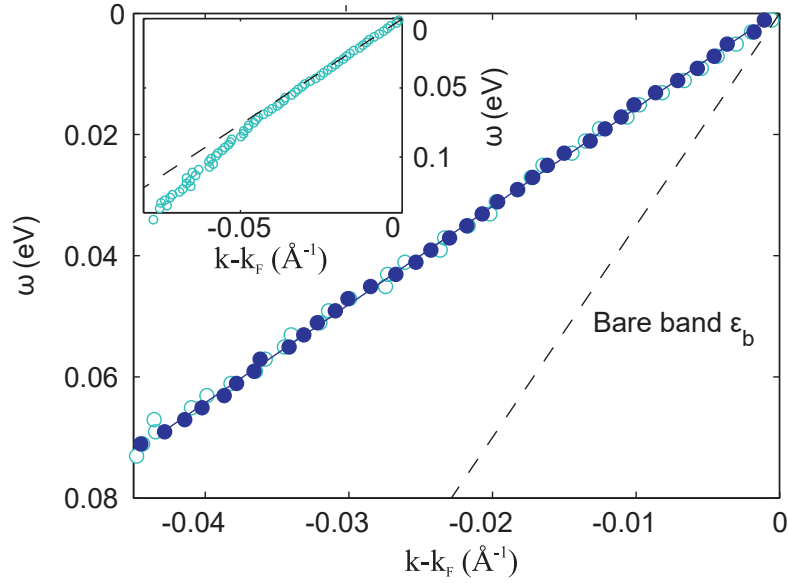


Figure 3.6 – **Low energy excitation dispersion** | of the excitation energy ω as function of the momentum $k - k_F$, extracted from the analysis of the momentum distribution curves (MDCs) of the two ARPES cuts shown in the inset of figure 3.5. The dashed line indicates the bare-band, estimated by assuming Kramers-Kronig consistency of the self-energy Σ . The dispersion is reproduced in a larger excitation energy interval in the inset, where one can notice a change in the slope around $\omega \sim 80$ meV (nodal kink, [53, 62, 63, 64, 65]). Adapted from reference [48].

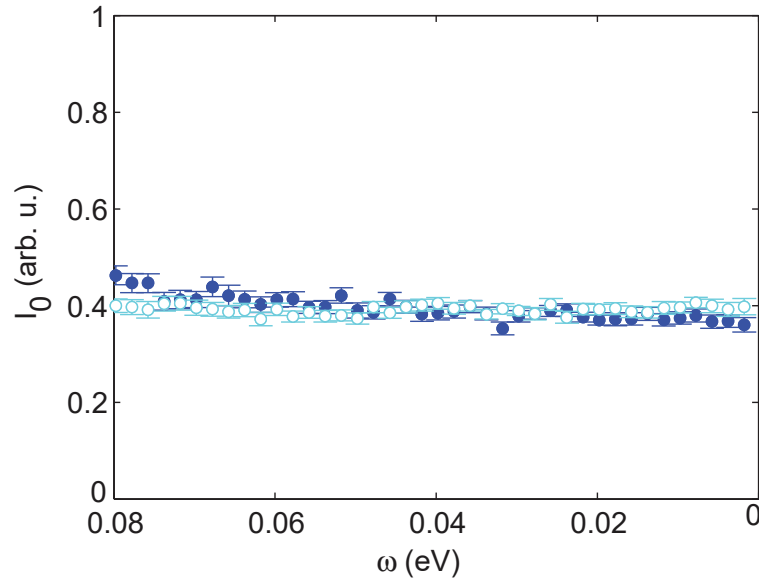


Figure 3.7 – **Low energy excitation amplitude** | I_0 , in arbitrary units, of the momentum distribution curves (MDCs) versus excitation energy ω , for the two cuts indicated the inset of figure 3.5, fitted to equation 3.1. Adapted from reference [48].

The ARPES intensity as function of ω can then be modeled by:

$$\mathcal{I}(\omega, \bar{k}) \propto \frac{v_F \eta \omega^2}{(\omega - v_F \bar{k})^2 + v_F^2 \eta^2 \omega^4} \bullet \mathcal{F}^D(\omega, T) \quad (3.15)$$

where v_F and η are experimentally determined ($v_F = 1.62(2)$ eVÅ and $\eta = 3.14(4)$ eV⁻²Å⁻¹, see section 3.1.2). Hence, the complete EDC lineshape is determined from the analysis of the MDCs, short of an intensity factor. The agreement between this parametrization of $\mathcal{I}(\omega, \bar{k})$ and the EDC lineshape is shown in panel 3.4(c) for various values of momentum. The solid lines indicate the evolution of equation 3.15, convoluted with the experimental resolution.

From the expression of Z found in equation 3.14, we can discuss the second condition for Landau Fermi quasi-particles: $-Z \bullet \Sigma'' < |\omega|$. We found, for $\omega < \omega_c$, $\Sigma''(\omega) \equiv -v_b \eta \omega^2$ (equation 3.10), with η experimentally determined and v_b *a priori* unknown. Since the quasi-particle residue was found inversely proportional to v_b , the product of these quantities can be evaluated without knowledge of the bare band velocity:

$$-Z \bullet \Sigma'' \simeq v_F \eta \omega^2 < |\omega| \quad \Rightarrow \quad |\omega| < \frac{1}{v_F \eta} \sim 0.19(6) \text{ eV}. \quad (3.16)$$

Meaning that, for $\omega < \omega_c = 0.18$ eV, the excitations satisfy both conditions for Landau Fermi quasi-particles.

In the following section, the Kramers-Kronig consistency will be treated, which allows to determine an explicit expression for Σ' and Z , leading to an experimental estimate of v_b .

3.1.4 Kramers-Kronig consistency

The real and imaginary part of the self energy are, alike the refractive index and many other properties of solids, bound together via the Kramers-Kronig relations [45]:

$$\begin{aligned} \Sigma(\omega) &= \Sigma'(\omega) + i \Sigma''(\omega); \\ \Sigma'(\omega) &= \frac{1}{\pi} \mathcal{P} \int_{-\infty}^{\infty} \frac{\Sigma''(\omega')}{\omega' - \omega} d\omega'; \\ \Sigma''(\omega) &= \frac{-1}{\pi} \mathcal{P} \int_{-\infty}^{\infty} \frac{\Sigma'(\omega')}{\omega' - \omega} d\omega'; \end{aligned} \quad (3.17)$$

where \mathcal{P} indicates principal value integralsⁱⁱⁱ.

ⁱⁱⁱusing principal value integral allows to compute improper integrals, through a limit operation. For example:
 $\mathcal{P} \int_{-\infty}^{\infty} \frac{F(u)}{u+10} du = \lim_{r \rightarrow \infty, \delta \rightarrow 0} [\int_{-r}^{10-\delta} \frac{F(u)}{u+10} du + \int_{10+\delta}^r \frac{F(u)}{u+10} du]$

3.1. Self-energy and quasiparticle renormalization effects

Therefore, the unknown real part Σ' can be derived from the imaginary part Σ'' :

$$\begin{aligned}\Sigma'(\omega) &= \frac{1}{\pi} \mathcal{P} \int_{-\omega_c}^{\omega_c} \frac{\Sigma''(\omega')}{\omega' - \omega} d\omega' \pm \frac{1}{\pi} \mathcal{P} \int_{\pm\omega_c}^{\pm W} \frac{\Sigma''(\omega')}{\omega' - \omega} d\omega' = \\ &\equiv \Sigma'_{qp}(\omega) + \Sigma'_{nqp}(\omega);\end{aligned}\quad (3.18)$$

where the integration has been truncated at the value W^{iv} and split over 3 intervals: $[-W, -\omega_c]$, $[-\omega_c, \omega_c]$ and $[\omega_c, W]$. We have derived an analytical expression for $\Sigma''(\omega)$, under the condition $\omega < \omega_c$. We can therefore directly estimate the low energy integral of $\Sigma'(\omega)$:

$$\Sigma'_{qp}(\omega) \simeq -\frac{1}{\pi} \eta v_b \mathcal{P} \int_{-\omega_c}^{\omega_c} \frac{\omega'^2}{\omega' - \omega} d\omega' = -\frac{2}{\pi} \eta v_b \omega_c \omega + O(\omega^2) \simeq -\gamma_{qp} \omega; \quad (3.19)$$

with $\gamma_{qp} = \frac{2}{\pi} \eta v_b \omega_c$. A detailed knowledge of $\Sigma''(\omega)$ at $\omega > \omega_c$ is missing, so that it is not feasible to extract $\Sigma'_{nqp}(\omega)$ from equation 3.18, since it would require the integration of an unknown function. Instead, it is useful to consider the relation to the quasi-particle residue:

$$Z^{-1}(\omega) = 1 - \frac{\partial \Sigma'(\omega)}{\partial \omega} = 1 - \frac{\partial [\Sigma'_{qp}(\omega) + \Sigma'_{nqp}(\omega)]}{\partial \omega} = 1 + \gamma_{qp} - \frac{\partial \Sigma'_{nqp}(\omega)}{\partial \omega}. \quad (3.20)$$

From equation 3.14, we deduce that the spectral function, and therefore the ARPES intensity I_0 , is proportional to Z . In figure 3.7 is shown the ω dependence of I_0 , extracted from the fit of the MDCs to equation 3.1, for the two cuts indicated in the inset of figure 3.5. Since I_0 has essentially no dependence on the energy, we can assume that $\frac{\partial \Sigma'_{nqp}(\omega)}{\partial \omega} \equiv -\gamma_{nqp}$ is constant, at the first order. In this case, for the quasi-particle residues we have:

$$Z^{-1}(\omega) \simeq 1 + \gamma_{qp} + \gamma_{nqp}; \quad (3.21)$$

which implies, at the first order in ω :

$$\begin{aligned}\Sigma'_{nqp}(\omega) &\simeq -\gamma_{nqp} \omega; \\ \Sigma'(\omega) &\simeq -(\gamma_{qp} + \gamma_{nqp}) \omega \equiv -\gamma \omega;\end{aligned}\quad (3.22)$$

with $\gamma \equiv \gamma_{qp} + \gamma_{nqp}$. Assuming $\Sigma''(\omega)$ follows a \sim linear dependence for $\omega > \omega_c$, allows to roughly estimate $\gamma_{nqp} \propto \ln \frac{C}{\omega_c}$, with C an unknown constant. From equation 3.19, $\gamma_{qp} \propto \omega_c$. For small values of ω_c , γ_{nqp} diverges logarithmically and $\gamma \sim \gamma_{nqp}$. For large values of ω_c , γ_{nqp} will tend to zero and $\gamma \sim \gamma_{qp}$. Notice that at the node ω_c has its maximum value, ~ 0.2 eV, as documented in figure 3.3. At the electronic scale, an energy of ~ 0.2 eV is very large. For a comparison, it is equivalent to a temperature of ~ 2000 K.

Under the assumption that ω_c is large enough to neglect γ_{nqp} , we can write $\gamma \simeq \gamma_{qp}$. In

^{iv}It is reasonable to assume a finite bandwidth, equivalent to W .

Chapter 3. Normal state fermiology of cuprates

this case, using equations 3.14 and 3.19 we can derive:

$$\frac{v_F}{v_b} = Z = \frac{1}{1 + \gamma} \simeq \frac{1}{1 + \gamma_{qp}} = \frac{1}{1 + \frac{2}{\pi} \eta v_b \omega_c} \Rightarrow v_b \simeq \frac{\pi v_F}{\pi - 2\eta v_F \omega_c}, \quad (3.23)$$

where v_F , η and ω_c are extracted from the analysis of the MDCs, see section 3.1.2. We can therefore extract an experimental estimate of the bare band velocity:

$$v_b \simeq 3.8 \text{ eV\AA}. \quad (3.24)$$

This value is found in good agreement with both the $\text{La}_{2-x}\text{Sr}_x\text{CuO}_4$ nodal Fermi velocity estimated by Local Density Approximation (LDA), $v_{LDA} = 3.5 \text{ eV\AA}$ [61], and values v_{s-c} derived through a numeric self-consistent method [52] - which, applied on cuprates, yields bare-band velocity v_{s-c} between 3.3 and 3.8 eV\AA, depending on the specif chemical formula [52]. The consistency between the extracted value of v_b and the literature values v_{LDA} , v_{s-c} suggests that, in the nodal direction, indeed $\gamma_{nqp} < \gamma_{qp}$ and $\gamma \simeq \gamma_{qp}$.

Under the hypothesis that Σ is momentum independent, the ratio between the bare-band mass m_b and the renormalized quasi-particle mass m^* is given by the quasi-particle residue Z , $m_b/m^* = Z$. Once we have derived an estimate for v_b , we can also evaluate Z . We find $Z \simeq 0.42(7)$, which implies, for the nodal Landau Fermi liquid quasi-particles in $\text{La}_{1.77}\text{Sr}_{0.23}\text{CuO}_4$, $m^* \simeq 2.4 m_b$.

3.1.5 Summary of results

In conclusion, we have provided a mathematical proof that the single-particle excitations observed along the nodal ARPES spectra of overdoped cuprates fulfill the conditions for Landau Fermi liquid quasiparticle. This result could be derived within a consistent description of momentum and energy distribution curves and without knowledge of the exact bare band. The self-consistent analysis is outlined in the following paragraphs, where the experimental result, model assumptions and concluding observations are grouped and summarized.

Experimental observations

From the phenomenological Lorentzian fits of the momentum distribution curves at low excitation energy, the renormalized dispersion ε_k , the Fermi velocity v_F and the scattering Γ were extracted:

$$\begin{aligned} \varepsilon_k &\simeq v_F(k - k_F); \\ v_F &\simeq 1.62 \text{ eV \AA}; \\ \Gamma &\simeq \Gamma(0) + \eta \bullet \omega^2, \quad \text{for } \omega < \omega_c; \end{aligned} \quad (3.25)$$

$$\begin{aligned}
 \Gamma(0) &\simeq 0.0117 \text{ \AA}^{-1}; \\
 \eta &\simeq 3.14 \text{ eV \AA}^{-1}; \\
 \omega_c &\simeq 0.18 \text{ eV}.
 \end{aligned}
 \tag{3.26}$$

Assumptions

The analysis focused on ARPES data collected at the node (at Fermi surface angle $\phi \simeq 45^\circ$), in a limited range of energies and momentum: $\omega < 0.2 \text{ eV}$; $|k - k_F| < 0.1 \text{ \AA}^{-1}$. Within these limits, the following assumptions for the matrix element $\mathcal{M}(\omega, k)$, the self energy Σ , the bare-band dispersion ε_b and the spectral function $\mathcal{A}(\omega, k)$ were made:

$$\begin{aligned}
 \mathcal{M}(\omega, k) &\equiv \text{constant}; \\
 \Sigma(\omega, k) &\equiv \Sigma(\omega); \\
 \varepsilon_b &\simeq v_b(k - k_F); \\
 \mathcal{A}(\omega, k) &= \mathcal{A}_{coh}(\omega, k) + \mathcal{A}_{incoh}(\omega, k) \simeq \mathcal{A}_{coh}(\omega, k).
 \end{aligned}
 \tag{3.27}$$

Following this model, the expression of the ARPES intensity was re-written:

$$\mathcal{I}(\omega, k) \propto \frac{\frac{\Sigma''(\omega)}{v_b}}{(k - \tilde{k})^2 + \left(\frac{\Sigma''(\omega)}{v_b}\right)^2} \bullet \mathcal{F}^D(\omega, T).
 \tag{3.28}$$

Derivation of the self energy

Focusing on the momentum dependence, $\mathcal{I}(\bar{\omega}, k)$ can be directly compared to the Lorentzian fit of the MDCs, leading to an experimental estimate of the imaginary part of the self energy:

$$\Sigma''(\omega) \simeq \begin{cases} -v_b \eta \omega^2, & \text{for } \omega < \omega_c. \\ \sim -\omega, & \text{for } \omega > \omega_c. \end{cases}
 \tag{3.29}$$

The real part could then be evaluated, from the Kramers-Kronig relations:

$$\Sigma'(\omega) \simeq -\gamma \omega,
 \tag{3.30}$$

with $\gamma = \gamma_{qp} + \gamma_{nqp}$, at the first order in ω .

Self consistent description of the ARPES intensity

This conclusion lead to explicit expressions for both the quasi particle residue:

$$Z = \frac{1}{1 + \gamma}; \quad (3.31)$$

and the ω dependence of the spectral function:

$$\mathcal{A}_{coh}(\omega, \bar{k}) \simeq \frac{1}{\pi} Z \frac{v_b Z \Gamma}{(\omega - v_b Z \bar{k})^2 + v_b^2 Z^2 \Gamma^2}, \quad (3.32)$$

where $\bar{k} = k - k_F$ correspond to the poles of the coherent spectral function in its momentum dependence, $\mathcal{A}_{coh}(\bar{\omega}, k)$.

Forcing consistency between the poles of the energy and momentum distribution curves implies $v_b Z = v_F$. As a consequence, the ω dependence of $\mathcal{A}_{coh}(\omega, k)$ is completely determined - short of an intensity factor - by constants extracted form the analysis of the momentum distribution curves:

$$\mathcal{A}_{coh}(\omega, \bar{k}) \propto \frac{v_F \eta \omega^2}{(\omega - v_F \bar{k})^2 + v_F^2 \eta^2 \omega^4}, \quad (3.33)$$

Notice that the lineshape derived from this model (equation 3.15) is in good agreement with the measured energy distribution curves, see panel 3.4(c).

Identification of Landau Fermi quasi-particles

From the derived expression of Z , follows that $-Z \bullet \Sigma'' = \frac{v_F \Sigma''}{v_b}$. Therefore the product $-Z \bullet \Sigma''$ could be evaluated without direct knowledge of v_b , in the limit $\omega < \omega_c \simeq 0.18$ eV - within which the analytical expression of Σ'' was extracted. $-Z \Sigma'' \simeq v_F \eta \omega^2$ is smaller than ω for $\omega < 0.19$ eV. Therefore, we found that both mathematical conditions for Landau Fermi quasi-particles [49, 50, 51]:

$$1. \Sigma'' \propto \omega^2$$

$$2. -Z \bullet \Sigma'' < |\omega|$$

are satisfied for $\omega < \omega_c$, and the observed low energy nodal excitations can indeed be described as Landau Fermi quasi-particles.

Under the further assumption that $\gamma_{nqp} \ll \gamma_{qp}$, the bare-band velocity and the ratio be-

3.1. Self-energy and quasiparticle renormalization effects

tween bare- and renormalized quasi-particle mass could be estimated:

$$\begin{aligned} v_b &\simeq 3.8 \text{ eV}\text{\AA}; \\ \frac{m_b}{m^*} = Z &\simeq 0.42 \quad \Leftrightarrow \quad m^* \simeq 2.4 m_b. \end{aligned} \tag{3.34}$$

3.2 Single particle spectral gap evolution, from underdoped to overdoped regime

From our analysis of the nodal spectra of $\text{La}_{1.77}\text{Sr}_{0.23}\text{CuO}_4$ in its normal state, we have identified the nature of the low energy nodal excitations in the strange metal phase of cuprates as coherent Landau Fermi quasiparticles. This description is however incompatible with the excitations found in the anti-nodal region. In other words, arcs of gapless Landau Fermi quasiparticles are separated by gapless non-Fermi liquid excitations.

A similar strong anisotropy is observed in under-doped cuprates. In this doping regime, gapless excitations are found in the nodal direction, while anti-nodal excitations appear gapped. This anti-nodal gap is observed at temperatures much higher than the superconductivity transition temperature T_C , and its origin remains elusive. Furthermore, in the same doping regime, charge order has been experimentally observed both in real and momentum space [68, 16, 17, 15, 14]. That is to say that, in the under-doped region of the phase diagram of cuprates, three distinct physical phenomena occur: unconventional superconductivity [69], partial anisotropic gapping [70], and charge order [71]. The exact relationship between these phenomena is still under debate [72, 73]. The anti-correlation between superconductivity and charge order, observed in $\text{La}_{2-x}\text{Ba}_x\text{CuO}_4$ [18] as documented in figure 3.8, suggests charge order emerges in competition with superconductivity. Our efforts, see reference [67], focused on the relation between charge order and the pseudo gap phase.

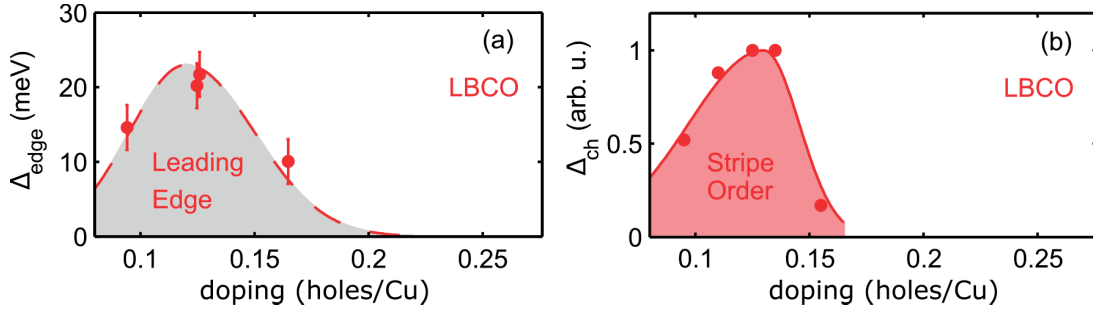


Figure 3.8 – **Doping dependence of the single particle gap and charge order strength in $\text{La}_{2-x}\text{Ba}_x\text{CuO}_4$ (LBCO)** | (a) Charge order parameter Δ_{ch} at $T=3$ K, estimated from the intensity of the charge order superdiffraction peaks (at zero field) observed via hard x-rays diffraction [18]. Suppression of superconductivity (through the application of a magnetic field) leads to an enhancement of the charge order strength, which is not observed for $x \sim 1/8$ doping (where superconductivity is suppressed even in zero field) [18]. (b) Doping dependence of the anti-nodal (*i.e.* along the main axes of the Brillouin zone) single particle gap at $T=20$ K, estimated from the leading edge of ARPES measurements[66]. Notice that for $x=1/8$, where the gap has its maximum value, superconductivity is completely suppressed and the charge stripe order is fully developed, see panel (a). Adapted from reference [67].

3.2. Single particle spectral gap evolution, from underdoped to overdoped regime

To reduce the complexity of the problem, we selected a cuprate compound with strongly suppressed superconductivity: $\text{La}_{1.6-x}\text{Nd}_{0.4}\text{Sr}_x\text{CuO}_4$. We performed a detailed systematic study of the normal state ($T > T_C$) ARPES spectra of $\text{La}_{1.6-x}\text{Nd}_{0.4}\text{Sr}_x\text{CuO}_4$, as a function of hole doping x , temperature, and Fermi surface angle. Particular attention was paid to the nodal and anti-nodal directions (corresponding to the Brillouin zone first diagonal and main axis, respectively). Furthermore, the anti-nodal lineshape evolution as function of doping was compared to that of $\text{La}_{2-x}\text{Sr}_x\text{CuO}_4$. The experimental conditions are detailed in section 3.2.1. The extracted spectra are discussed in section 3.2.2. The positive correlation found between the pseudogap strength and the electron scattering is presented in section 3.2.3. The results are summarized in section 3.2.4.

3.2.1 ARPES spectra

The phase diagram of $\text{La}_{1.6-x}\text{Nd}_{0.4}\text{Sr}_x\text{CuO}_4$, as a function of hole doping x and temperature T , is outlined in figure 3.9. Superconductivity appears at relatively low temperature, with maximum $T_C < 20$ K. At 1/8 doping, $T_C \approx 7$ K. As a result, low temperature studies of the pseudogap phase can be carried out without influences from superconductivity. The charge order on set temperature is compared to that of $\text{La}_{1.8-x}\text{Eu}_{0.2}\text{Sr}_x\text{CuO}_4$ [76], which peaks around 1/8 doping. Notice that charge order is expected to be the strongest around 1/8 doping and have a steep decrease in intensity with increasing hole doping, as experimentally observed in

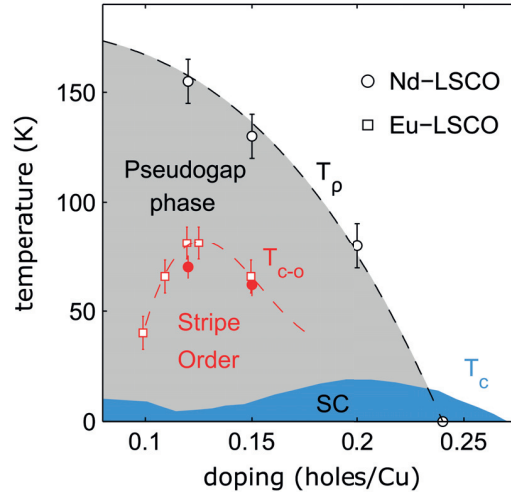


Figure 3.9 – $\text{La}_{1.6-x}\text{Nd}_{0.4}\text{Sr}_x\text{CuO}_4$ phase diagram in the low doping region |, as extrapolated from diffraction and resistivity experiments [71, 74, 75, 76]. The open dots indicate the pseudogap on set temperature T_p , determined from resistivity measurements as the temperature at which the resistivity deviates from the linear law observed at $T > T_p$ [74]. The charge ordering temperature T_{c-o} is estimated from x-ray diffraction experiments on $\text{La}_{1.6-x}\text{Nd}_{0.4}\text{Sr}_x\text{CuO}_4$, indicated by full dots [71, 75], and $\text{La}_{1.8-x}\text{Eu}_{0.2}\text{Sr}_x\text{CuO}_4$, open squares [76]. All lines are guides to the eye. Adapted from reference [67].

Chapter 3. Normal state fermiology of cuprates

$\text{La}_{2-x}\text{Ba}_x\text{CuO}_4$ [18] (see panel 3.8(a)). In all three compounds, charge density waves are found coupled to spin stripes [71, 77, 78, 79, 80, 81].

We focused on the hole doping regime varying from 1/8 hole content, in the charge order phase, to the over-doped side of the - strongly suppressed - superconducting dome, where the pseudogap gives way to the strange metal phase of cuprates. Specifically, the samples used for this study had hole content x equal to 0.12, 0.15, 0.20 and 0.24, and they were all studied in their normal state - *i.e.* at temperatures higher than T_C . Samples of ARPES spectra recorded along the anti-nodal direction are shown in figure 3.10, for the different values of doping explored.

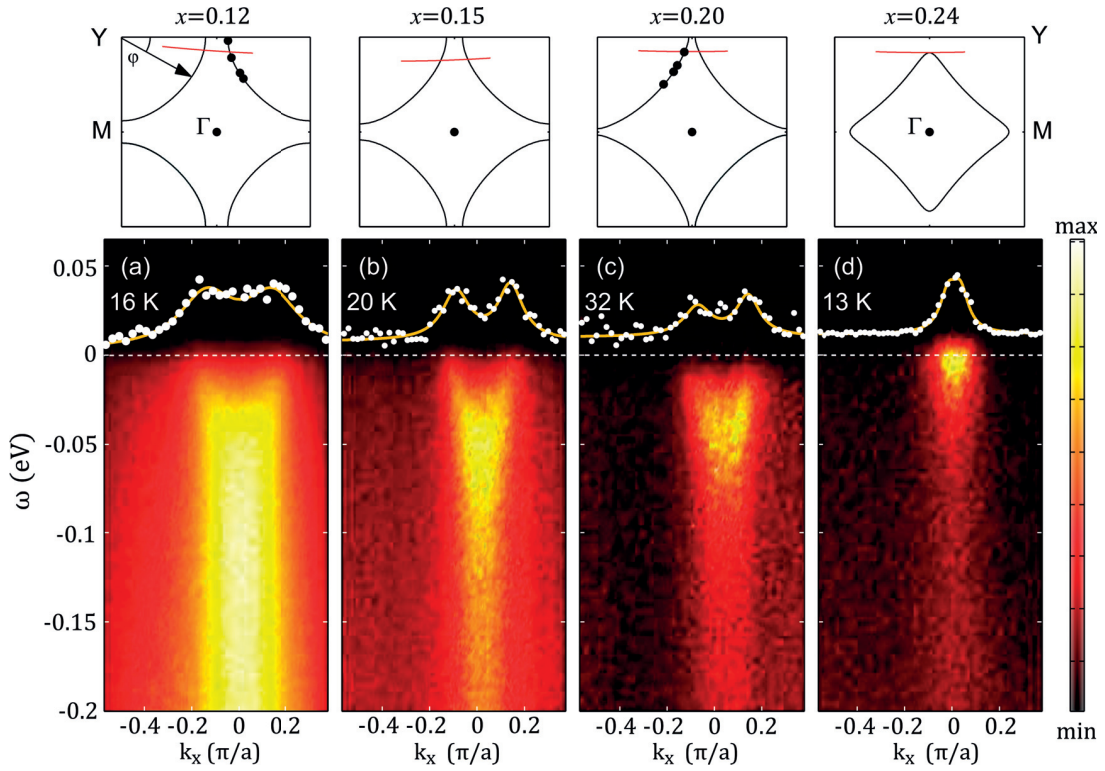


Figure 3.10 – **Samples of $\text{La}_{1.6-x}\text{Nd}_{0.4}\text{Sr}_x\text{CuO}_4$ ARPES spectra** | recorded along the anti-nodal direction (at Fermi surface angle $\phi \sim 10^\circ$) at dopings (a) $x = 0.12$ (b) $x = 0.15$ (c) $x = 0.20$ and (d) $x = 0.24$, in the normal state (at temperatures $T > T_C$, as indicated). The momentum distribution curves at the Fermi level (indicated by the dashed horizontal lines) are shown in full white circles. The solid golden lines are fit to double Lorentzian curves. The Fermi surface topology in the first Brillouin zone is sketched in the top panels, at doping as indicated. The red bars indicate the direction of the cuts shown in the lower panels. Full black points mark the underlying Fermi momenta k_F relevant for panels 3.16(c,d). Adapted from reference [67].

3.2. Single particle spectral gap evolution, from underdoped to overdoped regime

At higher doping (panel 3.10(d)), the spectral weight is mostly concentrated near the Fermi level, and progressively migrates towards deeper energies ω with decreasing doping. However, for all explored doping values, finite spectral weight was found at the Fermi energy, as documented by the momentum distribution curves of panels 3.10(a-d). Therefore, the underlying Fermi momenta k_F could be determined even within the pseudogap and charge order phases [82]. The value of k_F was estimated as the momenta at which peaks the intensity of the momentum distribution curves (MDCs) taken at $\omega = 0$ (Fermi level). The energy distribution curves (EDCs) discussed in the next sections are all extracted at momenta corresponding to k_F . The Fermi surface topology of $\text{La}_{1.6-x}\text{Nd}_{0.4}\text{Sr}_x\text{CuO}_4$ is similar to that of $\text{La}_{2-x}\text{Sr}_x\text{CuO}_4$ [83, 84], and is sketched in the top panels of 3.10 for the various compositions employed. Notice that between 0.20 and 0.24 hole doping, a van-Hove singularity crosses E_F , which changes the Fermi surface topology.

3.2.2 Analysis

3.2.2.1 Intrinsic lineshape and symmetrization

As already discussed in section 3.1.2, the ARPES intensity is affected by an ω dependent background (see figure 3.4). It is interesting to note that the lineshape of this background is consistent across all the measured compounds, in both $\text{La}_{1.6-x}\text{Nd}_{0.4}\text{Sr}_x\text{CuO}_4$ and $\text{La}_{2-x}\text{Sr}_x\text{CuO}_4$. We can then consider the ARPES spectra composed of an extrinsic background and an intrinsic signal. The relative ratio between these two components can vary in different experiments performed on the same compound, as illustrated in panel 3.11(a). This explains the origin of the small differences that can be observed in raw ARPES spectra. However, the intrinsic lineshape is found to be consistent across distinct experiments, when performed in the same conditions, see panel 3.11(b). The spectra shown in the remaining part of the chapter have all been normalized to the intensity of the extrinsic background, at $\omega = -0.2$ eV.

Symmetrization of energy distribution curves is a convenient way to visualize single particle gaps in ARPES measurements. The convenience of symmetrization is easily understood when one considers the formal expression of the ARPES intensity, within the three step model [22]. Neglecting matrix element effects, the ARPES intensity is proportional to the occupied spectral function:

$$\mathcal{I}(\omega, k) = I_0 \mathcal{A}(\omega, k) \bullet \mathcal{F}^D(\omega, T). \quad (3.35)$$

For the Fermi Dirac distribution it is found that $\mathcal{F}^D(-\omega, T) = 1 - \mathcal{F}^D(\omega, T)$, while $\mathcal{A}(-\omega, k) = \mathcal{A}(\omega, k)$, if particle-hole symmetry is assumed^v. Therefore, by adding $\mathcal{I}(-\omega, k)$ to $\mathcal{I}(\omega, k)$,

^vAlthough particle-hole asymmetry has been reported in the cuprates [85, 86], such an assumption allows a simpler analysis of the spectra, so that it is adopted for convenience. The value of the gap extracted in this fashion is indicative of the depth of the particle states and might differ from the actual particle-hole gap.

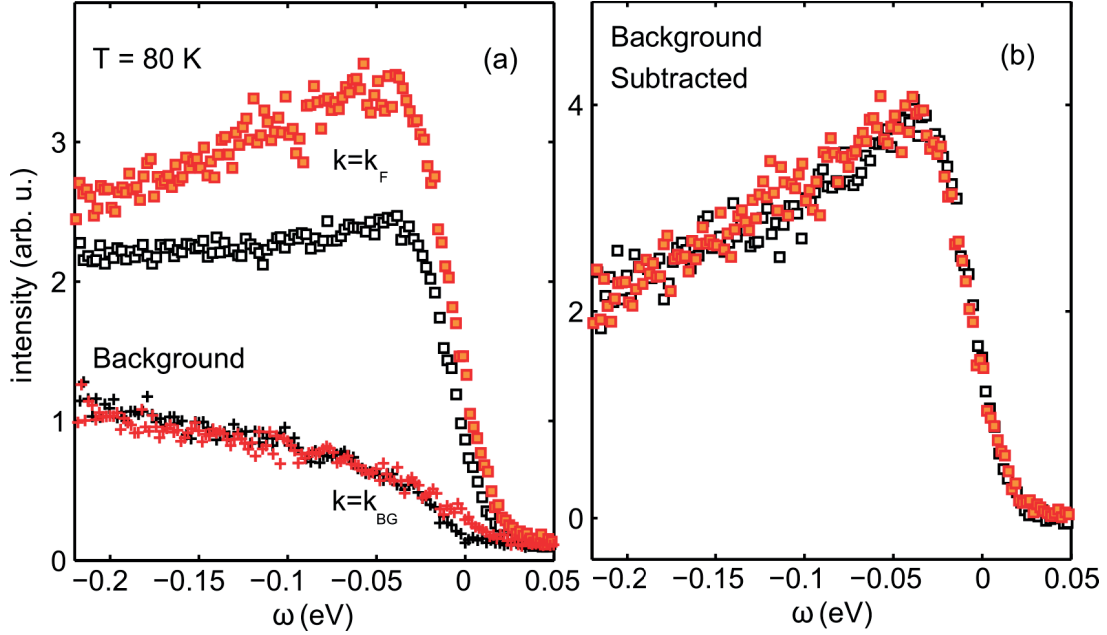


Figure 3.11 – **Intrinsic lineshape** | Direct comparison of anti-nodal ARPES spectra recorded on $\text{La}_{1.48}\text{Nd}_{0.4}\text{Sr}_{0.12}\text{CuO}_4$ samples at $T=80$ K, in the course of two distinct experiments. (a) Squares indicate the recorded (raw) intensity, at $k = k_F$, while crosses indicate the extrinsic background, at $k = k_{BG}$. Symbols open and full, black and red differentiate data taken in the two experiments. All spectra were normalized to the intensity of the relative background, at $\omega = -0.2$ eV. In this fashion it is evident that the raw lineshape recorded at k_F can change from one experiment to the next. (b) Same spectra after background removal, *i.e.* intrinsic lineshape of the raw spectra shown in panel (a). The intrinsic lineshape is consistent across different experiments, independently of the specific ratio between the intrinsic signal and the extrinsic background. Adapted from reference [67].

one finds:

$$\begin{aligned} \mathcal{I}_S(\omega, k) &= \mathcal{I}(-\omega, k) + \mathcal{I}(\omega, k) = I_0 [\mathcal{A}(\omega, k) \cdot (1 - \mathcal{F}^D(\omega, T)) + \mathcal{A}(\omega, k) \cdot \mathcal{F}^D(\omega, T)] = \\ &= I_0 \mathcal{A}(\omega, k). \end{aligned} \quad (3.36)$$

The Fermi Dirac distribution (containing the effect of thermal broadening) does not influence the symmetrized intensity $\mathcal{I}_S(\omega, k)$, and the spectral function $\mathcal{A}(\omega, k)$ is directly probed, for small values of $|\omega|$. Since the presence of a gap manifests around the Fermi level (corresponding to $\omega = 0$), this method is extremely useful for our scopes. We restricted the analysis in the range $|\omega| < 0.125$ eV.

An example of this procedure is shown in figure 3.12, in the case of a study of the gap temperature dependence in $\text{Bi}_2\text{Sr}_2\text{CaCu}_2\text{O}_{8+\delta}$ ($T_C=85$ K)[70]. In presence of a gap, the spectral weight is pushed away from the Fermi level. This effect is observed in the lower temperature curves

3.2. Single particle spectral gap evolution, from underdoped to overdoped regime

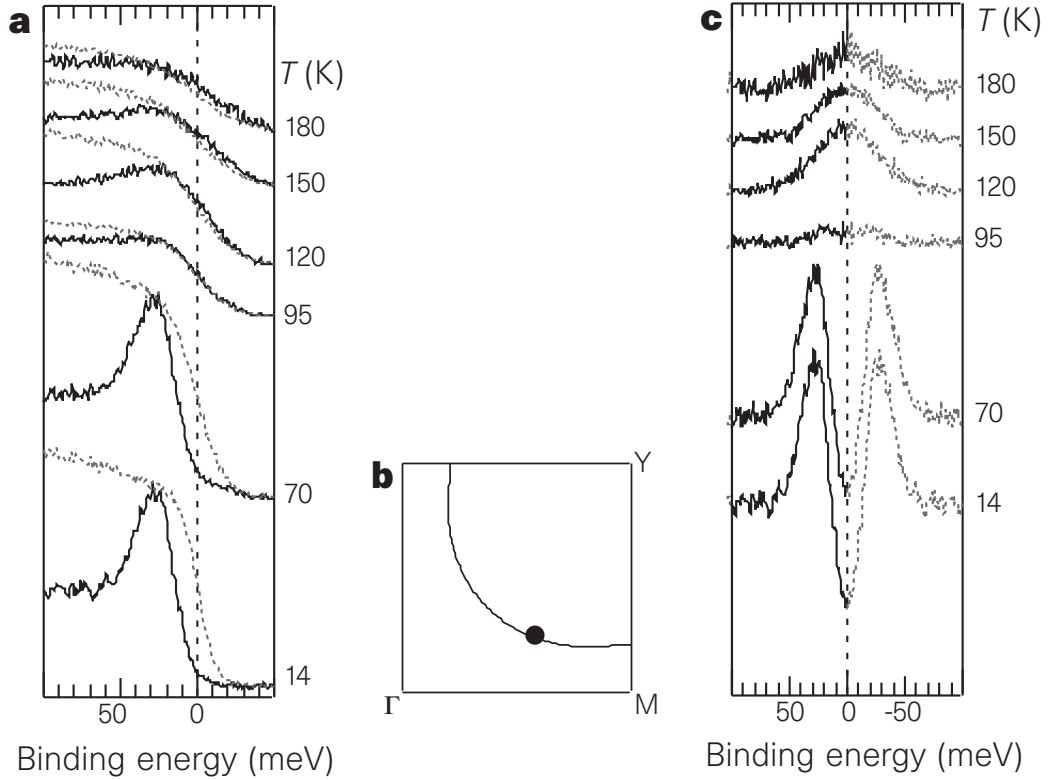


Figure 3.12 – **Symmetrization of energy distribution curves** | (a) Solid black curves are energy distribution curves (EDCs) taken on under-doped $\text{Bi}_2\text{Sr}_2\text{CaCu}_2\text{O}_{8+\delta}$ ($T_C=85$ K), at the same momentum but different temperatures. The gray dotted curves are a reference for the Fermi level, extracted from polycrystalline platinum in thermal and electric contact with the sample. (b) Sample Brillouin zone, the black full dot indicates the momentum at which the EDCs were extracted. (c) Symmetrization of the EDCs in panel (a). In this form, identification of the gap is more intuitive. Adapted from reference [70].

of panel 3.12(a), and clearly absent in the curve taken at 180 K. It is difficult to distinguish if curves taken at intermediate temperatures are affected by a smaller gap or gapless.

Upon symmetrization, a gapped EDC produces a double peaked structure, due to the depletion of states at the Fermi level. Symmetrized gapless curves on the other hand peak at the Fermi level, with a Voigt-like profile. Looking at panel 3.12(b), we can deduce that the gap is closed at $T=120$ K and at higher temperatures, but not completely closed at $T=95$ K.

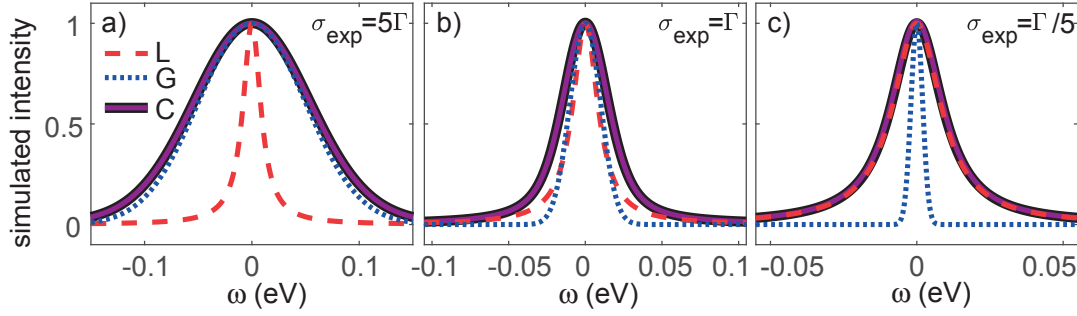


Figure 3.13 – **Effect of finite experimental resolution on gapless spectra** | Red dashed line simulates the symmetrized ARPES intensity at the Fermi momentum in absence of a gap, a Lorentzian curve (L) with half width at half maximum $\Gamma=0.01$ (as an example). The dotted blue line indicate a gaussian curve (G) indicating the experimental sensitivity, with standard deviation σ_{exp} . The result of convoluting the simulated intensity with the experimental gaussian (C) is indicated by the solid line. (a) If $\sigma_{exp} \gg \Gamma$, the convoluted curve can be approximated by a Gaussian. (b) When σ_{exp} and Γ are comparable, one obtains a Voigt profile. (c) If $\sigma_{exp} \ll \Gamma$, the effect of the experimental finite resolution can be neglected. The curves are normalized to their maximum value, to ease comparison.

3.2.2.2 Model of the symmetrized intrinsic lineshape

At small excitation energies, the symmetrized intrinsic lineshape is directly proportional to the coherent part of the spectral function [70]. Using equation 3.7, evaluated at $k = k_F$, one finds:

$$\mathcal{I}_S(\omega, k_F) \propto \mathcal{A}_{coh}(\omega, k_F) \propto \frac{-\Sigma''}{(\omega - \Sigma')^2 + \Sigma''^2}, \quad (3.37)$$

where the ω dependence of the self energy $\Sigma = \Sigma' + i\Sigma''$ has been neglected. In the case of gapless excitations, the spectral function evaluated in k_F should exhibit a pole at the Fermi level. This implies $\Sigma' = 0$. Therefore, the symmetrized ARPES intensity of gapless excitation assumes the functional form of a Lorentzian curve peaked around the Fermi level:

$$\mathcal{I}_S(\omega, k_F) \propto \mathcal{A}_{coh}(\omega, k_F) \propto \frac{\Gamma}{\omega^2 + \Gamma^2}, \quad (3.38)$$

with $\Sigma'' = -\Gamma$ and in a small energy interval. The intrinsic linewidth Γ is a measure of the excitation lifetime, discussed in terms of scattering rate. Assuming conservation of the spectra weight, larger values of Γ produce a broader, less intense peak. In other words, the excitations coherence is lowered by higher scattering rates.

The measured spectra are however also influenced by the instrumental resolution, which can be taken into account by Gaussian convolution. The effect of a finite instrumental resolution on gapless spectra is illustrated in figure 3.13. If the scattering rate is comparable with the experimental resolution, the measured spectra assume a Voigt profile, as shown in panel 3.13. If it is much smaller, as in panel 3.13(a), the convoluted profile will approximate a Gaussian

3.2. Single particle spectral gap evolution, from underdoped to overdoped regime

curve of width determined by the experimental resolution. In the opposite limit (panel 3.13(c), negligible experimental resolution) the intrinsic Lorentzian profile is preserved.

To model gapped spectra is more complex. Eliashberg theory, applied to the normal state, finds that, in presence of a spectral gap Δ , the Green function at the Fermi momentum is written:

$$\mathcal{G}(\omega, k_F) = \frac{1}{(\omega + i\Gamma) - \frac{\Delta^2}{(\omega + i\Gamma)}}, \quad (3.39)$$

where Γ is the scattering rate [87]. Phenomenologically, however, a simpler expression for $\mathcal{G}(\omega, k_F)$ has been adopted, in this work as well as in literature [70, 88, 89, 90, 91, 92]:

$$\mathcal{G}_{Ph}(\omega, k_F) = \frac{1}{(\omega + i\Gamma) - \frac{\Delta^2}{\omega}} = \mathcal{G}'_{Ph}(\omega, k_F) + i\mathcal{G}''_{Ph}(\omega, k_F). \quad (3.40)$$

From which:

$$\mathcal{A}_{Ph}(\omega, k_F) = \frac{1}{\pi} \mathcal{G}''_{Ph}(\omega, k_F) = \frac{1}{\pi} \frac{-\Gamma}{\left(\omega - \frac{\Delta^2}{\omega}\right)^2 + \Gamma^2}. \quad (3.41)$$

This phenomenological spectral function can be expressed as function of two dimensionless quantities, $\chi = \frac{\omega}{\Delta}$ and $\gamma = \frac{\Gamma}{\Delta}$:

$$\mathcal{A}_{Ph}(\omega, k_F) = \frac{1}{\pi} \frac{1}{\Delta} \frac{\gamma}{\left(\chi - \frac{1}{\chi}\right)^2 + \gamma^2}. \quad (3.42)$$

For the symmetrized ARPES intensity at Fermi momentum therefore we have:

$$\mathcal{I}_S(\omega, k_F) = I_0 \mathcal{A}_{Ph}(\omega, k_F) \propto \frac{\gamma}{\left(\chi - \frac{1}{\chi}\right)^2 + \gamma^2}. \quad (3.43)$$

This phenomenological model function maintains a Lorentzian lineshape, as well as the total spectral weight. The Lorentzian peak however is now divided into two mirrored peaks, centered in $\chi = \pm 1$ ($\omega = \pm \Delta$) of width $\gamma = \frac{\Gamma}{\Delta}$, renormalized by the spectral gap. As in the case of gapless spectra, increasing the scattering rate Γ (keeping the value of the gap unchanged) leads to broader and less intense peaks.

In figure 3.14 the modelled lineshape is plotted versus the ratio $\chi = \frac{\omega}{\Delta}$, for different values of $\gamma = \frac{\Gamma}{\Delta}$ and convoluted with different values of the experimental resolution, as indicated. All curves are normalized to their maximum value, for better visibility. In the convoluted curves, a gap can be identified under the condition that it is smaller or comparable to the experimental resolution. This limit situation is illustrated in panels 3.14(a,e,i). For larger values of σ_{exp} , the convolution of a gapped Lorentzian produces a Voigt-like profile, as in panels 3.14(d,g,h) and the gap cannot be resolved.

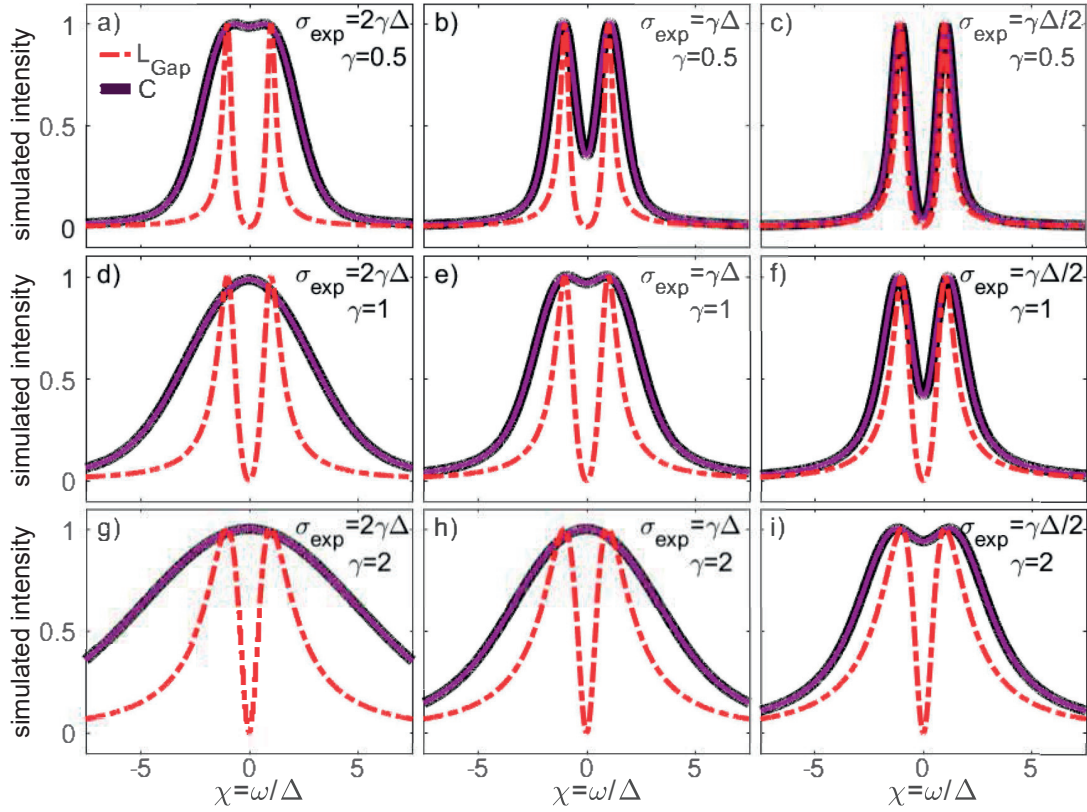


Figure 3.14 – **Effect of finite experimental resolution on gapped spectra** | In each panel, red dot-dashed line simulates the symmetrized ARPES intensity at the Fermi momentum in presence of a gap, a gapped Lorentzian curve (L_{Gap} , see equation 3.43). The solid line indicates the convolution (C) of curve L_{Gap} with a Gaussian of standard deviation equal the experimental resolution, σ_{exp} . The effect of different finite resolution ($\sigma_{exp} = 2\gamma, \gamma, \gamma/2$) is illustrated in the cases: (a-c) $\Delta > \Gamma$ ($\gamma < 1$); (d-f) $\Delta = \Gamma$ ($\gamma = 1$); (g-i) $\Delta < \Gamma$ ($\gamma > 1$). From top to bottom (e.g. from panel (c) to (i)), the ratio between the experimental resolution σ_{exp} and γ is constant. the evolution of the final profile can therefore be followed as function of the ratio between σ_{exp} and γ (horizontally) or between the gap Δ and the scattering rate Γ (vertically). All curves have been normalized to their maximum value, to ease comparison.

Notice that the combined effect of experimental resolution and scattering can hide the gap, but does not "empty" the peaks. This effect is emphasized in figure 3.15, where the value of the experimental resolution was fixed to half the value of the gap. The simulated scattering rate was varied between half the value of the gap and five times the gap. The symmetrical peaks are weakened and broadened but are not canceled. The curves were normalized to their maximum intensity. The curve at $\Gamma = 5\Delta$ was amplified by a factor of ~ 5 to match the intensity of the curve at $\Gamma = \Delta/2$.

If the gap is set to zero, equation 3.43 coincides with equation 3.38. The phenomenolog-

3.2. Single particle spectral gap evolution, from underdoped to overdoped regime

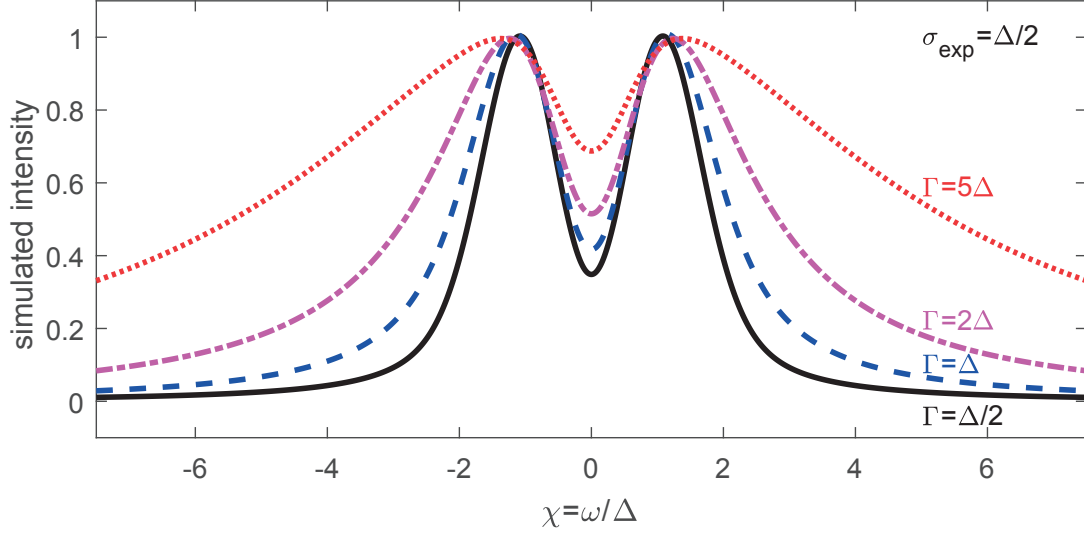


Figure 3.15 – **Influence on the convoluted lineshape of the scattering rate Γ** as indicated, for fixed values of the gap Δ and experimental resolution σ_{exp} . All curves have been normalized to their maximum value, to ease comparison.

ical symmetrized intensity of equation 3.43 can therefore be used to fit both gapped and gapless symmetrized spectra, taken at the Fermi momentum. The experimental resolution was fixed, for each experiment, to the value extracted from polycrystalline copper. The scattering rate Γ , the gap Δ and an intensity factor were left as free parameters. The results of such analysis are presented in the next sections.

3.2.2.3 Symmetrized spectra

Figure 3.16 allows direct comparison of symmetrized spectra taken at the (underlying, see figure 3.10) Fermi momentum, at different compositions (first two rows of panels from the left), in different point of momentum space (central panels) or at different temperatures (last two panels). Top panels 3.16(a-f) feature symmetrized "raw" spectra, while an extrinsic background, discussed in section 3.2.2.1 has been subtracted before symmetrization, to the spectra shown in the bottom panels 3.16(g-l). Solid lines are fits to equation 3.43, convoluted with the experimental resolution, which varied slightly across the experiments, within 6 and 9 meV. All spectra were recorded in the normal state. If not indicated, the sample temperature was just above T_C . With the exception of the central panels, all shown spectra were recorded in the anti-nodal region. Differences between the raw anti-nodal spectra of $\text{La}_{1.48}\text{Nd}_{0.4}\text{Sr}_{0.12}\text{CuO}_4$ (bottom spectra in panels 3.10(b,c)) originate from slightly different background-to-signal ratios, see figure 3.11.

First, we discuss the anti-nodal lineshape as function of the composition. Anti-nodal overdoped spectra of both $\text{La}_{2-x}\text{Sr}_x\text{CuO}_4$ and $\text{La}_{1.6-x}\text{Nd}_{0.4}\text{Sr}_x\text{CuO}_4$ (top spectra in panels 3.16(a-

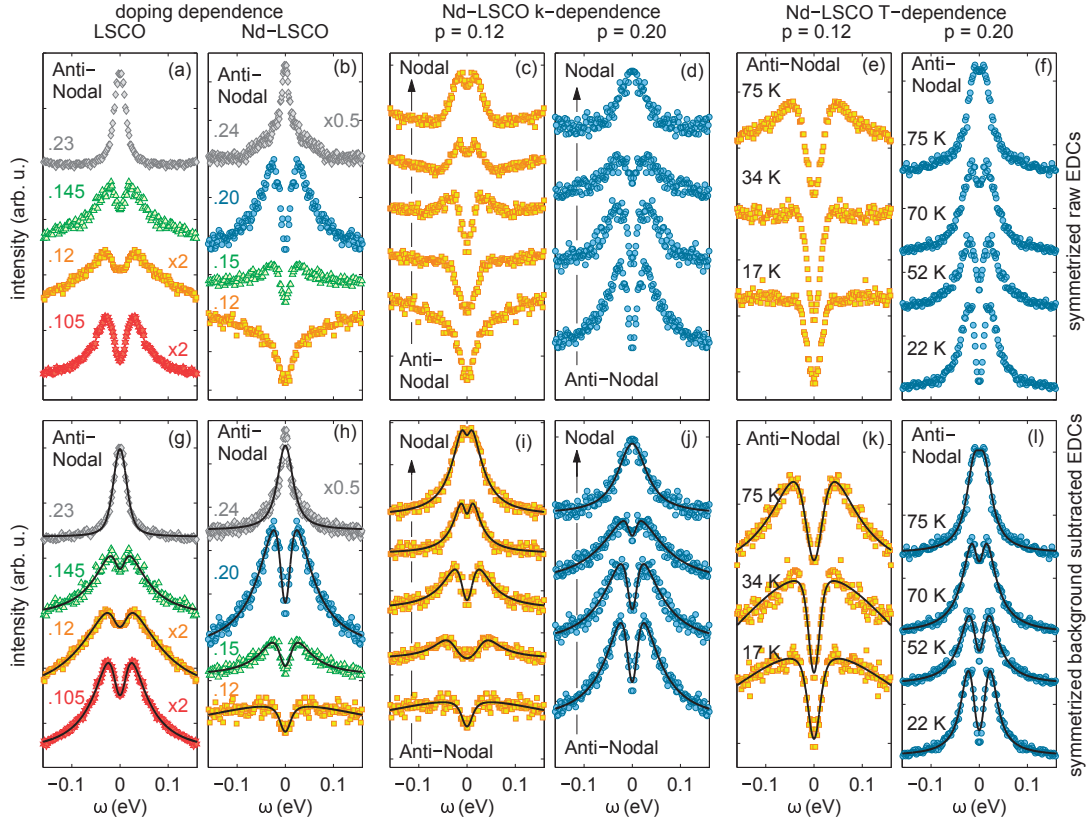


Figure 3.16 – **Evolution of the Symmetrized spectra with composition, Fermi surface angle and temperature** | in the normal state. If not indicated, the samples temperature was just above T_C . (a,b) Symmetrized anti-nodal energy distribution curves (EDCs) taken on $\text{La}_{2-x}\text{Sr}_x\text{CuO}_4$ (LSCO) and $\text{La}_{1.6-x}\text{Nd}_{0.4}\text{Sr}_x\text{CuO}_4$ (Nd-LSCO) samples at hole doping content $p = x$ as indicated. Spectra taken on $\text{La}_{2-x}\text{Sr}_x\text{CuO}_4$ $x = 0.105$ and $x = 0.145$ have been presented in references [90, 91, 93]. All $\text{La}_{2-x}\text{Sr}_x\text{CuO}_4$ samples were characterized by neutron scattering experiments [57, 94, 95]. (c,d) Momentum dependence of the symmetrized (EDCs) on $\text{La}_{1.6-x}\text{Nd}_{0.4}\text{Sr}_x\text{CuO}_4$ $x = p = 0.12$ and 0.20 , taken at underlying Fermi momenta indicated by the full black dots in top panels 3.10(a,c). (e,f) Temperature dependence of the anti-nodal symmetrized (EDCs), on $\text{La}_{1.6-x}\text{Nd}_{0.4}\text{Sr}_x\text{CuO}_4$ $x = p = 0.12$ and 0.20 . (g-l) background-free spectra as in the top panels, to emphasize the intrinsic symmetrized lineshape. Solid black lines are fit to equation 3.43, convoluted with the experimental resolution. An arbitrary shift was applied to the various spectra, normalized so that the extrinsic backgrounds superpose, see panel 3.11(a). If indicated, an additional factor was given, to improve visibility. From reference [67].

3.2. Single particle spectral gap evolution, from underdoped to overdoped regime

b,g-h)) exhibit a Voigt-like lineshape, which is not affected by background removal. As discussed in the previous section, such a profile suggests resolution-limited gapless excitations. At a smaller hole content, $x = 0.20$, a clear gap is observed in $\text{La}_{1.6-x}\text{Nd}_{0.4}\text{Sr}_x\text{CuO}_4$. Further reducing of the doping produces similar gapped lineshapes in $\text{La}_{2-x}\text{Sr}_x\text{CuO}_4$ at $x = 0.145, 0.12$ and $\text{La}_{1.6-x}\text{Nd}_{0.4}\text{Sr}_x\text{CuO}_4$ at $x = 0.15$. At these compositions, the anti-nodal lineshape is only slightly affected by the background removal. A very different lineshape is found in $\text{La}_{1.48}\text{Nd}_{0.4}\text{Sr}_{0.12}\text{CuO}_4$ (bottom spectra in panels 3.16(b,h)), where the peaks appear strongly depleted and background removal has a remarkable effect.

Shifting our attention to panels 3.16(c,i), an analogous evolution is found as a function of the Fermi surface angle, in $\text{La}_{1.48}\text{Nd}_{0.4}\text{Sr}_{0.12}\text{CuO}_4$. Moving from nodal to anti-nodal spectra (see top inset of panel 3.10(a)), the lineshape evolves from a gapless Voigt-like profile to a gapped lorentzian, whose double peaks appear systematically more depleted as we move deeper in the anti-nodal region. Notice that, the deeper into the anti-nodal region, the more striking is the effect of background removal.

Panels 3.16(d,j) show the momentum dependence of $\text{La}_{1.4}\text{Nd}_{0.4}\text{Sr}_{0.2}\text{CuO}_4$ spectra (see top inset of panel 3.10(c)). Moving from the node towards the anti-node, a gapless profile gives way to the opening of a gap. However, clear peaks are observed for all underlying Fermi momenta, in striking contrast to the behavior observed in $\text{La}_{1.48}\text{Nd}_{0.4}\text{Sr}_{0.12}\text{CuO}_4$. Removal of the background emphasizes the peaks, but does not substantially affect the lineshapes.

The temperature dependence of $\text{La}_{1.6-x}\text{Nd}_{0.4}\text{Sr}_x\text{CuO}_4$ anti-nodal spectra was investigated at these same values of doping: $x = 0.12$ (panels 3.16(e,k)) and in $x = 0.20$ (panels 3.16(f,l)). For $\text{La}_{1.48}\text{Nd}_{0.4}\text{Sr}_{0.12}\text{CuO}_4$, the normal state anti-nodal gap is observed at all explored temperatures. However, the intensity of the peaks is much higher outside of the charge stripe order ($T_{ch} \approx 70$ K [71]). At lower temperatures, the peaks are easily observed only after background subtraction. In the case of $\text{La}_{1.4}\text{Nd}_{0.4}\text{Sr}_{0.2}\text{CuO}_4$, at $T = 75$ K the normal state gap is either closed or smaller than the experimental resolution ($\sigma_{exp} = 6$ meV). At lower temperatures, the anti-nodal gap is clearly observed, and it appears to increase with cooling. Additionally, the peaks grow more pronounced with lower temperatures, a trend in direct opposition to that observed on $\text{La}_{1.48}\text{Nd}_{0.4}\text{Sr}_{0.12}\text{CuO}_4$ (where the peaks seem to lose coherence at lower temperatures).

3.2.2.4 Spectral weight transfer

This effect can be considered in terms of spectral weight conservation, for which it is convenient to refer to the un-symmetrized energy distribution curves. In figure 3.17, anti-nodal spectra taken on $\text{La}_{1.6-x}\text{Nd}_{0.4}\text{Sr}_x\text{CuO}_4$ at $x = 0.12, 0.20$ at 75 K are compared to spectra recorded on the same samples, but at temperatures just above T_C .

Upon cooling (deeper into the pseudogap state), the gap found in $\text{La}_{1.4}\text{Nd}_{0.4}\text{Sr}_{0.2}\text{CuO}_4$ seems to conserve the spectral weight. As the gap grows, the states near the Fermi level are more

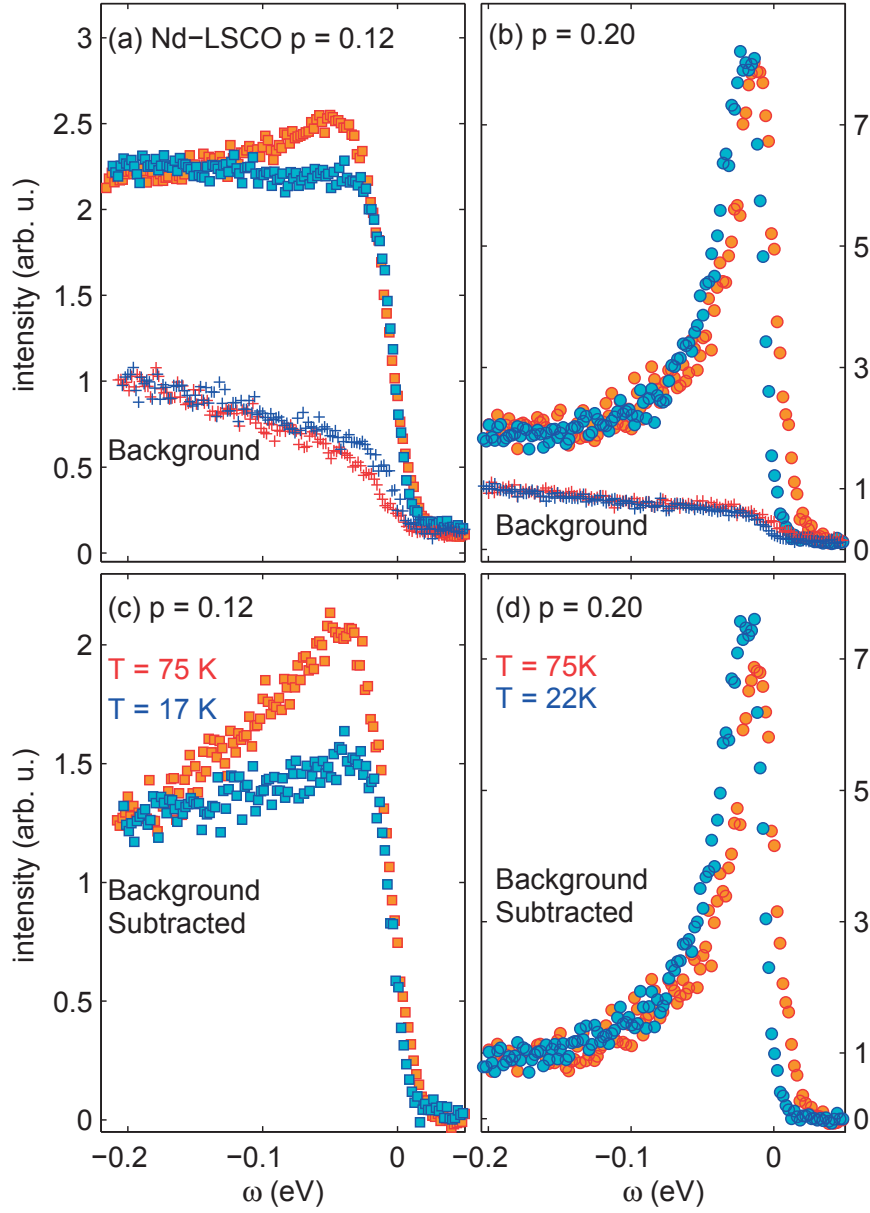


Figure 3.17 – **Spectral weight loss vs transfer** | (a) Raw anti-nodal spectra recorded on $\text{La}_{1.48}\text{Nd}_{0.4}\text{Sr}_{0.12}\text{CuO}_4$ at 75 K (red full squares) and at 17 K (blue squares), normalized so that the backgrounds (blue and red crosses) overlap. (b) $\text{La}_{1.4}\text{Nd}_{0.4}\text{Sr}_{0.2}\text{CuO}_4$ raw anti-nodal spectra recorded, at 75 K (red full circles) and 22 K (blue circles), normalized to superpose the backgrounds (blue and red crosses). The backgrounds are evaluated from energy distributed curves taken far from the underlying Fermi momentum (c),(d) Same anti-nodal spectra, after background removal. A net spectral weight loss is observed when cooling $\text{La}_{1.48}\text{Nd}_{0.4}\text{Sr}_{0.12}\text{CuO}_4$ into the charge order phase. In $\text{La}_{1.4}\text{Nd}_{0.4}\text{Sr}_{0.2}\text{CuO}_4$ spectral weight seems to shift towards deeper states upon cooling (deeper into the pseudogap state). Adapted from reference [67].

3.2. Single particle spectral gap evolution, from underdoped to overdoped regime

depleted, but the spectral weight "missing" is transferred to states at deeper energy, as evident in panel 3.17(d). In $\text{La}_{1.48}\text{Nd}_{0.4}\text{Sr}_{0.12}\text{CuO}_4$, on the other hand, lowering the temperature from 75 K to 17 K results in what appears as a net loss of spectral weight, see panel 3.17(c). Notice that the spectra have not been normalized to their intensity at deep energy, but rather to the background intensity, extracted from an energy distribution curve at momentum far from k_F . The apparent spectra weight loss is already noticeable in the raw spectra, panel 3.17(a), and emphasized by the background removal.

Even if a non-trivial redistribution is not ruled out, the behavior recorded at 1/8 doping considerably stands out, when compared to the other doping explored in $\text{La}_{1.6-x}\text{Nd}_{0.4}\text{Sr}_x\text{CuO}_4$ as well as $\text{La}_{2-x}\text{Sr}_x\text{CuO}_4$, including $\text{La}_{1.88}\text{Sr}_{0.12}\text{CuO}_4$.

3.2.2.5 Correlation between gap and scattering rate

Fitting of the background-free symmetrized spectra to equation 3.43, convoluted with the experimental resolution, allows to extract the single particle spectral gap Δ and the scattering rate Γ . In figure 3.18 are reported the result of such analysis, performed on spectra recorded along the underlying Fermi surface of $\text{La}_{1.48}\text{Nd}_{0.4}\text{Sr}_{0.12}\text{CuO}_4$ and $\text{La}_{1.4}\text{Nd}_{0.4}\text{Sr}_{0.2}\text{CuO}_4$, in their normal state (at temperatures just above T_C), or in the anti-nodal direction on $\text{La}_{1.6-x}\text{Nd}_{0.4}\text{Sr}_x\text{CuO}_4$ with $x = 0.12, 0.20, 0.24$ at various temperatures.

From the analysis of $\text{La}_{1.4}\text{Nd}_{0.4}\text{Sr}_{0.2}\text{CuO}_4$ spectra, a positive correlation emerges between the spectral gap and the scattering rate, in spectra taken at different values of (underlying) Fermi momentum or temperature. This relation between the anisotropic spectral gap observed above T_C , the pseudogap, and the electronic scattering is consistent with previous observation. In fact, it is established that the pseudogap maximized near the zone boundary, in the anti-node [70, 96, 97]. In parallel, the scattering rate has been reported to increase from the node towards the anti-node [53, 98].

In $\text{La}_{1.48}\text{Nd}_{0.4}\text{Sr}_{0.12}\text{CuO}_4$, gapless arcs centered in the node (Fermi arcs) were found to have finite length even at the lowest measured temperatures [82]. Since raw spectra can be affected by the extrinsic background, we refer to the intrinsic lineshape, obtained from the background removal (see figure 3.11), shown in panels 3.16(h,i,k). The low temperature lineshape evolution in momentum space is shown in panel 3.16(i), from the anti-node towards the node, until just before the Fermi arc tip. Spectra near the Fermi arc tip closely resemble those observed on $\text{La}_{1.4}\text{Nd}_{0.4}\text{Sr}_{0.2}\text{CuO}_4$, and fitting to equation 3.43, convoluted with the experimental resolution, yields values of Δ and Γ consistent with those extracted from $\text{La}_{1.4}\text{Nd}_{0.4}\text{Sr}_{0.2}\text{CuO}_4$ spectra. At the anti-node, however, the lineshape changes dramatically, as described in the previous sections. The double-peak structure appears to have lost coherence and the parameters extracted from fitting have a much smaller ratio Δ/Γ . As the temperature is raised above the charge order on set T_{c-o} , the anti-nodal lineshape recovers coherence and

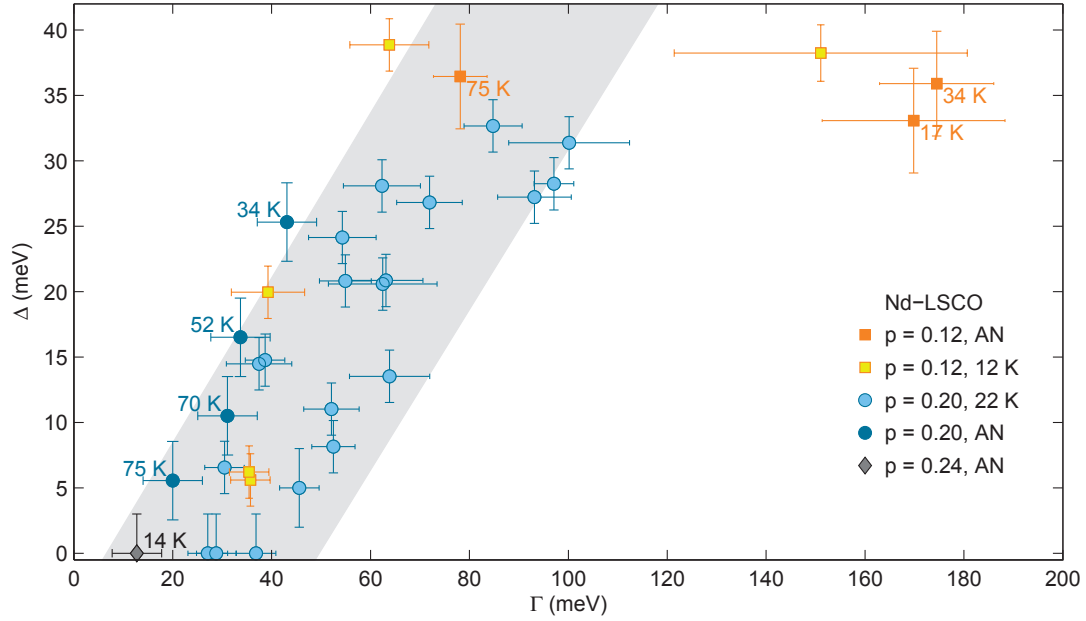


Figure 3.18 – **Correlation between spectral gap Δ and scattering rate Γ** | extracted by fitting to equation 3.43, convoluted with the experimental resolution, of symmetrized energy distribution curves. The curves were extracted along the underlying Fermi surface of $\text{La}_{1.48}\text{Nd}_{0.4}\text{Sr}_{0.12}\text{CuO}_4$ and $\text{La}_{1.4}\text{Nd}_{0.4}\text{Sr}_{0.2}\text{CuO}_4$ at temperatures as indicated, or in the anti-nodal (AN) direction on $\text{La}_{1.6-x}\text{Nd}_{0.4}\text{Sr}_x\text{CuO}_4$ at doping and temperatures as indicated. An extrinsic background was subtracted to all spectra, before symmetrization. The gray shaded area indicates schematically the positive correlation observed between the gap and the scattering rate. Adapted from reference [67].

the parameters extracted follow the trend of those estimated from $\text{La}_{1.4}\text{Nd}_{0.4}\text{Sr}_{0.2}\text{CuO}_4$ spectra.

The anti-nodal lineshape of $\text{La}_{1.36}\text{Nd}_{0.4}\text{Sr}_{0.24}\text{CuO}_4$ appears gapless, within the experimental resolution, already at temperatures just above the superconducting transition. The value of electron scattering extracted from fitting to equation 3.43, with $\Delta = 0$ and convoluted with the experimental resolution, is consistent with the values found near the node in $\text{La}_{1.4}\text{Nd}_{0.4}\text{Sr}_{0.2}\text{CuO}_4$.

3.2.3 Discussion

In conventional charge density wave systems, the order parameter Δ_{ch} coincides with the single-particle gap [99], and scales with the lattice distortion u [99]. Hard x-ray diffraction studies on $\text{La}_{2-x}\text{Ba}_x\text{CuO}_4$ have found u , and hence Δ_{ch} , to exhibit a strong doping dependence [18], see panel 3.8(a). Notice that the charge ordered ground state found in $\text{La}_{1.6-x}\text{Nd}_{0.4}\text{Sr}_x\text{CuO}_4$, $\text{La}_{1.8-x}\text{Eu}_{0.2}\text{Sr}_x\text{CuO}_4$ and $\text{La}_{2-x}\text{Ba}_x\text{CuO}_4$ at $x = 0.12$ is believed to be the same state [100]^{vi}.

^{vi}These three systems share the same low-temperature tetragonal crystal structure, exhibit similar thermopower [101, 102], as well as the same spin/charge stripe structure [78, 79, 80, 81], and superconductivity

3.2. Single particle spectral gap evolution, from underdoped to overdoped regime

The order parameter Δ_{ch} appears to have a sharp maximum at 1/8-doping. Increasing hole content from $x=0.12$ to 0.15, leads to a value of Δ_{ch} which is five times smaller, in zero field. At $x=0.20$ it is therefore reasonable to assume that Δ_{ch} is negligibly small and does not affect the lineshape. At this doping, the normal state gap can be studied without influence from charge order or superconductivity. The charge order on set temperature on the other hand is found to have a smooth doping dependence, see figure 3.9. It follows that, although charge order is present at various dopings, it is expected to have the strongest influence on spectra recorded at hole content $x=0.12$. In this doping regime however, the lineshape is also possibly affected by superconductivity, pseudogap and spin-freezing phenomena [103, 104]. Choosing $\text{La}_{1.6-x}\text{Nd}_{0.4}\text{Sr}_x\text{CuO}_4$ simplifies the problem by removing possible influences from superconductivity (since low temperature studies can be performed in the normal state). Furthermore, since spin and charge density waves are coupled [71], they can be treated as manifestations of the same phenomena.

Pseudogap and charge order

Dynamical mean-field theory (DMFT) calculations for the Hubbard model predict a positive correlation between scattering and spectral gap [105], consistently with our observations on $\text{La}_{1.4}\text{Nd}_{0.4}\text{Sr}_{0.2}\text{CuO}_4$. Within the DMFT approach [106, 107, 108, 109], electron correlations directly produce the opening of the pseudogap, which, as a secondary effect, enhances the system tendency towards further instabilities which then produce the superconducting and charge order ground states. However, charge density instabilities, unlike superconductivity, have not been directly found in DMFT calculations.

A different approach looks at the pseudogap as a precursor either to superconductivity [92, 96, 110] or to an order competing with superconductivity [15, 111, 112, 113], which could be identified with the charge order. As an example, the charge ordering onset temperature is comparable to the pseudogap temperature scale in $\text{Bi}_2\text{Sr}_2\text{CuO}_{6+x}$ [15], and a connection between the charge ordering vector and the vector nesting the tips of the Fermi arcs was found [15]. Therefore, a cooperative relation between the pseudogap and fluctuating charge density order was suggested [114, 115].

Charge order is expected to open a spectral gap [116, 117]. In two-dimensional charge density wave systems (such as transition metal dichalcogenides), anisotropic spectral gaps have indeed been reported above the charge order onset temperature [117, 118]. In cuprates, however, photoemission experiments have not clearly identified the single-particle gap originating from charge order.

With this in mind, the lineshape evolution of $\text{La}_{1.48}\text{Nd}_{0.4}\text{Sr}_{0.12}\text{CuO}_4$ assumes particular relevance, since the charge order parameters seems to peak at 1/8 doping (see panel 3.8(a)). In

is strongly suppressed at 1/8 doping.

Chapter 3. Normal state fermiology of cuprates

$\text{La}_{1.6-x}\text{Nd}_{0.4}\text{Sr}_x\text{CuO}_4$, $\text{La}_{1.8-x}\text{Eu}_{0.2}\text{Sr}_x\text{CuO}_4$ and $\text{La}_{2-x}\text{Ba}_x\text{CuO}_4$ at $x = 0.12$, strong low energy spectral weight suppression has been reported in the anti-node [66, 119, 120, 82], for which different interpretations have been suggested [66, 119]. One study, performed on $\text{La}_{2-x}\text{Ba}_x\text{CuO}_4$, speculated that the pseudo gap exhibits a d -wave character with maximum amplitude at $1/8$ doping [66]. Later experiments however reported strong corrections to the proposed d -wave symmetry [121, 122, 123], and a two-gap scenario was introduced [119]. The origin of the supposed additional anti-nodal gap was not identified.

The opening of a spectral gap depletes the states near the Fermi level, causing either suppression or redistribution of low energy spectral weight. For example, in $\text{Bi}_2\text{Sr}_2\text{CaCu}_2\text{O}_{8+x}$ a pronounced redistribution of spectral weight is found in the pseudogap phase [124], in an energy range extending beyond 200 meV.

The opening of the normal state gap can be observed on $\text{La}_{1.4}\text{Nd}_{0.4}\text{Sr}_{0.2}\text{CuO}_4$, in absence of charge order influences. As the temperature is lowered and the system enters the pseudo-gap phase, a gap opens in the anti-node and spectral weight is transferred at higher energies, within a range of $2-3\Delta < 100$ meV, see panels 3.17(b,d). The total amount of spectral weight found at the (underlying) Fermi momentum appears to be conserved.

The anti-nodal lineshape evolution in $\text{La}_{1.48}\text{Nd}_{0.4}\text{Sr}_{0.12}\text{CuO}_4$ (shown in panels 3.17(a,c) for the same temperature and energy range) appears very different. Cooling the sample inside the charge order phase produces an apparent net suppression of spectral weight in a 100 meV range. The momentum dependence, see panels 3.16(c,i) does not suggest a redistribution of this "missing" spectral weight in momentum space. It seems that, either the weight is transferred to much deeper energies (in a range larger than 5Δ) or it is not conserved.

Non conservation of spectral weight is a possible effect of a phase transition. One can in fact imagine that a different ground state might correspond to a substantially different spectral function. The appearance of charge order could therefore produce an effective loss of spectral weight. Within this hypothesis, we notice that charge order seems to affect mainly the anti-nodal region, within a 100 meV energy range.

3.2.4 Summary of results

The systematic ARPES study of the normal state of $\text{La}_{1.6-x}\text{Nd}_{0.4}\text{Sr}_x\text{CuO}_4$ has yielded insights into both the pseudogap and the charge-spin order phases. Anti-nodal spectra were recorded as a function of doping and temperature.

In the over-doped regime, the antinodal lineshape appears gapless. At hole content $x = 0.20$, a spectral gap opens in the anti-nodal region and spectral weight is re-distributed to deeper states, but conserved. A positive correlation between electron scattering Γ and single particle gap Δ is observed. This effect is predicted by dynamical mean-field theory calculations for the

3.2. Single particle spectral gap evolution, from underdoped to overdoped regime

Hubbard model.

In the under-doped regime, where charge order is fully developed, $x = 0.12$, spectral weight appears to be lost when cooling the sample inside the charge order phase. Furthermore, a similar ratio of Δ/Γ is found on spectra recorded outside the anti-node. Therefore, our observations on $\text{La}_{1.48}\text{Nd}_{0.4}\text{Sr}_{0.12}\text{CuO}_4$ are consistent with an additional source of anti-nodal spectral weight suppression, and suggest charge order could be at the origin of the apparent coherence loss observed in anti-nodal spectra at temperatures below T_{c-o} .

4 Orbital structure of single-layer ruthenates

In chapter 3 are presented the results of our investigation on different members of the family of cuprates. In this chapter our attention will shift to another family of transition metal oxides with a similarly rich phase diagram to that of the cuprates, see figure 4.1. Notably, both families present coexistence of Mott insulation (Ca_2RuO_4) and superconductivity (Sr_2RuO_4). It should be emphasized however that these phases present differences from those of cuprates. The cuprates superconducting gap has a d wave symmetry. Sr_2RuO_4 has been proposed as an electronic equivalent of superfluid He^3 , which would require a p wave superconducting gap [8].

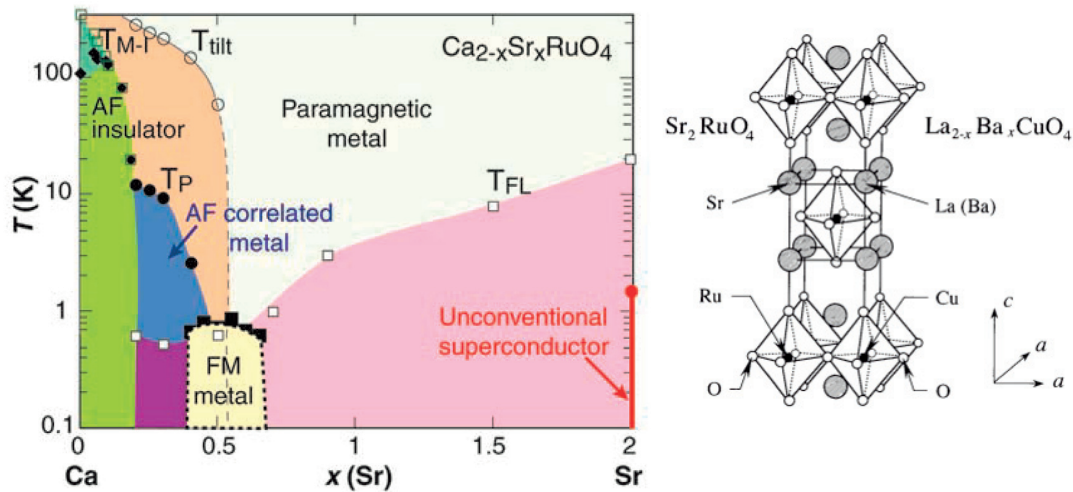


Figure 4.1 – Ca_2RuO_4 to Sr_2RuO_4 phase diagram | Phase diagram of single layered ruthenates, evolving from an anti-ferromagnetic insulator, at strontium content $x=0$, to an unconventional superconductor, at $x=2$. Strontium substitution doesn't affect the carrier density, but rather increases the electron bandwidth [125]. On the right, the inset shows a sketch of the crystal structure of Sr_2RuO_4 and $\text{La}_{2-x}\text{Ba}_x\text{CuO}_4$. The directions of the tetragonal principal axes are indicated (where $b=a$). The transition metal atoms, $\text{TM}=(\text{Ru},\text{Cu})$, form a square lattice in the TM-O_2 plane. The directions of interest in this plane are the TM-O-TM bond (referred to as $\pi - 0$), corresponding to a , and the TM-TM bond directions (referred to as $\pi - \pi$) [126].

Chapter 4. Orbital structure of single-layer ruthenates

In cuprates, the half-filled single $3d$ band is separated into an upper and a lower Hubbard band by strong coulomb repulsion U . In Ca_2RuO_4 , the valence band has $2/3$ occupancy in the $4d-t_{2g}$ states, as will be discussed in the following sections, and the Mott gap has been proposed to be orbital dependent [11, 12].

From a structural point of view, Sr_2RuO_4 has a distortion-free crystal structure and is iso-structural to the textbook perovskite example of $\text{La}_{2-x}\text{Ba}_x\text{CuO}_4$ (in its high temperature tetragonal phase), as illustrated in figure 4.1. Ca_2RuO_4 on the other hand presents rotation and tilting of the oxygen octahedra, introduced by the smaller size of calcium with respect to strontium. Interestingly, it has been reported [127] that, upon application of pressure, Ca_2RuO_4 undergoes a transition from an AF Mott insulator to a ferromagnetic metal. At the same time, pressure strongly affects the the crystal structure of Ca_2RuO_4 , with the progressive suppression of compression, rotation and finally tilting. Above ~ 90 kbar, all structural deformation deformations are suppressed. At this pressure, Ca_2RuO_4 exhibits superconducting behavior (corroborated by ac susceptibility and electrical resistivity measurements)[127].

A reasonable question therefore arises as to the link between spin-orbit coupling, crystal structure deformations and electronic properties, which was addressed in this work by performing a combined XAS and RIXS investigation on Sr_2RuO_4 and Ca_2RuO_4 .

The experimental conditions relevant for the XAS experiment are described in section 4.1, and complemented in section A.3. The observations derived from the XAS and RIXS experiments are discussed in sections 4.2 and 4.3 respectively. We adopted a simple model Hamiltonian, presented in section 4.4, to interpret the results.

4.1 Experimental conditions

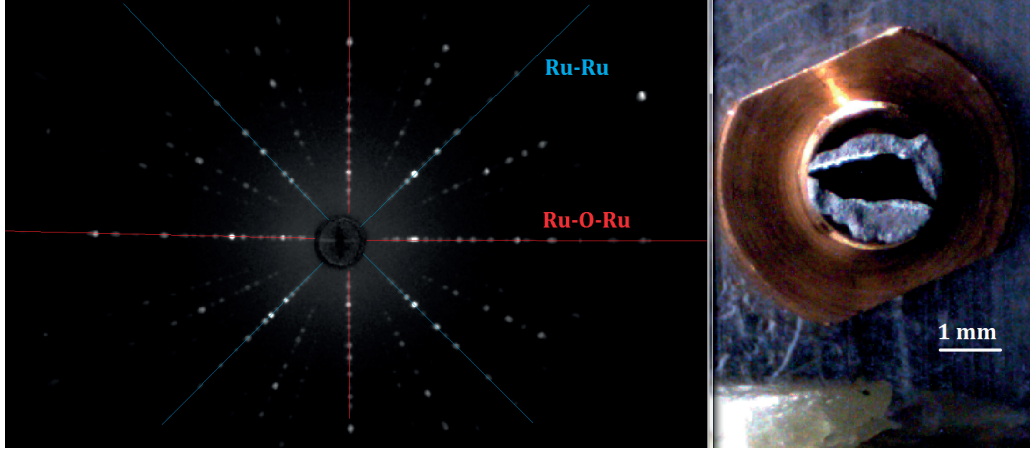


Figure 4.2 – **Laue pattern and image of a typical sample of Ca_2RuO_4** | From the relative orientation of the higher-order diffraction pattern with respect to the first order double cross (indicated in red and blue), we can recognize the orientation of the sample on the right. In this case, the sample is oriented with the Ru-O-Ru bonds aligned parallel to the frame of the picture, and the Ru-Ru bonds at 45 deg.

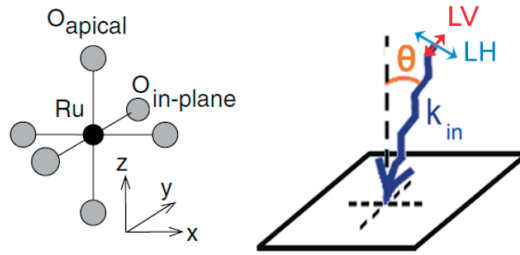


Figure 4.3 – **Schematics of the experimental geometry** | A photon beam of momentum \mathbf{k}_{in} hits the sample surface with angle θ from the surface normal (parallel to the c -axis of the sample). The polarization of the beam was systematically switched between linear horizontal (LH), parallel to the scattering plane (defined by \mathbf{k}_{in} and the surface normal in our configuration), and linear vertical (LV), orthogonal to the scattering plane.

In figure 4.2 a typical Laue pattern is reproduced, with an image of the relative sample on its side. The samples were mounted with the c -axis pointing in the direction normal to the sample holder, *i.e.* parallel to the X-ray beam generating the Laue diffraction pattern. The pattern observed is typical of perovskites structures and allows to discern the Ru-Ru (or $\pi - \pi$, in a tetragonal unit cell) direction from that of the Ru-O-Ru bonds (or $\pi - 0$).

The angle θ between the c -axis of the sample (out of plane) and the incident direction of the photon beam could be varied as illustrated in figure 4.3. The sign of θ is defined positive as in the figure, and will be relevant for the discussion of the RIXS results (section 4.3). In

this section, the quantity of interest is its absolute value $|\theta|$. The in-plane orientation of the sample was fixed so that the scattering plane contained both the c -axis (z direction in the figure) and Ru-O-Ru bond direction (x in the figure), for all values of θ . In other words, the oxygen p orbitals were aligned along the x , y or z direction.

4.1.1 Choice of the absorption resonance

Ruthenium is a $4d$ transition metal, with ground state chemically described as $[\text{Kr}] 4d^7 5s^1$, which changes to $[\text{Kr}] 4d^4 5s^0$ within the oxide compounds studied - in which ruthenium has valence state +4. An isolated Ru^{+4} ion would therefore possess 4 electrons in the 10-fold degenerate $4d$ orbitals, see figure 4.4. The presence of the oxygen atoms at the vertexes of a perovskite octahedra however remove the spacial isotropy, lifting the initial degeneracy. In fact, for an electron to occupy the orbitals pointing directly in the direction of the oxygen atoms (along which are distributed the oxygen p electrons) will require an higher energy. We label these orbitals ($d_{x^2-y^2}$, d_{z^2}) as e_g and those directed away from the oxygen atoms (d_{xy} , d_{xz} , d_{yz} , whose energy level is lowered by the crystal field) as t_{2g} . Furthermore, if the axes of the octahedra are not identical - as in the cases that we will discuss - energy differences are expected within the e_g and t_{2g} orbitals, since the choice of a \hat{z} direction is no longer arbitrary. Finally, we should not forget the effect of the spin-orbit coupling, which mixes the atomic orbitals and contributes to lifting the degeneracy. However, we will keep referring to the e_g and t_{2g} states, that can be used as a basis for the spin-orbit mixed electronic states.

We performed a XAS and RIXS combined study on Sr_2RuO_4 and Ca_2RuO_4 . To excite a core electron from the ruthenium $2p$ states to the partially-empty $4d$ valence states (corresponding to the $L_{II,III}$ absorption edges) one needs an energy of $\sim 2.8\text{-}3$ keV. For technical reasons, at the time of our investigations such an energy was not accessible, with sufficient energy resolution, at any RIXS instrument (or synchrotron facility, more generally). In fact, the wavelength of photons in this energy range (~ 5 Å) is too large to match inter-plane spacing in crystal monochromators and too small for the groove spacing of grating monochromators.

As a consequence, our attention moved to the oxygen K absorption edge, given that to excite a core electron from the oxygen $1s$ states into the $2p$ valence states requires "only" ~ 530 eV, an energy range which is far more accessible. Since these states are strongly hybridized with the $4d$ ruthenium valence states, we could still draw some conclusions on these latter, as summarized in section 4.5. Since we were operating at the oxygen absorption edge K (O-K edge), clean surfaces were created in-situ to reduce oxygen contamination.

4.1.2 Orbital tuning

The $1s$ initial state of the excited electron has spherical symmetry, therefore it doesn't introduce any geometrical selection rule. The polarization of the incoming beam was switched between linear horizontal (LH), parallel to the scattering plane, and linear vertical (LV), perpendicular

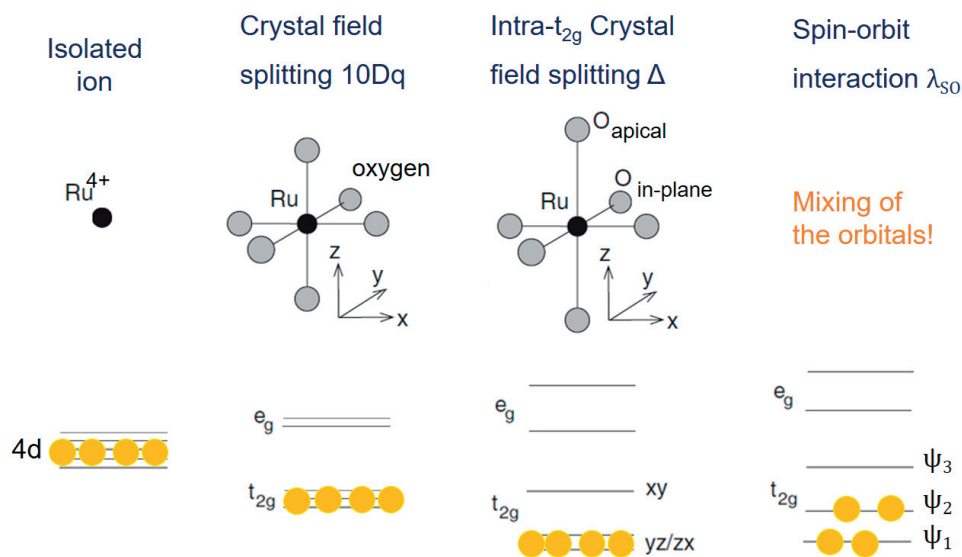


Figure 4.4 – **Schematics of degeneracy lifting of the 4d orbitals** | Illustration of the various effects which lift the degeneracy of 4d states in a Ru^{4+} ion within a ruthenate compound. An isolated Ru^{4+} ion would have a 5-fold degeneracy in the 4d orbitals, 10-fold if one considers the spin degree of freedom of the electrons. The presence of the oxygens, arranged in an octahedra, introduces an energy difference between the e_g orbitals ($d_{x^2-y^2}, d_{z^2}$) which point directly against the O^{2-} ions (electrons in such orbitals would feel a stronger repulsion due to the presence of the electrons in the oxygen 2p orbitals) and those - the t_{2g} orbitals (d_{xy}, d_{yz}, d_{xz}) - which point diagonally. Distortions in the O octahedra can further differentiate the energy levels, so that a splitting is produced also within the e_g and the t_{2g} orbitals. Taking into account the spin-orbit interaction produces a mixing of the orbitals, that can no longer be directly identified with the eigenstates of the orbital moment. However, we will continue to use d_{xy}, d_{yz}, d_{xz} as a base, on to which we project the electronic states ψ_1, ψ_2, ψ_3 . It is also worth to note that the oxygen sites are not equivalent. The O atoms in the apical sites experience a different chemical environment than those in planar positions. This translates in a different energy resonance in X-ray absorption processes.

to the scattering plane. This implies that the oscillating electric field of the beam was aligned along y (and hence p_y) for LV polarization, but along either x (at normal incidence, $\theta=0^\circ$) or along z (grazing incidence, $\theta=\pm 90^\circ$) in the case of LH polarization. As a consequence, by varying incident angle and/or polarization of the X-ray beam, it was possible to selectively enhance transitions into specific p-orbitals, as represented in figure 4.5.

At this point it should be emphasized that the O atoms in apical or planar positions experience a different chemical environment which changes the respective absorption resonances, in our case by $\Delta E \sim 1$ eV. Changing the energy of the photon beam therefore allows to select at which oxygen site (apical or planar) will occur the promotion of a 1s core electron to a 2p valence state. Furthermore, the Ru d-orbitals hybridize differently with the p orbitals of apical

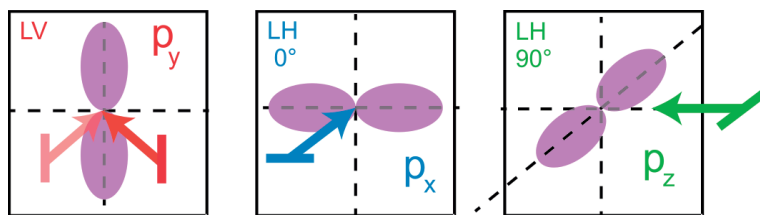


Figure 4.5 – ***p*-orbital selection** | By varying incident angle and polarization of the photon beam, coupling with orbitals directed along x, y or z direction is enhanced.

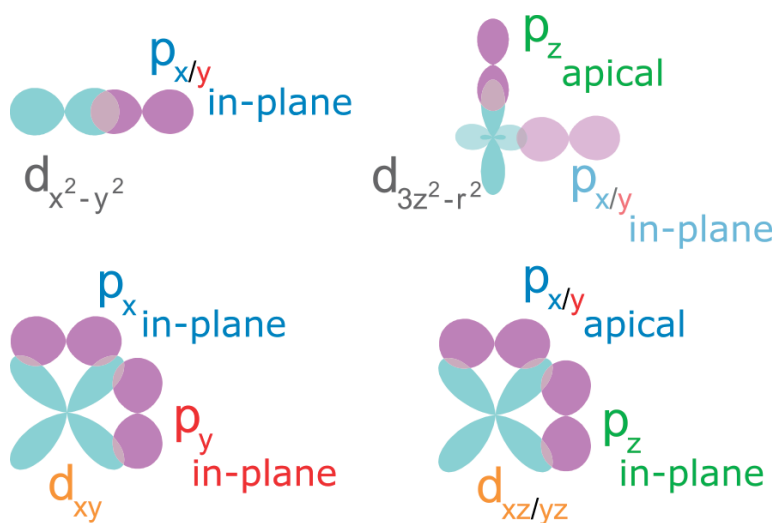


Figure 4.6 – ***O2p*-*Ru4d* hybridization** | Illustration of the main hybridization between the (top) e_g or (bottom) t_{2g} orbitals of ruthenium with the $2p$ orbitals of oxygen in apical or planar sites, as indicated. While other d states mainly hybridize with p orbitals originating from either apical or planar sites, the $d_{xz/yz}$ states hybridize with the p_z orbital of in-plane oxygen atoms, but also with the $p_{x/y}$ orbitals of apical oxygen. A similar situation occurs for the d_{z^2} orbital, that presents both out of plane and in-plane charge distribution.

or planar oxygen atoms, as depicted in figure 4.6.

The e_g states, pointing directly towards the vertex of the O octahedra, mainly hybridized either with the $p_{x/y}$ orbitals of oxygen atoms within the RuO_2 planes (case of $d_{x^2-y^2}$) or with the p_z orbital of oxygen atoms in apical sites. It should be noted that d_{z^2} orbital have some in-plane charge distribution which can be picked up through its hybridization with in-plane O orbitals. The t_{2g} states, separated in energy from the e_g by $\sim 2\text{-}4$ eV, on the other hand point away from the O atoms and hybridize mainly with orbitals originating from both sites, as visualized in the bottom panels of figure 4.6, with the exception of d_{xy} which has a pronounced planar character.

From these considerations, one can for example infer that in grazing incidence geometry with

LV(LH) polarization - which aligns the X-ray electric field with $Op_{y(z)}$ orbitals - absorption from apical oxygen atoms is related to the occupancy of Rud_{yz} (Rud_{z^2}). In the same conditions, absorption from the in-plane O atoms gives mostly information about the occupancy of $Rud_{x^2-y^2}$ and Rud_{xy} (Rud_{yz} and Rud_{xz}).

More generally, we have identified three parameters through which control (to some extent) the absorption process: (1) site-dependent energy resonance, (2) beam polarization and (3) angle of incidence. In table 4.7 the different configurations are summarized, and a green tick explicates to which Rud orbital one gains enhancement of experimental sensitivity.

	Apical O resonance			In-plane O resonance		
	LV (p_y)	LH N.I. (p_x)	LH G.I. (p_z)	LV (p_y)	LH N.I. (p_x)	LH G.I. (p_z)
$d_{x^2-y^2}$				✓	✓	
$d_{3z^2-r^2}$			✓	✓	✓	
d_{xy}				✓	✓	
d_{yz}	✓					✓
d_{xz}		✓				✓

Figure 4.7 – **Selective tuning of XAS sensitivity** | Summary of the experimental configurations and ability to tune the experimental sensitivity to the occupancy of different $Ru4d$ orbitals, mediated by hybridization with the $O2p$ orbitals. The smaller ticks indicate access to the d_{z^2} orbital through its in-plane spatial distribution.

In the next section, we will present XAS results on Ca_2RuO_4 and Sr_2RuO_4 , interpreted in light of the considerations described in this section.

4.2 XAS results

4.2.1 O K-edge absorption spectra of Ca_2RuO_4

Figure 4.8 shows the absorption spectra recorded on Ca_2RuO_4 at the O K-edge for both LV and LH polarization, for two angle of incidence $\theta = -5$ deg, 35 deg. A linear background was subtracted and spectra were normalized to the average intensity at photon energies > 546 eV. This

Chapter 4. Orbital structure of single-layer ruthenates

holds true for all XAS spectra shown in this chapter. The normalization procedure is illustrated in figure A.1 of appendix A.1. Close to normal incidence (top panel), LV and LH data - probing the p_y and p_x orbitals - superpose extremely well, which is not surprising since the x and y direction in the crystal are \sim equivalent. Moving towards grazing incidence, LH polarization worsens its coupling with p_x , but acquires some component along p_z . This is reflected by the data. Consistently with our assumptions, LV data shows no angular dependence (probing the same orbitals at all angles). The spectra recorded with LH polarization on the other hand exhibit a continuous evolution.

Already at an incident angle $\theta = 35$ deg (bottom panel), LV and LH data deviates from one another, particularly for photon energies below 536 eV. A shoulder develops into a well defined peak around 530 eV, while the strong peaks at ~ 529 eV and ~ 534.5 eV loose intensity. Also the peak at ~ 531.5 eV slowly grows with $|\theta|$, seemingly at the expenses of the one at ~ 532.5 eV. These features are labeled in the more detailed angle dependence shown in figure 4.9, separately for LV and LH spectra. Features A, D and E appear stronger when probed with LV (at all incident angles) or LH polarization in normal incidence, while features B and C are enhanced in grazing geometry with LH polarization. Using table 4.7, we can identify the orbitals of origin of the different features observed in figure 4.9.

In normal incidence, or using LV polarization, the 1s core electron is promoted to $2p_{x/y}$ orbitals in planar or apical oxygen sites. We interpret the peak at the lowest energy, A in the figure (at ~ 529 eV), as the absorption resonance of apical p orbitals hybridized with the t_{2g} states, d_{xz} and d_{yz} . As coupling is shifted towards transitions to p_z , this peak doesn't gain any additional contribution, since the p_z orbital of apical oxygen doesn't hybridize to any of the t_{2g} states. The two peaks at highest photon energy, D and E (at ~ 532.5 eV and ~ 534.5 eV), are compatible with absorption into the planar p_x, p_y orbitals hybridized with the e_g states. More specifically, we assume a main $p_{x/y}-d_{x^2-y^2}$ character for E and mostly $p_{x/y}-d_{z^2}$ for D. Also these two peaks loose intensity when coupling to p_z is improved, since planar p_z orbitals don't hybridize significantly with the e_g states. The two remaining peaks, B at ~ 530 eV and C at ~ 531.5 eV, on the contrary visibly increase in intensity with $|\theta|$. We assign peak B to the transition into the valence states originating from planar p orbitals hybridized with t_{2g} Ru states. With LV polarization or in normal incidence, one probes the hybridization $p_{x/y}-d_{xy}$. Moving towards grazing incidence (*i.e.* increasing $|\theta|$) and using LH polarization, the coupling to p_x worsens while that to p_z improves. Planar p_z hybridizes with both d_{xz} and d_{yz} , so the geometrical change implies an increase of the planar $p-t_{2g}$ resonance, as observed. Finally, peak C is associated with the transition from O1s to $p_z-d_{z^2}$ in the apical site.

Notice that the energy difference between the apical and planar resonance is ~ 1 eV both for the $p-t_{2g}$ (peaks B and A) and the $p-d_{z^2}$ states (peaks C and D), which is consistent with the chemical shift introduced by the covalent bonds apical oxygen shares with calcium [128, 129, 130, 131, 132]. Both our data and interpretation are in agreement with previous XAS work on Ca_2RuO_4 [128, 133]. It is convenient at this point to re-label the the features

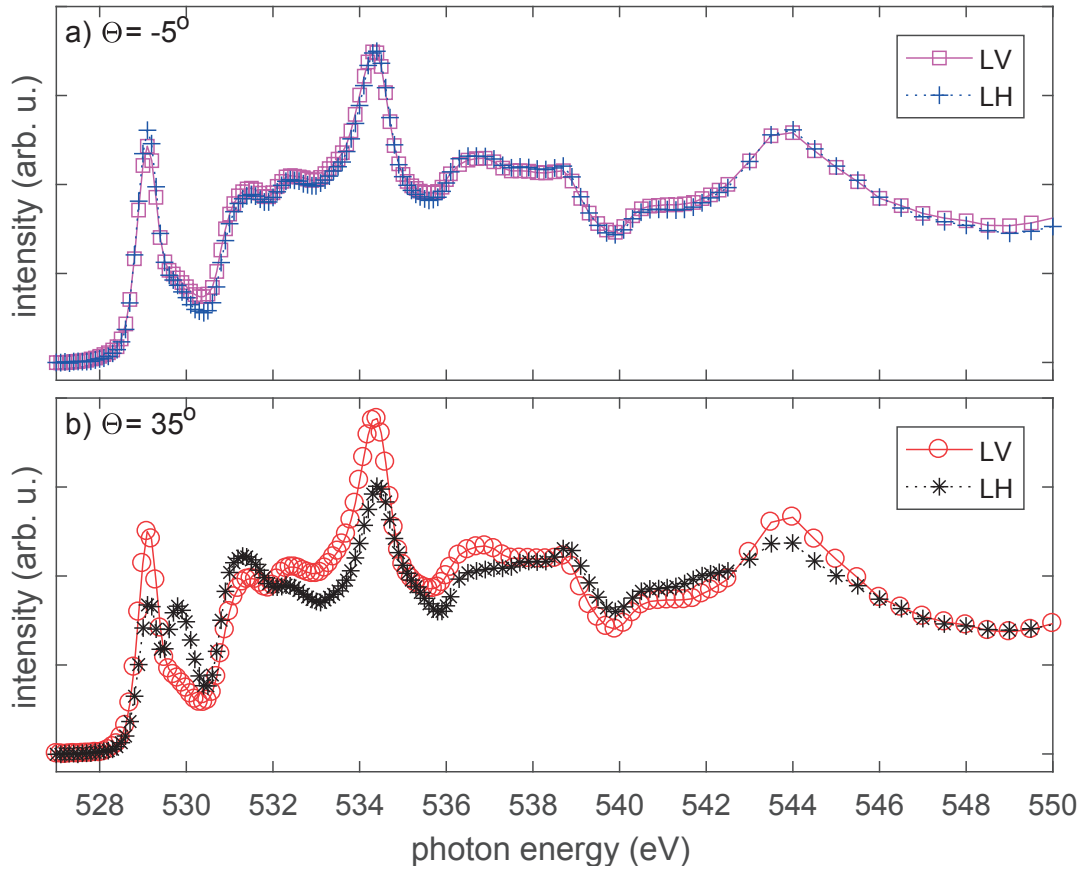


Figure 4.8 – **Full range O K-edge XAS on Ca_2RuO_4** | Unless specified, XAS spectra were recorded in total fluorescence yield.

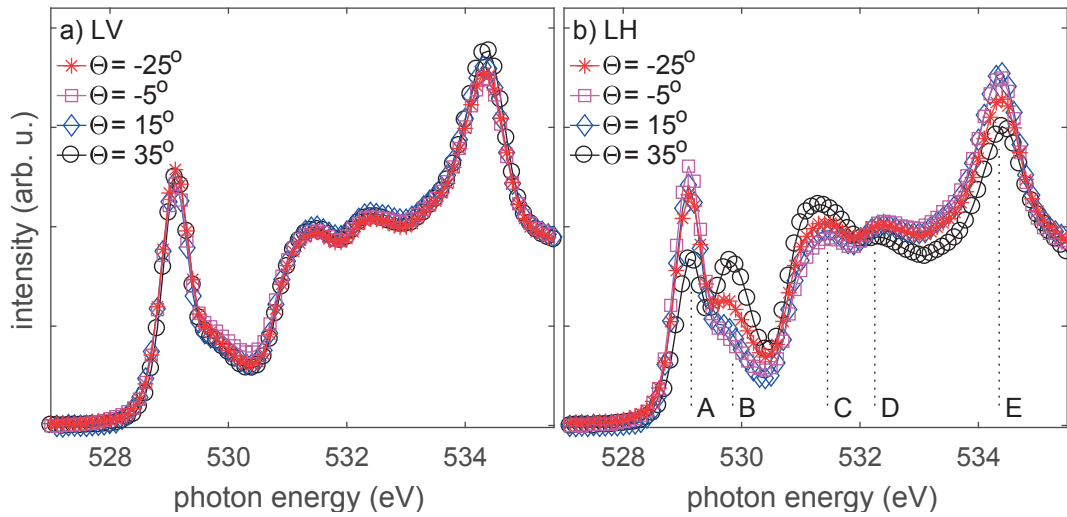


Figure 4.9 – **Angle dependence of LV and LH XAS on Ca_2RuO_4** | While LV data shows no angle dependence, LH spectra exhibit a progressive evolution .

observed in a way more directly related to their interpretation: t_A (apical resonance A), t_P (planar resonance B), z_A^2 (apical resonance C), z_P^2 (planar resonance D) and $x^2 - y_P^2$ (planar resonance E).

4.2.2 O-K edge absorption spectra of Sr_2RuO_4

We are now ready to discuss the XAS spectra of Sr_2RuO_4 . In figure 4.10 the full O K-edge absorption spectrum is compared to that of Ca_2RuO_4 . At first sight, the two materials present very different oxygen absorption edges. On a more careful observation however, there is a clear correspondence between the feature observed, although these are present with different relative intensities, and shifted in energy. This parallelism is particularly interesting in the energy range below 536 eV, reproduced in figure 4.11 for LV and LH polarization and different values of θ .

As expected, probing Sr_2RuO_4 with LV polarization produces the same XAS spectrum at all angles. In agreement with our previous discussion, when using LH polarization the signal undergoes a clear evolution as a function of $|\theta|$. The different features observed are in correspondence with the ones discussed from the Ca_2RuO_4 XAS signal, and are labeled accordingly, in agreement with literature reports [128, 130, 134, 135, 136].

Also in the case of Sr_2RuO_4 we observe a consistent chemical shift or ~ 1 eV between apical and planar sites in both the e_g (peaks $z_A^2 - z_P^2$) and t_{2g} (peaks $t_{2gA} - t_{2gP}$) absorption resonances. It is worth to highlight that in Sr_2RuO_4 the apical absorption resonance corresponding to promotion of the core electron into the p_z - $\text{Ru}d_{z^2}$ states (feature z_A^2) falls very close to the planar t_{2gP} . This explains the experimental observation of the peak around 530 eV significantly broadening with $|\theta|$ (in LH polarization, see appendix A.2). For this reason, we restricted our analysis on the relative intensities of features t_A and t_P on LV data.

To convince ourselves that the broad peak reported around 530 eV, in grazing incidence and with LH polarization, is due not only to planar oxygen orbitals hybridized with Ru t_{2g} states, but gains a significant contribution from apical p_z - $\text{Ru}d_{z^2}$ hybridization, it is useful to refer to the work of Noh *et al.* on $\text{Ca}_{2-x}\text{Sr}_x\text{RuO}_4$, $x=0.9-2$, reproduced in figure 4.12. Noh *et al.* have followed the evolution of the XAS signal with Sr content, in both normal (solid line) and grazing (open dots) incidence, with LH polarization. Full diamond markers indicate the energies corresponding to transitions to states originated from the indicated Ru $4d$ orbitals, where the subscript A or P refers to hybridization with either apical or planar O $2p$ orbitals.

The markers of the resonance of interest, z_A^2 , have been highlighted in red. Starting with the second spectra from the bottom of figure 4.12, we see that in $\text{Ca}_{1.85}\text{Sr}_{0.15}\text{RuO}_4$ the z_A^2 resonance is well separated from the planar $p_{x/y} - t_{2g}$ one (t_{2gP}), and is not observed in normal incidence. Changing the Sr content initially doesn't affect these observations. When Sr has substituted

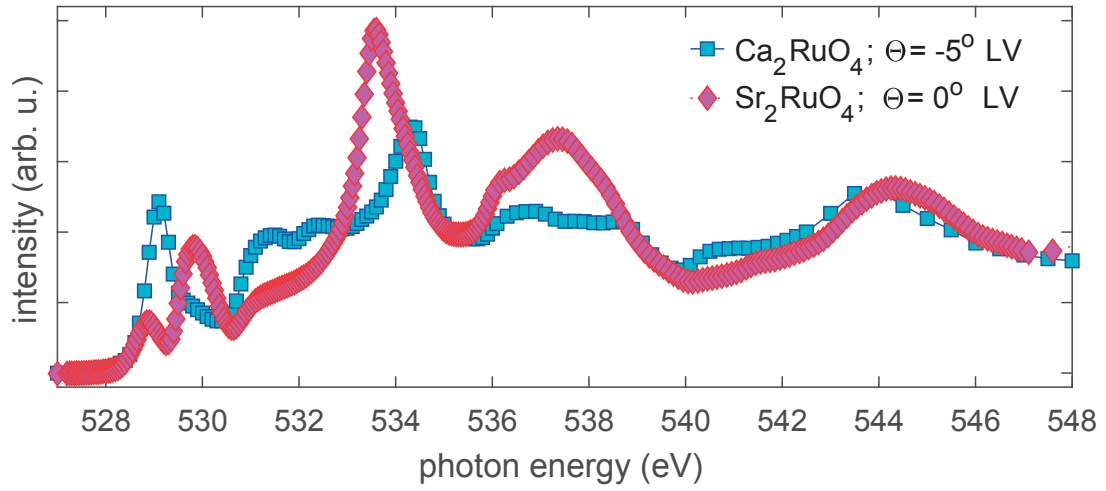


Figure 4.10 – **Full range O K-edge XAS on Sr_2RuO_4** | XAS spectrum of Sr_2RuO_4 recorded in normal incidence and LV polarization (red diamonds), compared to that of Ca_2RuO_4 (blue squares).

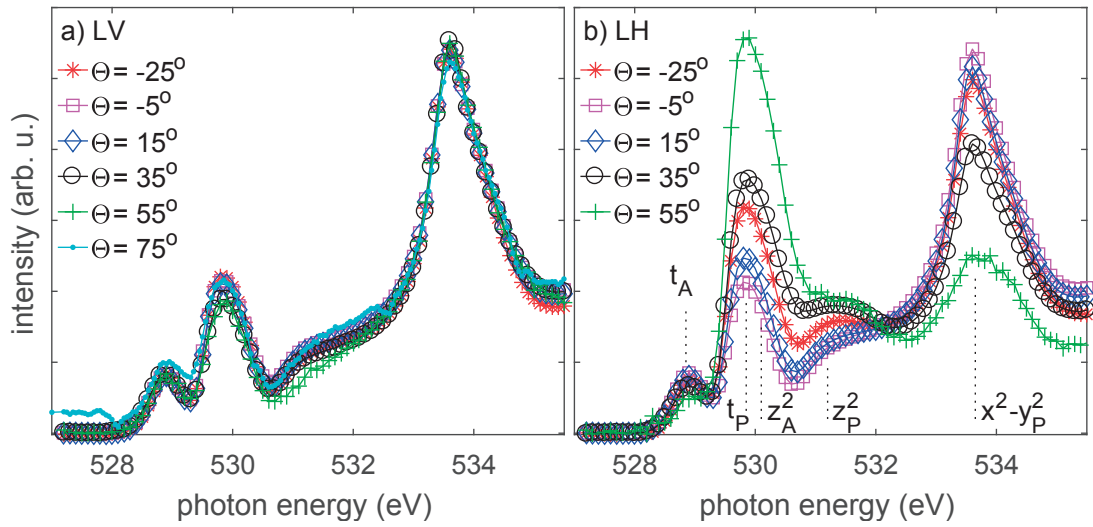


Figure 4.11 – **Angle dependence of LV and LH XAS on Sr_2RuO_4** | As observed on Ca_2RuO_4 , data collected with LV polarization has no dependence on θ , while LH spectra evolve progressively with it.

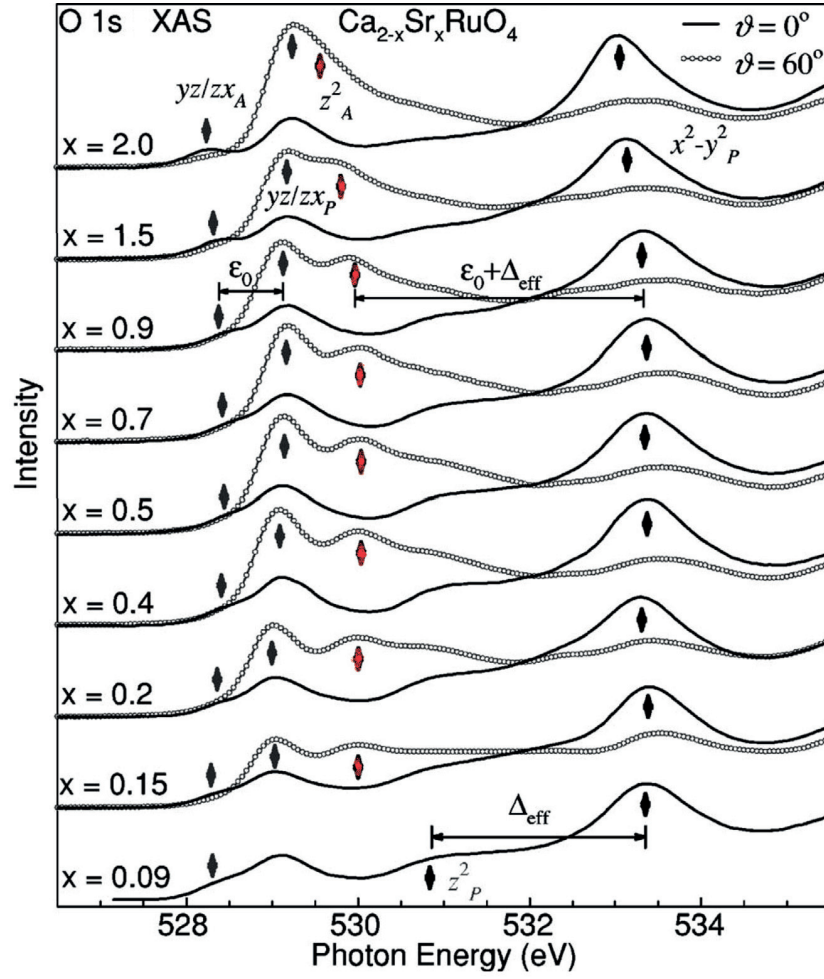


Figure 4.12 – $\text{Ca}_{2-x}\text{Sr}_x\text{RuO}_4$ XAS from literature | XAS spectra of $\text{Ca}_{2-x}\text{Sr}_x\text{RuO}_4$, with $x=0.09$ (bottom) to $x=2$ (top). The red marker indicates the apical p_z - $\text{Ru}d_{z^2}$ absorption resonance observed in grazing incidence geometry. Spectra were recorded with LH polarization and arbitrarily shifted to improve visibility. Adapted from [128].

about half the Ca atoms, the peaks grow closer together until they merge in Sr_2RuO_4 . However, at all values of x the z_A^2 feature is absent in normal incidence spectra. Furthermore, the width of the t_P resonance in normal incidence is conserved across all values of Sr content. These combined observations reassure us that the relative intensity of features t_A and t_P in LV polarization are not influenced by the vicinity of the z_A^2 resonance.

4.2.3 Estimation of crystal field splitting

Having identified the main character of the resonances labeled in figures 4.9 and 4.11, we can now extract an experimental estimation of the crystal field splitting in Sr_2RuO_4 and Ca_2RuO_4 .

By comparing the energy of the planar resonances t_P , z_P^2 and $x^2 - y_P^2$, we estimate a crystal field splitting of ~ 2.5 eV between the t_{2g} states and the e_g state with prevalent d_{z^2} character and ~ 4.5 eV to the one dominated by $d_{x^2-y^2}$ in Ca_2RuO_4 . In Sr_2RuO_4 these splitting are reduced to ~ 1.3 eV and ~ 3.8 eV, respectively.

It is interesting to note that the resonance t_P is peaked around ~ 529.85 eV in both Sr_2RuO_4 and Ca_2RuO_4 . The apical resonance t_A is instead lowered by ~ 0.3 eV when Sr atoms substitute Ca ones. If we use this difference to estimate the chemical shift introduced by the substitution, it is clear that to explain the differences observed in features z_P^2 and $x^2 - y_P^2$ (which shift by ~ 1 eV) it is necessary to refer to their different crystal structure. The compression of the O octahedra in Ca_2RuO_4 rises the energy of the d_{z^2} orbital, which is reflected in the states originating from it.

The experimental evaluation of the crystal field splitting represents our first conclusion, summarized in table 4.1. Next, the apical and planar t_{2g} resonances are analyzed in greater detail, and their relative intensity is discussed.

Table 4.1 – **Crystal field splitting evaluation** | The values were extracted solely based on the position of the peaks - and their evolution as function of the beam polarization and angle of incidence.

	$e_{g,1}-t_{2g}$	$e_{g,2}-t_{2g}$
Ca_2RuO_4	2.5 ± 0.25 eV	4.5 ± 0.5 eV
Sr_2RuO_4	1.3 ± 0.25 eV	3.8 ± 0.5 eV

4.2.4 Self-absorption

X-ray absorption spectra can be recorded in total fluorescence yield (TFY), or total electron yield (TEY). We performed our experiment with the samples at ~ 16 K, at which temperature Ca_2RuO_4 is an AF Mott insulator, and produces no signal in TEY mode. Instead, we used TFY data for both compounds. TFY signal can be affected by self-absorption, the process in which photons emitted due to the relaxation of the excited state (following the absorption process) are re-absorbed in their way out of the material, therefore potentially influencing the relative intensities.

The cross section for self absorption increases with the length of the path of the escaping photons within the material, meaning that it has a minimum at normal emission and maximizes in grazing emission. Our LV data show no significant angle dependence, which points towards little to no self absorption issues. To further ensure that the relative intensities aren't affected by self absorption in our data set, in figure 4.13 we produce a direct comparison between TFY and TEY signal, for both Sr_2RuO_4 and Ca_2RuO_4 . In order to record TEY data, Ca_2RuO_4 was warmed to ~ 125 K (a temperature above the AF ordering transition $T_{AF}=110$ K, corresponding to a sharp decrease in the resistivity of Ca_2RuO_4 [137] which makes it possible to record TEY

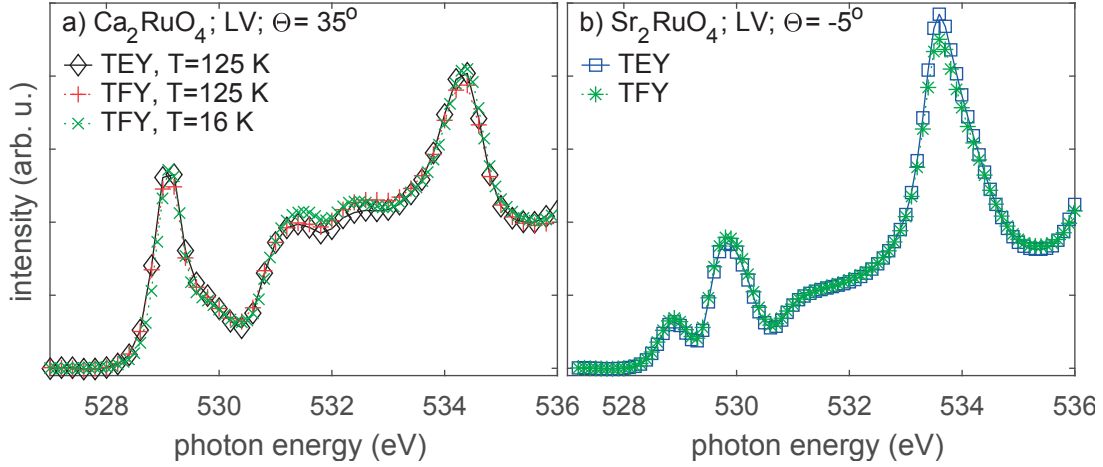


Figure 4.13 – **TFY vs TEY** | (a,b) Sr_2RuO_4 and Ca_2RuO_4 TFY compared to TEY spectra. In the case of Ca_2RuO_4 , it was necessary to warm the sample, so the TFY is shown both at base temperature ($T \approx 16$ K) and above the AF ordering temperature, at $T \approx 125$ K.

signal). The angle and polarization evolution of Sr_2RuO_4 TEY data follows that observed on TFY spectra. The remarkable agreement between TFY and TEY results in both compounds (top panels of figure 4.13) reassures us on the negligibility of self-absorption effects.

4.2.5 Estimation of orbital occupancy

Recent works based on first principle calculations[134, 135] have raised concerns over the non-negligible contribution of the Sr/Ca orbitals to the origin of states ~ 2 eV above threshold. This would invalidate, or at least compromise, conclusions on the Ru states drawn from analysis of these features. However, in the following we focused on the pre-edge features - at energies below 531 eV - to extract information on the t_{2g} orbitals occupancy. General consensus[128, 133, 134, 135, 130, 136] attributes these states to apical and planar $\text{O}2p\text{-Ru}t_{2g}$ hybridization. We can therefore move on to a more detailed analysis of TFY spectra in the range 527-531.5 eV. We are interested in an experimental estimation of the hole-occupancy in states originating from the t_{2g} orbitals, hence we focused on the $t_{A,P}$ absorption resonances.

According to our analysis, summarized in table 4.7, at the $p\text{-}t_{2g}$ absorption resonances probed with LV polarization, apical and planar oxygen sites provide complementary information. In fact, at each oxygen site absorption is mostly sensitive to the occupation of either the out of plane d_{yz} (case of apical site) or the planar d_{xy} orbital (probed via its hybridization with p_y oxygen orbitals). As explained in the previous paragraphs, LH data have a pronounced angle dependence and can probe states with both d_{xz} and d_{xy} symmetry. Another complication in the case of Sr_2RuO_4 comes from the close vicinity to t_P of the z_A^2 resonance, see paragraph 4.2.2, which is observed with LH polarization only and increases in intensity with the incident

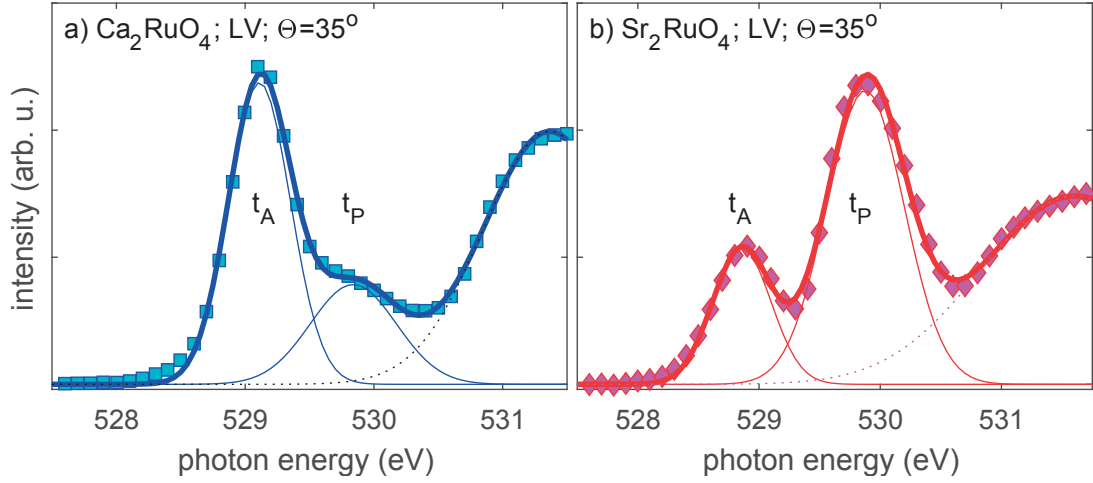


Figure 4.14 – **XAS fit** | (a,b) fit of Ca_2RuO_4 and Sr_2RuO_4 XAS spectra. The fitting function (thick solid line) is the sum of the three Gaussian shown, in solid thinner lines for the apical and planar $t_{A,P}$ absorption resonances, dashed for the next absorption peak, which constitutes a background.

angle θ , see appendix A.2. For these reasons, we focused on the data collected with LV polarization.

Figure 4.14 illustrates the fitting procedure, in the case of $\theta=35^\circ$ for both materials. The apical and planar resonances - t_A and t_P - are indicated. The fitting function, equation 4.1 and thick solid line in figure 4.14, is the sum of three Gaussian functions, one for each absorption resonance observed in the fitting range 527-531.5 eV. The first two curves, thin solid lines in figure 4.14, correspond to the p - t_{2g} absorption resonances in apical (t_A) and planar (t_P) site, the third, dotted lines in the figure, corresponds to the next resonance (z_A^2 in the case of Ca_2RuO_4 , z_P^2 for Sr_2RuO_4), which, in the context of the current analysis, constitutes a background (B):

$$F(x) = I_A e^{-\frac{(x-c_A)^2}{2\sigma_A^2}} + I_P e^{-\frac{(x-c_P)^2}{2\sigma_P^2}} + I_B e^{-\frac{(x-c_B)^2}{2\sigma_B^2}}. \quad (4.1)$$

With x = photon energy, $c_{A,P,B}$ center of the relative absorption resonances of intensity $I_{A,P,B}$ and full width at half maximum (FWHM) given by $2\sqrt{2\ln 2}\sigma_{A,P,B}$. The parameters extracted from fitting LV spectra to function 4.1 are plotted against $|\theta|$ in figure 4.15(a-c).

In panel 4.15(a), the center of the apical and planar resonances are compared for Ca_2RuO_4 (Ca_{214}) and Sr_2RuO_4 (Sr_{214}). As expected, the planar resonance t_P appears at the same energy in the two compounds, while the apical t_A is lowered by ~ 0.3 eV by the Sr-substitution of Ca. These resonances all have FWHM of ~ 0.6 - 0.7 eV ($\sim 0.25 - 0.3 \cdot 2\sqrt{2\ln 2}$, see figure 4.15(b)), contrarily to what observed in LH data (see appendix A.2). The intensities also appear quite stable across the different angle of incidence (figure 4.15(c)). Panel 4.15(d) shows the ratios of apical to

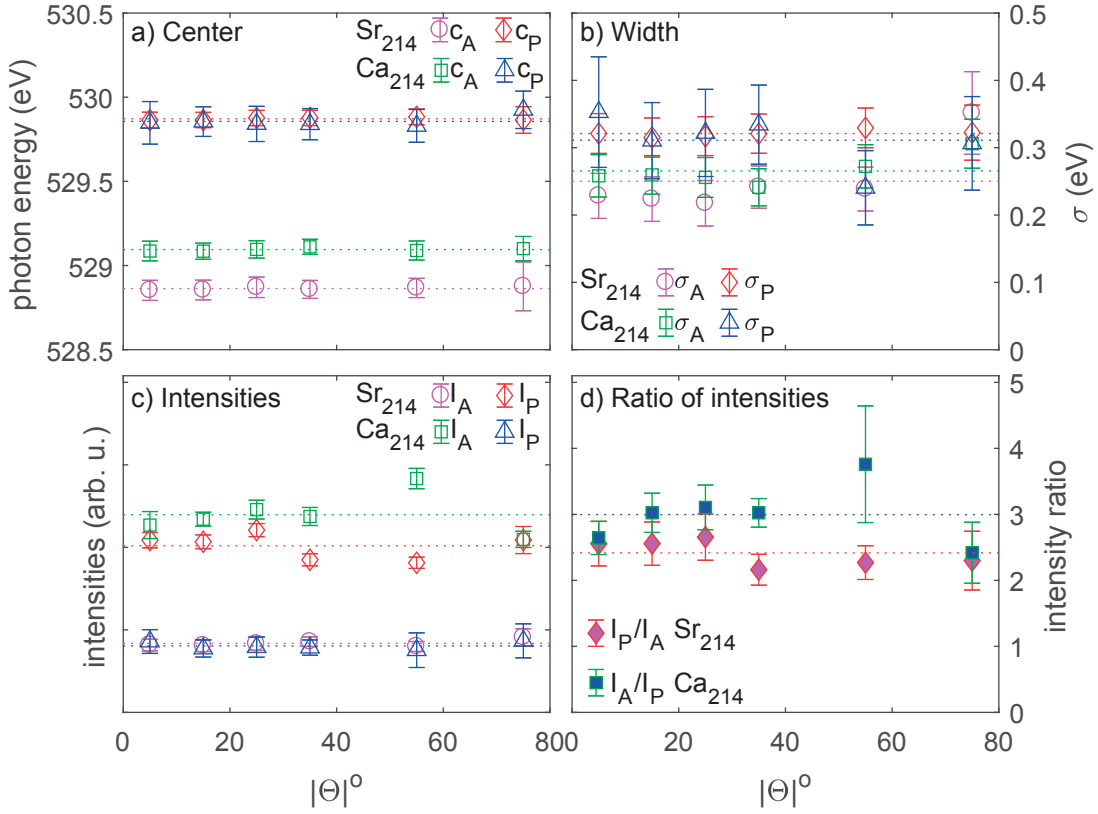


Figure 4.15 – **XAS fit results** | (a-c) Open markers indicate fitting parameters extracted from Ca_2RuO_4 (Ca_{214}) and Sr_2RuO_4 (Sr_{214}) for the apical (A) and planar (P) resonances. Panel (d) shows the intensity ratio, I_A/I_P in full squares for Ca_{214} and I_P/I_A in full diamonds for Sr_{214} . The relative intensity is almost perfectly reversed. Color-coded dotted lines mark the average values of the relative quantities.

planar intensity for Ca_2RuO_4 , R_{Ca} , and planar to apical for Sr_2RuO_4 data, R_{Sr} . I_P is found to be $\sim 1/3 I_A$ for Ca_2RuO_4 but $\sim 2.5 I_A$ in the case of Sr_2RuO_4 across all θ . At higher $|\theta|$, some minor variations are observed both in terms of width and intensity, which reflect in the intensity ratios and the propagated error. However, removing these last points from our measure doesn't significantly affect the average values of R_{Ca} and R_{Sr} or their weighted averages (which take into account the different confidence assigned to each measure). We conclude $R_{Ca} = 2.9 \pm 0.1$ and $R_{Sr} = 2.4 \pm 0.1$.

We assume $I_A \propto n_{yz} \cdot H_A$, hole-occupancy of the state with d_{yz} symmetry times the hybridization strength to the apical O, and similarly $I_P \propto n_{xy} \cdot H_P$. Furthermore, $n_{yz} \equiv n_{xz}$ since the two directions are indistinguishable in Sr_2RuO_4 and practically equivalent in Ca_2RuO_4 . From figure 4.14 and panels (c) and (d) in figure 4.15, it is evident that I_A and I_P have opposite relative intensities in the two compounds, suggesting that the hole probed via XAS is mostly delocalized in states at different symmetry ($d_{xz/yz}$ vs d_{xy} in Ca_2RuO_4 and Sr_2RuO_4 respec-

tively). This is consistent with the crystal structure deformations, that lift the energy of the $d_{xz/yz}$ states in Ca_2RuO_4 (as observed on the e_g states, see paragraph 4.2.3).

We have $R_{Ca} = I_A / I_P \cong \frac{n_{yz}}{n_{xy}} \cdot \frac{H_A}{H_P}$, and $R_{Sr} = I_P / I_A \cong \frac{n_{xy}}{n_{yz}} \cdot \frac{H_P}{H_A}$. To estimate the hybridization strength we assume a power-law dependence on the Ru-O bond length r , with $H_{P(A)} \propto r_{P(A)}^{-3.5}$ [138], as done on iridates [132]. The lengths of the Ru-O bonds for apical and planar oxygen change in the two compounds, so that $\frac{H_A}{H_P} \cong \frac{r_A}{r_P}^{-3.5} = \frac{1.972}{2.016}^{-3.5} \approx 1.08$ for Ca_2RuO_4 [137], and $\frac{H_P}{H_A} \cong \frac{r_P}{r_A}^{-3.5} = \frac{1.933}{2.059}^{-3.5} \approx 1.25$ for Sr_2RuO_4 [139]. We can therefore extract experimental estimation of upper and lower boundaries (with or without corrections to the hybridization strength) for the ratio in hole-occupancy of the states originating from d_{xy} , d_{xz} and d_{yz} :

$$\begin{aligned} 0.15 &\leq \left(\frac{n_{xy}}{n_{yz} + n_{xz}} \right)_{\text{Ca}_2\text{RuO}_4} \leq 0.20 \\ 1.00 &\leq \left(\frac{n_{xy}}{n_{yz} + n_{xz}} \right)_{\text{Sr}_2\text{RuO}_4} \leq 1.25 \end{aligned} \quad (4.2)$$

This represents the second conclusion drawn from the analysis of the XAS spectra.

4.3 RIXS results

4.3.1 Momentum transferred along the sample surface

The RIXS process can be discussed as an inelastic scattering event. Photons of energy $h\nu_{in}$ and momentum \mathbf{K}_{in} were directed to the sample and photons of energy $h\nu_{out}$ and momentum \mathbf{K}_{out} emerge. The angle between the in-coming and out-coming photon momenta is the scattering angle α , fixed to 50 deg by our experimental geometry. The plane identified by the directions of \mathbf{K}_{in} and \mathbf{K}_{out} is the scattering plane, which in our geometry contains the c -axis and cuts the samples along the Ru-O-Ru bonds, aligned along the direction of $\hat{\mathbf{x}}$.

The momentum transferred in the scattering event, $\mathbf{Q} = \mathbf{K}_{out} - \mathbf{K}_{in}$, has the direction of the bisector of α and modulus $|\mathbf{Q}| \approx 0.49 \text{ \AA}^{-1}$, for $h\nu_{in} = 528\text{-}532 \text{ eV}$ (see section 2.2.5). By varying the angle of incidence to the sample surface, θ , the component of momentum transferred into the sample plane is modified: $\mathbf{Q}_{//} = 0.49 \sin(\alpha/2 - \theta) \hat{\mathbf{x}} \text{ \AA}^{-1}$. For a more direct understanding of this value, it is convenient to refer to the size of the Brillouin zone vector in the relevant direction, \mathbf{q}_{BZ}^x .

The tetragonal unit cell of Sr_2RuO_4 aligns along the Ru-O-Ru bonds so that $\hat{\mathbf{x}}$ corresponds to the a axis. The orthorhombic unit cell of Ca_2RuO_4 is misaligned by ~ 45 deg with respect to $\hat{\mathbf{x}}$. Therefore, we adopt the following convention:

$Q_{//} \equiv h \mathbf{q}_{\text{BZ}}^x$, with $h \simeq 0.6 \sin(25 \text{ deg} - \theta)$ for Sr_2RuO_4 samples, where $\mathbf{q}_{\text{BZ}}^x = \mathbf{q}_{\text{BZ}}^a$.

$Q_{//} \equiv h' \mathbf{q}_{\text{BZ}}^x$, $h' \simeq 0.6 \sin(25 \text{ deg} - \theta)$ for Ca_2RuO_4 samples - where the prime is to indicate that in this case \mathbf{q}_{BZ}^x does not coincide with any of the Brillouin zone primitive vectors.

For both compounds, $q_{\text{BZ}}^x = \frac{\pi}{a_t} \sim 0.8 \text{ \AA}^{-1}$, with a_t size of the tetragonal unit cell. A detailed derivation is found in appendix A.3.

In the next sections the RIXS data recorded on Ca_2RuO_4 and Sr_2RuO_4 samples, kept at a temperature of $\sim 16 \text{ K}$, is presented and discussed.

4.3.2 Dependence on incident energy

For the investigation of both compounds, the incident energy $h\nu_{in}$ was varied between ~ 528 and $\sim 531 \text{ eV}$ at incident angle $\theta = 75 \text{ deg}$, so to explore the apical and planar $t_{A,P}$ absorption resonances observed in the XAS data. These absorption resonances correspond to the promotion of $1s$ core electron to the $2p$ valence states, hybridized with the t_{2g} ruthenium states (section 4.2). The direction of the oscillating electric field enhances absorption into specific states, summarized in table 4.2 for the three absorption resonances at lower energy, discussed in greater detail in section 4.2. The two explored polarizations, linear horizontal (LH) and linear vertical (LV), are taken in consideration in different incidence geometries, normal incidence (N.I.) and grazing incidence (G. I.).

When $\theta = 75 \text{ deg}$, the electric field $\mathbf{E}(t)$ of LH polarized in-coming photons aligns mostly with p_z , with projection along z of $E_z(t) = \sin\theta|\mathbf{E}(t)| = 0.96|\mathbf{E}(t)|$. However, coupling to p_x is not

Table 4.2 – Tuning of the absorption process with incident polarization and angle | Summary of the coupling enhancement to the valence states originating from the $\text{O}2p\text{-Ru}4d$ hybridization, for the absorption resonances at lower energy (see section 4.1). The apical absorption resonance to the $p\text{-}t_{2g}$ hybridized state (t_A) has energy of $\sim 528.85 \text{ eV}$ in Sr_2RuO_4 and $\sim 529.15 \text{ eV}$ in Ca_2RuO_4 . The planar $p\text{-}t_{2g}$ resonance (t_P) appears at $\sim 529.85 \text{ eV}$ in both samples. The next resonance, z_A^2 is associated to the promotion of the $1s$ core electron to a $p\text{-}e_g$ state with prevalent d_{z^2} character, in an apical oxygen atom. In Sr_2RuO_4 z_A^2 lies at $\sim 530.15 \text{ eV}$ and is not probed through the $p_{x/y}$ orbitals, but is only observed in linear horizontal (LH) polarization and away from normal incidence. In Ca_2RuO_4 , z_A^2 is observed at $\sim 531.5 \text{ eV}$ and is probed with both linear horizontal and vertical (LV) polarization and at all angle of incidence, but with varying intensity. The angle of incidence θ equals 0 deg in normal incidence (N.I.) and 90 deg in grazing incidence (G. I.).

		t_A	t_P	z_A^2
LH	$\theta = 0 \text{ deg}; \text{N.I.}$	$p_x - d_{xz}$	$p_x - d_{xy}$	$p_x - d_{z^2}$
	$\theta = 90 \text{ deg}; \text{G.I.}$		$p_z - d_{xz/yz}$	$p_z - d_{z^2}$
LV	all θ	$p_y - d_{yz}$	$p_y - d_{xy}$	$p_y - d_{z^2}$

completely inhibited, since $E_x(t) = \cos\theta|E(t)| = 0.25|E(t)|$. Therefore, in the energy range of interest, the core electron is preferentially sent into the hole states $p_z - d_{xz/yz}$ of the planar oxygen atoms (t_p resonance). In the case of Sr_2RuO_4 samples, in the explored energy range LH polarization can also select $p_z - d_{z^2}$ states of the apical oxygen ones (z_A^2 resonance, which lies at a higher energy - outside of the range considered - in Ca_2RuO_4). The states $p_x - d_{xz}$ of the apical O (resonance t_A) or the $p_x - d_{xy}$ in the planar sites (t_p resonance) can also be filled, with smaller cross section (reflected in the variation of the relative XAS intensity of the $t_{A,P}$ resonances). LV polarization on the other hand selects p_y and the holes states to be preferably filled are the $p_y - d_{yz}$ in the apical oxygens (resonance t_A) or the $p_y - d_{xy}$ in the planar ones (t_p resonance).

In Ca_2RuO_4 , we find that the hole occupancy of the states with d_{xy} symmetry is much lower than that of $d_{yz/xz}$ symmetry, see section 4.2.5 and equation 4.2. As a consequence, the planar resonance is probed more effectively through the $p_z - d_{xz/yz}$ states, accessed with LH polarization and grazing incidence. For this reason, we expect data collected with LH incident polarization to be more convenient to discuss our results on Ca_2RuO_4 . On the other hand, in the case of Sr_2RuO_4 it is LV data that we expect to be more useful. In fact, the z_A^2 resonance of Sr_2RuO_4 falls in close vicinity to the t_p one. This explains the observed broadening of the features observed in LH RIXS data of Sr_2RuO_4 at the t_p resonance, compared to that recorded with LV polarization (where z_A^2 is suppressed, see section 4.2.2 and figure 4.12).

In figures 4.16 and 4.17 are shown RIXS intensity maps taken at incident angle $\theta=75$ deg on Ca_2RuO_4 and Sr_2RuO_4 respectively, as function of incident energy (in the range 528.5-530.65 eV) and energy loss, for linear horizontal (panels (b) in the two figures) and vertical (panels (d)) incident polarization. At this incident angle, $h' \simeq 0.6 \sin(-50 \text{ deg}) \simeq -0.5$ so that the momentum transferred along the Ru-O-Ru bond direction values $\mathbf{Q}_{||} \simeq -0.5 \mathbf{q}_{\text{BZ}}^x$, with $q_{\text{BZ}}^x = \frac{\pi}{a_1}$. In panels 4.16(a) and 4.17(a) are shown RIXS intensity profiles taken at a specific incident energy and polarization, indicated by horizontal dotted lines in panels 4.16(b,c) and 4.17(d,e) respectively. All of the different excitations observed can be identified in these two spectra, and are labeled according to their dependence on energy loss and energy of the out-coming photons. The RIXS intensity in panels (b, d) was normalized to the intensity of the XAS signal at the corresponding incident energy, angle and polarization, reproduced in panels (c) and (e).

The vertical dashed lines in panels (b, d) serve as a guide to the eye for excitations with constant energy loss (which have a Raman-like behaviour), while the oblique dash-dotted lines indicates the dispersion of constant out-coming energy, typical of fluorescent excitations. At zero energy loss we observe the narrow peak due to the elastic process (el), whose full width at half maximum (FWHM = 0.06 eV) is defined by the experimental resolution. Between 0.3 and 0.4 eV we find an excitation which doesn't disperse in energy loss, in both compounds. We label this excitation, at Raman character, as R1. Next, in Ca_2RuO_4 around the planar t_p

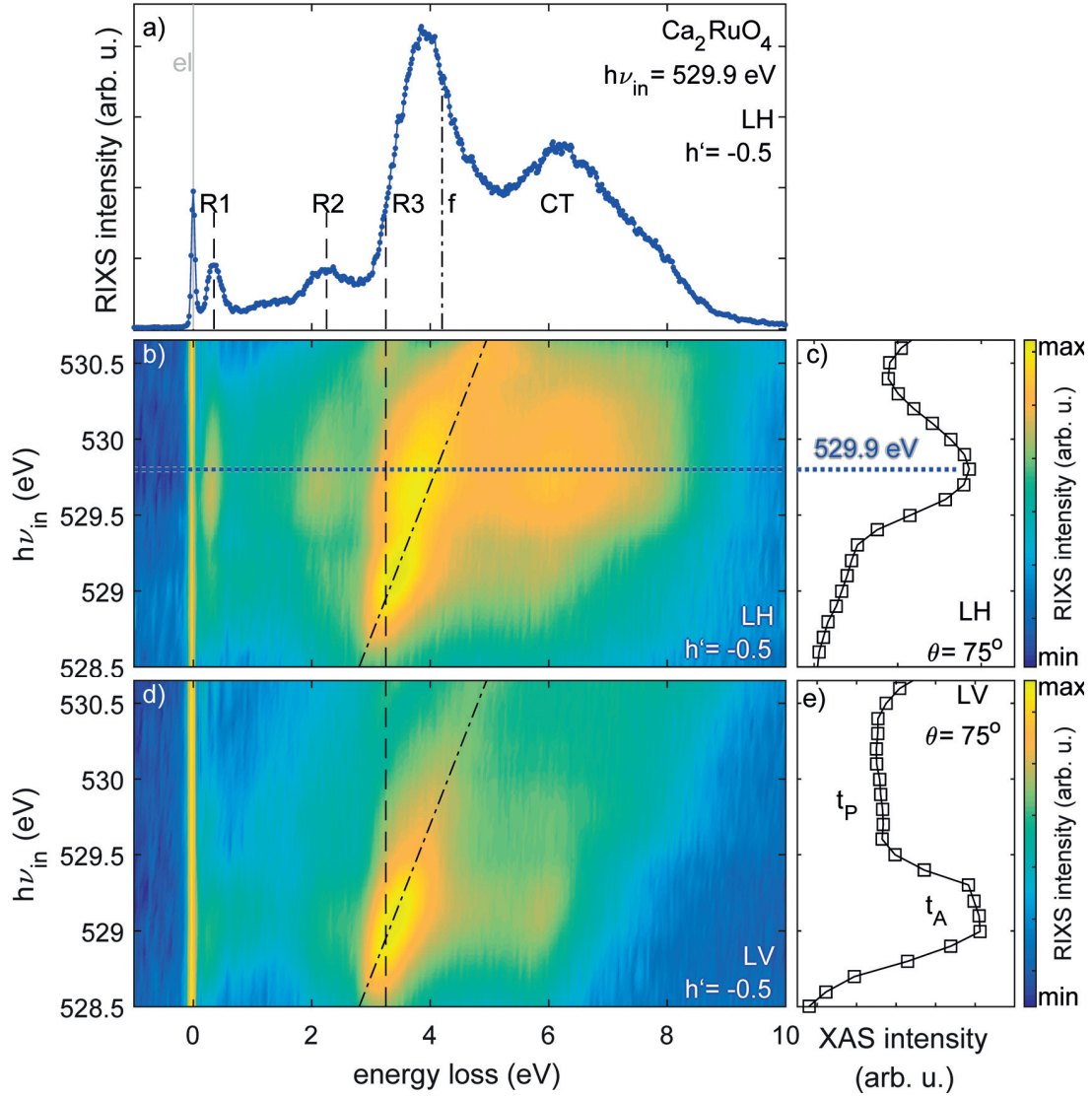


Figure 4.16 – **RIXS energy dependence of Ca_2RuO_4** | taken at $\theta = 75^\circ$ deg, corresponding to a momentum transfer of $-0.5 \mathbf{q}_{BZ}^x$, with $q_{BZ}^x = \frac{\pi}{a_t}$. a) RIXS spectrum recorded with linear horizontal (LH) polarized incident beam of energy $h\nu_{in} = 529.9$ eV. Dashed lines indicate peaks with a Raman character (R1-3), as opposed to fluorescent (f) features (dash-dotted line). The elastic peak (el) is indicated by the gray vertical line. The broad peak at high energy loss is attributed to charge transfer (CT). b) RIXS intensity map per incident photon energy, $h\nu_{in}$, versus energy loss, for LH incident polarization. The vertical dashed line and oblique dash-dotted one are guides to the eye for Raman-like and fluorescent-like dispersions. The blue horizontal dotted line indicates the $h\nu_{in}$ of the spectrum in panel (a). c) XAS Spectrum recorded at same θ , in LH polarization. The blue dotted line indicates the $h\nu_{in}$ of the spectrum in panel (a). d) RIXS intensity map recorded with linear vertical (LV) polarization, as function of the $h\nu_{in}$ vs energy loss. The Raman-like and fluorescent-like evolutions are indicated for guidance by the vertical dashed and the dash-dotted oblique lines, respectively. e) XAS intensity in LV polarization and same geometry, with $t_{A,P}$ indicated. RIXS spectra are normalized to the XAS intensity at the corresponding incident energy and polarization.

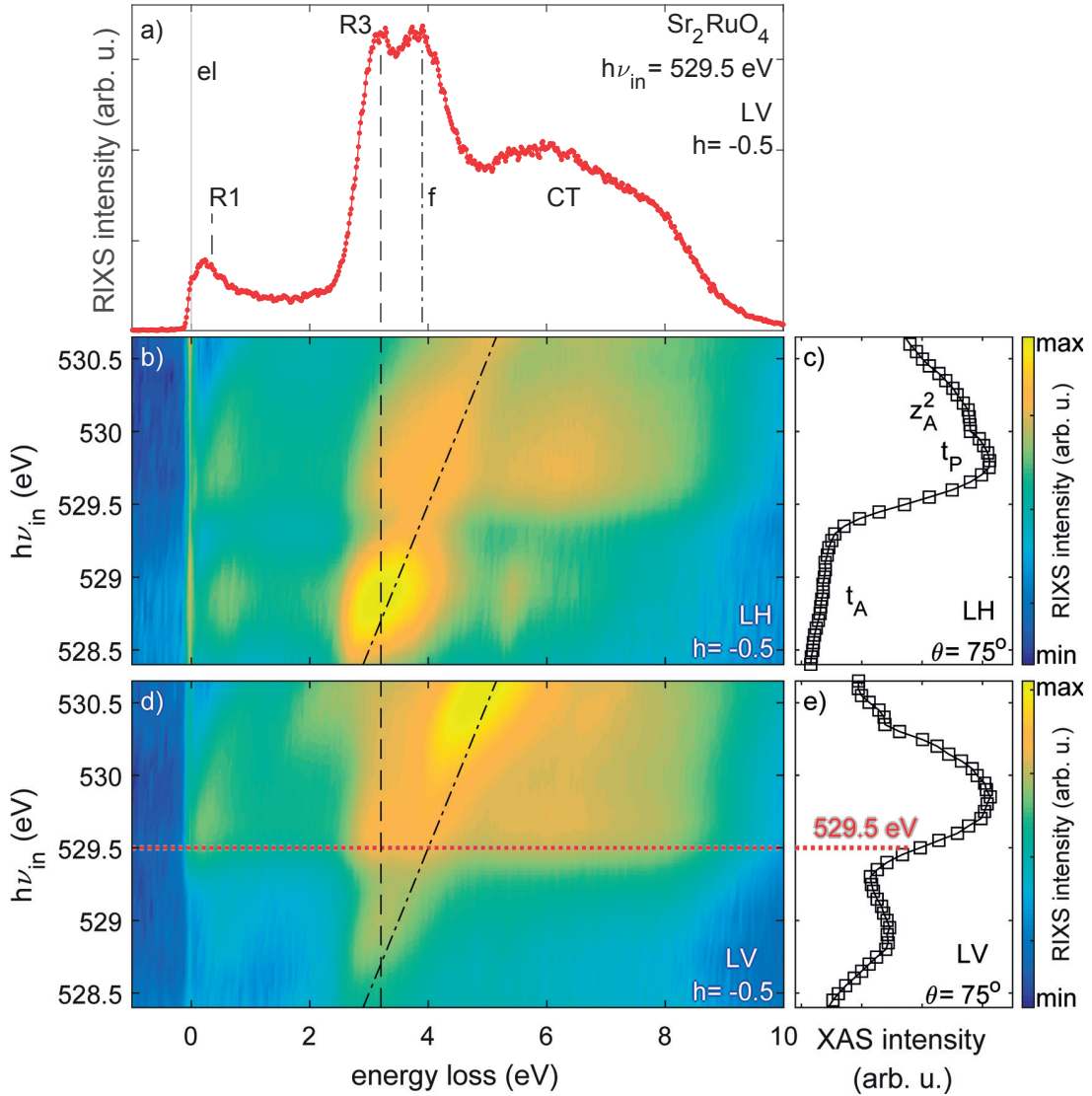


Figure 4.17 – **RIXS energy dependence Sr_2RuO_4** | taken at $\theta=75^\circ$, corresponding to a momentum transfer along the Ru-O-Ru bond direction of $-0.5 \mathbf{q}_{\text{BZ}}^x$, with $q_{\text{BZ}}^x = \frac{\pi}{a_t}$. a) RIXS spectrum recorded in linear vertical (LV) polarization at incident energy $h\nu_{\text{in}} = 529.5 \text{ eV}$. As in figure 4.16, dashed lines indicate peaks with a Raman character (R1, R3), as opposed to fluorescent (f) features (dash-dotted line). The elastic peak (el) is indicated by the gray vertical line. The broad peak at high energy loss is attributed to charge transfer (CT). b) map of the RIXS intensity per $h\nu_{\text{in}}$ versus energy loss, recorded with linear horizontal (LH) incident polarization. The vertical dashed line and oblique dash-dotted line are guides to the eye for Raman-like and fluorescent-like dispersions. c) XAS Spectrum at the same incident angle and polarization. The $t_{A,P}$ and z_A^2 absorption resonances are indicated. d) RIXS intensity map as function of $h\nu_{\text{in}}$ versus energy loss, in LV incident polarization. The Raman-like and fluorescent-like evolutions are indicated for guidance by the vertical dashed and the dash-dotted oblique lines, respectively. The red horizontal dotted line indicates the $h\nu_{\text{in}}$ of the spectrum in panel (a). e) XAS Spectrum at same θ , in LV polarization, with indication of the value of $h\nu_{\text{in}}$ for the RIXs spectrum in panel (a). RIXS data at each incident photon energy were normalized to the XAS intensity at the corresponding energy and polarization. 89

resonance with incident LH polarization, we observe a non-dispersive excitation, around 2.25 eV. This excitation is labeled R2. Between 3 and 4 eV is observed in both compounds a broad and intense peak which seems to be composed of two components, one non dispersive and one which appears to follow a fluorescent dispersion. We therefore assign two labels to this peak, R3 and *f*. The broad excitations at fluorescent character observed in both samples at large energy loss (>5 eV) are assigned to charge transfer (CT), described in section 2.2.4. Charge transfer excitations in a similar energy loss range (~4-8 eV) have been reported on cuprates [36, 140, 141].

Figures 4.18 and 4.19 compare the $h\nu_{out}$ dependence of RIXS spectra at different incident energy, and confirm the Raman character of excitations R1,2 (their dispersion is marked by color-coded vertical lines, and corresponds to constant energy loss). The following excitation, R3-f, exhibits a mixed Raman-fluorescent character and it could be considered as originating from 2 separate resonances, expressions of two competing relaxation processes. However, it is

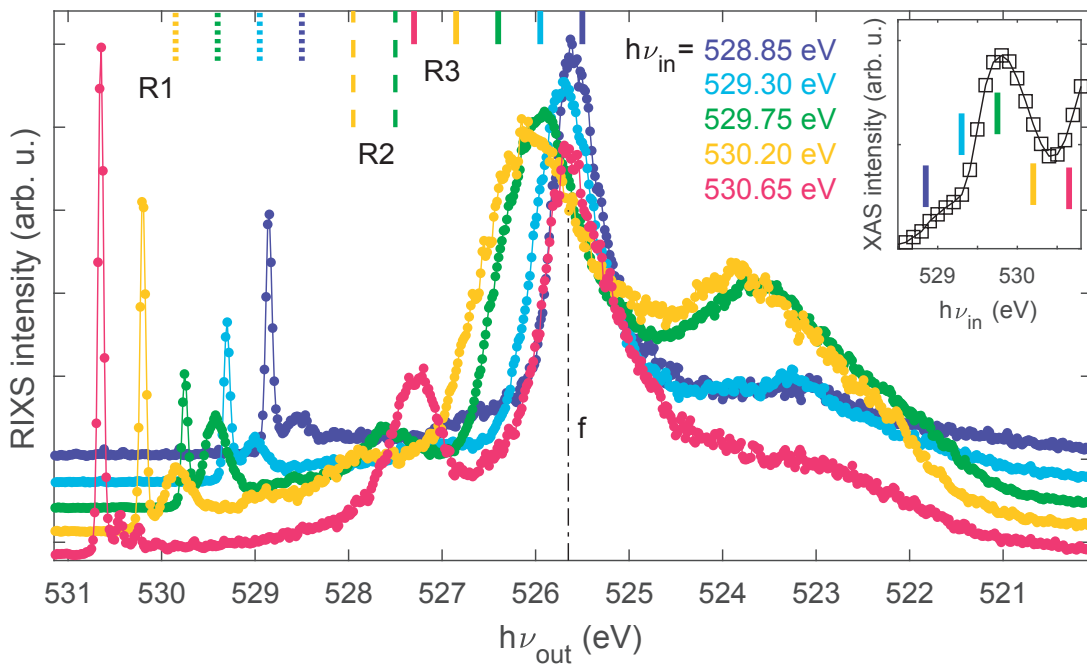


Figure 4.18 – **RIXS incident energy dependence on Ca_2RuO_4** | plotted versus the energy of the out-coming beam, in decreasing order for ease of comparison with figure 4.16. The spectra were taken with incident energy $h\nu_{in}$ as indicated, at $\theta=75$ deg and LH polarization. The color coded vertical dotted, dashed and solid lines on the top of the graph track the value of $h\nu_{out}$ at which the excitations R1, R2 and R3 are observed, respectively. The black vertical dash-dotted line indicates the position of the fluorescent resonance (f). In the inset is reproduced the XAS spectrum recorded with same incident angle and polarization. The color-coded vertical bars in the inset indicate the value of $h\nu_{in}$ at which the RIXS spectra were recorded. RIXS spectra were normalized to the intensity at 525.7 eV and arbitrarily shifted to improve visibility.

hard to disentangle the one from the other, especially in Ca_2RuO_4 .

The observed excitations do not exhibit the same relative intensity, but on the contrary appear to be enhanced or weakened depending on the incident energy and polarization, as outlined in table 4.3 with bold (gray) to indicate an enhanced (weak) resonance. The evaluation of the relative intensity is based on spectra normalized to the intensity of the XAS signal, as in figures 4.16 and 4.17 (see appendix A.5). However, the relative intensities of the spectra remain similar to that recorded by the spectrometer ("raw" intensities), so that table 4.3 applies as well to not-normalized spectra (plotted with their "raw" intensities). Note that the observed excitations are best resolved in the planar t_p resonance and with LH in the case of Ca_2RuO_4 , but LV for Sr_2RuO_4 samples.

We have assigned the broad excitation at large energy loss to charge transfer, whose intensity is a measure of the hybridization strength to the neighboring atoms (see section 2.2.4). The observation of a strong enhancement of this excitation at the planar absorption resonance is

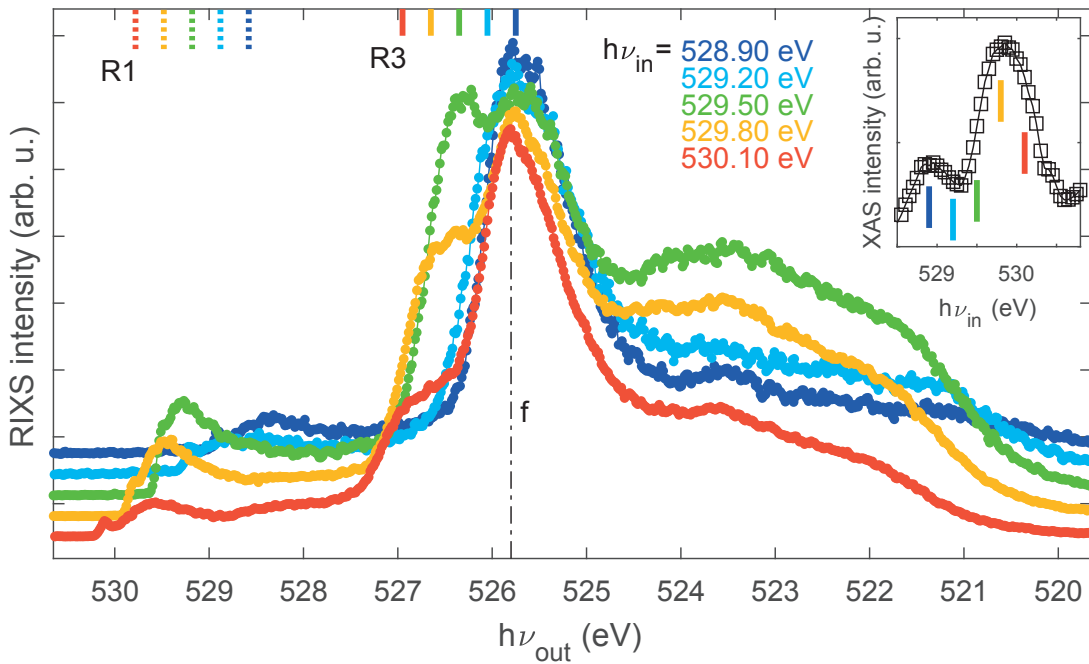


Figure 4.19 – **RIXS incident energy dependence on Sr_2RuO_4** | plotted versus the energy of the out-coming beam, in decreasing order for ease of comparison with figure 4.17. The spectra were taken with incident energy $h\nu_{in}$ as indicated, at $\theta=75$ deg and LV polarization. The color coded vertical dotted and solid lines on the top of the graph track the value of $h\nu_{out}$ at which the excitations R1 and R3 are observed, respectively. The black vertical dash-dotted line indicates the position of the fluorescent resonance (f). In the inset is reproduced the XAS spectrum recorded with same incident angle and polarization. The color-coded vertical bars in the inset indicate the value of $h\nu_{in}$ at which the RIXS spectra were recorded. RIXS spectra were normalized to the intensity at 525.8 eV and arbitrarily shifted to improve visibility.

consistent with the expected stronger hybridization of planar O atoms. To assign the remaining observed peaks, it is useful to compare their value with the energy difference of the features observed in the XAS spectra, see figure 4.20. We choose the spectra recorded with incident angle $\theta=35$ deg, where the apical and planar resonances are both easily distinguishable in Ca_2RuO_4 , using LH polarization. For Sr_2RuO_4 we refer to LV data. The horizontal bars, starting from the $t_{A/P}$ resonances in panels 4.20(a,b), have width corresponding to the value, in energy loss, of the excitations observed in the RIXS spectra (taken at incident energy $h\nu_{in}=t_{A/P}$, respectively).

The energy difference between the apical (planar) absorption peak at prevalent z^2 symmetry, $z_{A(P)}^2$, to the absorption resonance associated to the $p-t_{2g}$ hybridization, $t_{A(P)}$, roughly corresponds to the energy loss of the RIXS excitation R2. Also the R3-f excitation appears in correspondence with the energy difference between the absorption resonances of $p-t_{2g}$ and $p-e_g$ states. Therefore, we associate R2 and R3 to a relaxation process that leaves, in the final state, an electron in the $p-e_g$ valence states and a hole in those, at lower energy, of $p-t_{2g}$ origin. Which is to say that we interpret R2 and R3 as $d-d$ excitations.

The R1 excitation has magnitude of $\sim 0.3-0.4$ eV and fall within the width of the $t_{A,P}$ absorption resonances. It could be associated to excitations within the $p-t_{2g}$ states (intra- t_{2g} excitations). Raman excitations at energy loss below the eV could be related to collective modes, in which the energy lost by the scattered photons is used to create a quasi-particle such as a phonon (lattice excitation), a plasmon (charge excitation) or a magnon (spin excitation). We can rule out the phonon scenario, since they carry energy in a smaller range, not compatible with the observed energy loss. A plasmon scenario could be plausible in the metallic Sr_2RuO_4 but cannot be observed in the Mott insulator Ca_2RuO_4 . Since R1 is observed in the same energy range in the two compound it is reasonable to assume it has the same origin in both. Therefore, also the plasmon hypothesis is rejected. Spin excitations have a marked dependence on the transferred momentum (absorbed by the magnon), so that the energy loss associated with R1 would change as function of the angle of incidence. The energy loss due to intra- t_{2g} excitations, on the opposite, is not expected to vary with the transferred momentum.

The dependence on the angle of incidence, which allows to follow the momentum dispersion, is presented in the next section.

4.3.3 Dependence on incident angle

The different excitations observed are best resolved, in both compounds, at the planar absorption resonance t_P (see figures 4.16-4.17). Figure 4.21 presents the momentum dependence recorded with incoming energy $h\nu_{in} \sim t_P$, on Ca_2RuO_4 (panel (a)) and Sr_2RuO_4 (panel (b)), versus energy loss. The elastic peak is indicated by a vertical gray line crossing zero energy loss, while the features identified in the previous section are indicated by vertical dashed lines

Table 4.3 – **Recapitulation of the excitations observed in RIXS spectra and their relative intensity at incident angle $\theta=75$ deg** | To give a comprehensive scheme, we consider the apical and planar absorption resonances, t_A, P with both incident polarization adopted, linear horizontal (LH) and vertical (LV). For ease of comparison, we report the energy loss of excitations at Raman character, but the energy of the out-coming photons for fluorescent excitations. Bold and gray indicates strong and weak peaks, respectively. The comparison of relative intensities is based on spectra normalized to the corresponding XAS intensity, see figure A.6 of appendix A.5. Note that R3 and f appear in close vicinity, to the point that cannot always be distinguished the one from the other (see figures 4.16-4.19)

			Raman energy loss (eV)			Fluorescence $h\nu_{out}$ (eV)	
			R1	R2	R3	f	CT
Ca_2RuO_4	LH	t_A	~ 0.35	~ 2.25	~ 3.4	~ 525.7	$\sim 522-525$
		t_P	~ 0.35	~ 2.25	~ 3.4	~ 525.7	$\sim 522-525$
	LV	t_A	~ 0.35	~ 2.25	~ 3.4	~ 525.7	$\sim 522-525$
		t_P	~ 0.35	~ 2.25	~ 3.4	~ 525.7	$\sim 522-525$
Sr_2RuO_4	LH	t_A	~ 0.35		~ 3.2	~ 525.8	$\sim 521-525$
		t_P	~ 0.35		~ 3.2	~ 525.8	$\sim 521-525$
	LV	t_A	~ 0.35		~ 3.2	~ 525.8	$\sim 521-525$
		t_P	~ 0.35		~ 3.2	~ 525.8	$\sim 521-525$

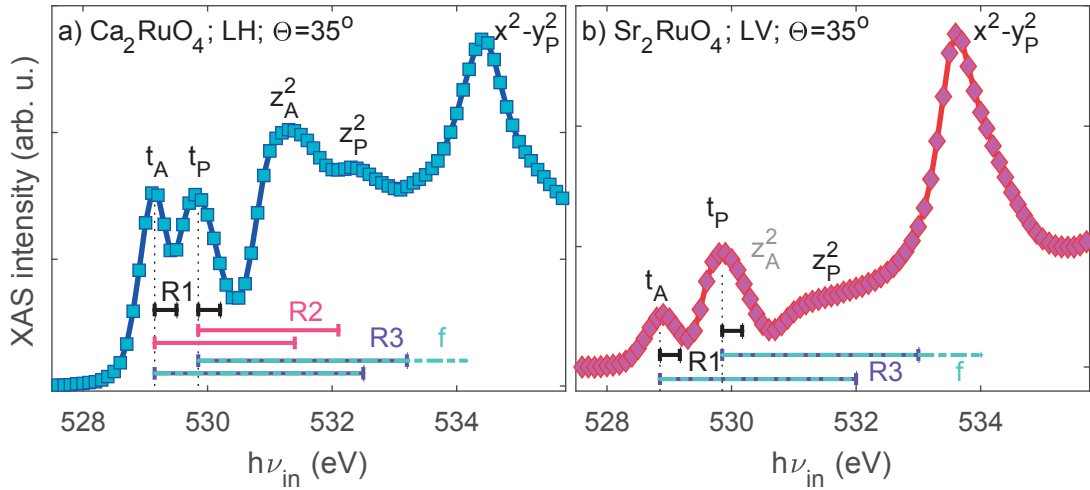


Figure 4.20 – **Comparison of the energy scale of RIXS excitations and XAS features** | a) XAS spectrum recorded with linear horizontal (LH) incident polarization at incident angle $\theta=35$ deg on Ca_2RuO_4 . b) XAS spectrum of Sr_2RuO_4 , taken in linear vertical (LV) incident polarization, at $\theta=35$ deg. The horizontal bars, starting from the apical or planar resonances t_A/P , indicate the value, in energy loss, of the excitations R1-3 and f, as observed in RIXS spectra taken at incident energy $h\nu_{in} = t_A/P$, respectively. At the apical resonance, R3 and f appear at approximately the same energy loss. At the planar resonance, they separate by $\sim 0.6-0.8$ eV.

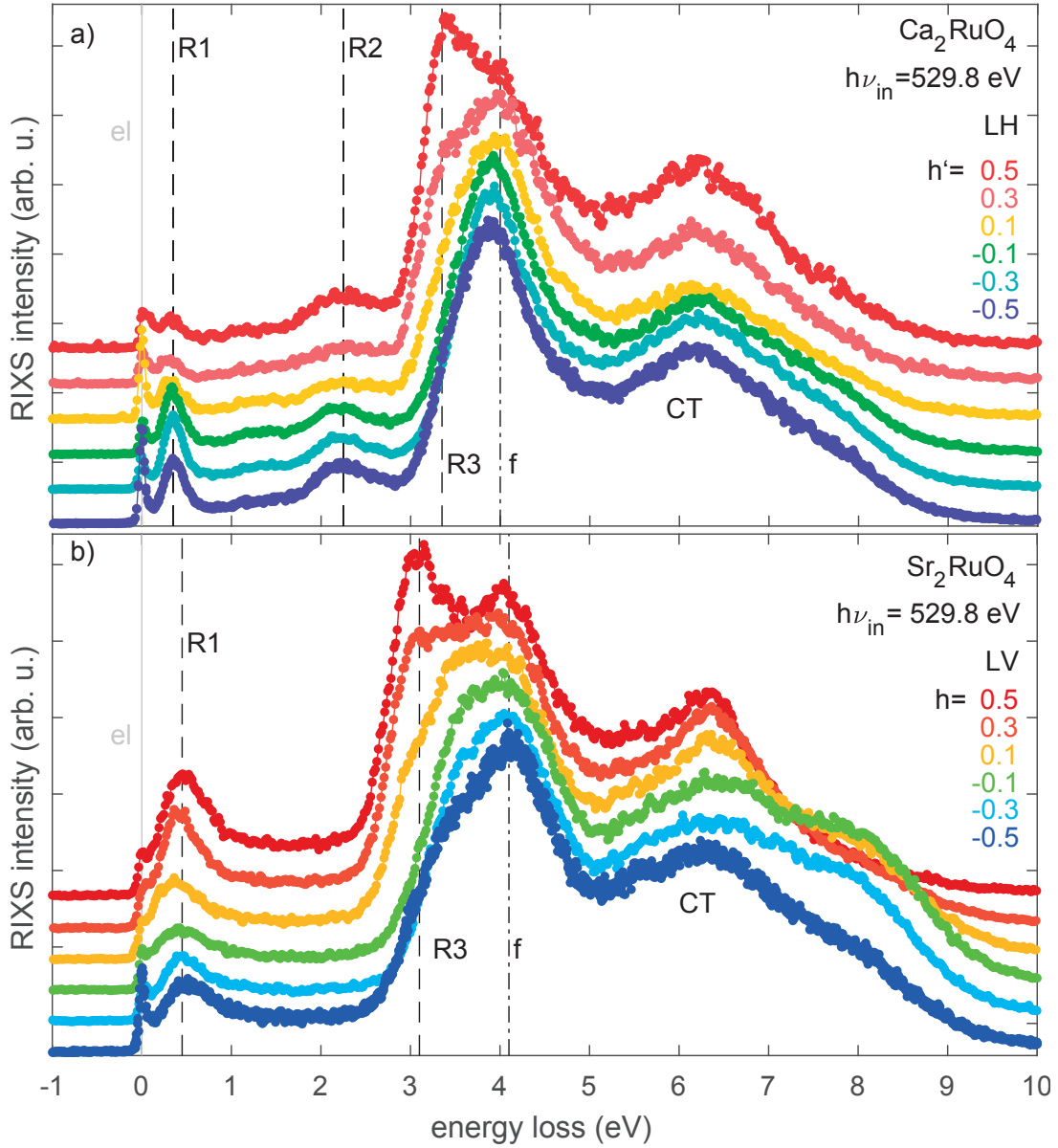


Figure 4.21 – **Dependence on transferred momentum** | (a) RIXS spectra recorded on Ca_2RuO_4 at incident energy $h\nu_{\text{in}}$ as indicated and linear horizontal (LH) incident polarization. The value of the transferred momentum is given in units of \mathbf{q}_{BZ}^x , with $Q_{\parallel} \simeq h' \mathbf{q}_{\text{BZ}}^x$ (b) Sr_2RuO_4 spectra taken with linear vertical (LV) incident polarization. the value of h gives the transferred momentum in units of \mathbf{q}_{BZ}^x : $Q_{\parallel} \simeq h \mathbf{q}_{\text{BZ}}^x$, with $q_{\text{BZ}}^x = \frac{\pi}{a_t}$. Dashed lines indicate peaks with a Raman character (R1-3), as opposed to fluorescent (f) features (dash-dotted line). The elastic peak (el) is indicated by the gray vertical line. The broad peak at high energy loss is attributed to charge transfer (CT). All spectra were normalized to the intensity at the energy loss corresponding to the feature f and arbitrarily shifted, to improve visibility.

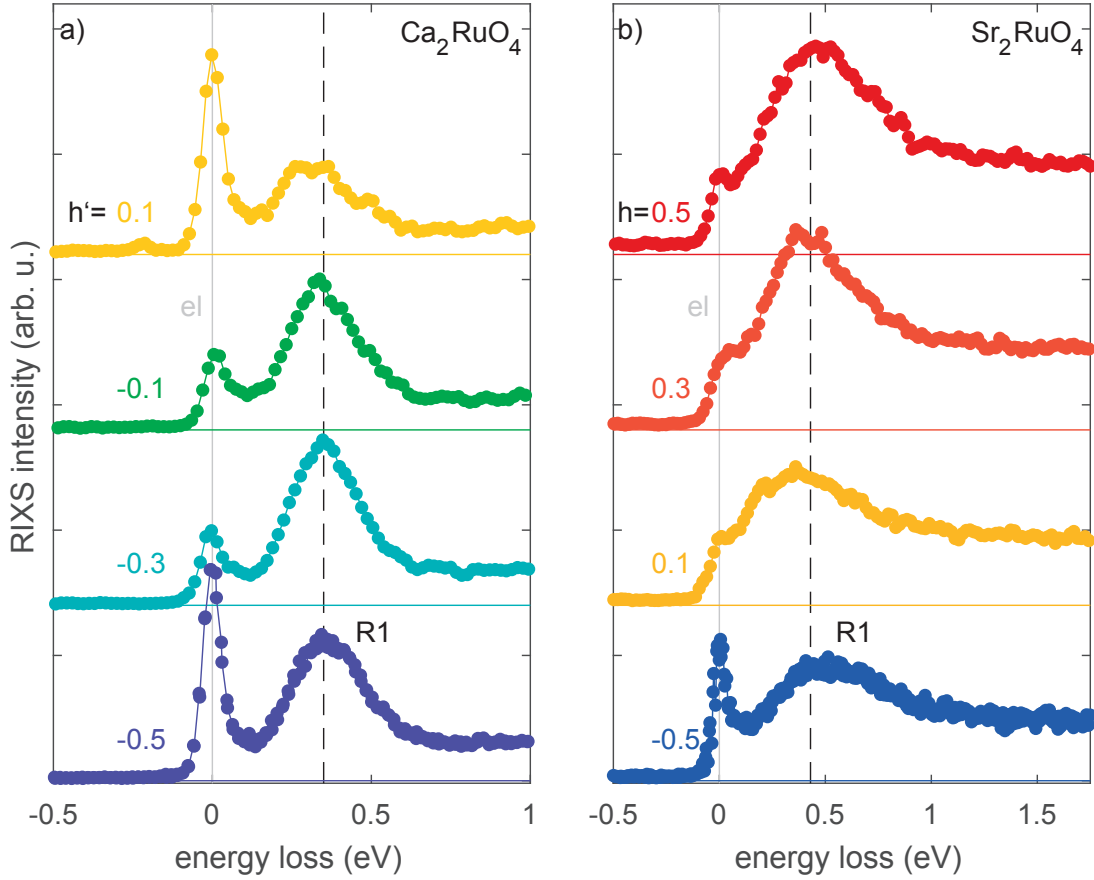


Figure 4.22 – **Zoom at low energy loss** | of RIXS spectra taken at the t_p resonance as function of the transferred momentum on (a) Ca_2RuO_4 (with linear horizontal incident polarization) and (b) Sr_2RuO_4 (with linear vertical incident polarization). The value of h' , h gives the transferred momentum in units of \mathbf{q}_{BZ}^x , with $q_{\text{BZ}}^x = \frac{\pi}{a_t}$. The elastic peak (el) is indicated by the gray vertical lines while the black dashed lines mark the position of feature R1. To improve visibility, all spectra were arbitrarily shifted and the color coded horizontal lines indicate zero intensity for the corresponding spectrum. The intensity is presented as recorded by the RIXS spectrometer.

(R1-3) or dash-dotted lines (f), at the energy loss observed for $h', h = -0.5$. At large energy loss are found the charge transfer (CT) features. The spectra were normalized to the intensity of the fluorescent feature f (at energy loss of 4.05 eV for Ca_2RuO_4 and 4.12 eV for Sr_2RuO_4 samples), and arbitrarily shifted to improve visibility.

At first sight, none of the features display an obvious dispersion as function of the transferred momentum. However, the relative intensities vary with the angle of incidence. It is interesting to note that the fluorescent excitation f seems to scale with the charge transfer intensity, while the relative intensity of excitation R3 increases with h, h' . This observation supports the hypothesis that R3 and f are manifestations of two competing relaxation processes. In

combination with the observed energy dependence, see figures 4.16-4.19, which clarifies the Raman character of R3 and the fluorescent one of f. It therefore appears justified to assign R3 to a $d-d$ excitation. Feature f, being of fluorescent character and exhibiting an intensity evolution similar to the CT broad feature, can be associated to charge transfer processes. The interpretation of feature R2 as due to a $d-d$ excitation is consistent with the non-dispersive behavior observed. Feature R1 does not show significant momentum dependence, even when examined in a restricted range of energy loss, see figure 4.22. The non-dispersive character, both as function of incident energy and transferred momentum, supports the hypothesis of an intra- t_{2g} process and contradicts the scenario of a magnon excitation, which would require the absorption of different amount of energy at different values of transferred momentum. In order to extract further information from the recorded data, a simple model is applied to the problem, described in the next section.

4.4 Model

As illustrated in figure 4.4, the electronic structure of perovskite materials is influenced by the crystal field, which introduces an energy difference between e_g and t_{2g} states but also between t_{2g} (or e_g) states. We indicate the energy difference introduced between e_g and t_{2g} as the crystal field splitting, and that between different t_{2g} orbitals as the intra- t_{2g} crystal field splitting, Δ_{i-t} - defined positive if it lifts the energy level of the d_{xy} orbital above that of d_{xz} and d_{yz} . The effect of the spin-orbit interaction λ_{SO} , found to be significant in ruthenates [133, 142, 143, 144, 145], can be thought as a mixing of the e_g and t_{2g} orbitals. Neglecting the Hund's coupling [132, 133, 142, 143, 144, 145, 146, 147, 148], the Hamiltonian of the system can be written as:

$$\mathcal{H} = \lambda_{SO} \mathbf{L} \cdot \mathbf{S} + \frac{\Delta_{i-t}}{3} \mathbf{L}_z^2 \quad (4.3)$$

where $\mathbf{S} = (\mathbf{S}_x, \mathbf{S}_y, \mathbf{S}_z)$ and $\mathbf{L} = (\mathbf{L}_x, \mathbf{L}_y, \mathbf{L}_z)$ are the spin and orbital momentum operators. Such effective model represent a strong simplification, while a more sophisticated model, which keeps into account the Coulomb interaction, is presented in reference [149]. Since we are interested in understanding the feature R1, observed well below 1 eV, we further neglect the e_g states and consider the orbitals $|xy\rangle$, $|xz\rangle$, $|yz\rangle$ as our base for the description of the t_{2g} electronic states ψ_1, ψ_2, ψ_3 [146, 147], as detailed in in appendix A.6. Including the spin degree of freedom, the Hamiltonian 4.3 can be expressed in its matrix form in the basis $\mathcal{B}_{t_{2g}}^1 = (|xy, +\rangle, |yz, -\rangle, |xz, -\rangle, |yz, +\rangle, |xz, +\rangle)$ (see section A.6.4):

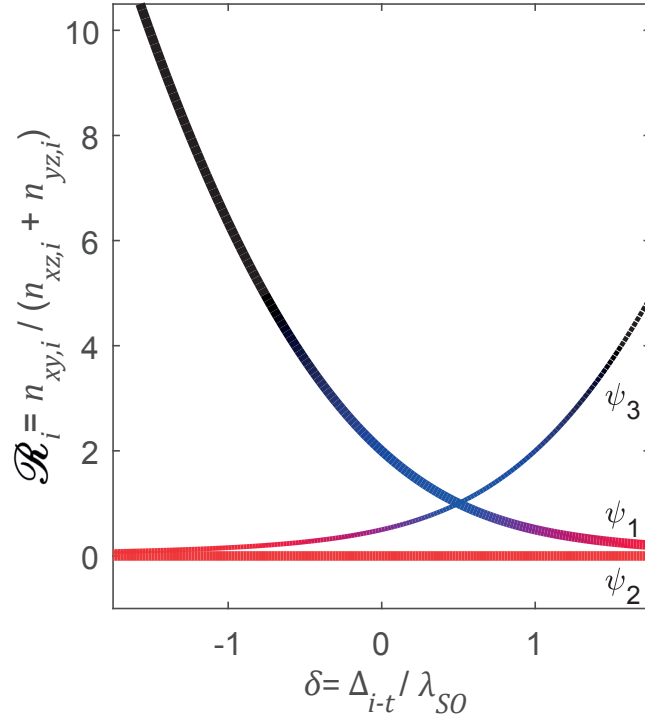


Figure 4.23 – **Expected occupation ratio of the eigenstates of Hamiltonian \mathcal{H}** | given in equation 4.3, as a function of δ . The eigenstates ψ_{1-3} are projected on the d_{xy} , d_{xz} and d_{yz} orbitals (see equation 4.6) so that \mathcal{R}_i represent the ratio between the different components. The thicker lines indicate $\mathcal{R}_{1,2}$, giving the ratio of the $\psi_{1,2}^\pm$ states, which lie at lower energy. The thinner line indicates the ratio \mathcal{R}_3 for the state at higher energy, ψ_3^\pm . Color further indicates the d_{xy} (blue) versus $d_{xz/yz}$ (red) prominent character of the states. Black indicates a strong d_{xy} character, corresponding to negligible $d_{xz/yz}$ component: $n_{xz/yz,i} \simeq 0$.

$$\mathcal{H}_{\mathcal{R}_{12g}} = \lambda_{SO} \mathbf{L} \cdot \mathbf{S} + \frac{\Delta_{i-t}}{3} \mathbf{L}_z^2 = \frac{\lambda_{SO}}{2} \begin{pmatrix} \frac{8}{3}\delta & -i & 1 & 0 & 0 & 0 \\ i & \frac{2}{3}\delta & i & 0 & 0 & 0 \\ 1 & -i & \frac{2}{3}\delta & 0 & 0 & 0 \\ 0 & 0 & 0 & \frac{8}{3}\delta & i & 1 \\ 0 & 0 & 0 & -i & \frac{2}{3}\delta & -i \\ 0 & 0 & 0 & 1 & i & \frac{2}{3}\delta \end{pmatrix} \quad (4.4)$$

Chapter 4. Orbital structure of single-layer ruthenates

where $\delta = \frac{\Delta_{i-t}}{\lambda_{SO}}$. In this form, it is evident that \mathcal{H} is exactly diagonalizable. The analytical solution to the eigenvalue problem of \mathcal{H} yields the doubly degenerate eigenvalues:

$$\begin{cases} E_1 = \frac{\lambda_{SO}}{4} \left(1 + \frac{10}{3}\delta - C \right) \\ E_2 = \frac{\lambda_{SO}}{2} \left(\frac{2}{3}\delta - 1 \right) \\ E_3 = \frac{\lambda_{SO}}{4} \left(1 + \frac{10}{3}\delta + C \right) \end{cases} \quad (4.5)$$

relative to the eigenstates:

$$\begin{cases} \psi_1^\pm \approx \sqrt{n_{xy,1}} |xy, \pm\rangle + \sqrt{n_{xz,1}} |xz, \mp\rangle \pm i\sqrt{n_{yz,1}} |yz, \mp\rangle = (\sqrt{n} - C) |xy, \pm\rangle + |xz, \mp\rangle \pm i |yz, \mp\rangle \\ \psi_2^\pm \approx \sqrt{n_{xy,2}} |xy, \pm\rangle + \sqrt{n_{xz,2}} |xz, \mp\rangle \mp i\sqrt{n_{yz,2}} |yz, \mp\rangle = |xz, \pm\rangle \mp i |yz, \pm\rangle \\ \psi_3^\pm \approx \sqrt{n_{xy,3}} |xy, \pm\rangle + \sqrt{n_{xz,3}} |xz, \mp\rangle \pm i\sqrt{n_{yz,3}} |yz, \mp\rangle = \sqrt{n} |xy, \pm\rangle + |xz, \mp\rangle \pm i |yz, \mp\rangle \end{cases} \quad (4.6)$$

with $C = \sqrt{9 + 4\delta(\delta - 1)}$ and $n = \frac{(-1+2\delta+C)^2}{4}$. The second eigenstate, ψ_2^\pm , originates from the mixing of d_{xz} and d_{yz} orbitals and has no component along $|xy, \pm\rangle$, $n_{xy,2} = 0$. All eigenstates have $n_{xz} = n_{yz}$, and we have written $n_{xz,i} = n_{yz,i} = 1$, for $i=1,2,3$. In this way, we extract only $n_{xy,i}$ and for the occupancy ratio we simply have: $\mathcal{R}_i = \frac{n_{xy,i}}{n_{xz,i} + n_{yz,i}} = \frac{n_{xy,i}}{2}$, for $i=1,2,3$. Notice that the occupancy of states at different symmetry is fully determined by the ratio between our two parameters $\delta = \frac{\Delta_{i-t}}{\lambda_{SO}}$, *i.e.* $\mathcal{R}_i \equiv \mathcal{F}(\delta)$, represented in figure 4.23. The orbital character described in figure 4.23 gives an indication on the favored symmetry as the value of δ changes. As an example, for $\delta < -1$ - *i.e.* $\Delta_{i-t} < 0$ and $|\Delta_{i-t}| > \lambda_{SO}$ - E_1 is much lower than $E_{2,3}$ and states at d_{xy} symmetry are strongly preferred, consistently with our understanding of the crystal field effects.

From the expression of the eigenvalues given in equation 4.5, it can be derived that E_3 is larger than both E_2 and E_1 , for all values of δ and $\lambda_{SO} \neq 0$. If the number of electrons occupying the states are 4, as is the case for the ruthenates materials consideredⁱ, $\mathcal{R}_{1,2}$ give the electron occupation of states $\psi_{1,2}^\pm$, while \mathcal{R}_3 expresses the hole occupancy, which can be probed by XAS. Furthermore, the RIXS technique is sensitive to the energy differences between the derived eigenvalues, which (in addition to their dependence on δ) depend explicitly on the

ⁱMore exactly, in the cases considered in this section, the hybridized states $p-t_{2g}$ are occupied by 6 electrons which are primarily localized around the oxygen atoms, and 4 electrons which spend most of their time around the ruthenium atom (for a total of 10 electron distributed in the 6 $p-t_{2g}$ orbitals, that, taking the spin degree of freedom into account, can host 12 electrons). In this picture, the states $p - \psi_{1,2}^\pm$ are fully occupied, while two vacancies (holes) are left in the $p - \psi_3^\pm$ states.

the spin-orbit coupling λ_{SO} , $\Delta E_{i,j} \equiv \mathcal{F}(\lambda_{SO}, \delta)$:

$$\begin{cases} \Delta E_{3,1} = \frac{\lambda_{SO}}{2} C \\ \Delta E_{3,2} = \frac{\lambda_{SO}}{4} (2\delta + 3 + C) \\ \Delta E_{2,1} = \frac{\lambda_{SO}}{4} (-2\delta - 3 + C). \end{cases} \quad (4.7)$$

Therefore, combining the observation made in the previous sections would allow a full determination of our problem and lead to an experimental estimation of both the intra- t_{2g} crystal field splitting and the spin-orbit coupling. This effort is presented in the next section.

4.4.1 Model application

In figure 4.24 are presented the expected values extracted from the analytical solution to the problem to the eigenvalues of \mathcal{H} . In panel 4.24(a) the energy of the eigenstates ψ_{1-3} are expressed in units of the spin-orbit strength λ_{SO} (solid lines), while the energy levels in absence of spin-orbit interaction are reported for comparison in dashed lines. The color indicates the orbital character of the relative eigenstates, with blue indicating a main d_{xy} character and red a state of main $d_{xz/yz}$ origin. The topology of the unoccupied ψ_3^\pm eigenstates is explicated in the top panels for various values of δ , while its ratio between the d_{xy} and $d_{xz/yz}$ components, \mathcal{R}_3 , is plotted in panel 4.24(b).

X-ray absorption spectroscopy (XAS) gives experimental access to the hole occupancy ratio between the states at d_{xy} symmetry versus those of $d_{xz/yz}$ origin (see section 4.2.5). In other words, we have derived an experimental estimate of the ratio \mathcal{R}_3 , expressed in equation 4.2 and reproduced in panel 4.24(b), together with hole occupancy ratios measured on iridate materials - extracted from references [132, 147, 150, 151]. In the limit $\delta \rightarrow 0$ (as is the case for $\{\text{Ba}, \text{Sr}\}_2\text{IrO}_4$ [132, 150, 151]), the states $\psi_{1,2}^\pm$ are degenerate and $\Delta_{3,2/1} = 1.5\lambda_{SO}$. In the opposite limit, $\lambda_{SO} \rightarrow 0$, $\psi_{1,2}^\pm$ are again degenerate and the splitting is determined by the intra- t_{2g} crystal field alone: $\Delta_{3,2/1} = \Delta_{i-t}$, see section A.6.3. In all other case, both λ_{SO} and Δ_{i-t} contribute, in varying measure, to the splitting of the ψ_{1-3} eigenstates of \mathcal{H} .

Since $\mathcal{R}_i = \mathcal{F}(\delta)$, from the estimated values of \mathcal{R}_3 we can derive an experimental estimate on δ , see panel 4.24(b). Keeping into account the indetermination in the values of \mathcal{R}_3 , we find:

$$\begin{aligned} 0.15 \leq (\mathcal{R}_3)_{Ca_2RuO_4} \leq 0.2 & \Leftrightarrow \delta \simeq -0.9 \pm 0.1 \\ 1 \leq (\mathcal{R}_3)_{Sr_2RuO_4} \leq 1.25 & \Leftrightarrow \delta \simeq 0.6 \pm 0.1. \end{aligned} \quad (4.8)$$

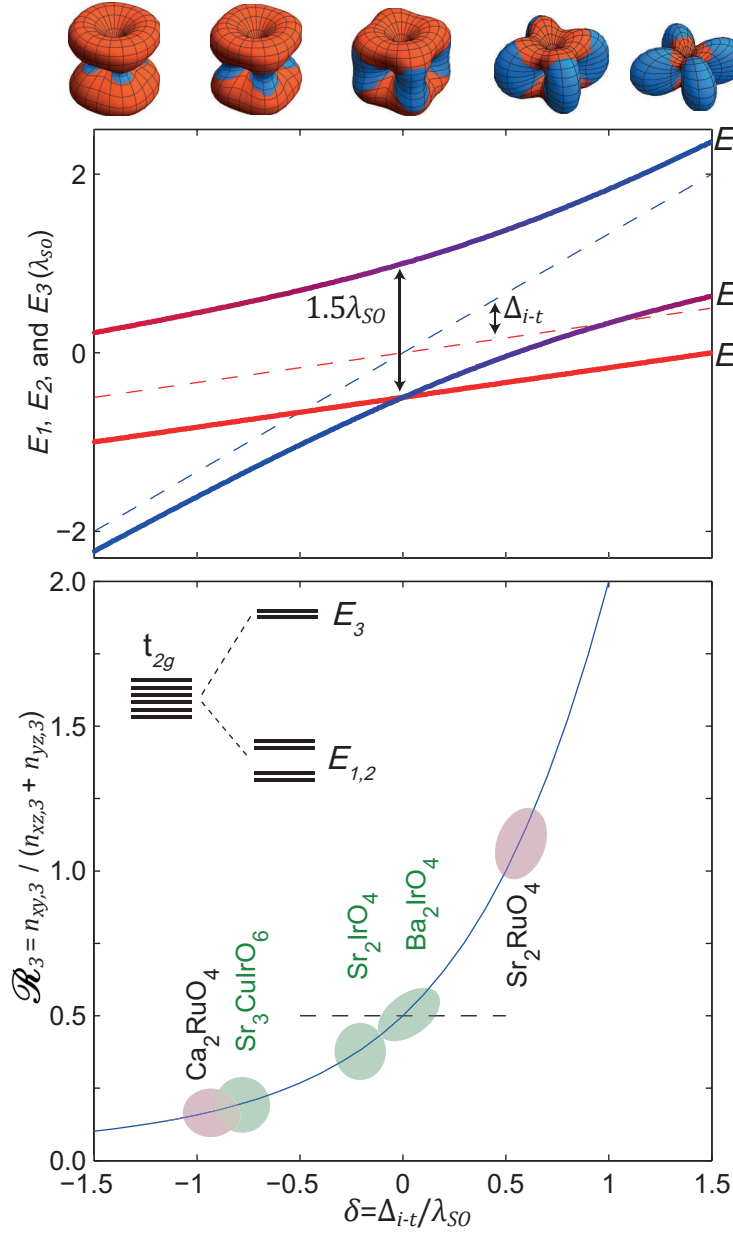


Figure 4.24 – **Analytical solution of the model Hamiltonian \mathcal{H}** | given in equation 4.3. (a) Expectation values, in units of the spin-orbit coupling λ_{SO} , for the eigenvalues E_{1-3} as a function of $\Delta_{i-t}/\lambda_{SO}$, where Δ_{i-t} is the intra- t_{2g} crystal field splitting. Dashed (solid) lines indicate the expected values of E_{1-3} in absence (presence) of the spin-orbit interaction, see section A.6.3. Color indicates the orbital character of the corresponding eigenstates, with blue (red) marking a d_{xy} (d_{xz}/yz) character. The orbital topology of the eigenstates ψ_3^\pm is illustrated in the top panels. (b) Model expectation for the orbital hole occupation ratio $\mathcal{R}_3(\frac{\Delta_{i-t}}{\lambda_{SO}}) = \frac{n_{xy,3}}{n_{xz,3} + n_{yz,3}}$ of the eigenstate ψ_3^\pm , compared with values extracted from Ca_2RuO_4 and Sr_2RuO_4 as well as iridate materials [132, 147, 150, 151]. The vertical dashed line marks the value of \mathcal{R}_3 corresponding to even occupation of the d_{xy} and d_{xz}/yz orbitals. The inset schematically illustrates how spin-orbit interaction and crystal field partially remove the t_{2g} degeneracy. Adapted from reference [152].

Which implies, for Ca_2RuO_4 :

$$\begin{cases} \Delta E_{3,1} \simeq (2.0 \pm 0.1) \lambda_{SO} \\ \Delta E_{3,2} \simeq (1.3 \pm 0.1) \lambda_{SO} \\ \Delta E_{2,1} \simeq (0.7 \pm 0.1) \lambda_{SO} \end{cases} \quad (4.9)$$

and for Sr_2RuO_4 :

$$\begin{cases} \Delta E_{3,1} \simeq (1.42 \pm 0.05) \lambda_{SO} \\ \Delta E_{3,2} \simeq (1.76 \pm 0.05) \lambda_{SO} \\ \Delta E_{2,1} \simeq (-0.35 \pm 0.05) \lambda_{SO}. \end{cases} \quad (4.10)$$

In principle, we would therefore expect to observe three distinct features in the RIXS spectra, corresponding to the energy differences between the derived eigenstates. However, the states $\psi_{1,2}^\pm$ are generally close in energy, so that in both compounds $\Delta E_{2,1}$ is found to be ~ 2 -4 times smaller than the average of $\Delta E_{3,2}$ and $\Delta E_{3,1}$, resulting to be comparable to the experimental resolution. We speculate that the corresponding feature, falling below the observed R1 peak and close to the elastic line, is not resolved by our experiment. Furthermore, following the same reasoning, since $\Delta E_{3,2}$ and $\Delta E_{3,1}$ are comparable in size - with difference expected in the order of the experimental resolution - the observed R1 feature is interpreted as corresponding to the average of the two excitations, $\overline{\Delta E}_{3,2-1} \simeq (1.6 \pm 0.1) \lambda_{SO}$.

Under these assumptions, we can extract an experimental evaluation of λ_{SO} from the recorded RIXS spectra, as illustrated by way of example on the RIXS spectra taken at incident angle $\theta = 55$ deg, in figure 4.25. Since feature R1 is observed in both compounds at energy loss of ~ 0.35 eV, we find $\overline{\Delta E}_{3,2-1} \simeq (1.6 \pm 0.1) \lambda_{SO} \simeq 0.35 \pm 0.03 \Rightarrow \lambda_{SO} \sim 0.21 \pm 0.02$ eV. From the estimated value of the ratio $\delta = \frac{\Delta_{i-t}}{\lambda_{SO}}$, see equation 4.8, we can now extract the value of the intra- t_{2g} crystal field to be $\Delta_{i-t} \simeq -0.19 \pm 0.04$ eV for Ca_2RuO_4 , and $\Delta_{i-t} \simeq -0.13 \pm 0.03$ eV in the case of Sr_2RuO_4 .

4.5 Summary of Results

We have performed a XAS and RIXS combined study on Ca_2RuO_4 and Sr_2RuO_4 samples, as function of incident angle, polarization and energy. The results of this analysis were published in PRB 91, 155104 (2015), reference [152], and are summarized in table 4.4.

After identifying the main character of the features observed in the XAS spectra, we estimated the energy difference between the states at e_g and t_{2g} origin. Furthermore, from an intensity

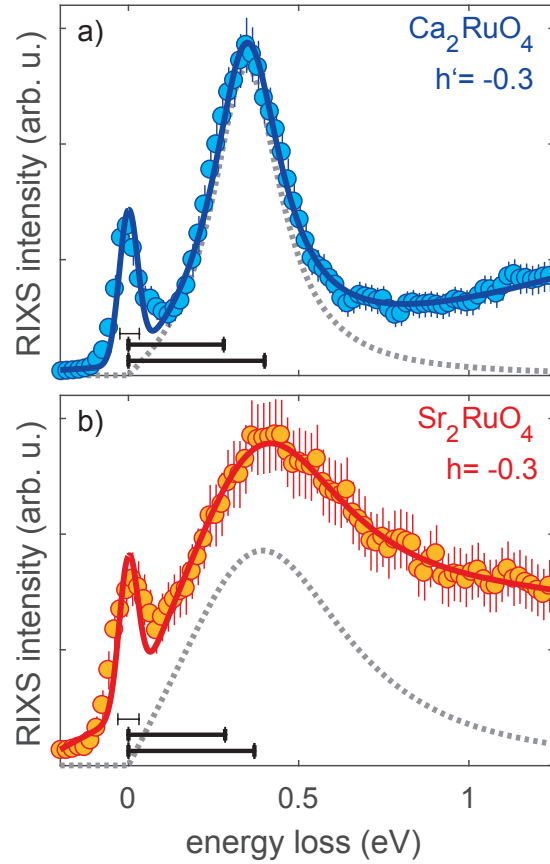


Figure 4.25 – **Interpretation of the low energy RIXS feature** | through the adopted model. The expected excitations (of value indicated by thick horizontal bars) are compared, as an example, with RIXS spectra recorded with incident angle $\theta=55$ deg, corresponding to a momentum transfer of $\mathbf{Q}_{//} \simeq -0.3 \mathbf{q}_{\text{BZ}}^x$, in linear horizontal incident polarization for Ca_2RuO_4 , panel (a), and linear vertical for Sr_2RuO_4 , panel (b). Vertical bars indicate the errors. The spectra were taken at the planar t_p absorption resonance. Solid lines are fits to a Gaussian (corresponding to the elastic process), an antisymmetric Lorentzian (reproduced separately with dotted gray lines), and a quadratic background. Thin horizontal bars around zero indicate the full width at half maximum of the elastic Gaussian, corresponding to the effective experimental resolution.

study of the pre-edge features observed below 530 eV - the apical and planar absorption resonances $t_{A,P}$ - the hole occupancy ratio \mathcal{R}_h between states at d_{xy} and $d_{xz,yz}$ symmetry was extracted. The features observed in the RIXS spectra were classified according to their dispersive behavior (as function on the energy lost by the scattered photons) and associated to fluorescent or Raman relaxation processes. The fluorescent component, at energy loss larger than 4 eV, is attributed to charge transfer interactions. The Raman-like features at energy loss greater than 1 eV are compatible with relaxation processes in which the core electron is promoted to states at $p - e_g$ character while an electron in the $p - t_{2g}$ valence states fills the core hole. These processes are referred to as $d - d$ excitations. The low energy Raman features

in the RIXS spectra was attributed to intra- t_{2g} processes, intra- t_{2g} ΔE . In order to interpret this feature, we adopted a simple model Hamiltonian \mathcal{H} , whose exact solutions -eigenvalues E_{1-3} and eigenstates ψ_{1-3} - are univocal functions of two parameters, the intra- t_{2g} crystal field Δ_{i-t} and the strength of the spin-orbit coupling, λ_{SO} . Notice that the mixing of orbitals observed cannot be explained as a result of crystal field alone but, on the contrary, requires a non-negligible spin-orbit coupling.

The ratio between d_{xy} and $d_{xz,yz}$ components of the extracted eigenstate ψ_3^\pm represent one observable physical quantity, the hole occupancy ratio $\mathcal{R}_h = \mathcal{R}_3$, probed via XAS. Our results suggest that the unoccupied state is strongly dominated by $d_{xz,yz}$ orbitals in Ca_2RuO_4 , while has a main d_{xy} character in Sr_2RuO_4 . A second physical quantity which can be experimentally observed is the splitting between the ψ_3^\pm and $\psi_{1,2}^\pm$ eigenstates, intra- t_{2g} $\Delta E = \overline{\Delta E}_{3,2-1}$, which is accessed with RIXS. In other words, we derived a system of two equation in two unknown, whose solution yields an experimental estimate of both model parameters, λ_{SO} and Δ_{i-t} . Within the model adopted, λ_{SO} was estimated to value ~ 0.2 eV in both compounds. The value of Δ_{i-t} was found to be ~ -0.2 eV in Ca_2RuO_4 and ~ 0.1 eV in Sr_2RuO_4 samples. The sign flip of the intra- t_{2g} crystal field Δ_{i-t} between the two compounds is consistent with the compression of the oxygen octahedra in the crystal structure of Ca_2RuO_4 , opposed to the elongation in that of Sr_2RuO_4 .

Table 4.4 – **Summary of results** | extracted from the XAS-RIXS combined study on $(\text{Ca,Sr})_2\text{RuO}_4$. The results are listed according to the specific mean employed for the extraction: X-ray absorption spectroscopy, resonant inelastic X-ray spectroscopy or application of the model Hamiltonian $\mathcal{H} = \lambda_{SO}\mathbf{L} \cdot \mathbf{S} + \frac{\Delta_{i-t}}{3}\langle L_z \rangle^2$.

	XAS		\mathcal{R}_h	RIXS intra- t_{2g} ΔE (eV)	Model application	
	$e_{g,1-t_{2g}}$ (eV)	$e_{g,2-t_{2g}}$ (eV)			λ_{SO} (eV)	Δ_{i-t} (eV)
Ca_2RuO_4	~ 2.5	~ 4.5	0.15-0.20	~ 0.35	~ 0.2	~ -0.2
Sr_2RuO_4	~ 1.3	~ 3.8	1.00-1.25	~ 0.35	~ 0.2	~ 0.1

5 Conclusions

This doctoral project has investigated the role of electron correlations through synchrotron-based spectroscopic techniques: angle resolved photoemission spectroscopy and resonant inelastic X-ray scattering. The main results obtained are summarized here.

Our high quality nodal spectra of $\text{La}_{1.77}\text{Sr}_{0.23}\text{CuO}_4$ [53] allowed a careful self-consistent analysis, through which we could verify the fulfillment of the mathematical conditions for coherent Landau quasi-particles. Enforcing Kramers-Kronig consistency, we could provide an experimental ARPES proof that low energy excitations in the strange-metal phase of cuprates are true Landau Fermi liquid quasi-particles [48].

On the other side of the superconducting dome, the observed quasi-particles exhibit a momentum-dependent gap of unknown origin, the pseudogap. The systematic ARPES study performed on $\text{La}_{1.6-x}\text{Nd}_{0.4}\text{Sr}_x\text{CuO}_4$ enabled identification of a doping regime in which the pseudogap can be investigated without influences from charge-order. Our investigation found that the magnitude of the single particle gap in this regime is correlated to single-particle scattering, with larger scattering implying a larger pseudogap [67]. This experimental observation taps into the on-going dispute on the origin of the pseudogap and its relation to superconductivity and charge order, and suggests competition between these phenomena.

Interestingly, a pseudogap has been reported in Mott insulator Sr_2IrO_4 [13] – a transition metal oxide with much stronger spin-orbit coupling than the cuprates – along with hints to superconductivity [153], although an unambiguous experimental proof (such as transport measurements) remains lacking. These considerations raise the question on the relevance of spin-orbit coupling and orbital physics in the determination of electronic properties in strongly correlated systems and lead us to the last chapter of this thesis, where the experiments performed on ruthenate compounds are discussed.

We identified in $(\text{Ca,Sr})_2\text{RuO}_4$ an intermediary system, given its electronic configuration – similar to that of the iridates – and the display of both Mott insulating and superconducting

Chapter 5. Conclusions

ground states, as is the case of the cuprates. Our combined RIXS and XAS investigation resulted in a consistent description of the low energy electronic excitations, within a simple model Hamiltonian [152]. Our findings suggest that both the spin orbit coupling and the structural distortions in the perovskite crystal structure of these systems play a major role in defining their electronic properties. Our subsequent ARPES study of Ca_2RuO_4 [149], reproduced in appendix B, confirmed the importance of the crystal field, and further identified in the Hund's coupling a crucial element to the shaping of the band structure. Ca_2RuO_4 was also the object of explorative spin resolved ARPES experiments, carried out at the COPHEE beamline of the Swiss Light Source. The results of these investigations are in the process of being analyzed.

'We're all stories, in the end.
Just make it a good one, eh?'

— Steven Moffat
Doctor Who Season 5, Episode 13

A Additional information

Section A.1: normalization procedure adopted for the XAS data presented in section 4.2.

Section A.2: discussion of the fit of LH XAS data on Sr_2RuO_4 .

Section A.3: RIXS experimental geometry and derivation of the momentum transferred along the sample surface.

Section A.4: the same RIXS spectra are plotted in function of their energy loss as well as the energy of the out-coming photons.

Section A.5: RIXS spectra relevant for the relative intensity summary presented in table 4.3, in section 4.3.3.

Section A.6: analytical solution of the model Hamiltonian introduced in section 4.4.

A.1 XAS: data normalization

Linear fit of raw XAS spectra (in the energy region below 528 eV for Ca_2RuO_4 , 527.7 eV for Sr_2RuO_4 corresponding to ~ 1 eV below the first absorption peak in the two compounds) constitute a background signal, due to the off-resonance tails of absorption peaks at lower energies. These linear backgrounds were extrapolated to the full energy range and subtracted from the spectra, which were then normalized to the background-free spectral weight at high energy (between 546 and 550 eV). The normalization procedure is illustrated in figure A.1 as an example in the case of the spectra shown in figure 4.8.

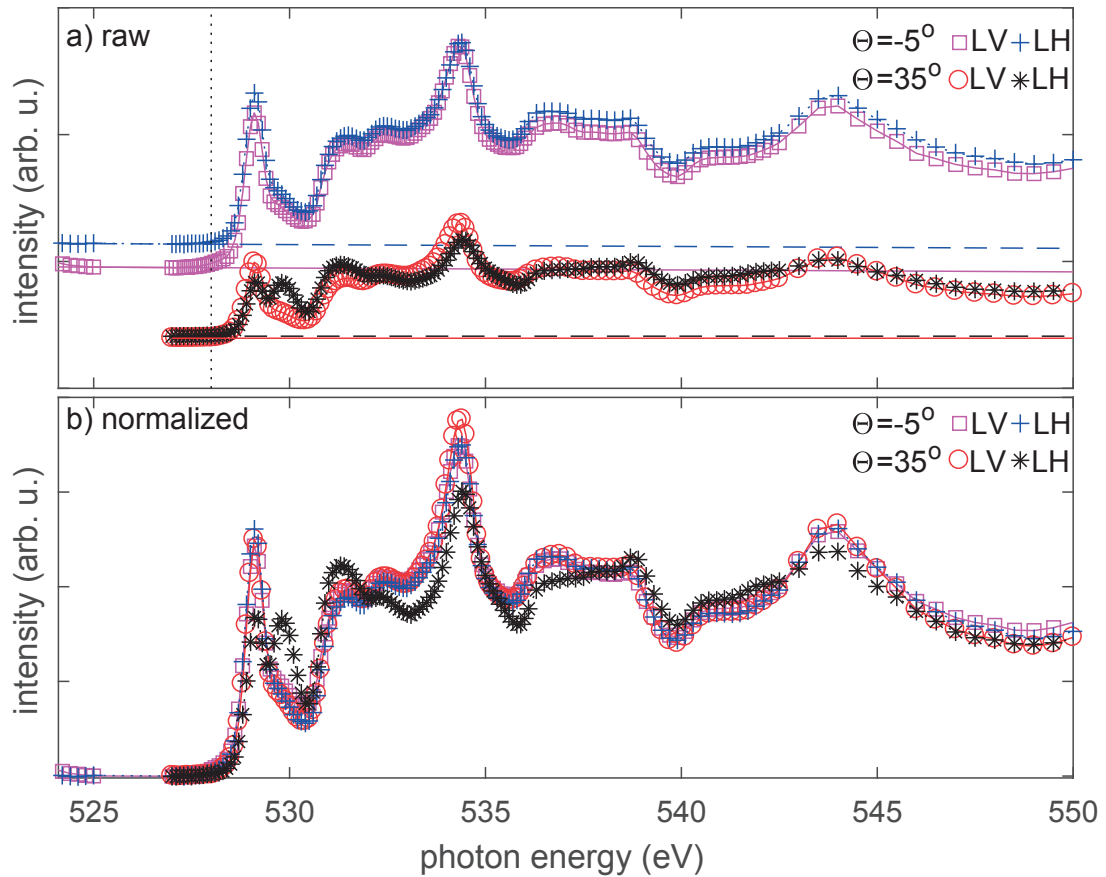


Figure A.1 – **XAS data normalization** | (a) Raw XAS spectra recorded on Ca_2RuO_4 at $\Theta = -5^\circ$ and 35° with LV and LH polarizations, as indicated. Solid (dashed) lines indicate the background, estimated from fit of LV (LH) spectra in the energy region below 528 eV (dotted vertical line) and extrapolated between 528 and 550 eV. (b) Normalized data. After subtraction of a linear background and normalization (to the average intensity at energies higher than 546 eV), LV data at different angle superpose across the full energy range. LH data also overlap in some energy ranges, but the intensity of the most relevant features changes with Θ .

Appendix A. Additional information

Data normalized in such way overlaps across the full energy range in case of LV polarization, as expected. LH spectra instead show changes in the relative intensity of the peaks consistent with our expectations, detailed in section 4.1.

A.2 XAS: fit of LH spectra

To fit the LH spectra, the center and width of the t_A and background resonances were fixed to the values extracted from the fit to 4.1 on LV data taken at the same incident angle. The free parameters in the LH fit hence were I_A , I_B and intensity, center and width of the t_P resonance, I_P , c_P and σ_P :

$$F_{LH}(x) = I_A e^{-\frac{(x-c_{A,LV})^2}{2\sigma_{A,LV}^2}} + I_P e^{-\frac{(x-c_P)^2}{2\sigma_P^2}} + I_B e^{-\frac{(x-c_{B,LV})^2}{2\sigma_{B,LV}^2}}. \quad (\text{A.1})$$

With x =photon energy. In figure A.2 is shown a fit to function A.1 of XAS data taken on Sr_2RuO_4 with LH polarization and incident angle $\Theta=35^\circ$.

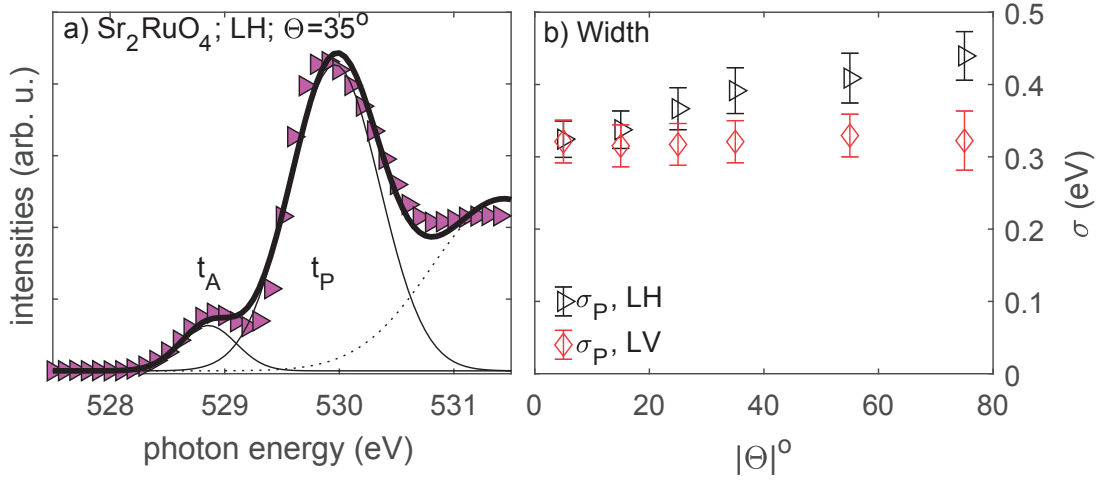


Figure A.2 – **XAS fit** | (a) fit of Sr_2RuO_4 XAS spectra recorded at $\Theta=35^\circ$ with Lh polarization. The fitting function (thick solid line) is the sum of the three Gaussian shown, in solid thinner lines for the apical and planar $t_{A,P}$ absorption resonances, dashed for the next absorption peak, which constitutes a background. See equation 4.1. (b) Standard deviation of the second Gaussian function, corresponding to the t_P resonance, extracted from LH (black triangles) or LV (red diamonds) data.

Fitting only one Gaussian function around 530 eV leads to a poor agreement to the data. Moreover, the standard deviation of this Gaussian function considerably increases with $|\Theta|$ (corresponding to an increase in the FWHM of $\sim 50\%$), further supporting the hypothesis of a second absorption peak arising around 530 eV, in LH spectra at large incident angle (see paragraph 4.2.2 and figure 4.12). The FWHM of the Gaussian fit to t_P , within function A.1, increases from ~ 0.7 eV to ~ 1 eV going from 5° to 75° .

A.3 RIXS: momentum transfer

The experimental geometry is illustrated in figure A.3. As discussed in section 4.1, the samples were aligned with the c -axis normal to the surface, directed along z in the figure. The in-plane orientation was such that the Ru-O-Ru bonds align with x and y in the figure. The samples can be rotated around the y direction to vary the angle of incidence θ . As discussed in section 4.1, the linear polarizations adopted align the oscillating electric field either along the y direction (linear vertical, LV) or on the $x-z$ plane (linear horizontal, LH).

The RIXS process can be treated as a scattering event, where photons of energy $h\nu_{in}$ and momentum \mathbf{K}_{in} are directed to the sample and photons of energy $h\nu_{out}$ and momentum \mathbf{K}_{out} emerge. The incident energy was varied within a few eV around the oxygen K-shell absorption edge. The scattering plane, defined by \mathbf{K}_{in} and \mathbf{K}_{out} , contains the c -axis and cuts the samples along the Ru-O-Ru bonds. The direction of the RIXS spectrometer (see figure 2.12 in section 2.2.3) determines the scattering angle α by fixing the direction of \mathbf{K}_{out} . The transferred momentum $\mathbf{Q} = \mathbf{K}_{out} - \mathbf{K}_{in}$ is therefore completely determined, having the direction of the bisector of α and modulus $|\mathbf{Q}| \approx 0.49 \text{ \AA}^{-1}$, for $h\nu_{in} = 528\text{-}532 \text{ eV}$ (see section 2.2.5). The quantity of interest, the component of momentum transferred into the sample

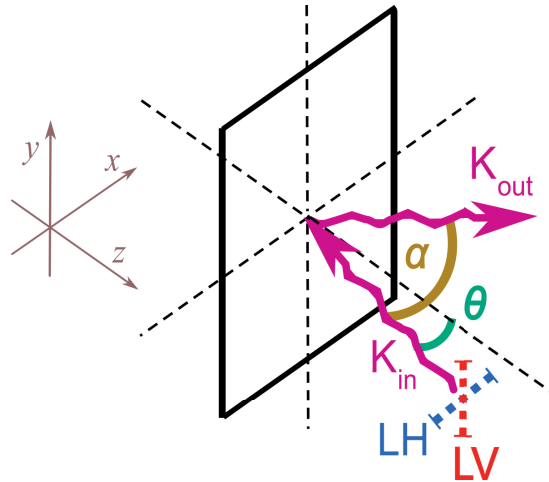


Figure A.3 – **Scattering geometry of the RIXS process** | The coordinate system is chosen integral with the sample, represented here as a square plane. The scattering angle α is fixed to 50deg by the direction of incidence (\mathbf{K}_{in}) and the direction of the RIXS spectrometer (which fixes the direction of the measured beam of momentum \mathbf{K}_{out}). The sample can be rotated around the y direction, so to change the angle θ between \mathbf{K}_{in} and the normal to the sample surface, *i.e.* the z direction. The scattering plane, defined by \mathbf{K}_{in} and \mathbf{K}_{out} , cut the sample along x . The polarization of the incident beam was systematically switched during the experiment, between linear horizontal (LH, which lies on the scattering plane) and linear vertical (LV, always directed along y and perpendicular to the scattering plane).

Appendix A. Additional information

plane, changes with θ :

$$Q_{//} = |\mathbf{Q}| \sin(25 \text{ deg} - \theta) \approx 0.49 \sin(25 \text{ deg} - \theta) \equiv q(\theta) \text{ \AA}^{-1}. \quad (\text{A.2})$$

Given the geometry of our experiment, $\mathbf{Q}_{//} = q(\theta) \hat{\mathbf{x}} \text{ \AA}^{-1}$. For a more direct understanding of the meaning of $\mathbf{Q}_{//}$, it is useful to express its value in unit of the Brillouin zone vector: $\mathbf{Q}_{//} = \frac{q(\theta)}{q_{BZ}^x} \mathbf{q}_{BZ}^x$, with \mathbf{q}_{BZ}^x Brillouin zone vector along the x direction, indicated in figure A.4.

Sr_2RuO_4 has a tetragonal unit cell, with sides $a=b=3.870 \text{ \AA}$ along the Ru-O-Ru bond directions [139], *i.e.* our x and y directions. Therefore $\mathbf{q}_{BZ}^a = \mathbf{q}_{BZ}^x = \frac{\pi}{a} \hat{\mathbf{x}} \sim 0.81 \text{ \AA}^{-1}$ and $\mathbf{Q}_{//} \simeq 0.6 \sin(25 \text{ deg} - \theta) \mathbf{q}_{BZ}^x$.

Ca_2RuO_4 has a larger orthogonal unit cell, corresponding to a smaller Brillouin zone - experimentally observed during our ARPES study on Ca_2RuO_4 [149]. The unit cell vectors in the Ru-O₂ plane have modulus: $a=5.410 \text{ \AA}$ and $b=5.492 \text{ \AA}$ [137], and are directed approximately along the first and second bisector of x and y directions in our geometry. In we take the average value, $\bar{a} = 5.45 \text{ \AA}$, we can define the Brillouin zone vector $q_{BZ}^a = \frac{\pi}{\bar{a}} \sim 0.6 \text{ \AA}^{-1}$, not parallel to $\hat{\mathbf{x}}$. To find q_{BZ}^x , is sufficient to consider that it lies along the diagonal of the orthorhombic Brillouin zone: $q_{BZ}^x = \sqrt{2} q_{BZ}^a \simeq 0.8 \text{ \AA}^{-1}$. Alternatively, one can consider the average value of the Ru-O-Ru bonds in the Ru-O₂ planes, $a' = \frac{3.972+3.986}{2} \simeq 3.98 \text{ \AA}$ [137], and use this value to find the Brillouin zone vector along the x direction: $q_{BZ}^x = \frac{\pi}{a'} \sim 0.8 \text{ \AA}^{-1}$, consistently with our previous estimate. To conclude, for Ca_2RuO_4 we find the in-plane transferred momentum to be $\mathbf{Q}_{//} \simeq 0.6 \sin(25 \text{ deg} - \theta) \mathbf{q}_{BZ}^x$, along the diagonal of the Brillouin zone.

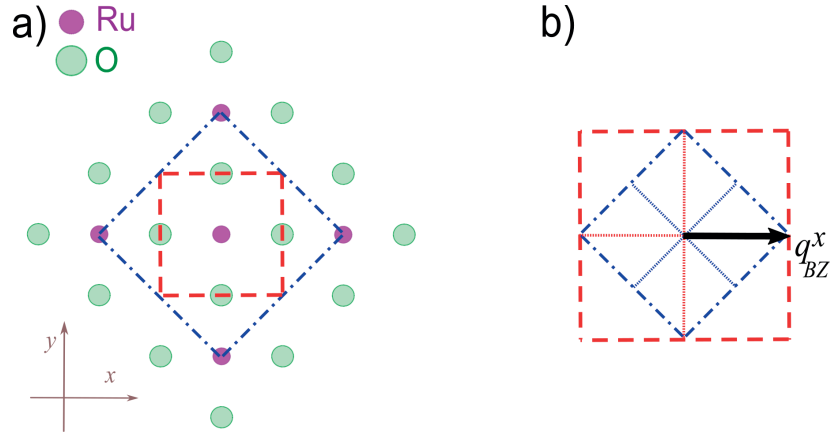


Figure A.4 – **Orthorhombic and tetragonal unit cell and Brillouin zone** | a) Schematics of the Ru-O₂ planes, with the orthorhombic and tetragonal unit cells drawn with blue dash-dotted and red dashed lines, respectively. b) Orthorhombic (blue dash-dotted line) and tetragonal (red dashed line) Brillouin zone. In black is indicated the Brillouin zone vector along $\hat{\mathbf{x}}$, \mathbf{q}_{BZ}^x .

A.4 RIXS: energy loss vs out-coming energy

Here we present a direct comparison of the two plotting options for RIXS spectra. As an example, we choose spectra recorded at incident energy $h\nu_{in}$ corresponding to the apical and planar t_{2g} - p absorption resonances and at an off-resonance energy, as indicated in figure A.5. The three spectra are plotted versus the energy of the out-coming photons, $h\nu_{out}$, or the energy loss, $h\nu_{in}-h\nu_{out}$.

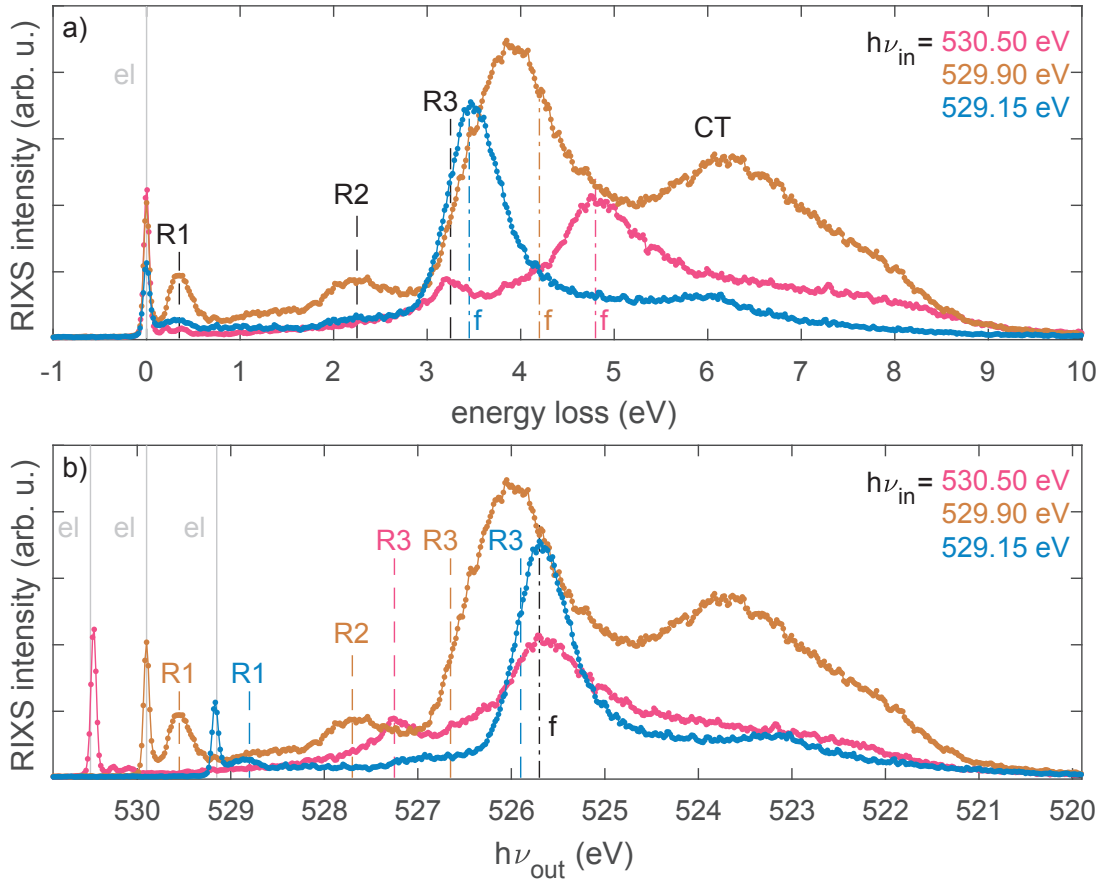


Figure A.5 – **Comparison of RIXS spectra plotted versus out-coming energy or energy loss** | taken at $\theta=75^\circ$ on Ca_2RuO_4 , with incident energy as indicated and linear horizontal (LH) polarization. a) RIXS intensity versus energy loss. b) RIXS intensity versus energy of the out-coming photons, in decreasing order to better compare with panel (a). Intensity of the spectra as recorded by the spectrometer. In both panels dashed vertical lines indicate peaks with a Raman character (R1-3), as opposed to fluorescent (f) features (dash-dotted line). The elastic peak (el) is indicated by the gray vertical line. The broad peak at high energy loss is attributed to charge transfer (CT).

For a more comfortable comparison, the x axis of panel A.5(b) is reversed (since smaller $h\nu_{out}$ corresponds to higher energy loss). The character of the observed excitations can be classified

Appendix A. Additional information

based on their dependence on the energy loss and $h\nu_{out}$. Excitations with a Raman character correspond to the energy difference of discrete levels, which manifest at constant energy loss. Fluorescent excitations of the other hand appear at constant $h\nu_{out}$.

A.5 RIXS: direct comparison of apical and planar spectra

Figure A.6 presents a direct comparison of RIXS spectra recorded in the apical and planar resonances for Ca_2RuO_4 and Sr_2RuO_4 :

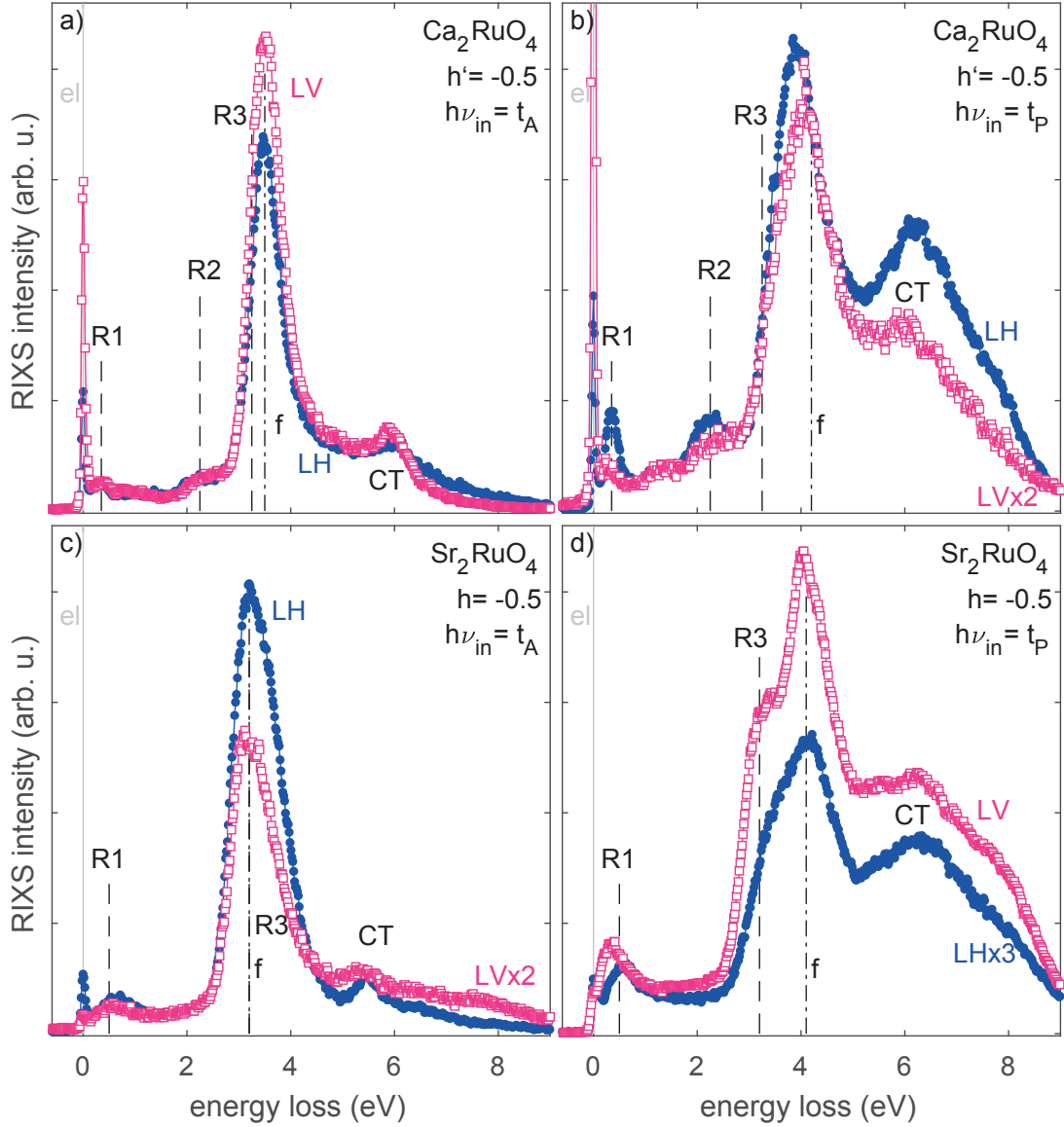


Figure A.6 – **Direct comparison of RIXS spectra** | taken at $\theta=75^\circ$. a,b) Spectra taken on Ca_2RuO_4 with incoming LH and LV polarized photons at 529.15 eV (t_A absorption resonance, panel (a)) and 529.9 eV (t_P , (b)). c,d) Sr_2RuO_4 data recorded at 528.9 eV (t_A , (c)) and 529.8 eV (t_P , (d)). Spectra are normalized to the corresponding XAS intensity (see figures 4.16 and 4.17). If indicated, spectra were amplified for visibility. In all panels, dashed lines indicate peaks with a Raman character (R1-3), as opposed to fluorescent (f) (dash-dotted). Gray lines indicate the elastic peak (el). Charge transfer (CT) excitations are observed at high energy loss.

Appendix A. Additional information

The spectra presented were normalized to the intensity of the XAS signal at the same incident angle polarization and energy (XAS-normalized), as done in figures 4.16 and 4.17. To improve the visibility, the intensity of LV spectra in panels (b) and (c) was doubled, while the LH spectrum of panel (d) was tripled.

Comparing the same spectra in their "raw" intensities (as recorded by the RIXS spectrometer) leads to similar conclusion, with the major relative change in the LH data of panel (d). In this case, it would suffice to double this spectrum to obtain the same visibility for the different features. In other words, table 4.3 is representative of the relative intensities in the RIXS spectra at these incident energies, both for the XAS-normalized and the "raw" case.

A.6 Solution of model Hamiltonian

A.6.1 Definitions and useful relations

The hamiltonian to solve **in the t_{2g} sub-space** is, from eq.1 in PRB 91, 155104 (2015) [132, 133, 142, 143, 144, 145, 146, 147, 148]:

$$\mathcal{H} = \lambda_{SO} \mathbf{L} \cdot \mathbf{S} + \frac{\Delta_{i-t}}{3} \mathbf{L}_z^2 \quad (\text{A.3})$$

where $\mathbf{S} = (\mathbf{S}_x, \mathbf{S}_y, \mathbf{S}_z)$ and $\mathbf{L} = (\mathbf{L}_x, \mathbf{L}_y, \mathbf{L}_z)$ are the spin and orbital momentum operators and λ_{SO} is the spin-orbit coupling constant. The intra- t_{2g} crystal field splitting Δ_{i-t} is defined so that $\Delta_{i-t} > 0$ lifts d_{xy} above d_{xz} and d_{yz} . Notice that in the cubic orbital basis, restricted to t_{2g} states, \mathbf{L}_z^2 is a diagonal operator, so that $\mathbf{L}_z^2 = \langle L_z \rangle^2$, as shown explicitly in section A.6.2. Here, the expressions for the 5d states:

$$\left. \begin{aligned} |z^2\rangle &= d_{z^2} = Y_2^0 \\ |x^2 - y^2\rangle &= d_{x^2-y^2} = \frac{i}{\sqrt{2}} (Y_2^{-2} + Y_2^2) \end{aligned} \right\} \quad e_g \text{ states} \quad (\text{A.4})$$

$$\left. \begin{aligned} |xy\rangle &= d_{xy} = \frac{1}{\sqrt{2}} (Y_2^{-2} - Y_2^2) \\ |xz\rangle &= d_{xz} = \frac{1}{\sqrt{2}} (Y_2^{-1} - Y_2^1) \\ |yz\rangle &= d_{yz} = \frac{i}{\sqrt{2}} (Y_2^{-1} + Y_2^1) \end{aligned} \right\} \quad t_{2g} \text{ states} \quad (\text{A.5})$$

where Y_l^m indicate the well known spherical harmonics. The spherical harmonics can therefore be written as:

$$\begin{aligned} Y_2^0 &= |z^2\rangle \\ Y_2^1 &= \frac{-1}{\sqrt{2}} (|xz\rangle + i|yz\rangle) \\ Y_2^{-1} &= \frac{1}{\sqrt{2}} (|xz\rangle - i|yz\rangle) \\ Y_2^2 &= \frac{-1}{\sqrt{2}} (|xy\rangle + i|x^2 - y^2\rangle) \\ Y_2^{-2} &= \frac{1}{\sqrt{2}} (|xy\rangle - i|x^2 - y^2\rangle) \end{aligned} \quad (\text{A.6})$$

For the solution of the hamiltonian is convenient to make use of the operators of creation and

Appendix A. Additional information

annihilation of the spin and orbital moment:

$$\begin{aligned}
 \mathbf{L}_+ &= \mathbf{L}_x + i\mathbf{L}_y \\
 \mathbf{L}_- &= \mathbf{L}_x - i\mathbf{L}_y \\
 \mathbf{S}_+ &= \mathbf{S}_x + i\mathbf{S}_y \\
 \mathbf{S}_- &= \mathbf{S}_x - i\mathbf{S}_y
 \end{aligned} \tag{A.7}$$

With $\mathbf{L}_\pm Y_l^m = \sqrt{l(l+1) - m(m \pm 1)} Y_l^{m \pm 1}$, $\mathbf{S}_\pm |\pm\rangle = 0$ and $\mathbf{S}_\pm |\mp\rangle = \sqrt{\frac{3}{4} \pm \frac{1}{2}(\pm \frac{1}{2})} |\pm\rangle = |\pm\rangle$.

Also, please note the relations:

$$\begin{aligned}
 \mathbf{L}_+ + \mathbf{L}_- &= 2\mathbf{L}_x \\
 \mathbf{L}_+ - \mathbf{L}_- &= 2i\mathbf{L}_y \\
 \mathbf{S}_+ + \mathbf{S}_- &= 2\mathbf{S}_x \\
 \mathbf{S}_+ - \mathbf{S}_- &= 2i\mathbf{S}_y
 \end{aligned} \tag{A.8}$$

Below we compute how the operators \mathbf{L}_\pm act on the t_{2g} states, using eq.A.5 and A.6:

$$\begin{aligned}
 \mathbf{L}_+ |xy\rangle &= \frac{1}{\sqrt{2}} \mathbf{L}_+ (Y_2^{-2} - Y_2^2) = \frac{1}{\sqrt{2}} \left(\sqrt{2(2+1) + 2(-1)} Y_2^{-1} + |0\rangle \right) = \sqrt{2} Y_2^{-1} = \\
 &= \sqrt{2} \frac{1}{\sqrt{2}} (|xz\rangle - i|yz\rangle) = |xz\rangle - i|yz\rangle \\
 \mathbf{L}_- |xy\rangle &= \frac{1}{\sqrt{2}} \mathbf{L}_- (Y_2^{-2} - Y_2^2) = \frac{1}{\sqrt{2}} \left(|0\rangle - \sqrt{2(2+1) - 2(+1)} Y_2^1 \right) = -\sqrt{2} Y_2^1 = \\
 &= -\sqrt{2} \frac{-1}{\sqrt{2}} (|xz\rangle + i|yz\rangle) = |xz\rangle + i|yz\rangle \\
 \mathbf{L}_+ |xz\rangle &= \frac{1}{\sqrt{2}} \mathbf{L}_+ (Y_2^{-1} - Y_2^1) = \frac{1}{\sqrt{2}} \left(\sqrt{2(2+1) + 1(-1+1)} Y_2^0 - \sqrt{2(2+1) - 1(1+1)} Y_2^2 \right) = \\
 &= \frac{1}{\sqrt{2}} \left(\sqrt{6} Y_2^0 - \sqrt{4} Y_2^2 \right) = \sqrt{3} |z^2\rangle - \sqrt{2} \frac{-1}{\sqrt{2}} (|xy\rangle + i|x^2 - y^2\rangle) = \\
 &= \sqrt{3} |z^2\rangle + |xy\rangle + i|x^2 - y^2\rangle \\
 \mathbf{L}_- |xz\rangle &= \frac{1}{\sqrt{2}} \mathbf{L}_- (Y_2^{-1} - Y_2^1) = \frac{1}{\sqrt{2}} \left(\sqrt{2(2+1) + 1(-1-1)} Y_2^{-2} - \sqrt{2(2+1) - 1(1-1)} Y_2^0 \right) = \\
 &= \frac{1}{\sqrt{2}} \left(\sqrt{4} Y_2^{-2} - \sqrt{6} Y_2^0 \right) = -\sqrt{3} |z^2\rangle + \sqrt{2} \frac{1}{\sqrt{2}} (|xy\rangle - i|x^2 - y^2\rangle) = \\
 &= -\sqrt{3} |z^2\rangle + |xy\rangle - i|x^2 - y^2\rangle
 \end{aligned} \tag{A.9}$$

$$\begin{aligned}
 \mathbf{L}_+ |yz\rangle &= \frac{i}{\sqrt{2}} \mathbf{L}_+ (Y_2^{-1} + Y_2^1) = \frac{i}{\sqrt{2}} \left(\sqrt{2(2+1)+1(-1+1)} Y_2^0 + \sqrt{2(2+1)-1(1+1)} Y_2^2 \right) = \\
 &= \frac{i}{\sqrt{2}} \left(\sqrt{6} Y_2^0 + \sqrt{4} Y_2^2 \right) = \sqrt{3} i |z^2\rangle + \sqrt{2} i \frac{-1}{\sqrt{2}} (|xy\rangle + i |x^2 - y^2\rangle) = \\
 &= \sqrt{3} i |z^2\rangle - i |xy\rangle + |x^2 - y^2\rangle \\
 \mathbf{L}_- |yz\rangle &= \frac{i}{\sqrt{2}} \mathbf{L}_- (Y_2^{-1} + Y_2^1) = \frac{i}{\sqrt{2}} \left(\sqrt{2(2+1)+1(-1-1)} Y_2^{-2} + \sqrt{2(2+1)-1(1-1)} Y_2^0 \right) = \\
 &= \frac{i}{\sqrt{2}} \left(\sqrt{4} Y_2^{-2} + \sqrt{6} Y_2^0 \right) = \sqrt{3} i |z^2\rangle + \sqrt{2} i \frac{1}{\sqrt{2}} (|xy\rangle - i |x^2 - y^2\rangle) = \\
 &= \sqrt{3} i |z^2\rangle + i |xy\rangle + |x^2 - y^2\rangle
 \end{aligned} \tag{A.10}$$

i.e. :

$$\begin{aligned}
 \mathbf{L}_\pm |xy\rangle &= |xz\rangle \mp i |yz\rangle \\
 \mathbf{L}_\pm |xz\rangle &= (\pm \sqrt{3} |z^2\rangle \pm i |x^2 - y^2\rangle) + |xy\rangle \\
 \mathbf{L}_\pm |yz\rangle &= (\sqrt{3} i |z^2\rangle + |x^2 - y^2\rangle) \mp i |xy\rangle
 \end{aligned} \tag{A.11}$$

Appendix A. Additional information

A.6.2 Proof of $\mathbf{L}_z^2 = \langle \mathbf{L}_z \rangle^2$

Let's start with writing the matrix representation of \mathbf{L}_z^2 , in the t_{2g} subspace.

First, we calculate \mathbf{L}_z explicitly:

$$\begin{aligned}\mathbf{L}_z |xy\rangle &= \frac{1}{\sqrt{2}} \mathbf{L}_z (Y_2^{-2} - Y_2^2) = \frac{1}{\sqrt{2}} (-2Y_2^{-2} - 2Y_2^2) = \frac{-2}{\sqrt{2}} (Y_2^{-2} + Y_2^2) \\ \mathbf{L}_z |xz\rangle &= \frac{1}{\sqrt{2}} \mathbf{L}_z (Y_2^{-1} - Y_2^1) = \frac{1}{\sqrt{2}} (-1Y_2^{-1} - 1Y_2^1) = \frac{-1}{\sqrt{2}} (Y_2^{-1} + Y_2^1) = \frac{-1}{\sqrt{2}} \frac{\sqrt{2}}{i} |yz\rangle = i |yz\rangle \\ \mathbf{L}_z |yz\rangle &= \frac{i}{\sqrt{2}} \mathbf{L}_z (Y_2^{-1} + Y_2^1) = \frac{i}{\sqrt{2}} (-1Y_2^{-1} + 1Y_2^1) = \frac{-i}{\sqrt{2}} (Y_2^{-1} - Y_2^1) = \frac{-i}{\sqrt{2}} \frac{\sqrt{2}}{1} |xz\rangle = -i |xz\rangle\end{aligned}\tag{A.12}$$

i.e.:

$$\begin{aligned}\mathbf{L}_z |xy\rangle &= \frac{-2}{\sqrt{2}} (Y_2^{-2} + Y_2^2) \\ \mathbf{L}_z |xz\rangle &= i |yz\rangle \\ \mathbf{L}_z |yz\rangle &= -i |xz\rangle\end{aligned}\tag{A.13}$$

Now, we can compute \mathbf{L}_z^2 :

$$\begin{aligned}\mathbf{L}_z^2 |xy\rangle &= \mathbf{L}_z (\mathbf{L}_z |xy\rangle) = \frac{-2}{\sqrt{2}} \mathbf{L}_z (Y_2^{-2} + Y_2^2) = \frac{-2}{\sqrt{2}} (-2Y_2^{-2} + 2Y_2^2) = \frac{+4}{\sqrt{2}} (Y_2^{-2} - Y_2^2) = 4 |xy\rangle \\ \mathbf{L}_z^2 |xz\rangle &= \mathbf{L}_z (\mathbf{L}_z |xz\rangle) = i \mathbf{L}_z |yz\rangle = i(-i |xz\rangle) = |xz\rangle \\ \mathbf{L}_z^2 |yz\rangle &= \mathbf{L}_z (\mathbf{L}_z |yz\rangle) = -i \mathbf{L}_z |xz\rangle = -i(i |yz\rangle) = |yz\rangle\end{aligned}\tag{A.14}$$

i.e.:

$$\begin{aligned}\mathbf{L}_z^2 |xy\rangle &= 4 |xy\rangle \\ \mathbf{L}_z^2 |xz\rangle &= |xz\rangle \\ \mathbf{L}_z^2 |yz\rangle &= |yz\rangle\end{aligned}\tag{A.15}$$

Hence, the matrix representation of \mathbf{L}_z^2 in the t_{2g} basis $(|xy\rangle, |xz\rangle, |yz\rangle)$ is:

$$\mathbf{L}_z^2 = \begin{pmatrix} 4 & 0 & 0 \\ 0 & 1 & 0 \\ 0 & 0 & 1 \end{pmatrix}\tag{A.16}$$

Now, we want to calculate $\langle L_z \rangle^2$ in the t_{2g} sub-space. As evident from eq.A.13, \mathbf{L}_z^2 projects the $|xy\rangle$ state out of the sub-space we are interested in. Therefore, in order to derive $\langle L_z \rangle^2$, we will initially consider the full 5d space.

$$\begin{aligned}\mathbf{L}_z |z^2\rangle &= \mathbf{L}_z Y_2^0 = |0\rangle \\ \mathbf{L}_z |x^2 - y^2\rangle &= \frac{i}{\sqrt{2}} \mathbf{L}_z (Y_2^{-2} + Y_2^2) = \frac{i}{\sqrt{2}} (-2Y_2^{-2} + 2Y_2^2) = \frac{-2i}{\sqrt{2}} (Y_2^{-2} - Y_2^2) = -2i |xy\rangle \\ \mathbf{L}_z |xy\rangle &= \frac{-2}{\sqrt{2}} (Y_2^{-2} + Y_2^2) = 2i |x^2 - y^2\rangle\end{aligned}\quad (\text{A.17})$$

i.e. :

$$\begin{aligned}\mathbf{L}_z |z^2\rangle &= |0\rangle \\ \mathbf{L}_z |x^2 - y^2\rangle &= -2i |xy\rangle \\ \mathbf{L}_z |xy\rangle &= 2i |x^2 - y^2\rangle \\ \mathbf{L}_z |xz\rangle &= i |yz\rangle \\ \mathbf{L}_z |yz\rangle &= -i |xz\rangle\end{aligned}\quad (\text{A.18})$$

We can therefore write $\langle L_z \rangle$ in the full 5d space using the results of eq.A.18:

$$\begin{aligned}\langle L_z \rangle &= \begin{pmatrix} \langle z^2 | \mathbf{L}_z | z^2 \rangle & \langle z^2 | \mathbf{L}_z | x^2 - y^2 \rangle & \dots \\ \langle x^2 - y^2 | \mathbf{L}_z | z^2 \rangle & \langle x^2 - y^2 | \mathbf{L}_z | x^2 - y^2 \rangle & \dots \\ \langle xy | \mathbf{L}_z | z^2 \rangle & \langle xy | \mathbf{L}_z | x^2 - y^2 \rangle & \dots \\ \langle xz | \mathbf{L}_z | z^2 \rangle & \langle xz | \mathbf{L}_z | x^2 - y^2 \rangle & \dots \\ \langle yz | \mathbf{L}_z | z^2 \rangle & \langle yz | \mathbf{L}_z | x^2 - y^2 \rangle & \dots \end{pmatrix} \\ &= \begin{pmatrix} \dots & \langle z^2 | \mathbf{L}_z | xy \rangle & \langle z^2 | \mathbf{L}_z | xz \rangle & \langle z^2 | \mathbf{L}_z | yz \rangle \\ \dots & \langle x^2 - y^2 | \mathbf{L}_z | xy \rangle & \langle x^2 - y^2 | \mathbf{L}_z | xz \rangle & \langle x^2 - y^2 | \mathbf{L}_z | yz \rangle \\ \dots & \langle xy | \mathbf{L}_z | xy \rangle & \langle xy | \mathbf{L}_z | xz \rangle & \langle xy | \mathbf{L}_z | yz \rangle \\ \dots & \langle xz | \mathbf{L}_z | xy \rangle & \langle xz | \mathbf{L}_z | xz \rangle & \langle xz | \mathbf{L}_z | yz \rangle \\ \dots & \langle yz | \mathbf{L}_z | xy \rangle & \langle yz | \mathbf{L}_z | xz \rangle & \langle yz | \mathbf{L}_z | yz \rangle \end{pmatrix} = \\ &= \begin{pmatrix} 0 & 0 & 0 & 0 & 0 \\ 0 & 0 & \langle x^2 - y^2 | \mathbf{L}_z | xy \rangle & 0 & 0 \\ 0 & \langle xy | \mathbf{L}_z | x^2 - y^2 \rangle & 0 & 0 & 0 \\ 0 & 0 & 0 & 0 & \langle xz | \mathbf{L}_z | yz \rangle \\ 0 & 0 & 0 & \langle yz | \mathbf{L}_z | xz \rangle & 0 \end{pmatrix} = \\ &= \begin{pmatrix} 0 & 0 & 0 & 0 & 0 \\ 0 & 0 & 2i & 0 & 0 \\ 0 & -2i & 0 & 0 & 0 \\ 0 & 0 & 0 & 0 & i \\ 0 & 0 & 0 & -i & 0 \end{pmatrix}\end{aligned}\quad (\text{A.19})$$

Appendix A. Additional information

We can now compute $\langle L_z \rangle^2$, in the full 5d space:

$$\begin{aligned}
 \langle L_z \rangle^2 &= \begin{pmatrix} 0 & 0 & 0 & 0 & 0 \\ 0 & 0 & 2i & 0 & 0 \\ 0 & -2i & 0 & 0 & 0 \\ 0 & 0 & 0 & 0 & -i \\ 0 & 0 & 0 & i & 0 \end{pmatrix} \begin{pmatrix} 0 & 0 & 0 & 0 & 0 \\ 0 & 0 & 2i & 0 & 0 \\ 0 & -2i & 0 & 0 & 0 \\ 0 & 0 & 0 & 0 & i \\ 0 & 0 & 0 & -i & 0 \end{pmatrix} = \\
 &= \begin{pmatrix} 0 & 0 & 0 & 0 & 0 \\ 0 & -4i^2 & 0 & 0 & 0 \\ 0 & 0 & -4i^2 & 0 & 0 \\ 0 & 0 & 0 & -i^2 & 0 \\ 0 & 0 & 0 & 0 & -i^2 \end{pmatrix} = \begin{pmatrix} 0 & 0 & 0 & 0 & 0 \\ 0 & 4 & 0 & 0 & 0 \\ 0 & 0 & 4 & 0 & 0 \\ 0 & 0 & 0 & 1 & 0 \\ 0 & 0 & 0 & 0 & 1 \end{pmatrix}
 \end{aligned} \tag{A.20}$$

restricting ourselves to the t_{2g} subspace, we find:

$$\langle L_z \rangle^2_{t_{2g}} = \begin{pmatrix} 4 & 0 & 0 \\ 0 & 1 & 0 \\ 0 & 0 & 1 \end{pmatrix} = \mathbf{L}_{\mathbf{z} t_{2g}}^2 \tag{A.21}$$

As anticipated in the previous section.

A.6.3 Spin orbit coupling

We want to evaluate $\mathbf{L} \cdot \mathbf{S}$, making use of the relations presented in eq.A.8:

$$\mathbf{L} \cdot \mathbf{S} = \mathbf{L}_x \mathbf{S}_x + \mathbf{L}_y \mathbf{S}_y + \mathbf{L}_z \mathbf{S}_z = \mathbf{L}_z \mathbf{S}_z + \frac{\mathbf{L}_+ \mathbf{S}_- + \mathbf{L}_- \mathbf{S}_+}{2} \quad (\text{A.22})$$

The complete basis in the t_{2g} sub-space includes the spin orientation: $\mathcal{B}_{t_{2g}} = (|xy, +\rangle, |xz, +\rangle, |yz, +\rangle, |xy, -\rangle, |xz, -\rangle, |yz, -\rangle)$. Using the results presented in eq.A.11 and A.13, we want to write the matrix expression for $\mathbf{L} \cdot \mathbf{S}$ in this basis:

$$\begin{aligned} \mathbf{L} \cdot \mathbf{S} |xy, +\rangle &= \left(\mathbf{L}_z \mathbf{S}_z + \frac{\mathbf{L}_+ \mathbf{S}_- + \mathbf{L}_- \mathbf{S}_+}{2} \right) |xy, +\rangle = |0\rangle + \frac{|xz, -\rangle - i |yz, -\rangle + |0\rangle}{2} = \\ &= \frac{1}{2} (|xz, -\rangle - i |yz, -\rangle) \\ \mathbf{L} \cdot \mathbf{S} |xz, +\rangle &= \left(\mathbf{L}_z \mathbf{S}_z + \frac{\mathbf{L}_+ \mathbf{S}_- + \mathbf{L}_- \mathbf{S}_+}{2} \right) |xz, +\rangle = \frac{i}{2} |yz, +\rangle + \frac{|xy, -\rangle + |0\rangle}{2} = \\ &= \frac{1}{2} (i |yz, +\rangle + |xy, -\rangle) \\ \mathbf{L} \cdot \mathbf{S} |yz, +\rangle &= \left(\mathbf{L}_z \mathbf{S}_z + \frac{\mathbf{L}_+ \mathbf{S}_- + \mathbf{L}_- \mathbf{S}_+}{2} \right) |yz, +\rangle = \frac{-i}{2} |xz, +\rangle + \frac{-i |xy, -\rangle + |0\rangle}{2} = \\ &= \frac{-i}{2} (|xz, +\rangle + |xy, -\rangle) \\ \mathbf{L} \cdot \mathbf{S} |xy, -\rangle &= \left(\mathbf{L}_z \mathbf{S}_z + \frac{\mathbf{L}_+ \mathbf{S}_- + \mathbf{L}_- \mathbf{S}_+}{2} \right) |xy, -\rangle = |0\rangle + \frac{|0\rangle + |xz, +\rangle + i |yz, -\rangle}{2} = \\ &= \frac{1}{2} (|xz, +\rangle + i |yz, +\rangle) \\ \mathbf{L} \cdot \mathbf{S} |xz, -\rangle &= \left(\mathbf{L}_z \mathbf{S}_z + \frac{\mathbf{L}_+ \mathbf{S}_- + \mathbf{L}_- \mathbf{S}_+}{2} \right) |xz, -\rangle = \frac{-i}{2} |yz, -\rangle + \frac{|0\rangle + |xy, +\rangle}{2} = \\ &= \frac{1}{2} (-i |yz, -\rangle + |xy, +\rangle) \\ \mathbf{L} \cdot \mathbf{S} |yz, -\rangle &= \left(\mathbf{L}_z \mathbf{S}_z + \frac{\mathbf{L}_+ \mathbf{S}_- + \mathbf{L}_- \mathbf{S}_+}{2} \right) |yz, -\rangle = \frac{i}{2} |xz, -\rangle + \frac{|0\rangle + i |xy, +\rangle}{2} = \\ &= \frac{i}{2} (|xz, -\rangle + |xy, +\rangle) \end{aligned} \quad (\text{A.23})$$

From these relations, the matrix expression for $\mathbf{L} \cdot \mathbf{S}$ results in:

$$\mathbf{L} \cdot \mathbf{S} = \frac{1}{2} \begin{pmatrix} 0 & 0 & 0 & 0 & 1 & -i \\ 0 & 0 & i & 1 & 0 & 0 \\ 0 & -i & 0 & -i & 0 & 0 \\ 0 & 1 & i & 0 & 0 & 0 \\ 1 & 0 & 0 & 0 & 0 & -i \\ i & 0 & 0 & 0 & i & 0 \end{pmatrix} \quad (\text{A.24})$$

Appendix A. Additional information

A.6.4 Solution

We can now write our Hamiltonian in its matrix form:

$$\mathcal{H}_{\mathcal{B}_{t_{2g}}} = \lambda_{SO} \mathbf{L} \cdot \mathbf{S} + \frac{\Delta_{i-t}}{3} \langle L_z \rangle^2 = \begin{pmatrix} 4\frac{\Delta_{i-t}}{3} & 0 & 0 & 0 & \frac{\lambda_{SO}}{2} & -i\frac{\lambda_{SO}}{2} \\ 0 & \frac{\Delta_{i-t}}{3} & i\frac{\lambda_{SO}}{2} & \frac{\lambda_{SO}}{2} & 0 & 0 \\ 0 & -i\frac{\lambda_{SO}}{2} & \frac{\Delta_{i-t}}{3} & -i\frac{\lambda_{SO}}{2} & 0 & 0 \\ 0 & \frac{\lambda_{SO}}{2} & i\frac{\lambda_{SO}}{2} & 4\frac{\Delta_{i-t}}{3} & 0 & 0 \\ \frac{\lambda_{SO}}{2} & 0 & 0 & 0 & \frac{\Delta_{i-t}}{3} & -i\frac{\lambda_{SO}}{2} \\ i\frac{\lambda_{SO}}{2} & 0 & 0 & 0 & -i\frac{\lambda_{SO}}{2} & \frac{\Delta_{i-t}}{3} \end{pmatrix} \quad (\text{A.25})$$

This matrix is almost in a block-diagonal form. Changing the order in the basis to $\mathcal{B}_{t_{2g}}^1 = (|xy, +\rangle, |yz, -\rangle, |xz, -\rangle, |yz, +\rangle, |xz, +\rangle)$ transforms the hamiltonian in:

$$\mathcal{H}_{\mathcal{B}_{t_{2g}}^1} = \frac{\lambda_{SO}}{2} \begin{pmatrix} \frac{8}{3}\delta & -i & 1 & 0 & 0 & 0 \\ i & \frac{2}{3}\delta & i & 0 & 0 & 0 \\ 1 & -i & \frac{2}{3}\delta & 0 & 0 & 0 \\ 0 & 0 & 0 & \frac{8}{3}\delta & i & 1 \\ 0 & 0 & 0 & -i & \frac{2}{3}\delta & -i \\ 0 & 0 & 0 & 1 & i & \frac{2}{3}\delta \end{pmatrix} \quad (\text{A.26})$$

where $\delta = \frac{\Delta_{i-t}}{\lambda_{SO}}$.

We can now derive the eigenvalues and eigenvectors of our diagonalizable Hamiltonian:

$$T^{-1} \mathcal{H}_{\mathcal{B}_{t_{2g}}^1} T = \frac{\lambda_{SO}}{2} \begin{pmatrix} A & 0 & 0 & 0 & 0 & 0 \\ 0 & A & 0 & 0 & 0 & 0 \\ 0 & 0 & \frac{1}{2}(B-C) & 0 & 0 & 0 \\ 0 & 0 & 0 & \frac{1}{2}(B-C) & 0 & 0 \\ 0 & 0 & 0 & 0 & \frac{1}{2}(B+C) & 0 \\ 0 & 0 & 0 & 0 & 0 & \frac{1}{2}(B+C) \end{pmatrix} \quad (\text{A.27})$$

With $A = (\frac{2}{3}\delta - 1)$, $B = (\frac{10}{3}\delta + 1)$, $C = \sqrt{9 + 4\delta(\delta - 1)}$ and T approximately given by:

$$T \approx \begin{pmatrix} 0 & 0 & 0 & \sqrt{n} - C & 0 & \sqrt{n} \\ 0 & -i & 0 & i & 0 & i \\ 0 & 1 & 0 & 1 & 0 & 1 \\ 0 & 0 & \sqrt{n} - C & 0 & \sqrt{n} & 0 \\ i & 0 & -i & 0 & -i & 0 \\ 1 & 0 & 1 & 0 & 1 & 0 \end{pmatrix} \quad (\text{A.28})$$

where $n = \frac{(-1+2\delta+C)^2}{4}$. In other words, we found the doubly degenerate eigenvalues E_1, E_2, E_3

and eigenstates (not normalized) of our simple model:

$$\begin{cases} E_1 = \frac{\lambda_{SO}}{4} (B - C) = \frac{\lambda_{SO}}{4} \left(1 + \frac{10}{3} \delta - \sqrt{9 + 4\delta(\delta - 1)} \right) \\ E_2 = \frac{\lambda_{SO}}{2} A = \frac{\lambda_{SO}}{2} \left(\frac{2}{3} \delta - 1 \right) \\ E_3 = \frac{\lambda_{SO}}{4} (B + C) = \frac{\lambda_{SO}}{4} \left(1 + \frac{10}{3} \delta + \sqrt{9 + 4\delta(\delta - 1)} \right) \end{cases} \quad (\text{A.29})$$

$$\begin{cases} \psi_1^\pm \approx (\sqrt{n} - C) |xy, \pm\rangle + |xz, \mp\rangle \pm i |yz, \mp\rangle \\ \psi_2^\pm \approx |xz, \pm\rangle \mp i |yz, \pm\rangle \\ \psi_3^\pm \approx \sqrt{n} |xy, \pm\rangle + |xz, \mp\rangle \pm i |yz, \mp\rangle \end{cases} \quad (\text{A.30})$$

Since we are interested in the occupancy ratio, we implicitly write for the orbital hole occupation $n_{xz} = n_{yz} = 1$. In this way, we extract only n_{xy} and for the ratio we simply have $R = n_{xy} / (n_{xz} + n_{yz}) = n_{xy} / 2$.

A.6.4.1 Limit cases

If $\Delta_{i-t}=0$, $\delta=0$ and we find $A=-1$, $B=1$, $C=3$ and $n=1$:

$$\begin{cases} E_1 = \frac{\lambda_{SO}}{4} (B - C) = -\frac{\lambda_{SO}}{2} \\ E_2 = \frac{\lambda_{SO}}{2} A = -\frac{\lambda_{SO}}{2} \\ E_3 = \frac{\lambda_{SO}}{4} (B + C) = \lambda_{SO} \end{cases} \quad (\text{A.31})$$

$$\begin{cases} \psi_1^\pm \approx (\sqrt{n} - C) |xy, \pm\rangle + |xz, \mp\rangle \pm i |yz, \mp\rangle = -2 |xy, \pm\rangle + |xz, \mp\rangle \pm i |yz, \mp\rangle \\ \psi_2^\pm \approx |xz, \pm\rangle \mp i |yz, \pm\rangle \\ \psi_3^\pm \approx \sqrt{n} |xy, \pm\rangle + |xz, \mp\rangle \pm i |yz, \mp\rangle = |xy, \pm\rangle + |xz, \mp\rangle \pm i |yz, \mp\rangle \end{cases} \quad (\text{A.32})$$

With states ψ_1^\pm and ψ_2^\pm degenerate, and the holes in state ψ_3^\pm occupying evenly the $|xy, \pm\rangle$, $|xz, \mp\rangle$ and $|yz, \mp\rangle$ orbitals, as reported in the literature [132]. In absence of distortions, the t_{2g} orbitals are expected to mix evenly into the $\psi_{1,2}^\pm$ and ψ_3^\pm states, with a difference in energy, introduced by the spin orbit coupling, of $E_3 - E_{1,2} = 1.5\lambda_{SO}$.

Appendix A. Additional information

If we assume $\lambda_{SO}=0$, we find:

$$\begin{cases} E_1 = \frac{1}{4} \left(\frac{10}{3} \Delta_{i-t} - \sqrt{4} \Delta_{i-t} \right) = \frac{\Delta_{i-t}}{3} \\ E_2 = \frac{1}{2} \left(\frac{2}{3} \Delta_{i-t} \right) = \frac{\Delta_{i-t}}{3} \\ E_3 = \frac{1}{4} \left(\frac{10}{3} \Delta_{i-t} + \sqrt{4} \Delta_{i-t} \right) = \frac{4}{3} \Delta_{i-t} \end{cases} \quad (\text{A.33})$$

For the eigenstates:

$$\begin{cases} \psi_1^\pm = |yz, \pm\rangle \\ \psi_2^\pm = |xz, \pm\rangle \\ \psi_3^\pm = |xy, \pm\rangle \end{cases} \quad (\text{A.34})$$

With states ψ_1^\pm and ψ_2^\pm degenerate, and the state ψ_3^\pm of purely $|xy, \pm\rangle$ character. In absence of spin-orbit coupling, the t_{2g} splitting is given by the crystal field: $E_3 - E_{1,2} = \Delta_{i-t}$.

A.6.5 Summary

In conclusion, the eigenstates in the t_{2g} sub-space can, within this simple model, be approximately described by the three so-called Kramers doublets (ψ_1^\pm , ψ_2^\pm , and ψ_3^\pm), that are superpositions of d_{xy}^\pm , d_{yz}^\pm , and d_{xz}^\pm [146, 147]:

$$\psi_1^\pm = (\sqrt{n_{xy}} - C) d_{xy}^\mp + d_{xz}^\mp \pm i d_{yz}^\pm; \psi_2^\pm = d_{xz}^\pm \mp i d_{yz}^\pm \text{ and } \psi_3^\pm = \sqrt{n_{xy}} d_{xy}^\pm + d_{xz}^\mp \pm i d_{yz}^\mp.$$

With hole occupancy:

$$n_{xy} = \frac{[2\delta - 1 + C]^2}{4} \quad (\text{A.35})$$

where $\delta = \Delta_{i-t}/\lambda_{SO}$ and $C = \sqrt{9 + 4\delta(\delta - 1)}$ – see PRB **91**, 155104 (2015). The Eigenenergies (E_3, E_2 and E_1) are split by:

$$E_3 - E_1 = \frac{\lambda_{SO} C}{2} \quad \text{and} \quad E_3 - E_2 = \frac{\lambda_{SO}}{4} (C + 3 + 2\delta). \quad (\text{A.36})$$

The orbital hole occupancies (n_{xy} , $n_{xz} = n_{yz}$) and the level splittings are given (within this simple model) solely by the parameters λ_{SO} and Δ_{i-t} , in the limit $\delta \rightarrow 0$ (the case of $\{\text{Ba}, \text{Sr}\}_2\text{IrO}_4$ [132, 150, 151]), then $E_2 = E_1$ are four time degenerate and $E_3 - E_{1,2} = 1.5\lambda_{SO}$.

B Other published results

In this section are reproduced additional published results to which the author contributed.

ARTICLE

Received 7 Oct 2016 | Accepted 3 Mar 2017 | Published 5 May 2017

DOI: 10.1038/ncomms15176

OPEN

Hallmarks of Hund's coupling in the Mott insulator Ca_2RuO_4

D. Sutter^{1,*}, C.G. Fatuzzo^{2,*}, S. Moser³, M. Kim^{4,5}, R. Fittipaldi^{6,7}, A. Vecchione^{6,7}, V. Granata^{6,7}, Y. Sassa⁸, F. Cossalter¹, G. Gatti², M. Grioni², H.M. Rønnow², N.C. Plumb⁹, C.E. Matt⁹, M. Shi⁹, M. Hoesch¹⁰, T.K. Kim¹⁰, T.-R. Chang^{11,12}, H.-T. Jeng^{11,13}, C. Jozwiak³, A. Bostwick³, E. Rotenberg³, A. Georges^{4,5,14}, T. Neupert¹ & J. Chang¹

A paradigmatic case of multi-band Mott physics including spin-orbit and Hund's coupling is realized in Ca_2RuO_4 . Progress in understanding the nature of this Mott insulating phase has been impeded by the lack of knowledge about the low-energy electronic structure. Here we provide—using angle-resolved photoemission electron spectroscopy—the band structure of the paramagnetic insulating phase of Ca_2RuO_4 and show how it features several distinct energy scales. Comparison to a simple analysis of atomic multiplets provides a quantitative estimate of the Hund's coupling $J = 0.4$ eV. Furthermore, the experimental spectra are in good agreement with electronic structure calculations performed with Dynamical Mean-Field Theory. The crystal field stabilization of the d_{xy} orbital due to *c*-axis contraction is shown to be essential to explain the insulating phase. These results underscore the importance of multi-band physics, Coulomb interaction and Hund's coupling that together generate the Mott insulating state of Ca_2RuO_4 .

¹Physik-Institut, Universität Zürich, Winterthurerstrasse 190, Zürich CH-8057, Switzerland. ²Institute of Physics, École Polytechnique Fédérale de Lausanne (EPFL), Lausanne CH-1015, Switzerland. ³Advanced Light Source (ALS), Berkeley, California 94720, USA. ⁴College de France, Paris Cedex 05 75231, France. ⁵Centre de Physique Théorique, Ecole Polytechnique, CNRS, Univ Paris-Saclay, Palaiseau 91128, France. ⁶CNR-SPIN, Fisciano, Salerno I-84084, Italy. ⁷Dipartimento di Fisica 'E.R. Caianiello', Università di Salerno, Fisciano, Salerno I-84084, Italy. ⁸Department of Physics and Astronomy, Uppsala University, Uppsala S-75121, Sweden. ⁹Swiss Light Source, Paul Scherrer Institut, Villigen PSI CH-5232, Switzerland. ¹⁰Diamond Light Source, Harwell Campus, Didcot OX11 0DE, UK. ¹¹Department of Physics, National Tsing Hua University, Hsinchu 30013, Taiwan. ¹²Department of Physics, National Cheng Kung University, Tainan 701, Taiwan. ¹³Institute of Physics, Academia Sinica, Taipei 11529, Taiwan. ¹⁴Department of Quantum Matter Physics, University of Geneva, Geneva 4 1211, Switzerland. * These authors contributed equally to this work. Correspondence and requests for materials should be addressed to D.S. (email: dsutter@physik.uzh.ch) or to J.C. (email: johan.chang@physik.uzh.ch).

Electronic instabilities driving superconductivity, density wave orders and Mott metal–insulator transitions produce a characteristic energy scale below an onset temperature^{1–3}. Typically, this energy scale manifests itself as a gap in the electronic band structure around the Fermi level. Correlated electron systems have a tendency for avalanches, where one instability triggers or facilitates another⁴. The challenge is then to disentangle the driving and secondary phenomena. In many Mott insulating systems, such as La_2CuO_4 and Ca_2RuO_4 , long-range magnetic order appears as a secondary effect. In such cases, the energy scale associated with the Mott transition is much larger than that of magnetism. The Mott physics of the half-filled single-band $3d$ electron system La_2CuO_4 emerges due to a high ratio of Coulomb interaction to band width. This simple scenario does not apply to Ca_2RuO_4 . There the orbital and spin degrees of freedom of the $2/3$ -filled (with four electrons) t_{2g} -manifold implies that Hund's coupling enters as an important energy scale⁵. Moreover, recent studies of the antiferromagnetic ground state of Ca_2RuO_4 suggest that spin–orbit interaction also plays a significant role in shaping the magnetic moments^{6–8}, as well as the splitting of the t_{2g} states⁹.

Compared to Sr_2RuO_4 (refs 10,11), which may realize a chiral p -wave superconducting state, relatively little is known about the electronic band structure of Ca_2RuO_4 (ref. 12). Angle integrated photoemission spectroscopy has revealed the existence of Ru states with binding energy 1.6 eV (ref. 13)—an energy scale much larger than the Mott gap $\sim 0.4\text{ eV}$ estimated from transport experiments¹⁴. Moreover, angle-resolved photoemission spectroscopy (ARPES) experiments on $\text{Ca}_{1.8}\text{Sr}_{0.2}\text{RuO}_4$ —the critical composition for the metal–insulator transition—have led to contradicting interpretations^{15,16} favouring or disavowing the so-called orbital-selective scenario where a Mott gap opens only on a subset of bands^{17,18}. Extending this scenario to Ca_2RuO_4 would imply orbital-dependent Mott gaps¹⁸. The electronic structure should thus display two Mott energy scales (one of d_{xy} and another for the d_{xz}, d_{yz} states). A different explanation for the Mott state of Ca_2RuO_4 is that the c -axis compression of the S-Pbca insulating

phase induces a crystal field stabilization of the d_{xy} orbital, leading to half-filled d_{xz}, d_{yz} bands and completely filled d_{xy} states^{19,20}. In this case, only one Mott gap on the d_{xz}, d_{yz} bands will be present with band insulating d_{xy} states. The problem has defied a solution due to a lack of experimental knowledge about the low-energy electronic structure.

Here we present an ARPES study of the electronic structure in the paramagnetic insulating state (at 150 K) of Ca_2RuO_4 . Three different bands—labelled *A*, *B* and *C* band—are identified and their orbital character is discussed through comparison to first-principle Density Functional Theory (DFT) band structure calculations. The observed band structure is incompatible with a single insulating energy scale acting uniformly on all orbitals. A phenomenological Green's function incorporating an enhanced crystal field and a spectral gap in the self-energy is used to describe the observed band structure on a qualitative level. Further insight is gained from Dynamical Mean-Field Theory (DMFT) calculations including Hund's coupling and Coulomb interaction. The Hund's coupling splits the d_{xy} band allowing quantitative estimate of this parameter. The Coulomb interaction is mainly responsible for the insulating behaviour of the d_{xz}, d_{yz} bands. The experimental results, together with our theoretical analysis, clarify the origin of the Mott phase in the multi-orbital system Ca_2RuO_4 . Furthermore, they provide a natural explanation as to why previous experiments have identified different values for the energy gap.

Results

Crystal and electronic structure. Ca_2RuO_4 is a layered perovskite, where the Mott transition coincides with a structural transition at $T_s \sim 350\text{ K}$, below which the c -axis lattice constant is reduced. We study the paramagnetic insulating state ($T = 150\text{ K}$) of Ca_2RuO_4 with orthorhombic S-Pbca crystal structure ($a = 5.39\text{ \AA}$, $b = 5.59\text{ \AA}$ and $c = 11.77\text{ \AA}$). It is worth noting that due to this nonsymmorphic crystal structure, Ca_2RuO_4 could not form a Mott insulating ground state at other fillings than $1/3$ and $2/3$ (ref. 21). In Fig. 1, the experimentally measured electronic

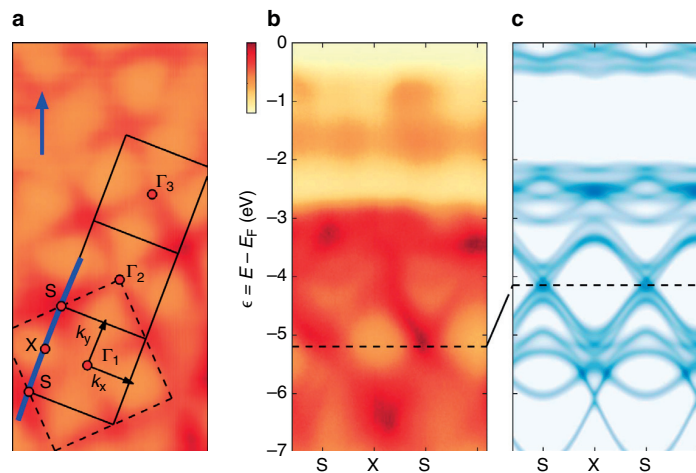


Figure 1 | Oxygen band structure of Ca_2RuO_4 . ARPES recorded with right-handed circularly polarized (C^+) 65 eV photons in the paramagnetic (150 K) insulating state of Ca_2RuO_4 , compared to DFT band structure calculations. Incident direction of the light is indicated by the blue arrow. Dark colours correspond to high intensities. **(a)** Constant energy map displaying the photoemission spectral weight at binding energy $\epsilon = E - E_F = -5.2\text{ eV}$. Solid and dashed lines mark the in-plane projected orthorhombic and tetragonal zone boundaries, respectively. Γ_i with $i = 1, 2, 3$ label orthorhombic zone centres. S and X label the zone corners and boundaries, respectively. **(b)** Spectra recorded along the zone boundary (blue line in **a**). Oxygen-dominated bands are found between $\epsilon = -7$ and -3 eV , whereas the ruthenium bands are located above -2.5 eV . **(c)** First-principle DFT band structure calculation. Within an arbitrary shift, indicated by the dashed line, qualitative agreement with the experiment is found for the oxygen bands.

structure is compared to a first-principle DFT calculation of the bare non-interacting bands. We observe two sets of states: near the Fermi level the electronic structure is comprised of Ru-dominated bands, while oxygen bands are present only for $\epsilon = E - E_F < -2.5$ eV. Up to an overall energy shift, good agreement between the calculated DFT and observed Ca_2RuO_4 oxygen band structure is found.

Non-dispersing ruthenium bands. The structure of the ruthenium bands near the Fermi level is the main topic of this paper, as these are the states influenced by Mott physics. A compilation of ARPES spectra, recorded along high-symmetry

directions, is presented in Figs 2 and 3a. In consistency with previous angle-integrated photoemission experiments¹³, a broad and flat band is found around the binding energy $\epsilon = -1.7$ eV. However, we also observe spectral weight closer to the Fermi level ($\epsilon \sim -0.8 \pm 0.2$ eV), especially near the zone boundaries (see Fig. 2a,d). These two flat ruthenium bands (labelled *A* and *B*) are revealed as a double peak structure in the energy distribution curves—Fig. 2c,f. Between the *A* band and the Fermi level, the spectral weight is suppressed. In fact, complete suppression of spectral weight is found for -0.2 eV $< \epsilon < 0$ eV (see Fig. 2c). This energy scale is in reasonable agreement with the activation energy ~ 0.4 eV extracted from resistivity experiments¹⁴.

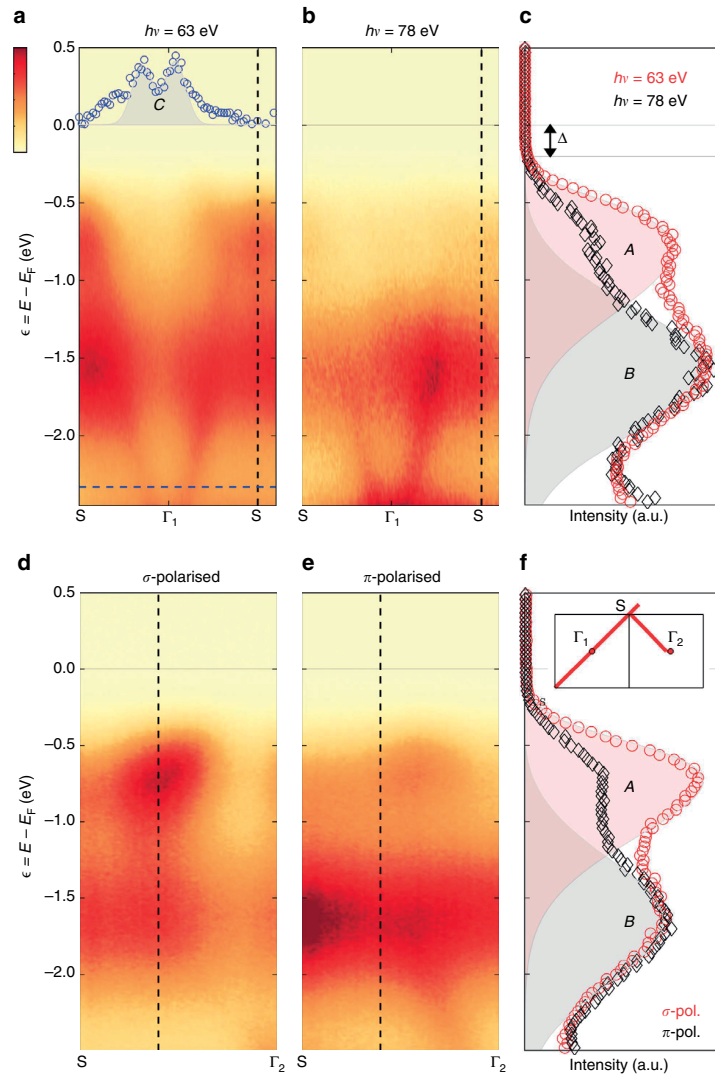


Figure 2 | Ruthenium band structure. (a,b) Photoemission spectra recorded along the high-symmetry direction $\Gamma_1 - S$ for incident circularly polarized light with photon energies $h\nu$ as indicated. Dark colours correspond to high intensities. Blue points in **a** show the momentum distribution curve at the binding energy indicated by the horizontal dashed line. The double peak structure is attributed to the *C* band. (c) Energy distribution curves (EDCs) at the S point, normalized at binding energy $\epsilon = E - E_F = -1.8$ eV. (d,e) Linear light polarization dependence along the $S - \Gamma_2$ direction at $h\nu = 65$ eV. (f) EDCs at the momentum indicated by the vertical dashed lines. In both (c,f), the *A* and *B* bands are indicated by red and grey shading, respectively.

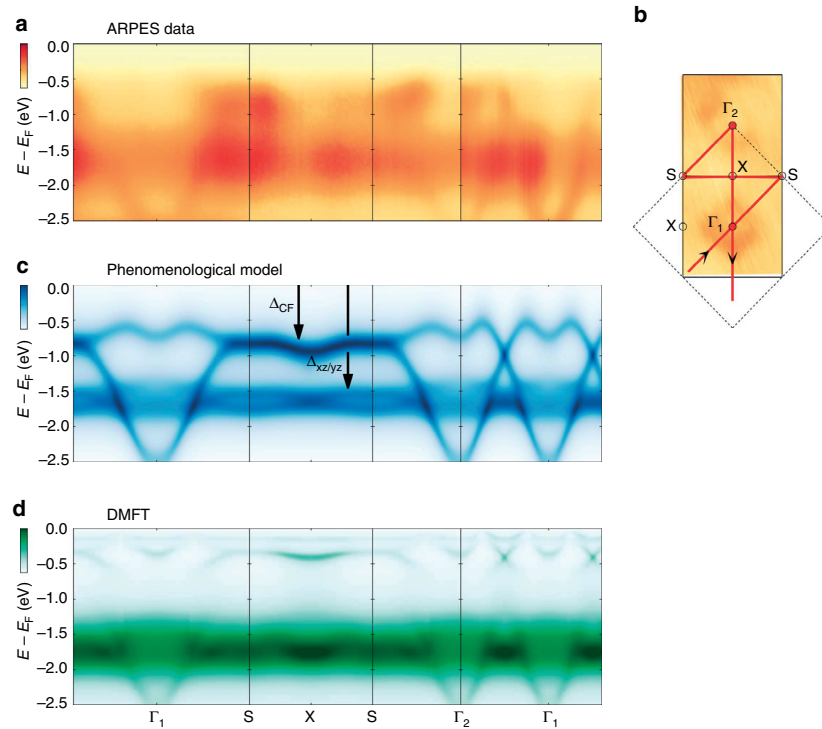


Figure 3 | Band structure along high-symmetry directions. (a) ARPES spectra recorded along high-symmetry directions with 65 eV circularly polarized light. (b) Constant energy map at binding energy $E - E_F = -2.7$ eV. (c) DFT-derived spectra for Ca_2RuO_4 , upon inclusion of a Mott gap $\Delta_{KZ/YZ} = 1.55$ eV acting on d_{xz} , d_{yz} bands and an enhanced crystal field $\Delta_{CF} = 0.6$ eV, shifting spectral weight of the d_{xy} bands (for details, see Methods section) and plotted with spectral weight representation. (d) DMFT calculation of the spectral function, with Coulomb interaction $U = 2.3$ eV and a Hund's coupling $J = 0.4$ eV. Dark colours correspond to high intensities.

Fast dispersing ruthenium bands. In addition to the flat \mathcal{A} and \mathcal{B} bands, a fast dispersing circular-shaped band is observed (Fig. 3b) around the Γ -point (zone centre) in the interval $-2.5 \text{ eV} < \epsilon < -2 \text{ eV}$ —see Figs 2a,b and 3a. A weaker replica of this band is furthermore found around Γ_2 (Fig. 3a,b). The band velocity, estimated from momentum distribution curves (Fig. 2a), yields $v = (2.6 \pm 0.4) \text{ eV \AA}$. As this band, which we label \mathcal{C} , disperses away from the zone centre, it merges with the most intense flat \mathcal{B} band. From the data, it is difficult to conclude with certainty whether the \mathcal{C} band disperses between the \mathcal{A} and \mathcal{B} bands. As this feature is weak in the spectra recorded with 78 eV photons (Fig. 2b), it makes sense to label \mathcal{A} and \mathcal{C} as distinct bands.

Orbital band character. Next we discuss the orbital character of the observed bands. As a first step, comparison to the band structure calculations is made. Although details can vary depending on exact methodology, all band structure calculations of Ca_2RuO_4 find a single fast dispersing branch^{22–25}. Our DFT calculation reveals that the fast dispersing band has predominantly d_{xy} character (Fig. 4a). We thus conclude that the in-plane extended d_{xy} orbital is responsible for the \mathcal{C} band. Within the DFT calculation, the d_{xz} and d_{yz} bare bands are relatively flat throughout the entire zone. This is also the characteristic of the observed \mathcal{B} band. It is thus natural to assign a dominant d_{xz} , d_{yz} contribution to this band. The orbital character of the \mathcal{A} band is not obviously derived from comparisons to DFT

calculations. In principle, photoemission matrix element effects carry information about orbital symmetries. As shown in Fig. 2, the \mathcal{A} band displays strong matrix element effects as a function of photon energy and photon polarization. However, probing with 65 eV light, the spectral weight of the \mathcal{A} band is not displaying any regularity within the (k_x, k_y) plane—see Supplementary Fig. 1. The contrast between linear horizontal and vertical light therefore vary strongly with momentum. This fact precludes any simple conclusions based on matrix element effects.

Discussion

Having explored the orbital character of the electronic states, we discuss the band structure in a more general context. Bare band structure calculations, not including Coulomb interaction, find that states at the Fermi level have d_{xy} and d_{xz}/d_{yz} character (see Fig. 4a). Including a uniform Coulomb interaction U results in a single Mott gap acting equally on all orbitals. Generally, this produces one single flat band inconsistent with the observation of two distinct flat bands (\mathcal{A} and \mathcal{B}). Adding in a phenomenological manner orbital-dependent Mott gaps to the self-energy produces two sets of flat bands. For example, one can introduce $\Delta_{xy} = 0.2$ eV and $\Delta_{xz,yz} = 1.5$ eV to mimic the \mathcal{A} and \mathcal{B} bands. However, such Mott gaps are not shifting the bottom of the fast V-shaped dispersion to the observed position. Better agreement with the observed band structure is found, when a Mott gap $\Delta_{xz,yz} = 1.55$ eV is added to the self-energy of the d_{xz} , d_{yz} states and a crystal field-induced downward shift $\Delta_{CF} = 0.6$ eV of

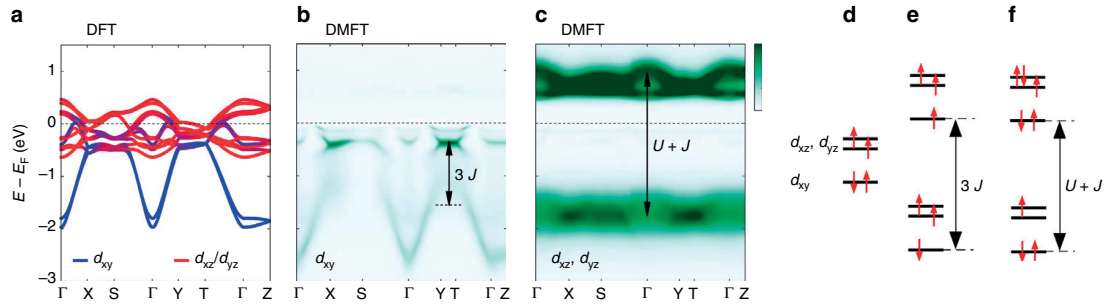


Figure 4 | Calculated orbital band character. (a) DFT calculation of the bare band structure. d_{xy} and d_{xz} , d_{yz} characters are indicated by blue and red colours, respectively. (b,c) Are the spectral function calculated within the DMFT approach and projected on the d_{xy} and d_{xz} , d_{yz} orbitals, respectively. Dark colours correspond to high intensities. The indicated energy splittings stem from a t_{2g} multiplet analysis in the atomic limit. (d) Ground-state multiplet defined by the crystal field and Hund's coupling J . (e) d_{xy} electron removal configurations split by $3J$ (see main text for explanation). (f) Representation of the twofold degenerate d_{xz} , d_{yz} electron addition and removal states, split by $U+J$.

the d_{xy} states is introduced. As shown in Fig. 3c, this reproduces two flat bands and simultaneously positions correctly the fast dispersing C band. From the fact that the bottom of the C band is observed well below the B band, we conclude that an—interaction enhanced—crystal field splitting is shifting the d_{xy} band below the Fermi level.

A similar structure emerges from DMFT calculations²⁶ including $U=2.3$ eV and Hund's coupling $J=0.4$ eV. The obtained spectral function (Fig. 3d) is generally in good agreement with the experimental observations (Fig. 3a). Both the C and B bands are reproduced with the previously assigned d_{xy} and d_{xz} , d_{yz} orbital character (Fig. 4b,c). The A band is also present in the DMFT calculation around -0.5 eV $< \epsilon < 0$ eV. Even though it is not smoothly connected with the C band, it has in fact d_{xy} character (Fig. 4b). By analysing the multiplet eigenstates (Fig. 4d) and electronic transitions in the atomic limit of an isolated t_{2g} shell, we can provide a simple qualitative picture of both observations: (i) the energy splitting between the A and C bands having d_{xy} orbital character, which we find to be of order $3J$, and (ii) the d_{xz} and d_{yz} orbital-driven B band splitting across the Fermi level, found to be of order $U+J$. Within this framework, the atomic ground state has a fully occupied d_{xy} orbital, while the d_{xz} , d_{yz} orbitals are occupied by two electrons with parallel spins ($S=1$) and thus effectively half-filled. The Mott gap developing in the d_{xz} , d_{yz} doublet is thus $U+J$ in the atomic limit⁵, corresponding to the electronic transition where one electron is either removed from this doublet or added to this doublet (leading to a double occupancy). In contrast, there are two possible atomic configuration that can be reached when removing one electron out of the fully filled d_{xy} orbital (Fig. 4d). One of these final states (high spin) has $S=3/2$, $L=0$ (corresponding pictorially to one electron in each orbital all with parallel spins), while the other (low spin) has $S=1/2$, $L=2$ (corresponding to the case when the remaining electron in the d_{xy} orbital has a spin opposite to those in d_{xz} , d_{yz}). The energy difference between these two configurations is $3J$, thus accounting for the observed ARPES splitting between the two d_{xy} removal peaks. Furthermore, this analysis allows to assess, from the experimental value of this splitting ~ 1.2 eV, that the effective Hund's coupling for the t_{2g} shell is of the order of 0.4 eV. This is consistent with previous theoretical work in ruthenates^{27,28} and provides a direct quantitative experimental estimate of this parameter. Because the high spin state is energetically favourable with respect to the low spin state (by $\sim 3J$), it can be assigned to the A band near the Fermi level, while the low spin state can be

assigned to the C band (See ref. 5 for a detailed description of the atomic multiplets of the t_{2g} Kanamori Hamiltonian). The Hund's coupling has thus profound impact on the electronic structure of the paramagnetic insulating state of Ca_2RuO_4 . The fact that Hund's coupling mainly influence the d_{xy} electronic states highlights orbital differentiation as a key characteristic of the Mott transition. Moreover, our findings emphasize the importance of the crystal field stabilization of the d_{xy} orbital^{19,20}. To further understand the interplay between U and J , detailed experiments through the metal–insulator transition of $\text{Ca}_{2-x}\text{Sr}_x\text{RuO}_4$ would be of great interest.

Methods

Experimental. High-quality single crystals of Ca_2RuO_4 were grown by the flux-feeding floating-zone technique^{29,30}. ARPES experiments were carried out at the SIS, I05 and MAESTRO beamlines at the Swiss Light Source, the Diamond Light Source and the Advanced Light Source. Both horizontal and vertical electron analyser geometry were used. Samples were cleaved *in situ* using the top-post cleaving method. All spectra were recorded in the paramagnetic insulating phase ($T=150$ K), resulting in an overall energy resolution of approximately 50 meV. To avoid charging effects, care was taken to ensure electronic grounding of the sample. Using silver epoxy (EPO-TEK E4110) cured just below $T=350$ K (inside the S-Pbca phase—space group 61) for 12 h, no detectable charging was observed when varying the photon flux.

DFT band structure calculations. We computed electronic structures using the projector augmented wave method^{31,32} as implemented in the VASP^{33,34} package within the generalized gradient approximation³⁵. Experimental lattice constants ($a=5.39$ Å, $b=5.59$ Å and $c=11.77$ Å) and a $12 \times 10 \times 4$ Monkhorst-Pack k -point mesh was used in the computations with a cutoff energy of 400 eV. The spin-orbit coupling effects are included self-consistently. In order to model Mott physics, we constructed a first-principles tight-binding model Hamiltonian, where the Bloch matrix elements were calculated by projecting onto the Wannier orbitals^{36,37}, which used the VASP2WANNIER90 interface³⁸. We used Ru t_{2g} orbitals to construct Wannier functions without using the maximizing localization procedure. The resulting 24-band spin-orbit coupled model with Bloch Hamiltonian matrix \hat{H}_k^0 reproduces well the first-principle electronic structure near the Fermi energy. To model the spectral function, we added a gap with a leading divergent $1/\omega$ term to the self-energy $\hat{\Sigma}(\omega) = \hat{P}_{xz,yz} \Delta_{xz,yz}^2 / (\omega + \mathcal{O}(\omega^0))$. To the Hamiltonian, we added a shift $\hat{H}_k = \hat{H}_k^0 - \hat{P}_{xy} \Delta_{CF}$. \hat{P}_{xy} and $\hat{P}_{xz,yz}$ are projectors on the d_{xy} and d_{xz} , d_{yz} orbitals, respectively, while $\Delta_{xz,yz}$ is the weight of the poles and Δ_{CF} mimics an enhanced crystal field. From the imaginary part of the Green's function $\hat{G}(\mathbf{k}, \omega) = [\omega - \hat{H}_k - \hat{\Sigma}(\omega)]^{-1}$ with the two adjustable parameters Δ_{CF} and $\Delta_{xz,yz}$, we obtained the spectral function $A(\mathbf{k}, \omega)$ by taking the trace over all orbital and spin degrees of freedom.

DFT + DMFT band structure calculations. We calculate the electronic structure within DFT + DMFT using the full potential implementation³⁹ and the TRIQS library^{40,41}. In the DFT part of the computation, the Wien2k package⁴² was used.

The local-density approximation (LDA) is used for the exchange-correlation functional. For projectors on the correlated t_{2g} orbital in DFT + DMFT, Wannier-like t_{2g} orbitals are constructed out of Kohn-Sham bands within the energy window $(-2, 1)$ eV with respect to the Fermi energy. We use the full rotationally invariant Kanamori interaction in order to ensure a correct description of atomic multiplets⁵. To solve the DMFT quantum impurity problem, we used the strong-coupling continuous-time Monte Carlo impurity solver⁴³ as implemented in the TRIQS library⁴⁴. In the U and J parameters of the Kanamori interaction, we used $U = 2.3$ eV and $J = 0.4$ eV, which successfully explains the correlated phenomena of other ruthenate such as Sr_2RuO_4 and ARuO_3 ($A = \text{Ca}, \text{Sr}$) within the DFT + DMFT framework^{27,28}.

Data availability. All relevant data are available from the authors.

References

- Imada, M., Fujimori, A. & Tokura, Y. Metal-insulator transitions. *Rev. Mod. Phys.* **70**, 1039–1263 (1998).
- Monceau, P. Electronic crystals: an experimental overview. *Adv. Phys.* **61**, 325–581 (2012).
- Hashimoto, M., Vishik, I. M., He, R.-H., Devereaux, T. P. & Shen, Z.-X. Energy gaps in high-transition-temperature cuprate superconductors. *Nat. Phys.* **10**, 483–495 (2014).
- Fradkin, E., Kivelson, S. A. & Tranquada, J. M. Colloquium: Theory of intertwined orders in high temperature superconductors. *Rev. Mod. Phys.* **87**, 457–482 (2015).
- Georges, A., de' Medici, L. & Mravlje, J. Strong correlations from Hund's coupling. *Annu. Rev. Condens. Matter Phys.* **4**, 137–178 (2013).
- Kunkemöller, S. *et al.* Highly anisotropic magnon dispersion in Ca_2RuO_4 : evidence for strong spin orbit coupling. *Phys. Rev. Lett.* **115**, 247201 (2015).
- Jain, A. *et al.* Soft spin-amplitude fluctuations in a Mott-insulating ruthenate <http://arxiv.org/abs/1510.07011> (2015).
- Khalilullin, G. Excitonic magnetism in Van Vleck type d^4 Mott insulators. *Phys. Rev. Lett.* **111**, 197201 (2013).
- Fatuzzo, C. G. *et al.* Spin-orbit-induced orbital excitations in Sr_2RuO_4 and Ca_2RuO_4 : a resonant inelastic x-ray scattering study. *Phys. Rev. B* **91**, 155104 (2015).
- Damasceli, A. *et al.* Fermi surface, surface states, and surface reconstruction in Sr_2RuO_4 . *Phys. Rev. Lett.* **85**, 5194–5197 (2000).
- Zabolotnyy, V. B. *et al.* Surface and bulk electronic structure of the unconventional superconductor Sr_2RuO_4 : unusual splitting of the band. *New J. Phys.* **14**, 063039 (2012).
- Puchkov, A. V. *et al.* Layered ruthenium oxides: from band metal to Mott insulator. *Phys. Rev. Lett.* **81**, 2747–2750 (1998).
- Mizokawa, T. *et al.* Spin-orbit coupling in the Mott insulator Ca_2RuO_4 . *Phys. Rev. Lett.* **87**, 077202 (2001).
- Nakatsuji, S. *et al.* Mechanism of hopping transport in disordered Mott insulators. *Phys. Rev. Lett.* **93**, 146401 (2004).
- Neupane, M. *et al.* Observation of a novel orbital selective Mott transition in $\text{Ca}_{1.8}\text{Sr}_{0.2}\text{RuO}_4$. *Phys. Rev. Lett.* **103**, 097001 (2009).
- Shimoyamada, A. *et al.* Strong mass renormalization at a local momentum space in multiorbital $\text{Ca}_{1.8}\text{Sr}_{0.2}\text{RuO}_4$. *Phys. Rev. Lett.* **102**, 086401 (2009).
- Anisimov, V., Nekrasov, I., Kondakov, D., Rice, T. & Sigrist, M. Orbital-selective Mott-insulator transition in $\text{Ca}_{2-x}\text{Sr}_x\text{RuO}_4$. *Eur. Phys. J. B* **25**, 191 (2002).
- Koga, A., Kawakami, N., Rice, T. M. & Sigrist, M. Orbital-selective Mott transitions in the degenerate Hubbard model. *Phys. Rev. Lett.* **92**, 216402 (2004).
- Liebsch, A. & Ishida, H. Subband filling and Mott transition in $\text{Ca}_{2-x}\text{Sr}_x\text{RuO}_4$. *Phys. Rev. Lett.* **98**, 216403 (2007).
- Gorelov, E. *et al.* Nature of the Mott Transition in Ca_2RuO_4 . *Phys. Rev. Lett.* **104**, 226401 (2010).
- Watanabe, H., Po, H. C., Vishwanath, A. & Zaletel, M. Filling constraints for spin-orbit coupled insulators in symmorphic and nonsymmorphic crystals. *PNAS* **112**, 14551–14556 (2015).
- Park, K. T. Electronic structure calculations for layered LaSrMnO_4 and Ca_2RuO_4 . *J. Phys. Condens. Matter* **13**, 9231 (2001).
- Liu, G.-Q. Spin-orbit coupling induced Mott transition in $\text{Ca}_{2-x}\text{Sr}_x\text{RuO}_4$ ($0 \leq x \leq 0.2$). *Phys. Rev. B* **84**, 235136 (2011).
- Acharya, S., Dey, D., Maitra, T. & Taraphder, A. The isoelectronic series $\text{Ca}_{2-x}\text{Sr}_x\text{RuO}_4$: structural distortion, effective dimensionality, spin fluctuations and quantum criticality. *arXiv:1605.05215* (2016).
- Woods, L. M. Electronic structure of Ca_2RuO_4 : a comparison with the electronic structures of other ruthenates. *Phys. Rev. B* **62**, 7833–7838 (2000).
- Georges, A., Kotliar, G., Krauth, W. & Rozenberg, M. J. Dynamical mean-field theory of strongly correlated fermion systems and the limit of infinite dimensions. *Rev. Mod. Phys.* **68**, 13–125 (1996).
- Mravlje, J. *et al.* Coherence-incoherence crossover and the mass-renormalization puzzles in Sr_2RuO_4 . *Phys. Rev. Lett.* **106**, 096401 (2011).
- Dang, H. T., Mravlje, J., Georges, A. & Millis, A. J. Electronic correlations, magnetism, and Hund's rule coupling in the ruthenium perovskites SrRuO_3 and CaRuO_3 . *Phys. Rev. B* **91**, 195149 (2015).
- Fukazawa, H., Nakatsuji, S. & Maeno, Y. Intrinsic properties of the Mott insulator $\text{Ca}_2\text{RuO}_{4+\delta}$. *Physica B* **281**, 613–614 (2000).
- Nakatsuji, S. & Maeno, Y. Synthesis and single-crystal growth of $\text{Ca}_{2-x}\text{Sr}_x\text{RuO}_4$. *J. Solid State Chem.* **156**, 26–31 (2001).
- Blöchl, P. E. Projector augmented-wave method. *Phys. Rev. B* **50**, 17953–17979 (1994).
- Kresse, G. & Joubert, D. From ultrasoft pseudopotentials to the projector augmented-wave method. *Phys. Rev. B* **59**, 1758–1775 (1999).
- Kresse, G. & Hafner, J. *Ab initio* molecular dynamics for open-shell transition metals. *Phys. Rev. B* **48**, 13115–13118 (1993).
- Kresse, G. & Furthmüller, J. Efficient iterative schemes for *ab initio* total-energy calculations using a plane-wave basis set. *Phys. Rev. B* **54**, 11169–11186 (1996).
- Perdew, J. P., Burke, K. & Ernzerhof, M. Generalized gradient approximation made simple. *Phys. Rev. Lett.* **77**, 3865–3868 (1996).
- Marzari, N. & Vanderbilt, D. Maximally localized generalized Wannier functions for composite energy bands. *Phys. Rev. B* **56**, 12847–12865 (1997).
- Souza, I., Marzari, N. & Vanderbilt, D. Maximally localized Wannier functions for entangled energy bands. *Phys. Rev. B* **65**, 035109 (2001).
- Franchini, C. *et al.* Maximally localized Wannier functions in LaMnO_3 within PBE + U, hybrid functionals and partially self-consistent GW: an efficient route to construct *ab initio* tight-binding parameters for e_g perovskites. *J. Phys. Condens. Matter* **24**, 235602 (2012).
- Aichhorn, M. *et al.* Dynamical mean-field theory within an augmented plane-wave framework: assessing electronic correlations in the iron pnictide LaFeAsO . *Phys. Rev. B* **80**, 085101 (2009).
- Aichhorn, M. *et al.* TRIQS/DFTTools: a TRIQS application for *ab initio* calculations of correlated materials. *Comput. Phys. Commun.* **204**, 200–208 (2016).
- Parcollet, A. *et al.* TRIQS: a toolbox for research on interacting quantum systems. *Comput. Phys. Commun.* **196**, 398–415 (2015).
- Blaha, P., Schwarz, K., Madsen, G., Kvasnicka, D. & Luitz, J. WIEN2k: an augmented plane wave plus local orbitals program for calculating crystal properties. *Technische Universität Wien* (2001).
- Gull, E. *et al.* Continuous-time Monte Carlo methods for quantum impurity models. *Rev. Mod. Phys.* **83**, 349–404 (2011).
- Seth, P., Krivenko, I., Ferrero, M. & Parcollet, O. TRIQS/CTHYB: a continuous-time quantum Monte Carlo hybridisation expansion solver for quantum impurity problems. *Comput. Phys. Commun.* **200**, 274–284 (2016).

Acknowledgements

D.S., J.C., C.G.F. and H.M.R. acknowledge support by the Swiss National Science Foundation and its Sinergia network MPBH. Y.S. is supported by the Wenner-Gren foundation. T.-R.C. and H.-T.J. are supported by the Ministry of Science and Technology, National Tsing Hua University, National Cheng Kung University and Academia Sinica, Taiwan. T.-R.C. and H.-T.J. also thank NCHC, CINC-NTU and NCTS, Taiwan for technical support. A.G. and M.K. acknowledge the support of the European Research Council (ERC-319286 QMAC, ERC-617196 CORRELMAT) and the Swiss National Science Foundation (NCCR MARVEL). S.M. acknowledges support by the Swiss National Science Foundation (Grant No. P2ELP2-155357). This work was performed at the SIS, I05 and MAESTRO beamlines at the Swiss Light Source, Diamond Light Source and Advanced Light Source, respectively. We acknowledge Diamond Light Source for time on beamline I05 under proposal SI14617 and SI12926 and thank all the beamline staff for technical support. The Advanced Light Source is supported by the Director, Office of Science, Office of Basic Energy Sciences, of the U.S. Department of Energy under Contract No. DE-AC02-05CH11231. M.K. and A.G. are grateful to M. Ferrero, O. Parcollet and P. Seth for discussions and support.

Authors contributions

R.F., A.V. and V.G. grew and prepared the Ca_2RuO_4 single crystals. D.S., C.G.F., M.S., F.C., Y.S., G.G., M.G., H.M.R., N.C.P., C.E.M., M.S., M.H., T.K.K. and J.C., prepared and carried out the ARPES experiment. D.S., C.G.F., F.C. and J.C. performed the data analysis. T.-R.C., H.-T.J. and T.N. made the DFT band structure calculations. M.K. and A.G. performed and analysed the DMFT calculations. All authors contributed to the manuscript.

Additional information

Supplementary Information accompanies this paper at <http://www.nature.com/naturecommunications>

Competing interests: The authors declare no competing financial interests.

Reprints and permission information is available online at <http://npg.nature.com/reprintsandpermissions/>

How to cite this article: Sutter, D. *et al.* Hallmarks of Hunds coupling in the Mott insulator Ca_2RuO_4 . *Nat. Commun.* **8**:15176 doi: 10.1038/ncomms15176 (2017).

Publisher's note: Springer Nature remains neutral with regard to jurisdictional claims in published maps and institutional affiliations.



This work is licensed under a Creative Commons Attribution 4.0 International License. The images or other third party material in this article are included in the article's Creative Commons license, unless indicated otherwise in the credit line; if the material is not included under the Creative Commons license, users will need to obtain permission from the license holder to reproduce the material. To view a copy of this license, visit <http://creativecommons.org/licenses/by/4.0/>

© The Author(s) 2017

Damped spin-excitations in a doped cuprate superconductor with orbital hybridization

O. Ivashko,¹ N. E. Shaik,² X. Lu,³ C. G. Fatuzzo,² M. Dantz,³ P. G. Freeman,⁴
D. E. McNally,³ D. Destraz,¹ N. B. Christensen,⁵ T. Kurosawa,⁶ N. Momono,^{6,7}
M. Oda,⁶ C. E. Matt,¹ C. Monney,¹ H. M. Rønnow,² T. Schmitt,³ and J. Chang^{1,*}

¹Physik-Institut, Universität Zürich, Winterthurerstrasse 190, CH-8057 Zürich, Switzerland

²Institute for Condensed Matter Physics, École Polytechnique Fédérale de Lausanne (EPFL), CH-1015 Lausanne, Switzerland

³Swiss Light Source, Paul Scherrer Institut, CH-5232 Villigen PSI, Switzerland

⁴Jeremiah Horrocks Institute for Mathematics, Physics and Astronomy,

University of Central Lancashire, PR1 2HE Preston, United Kingdom

⁵Department of Physics, Technical University of Denmark, DK-2800 Kongens Lyngby, Denmark.

⁶Department of Physics, Hokkaido University - Sapporo 060-0810, Japan

⁷Department of Applied Sciences, Muroran Institute of Technology, Muroran 050-8585, Japan

A resonant inelastic x-ray scattering (RIXS) study of overdamped spin-excitations in slightly underdoped $\text{La}_{2-x}\text{Sr}_x\text{CuO}_4$ (LSCO) with $x = 0.12$ and 0.145 is presented. Three high-symmetry directions have been investigated: (1) the anti-nodal $(0,0) \rightarrow (1/2,0)$, (2) the nodal $(0,0) \rightarrow (1/4,1/4)$ and (3) the zone boundary direction $(1/2,0) \rightarrow (1/4,1/4)$ connecting these two. The overdamped excitations exhibit strong dispersions along (1) and (3), whereas a much more modest dispersion is found along (2). This is in strong contrast to the un-doped compound La_2CuO_4 (LCO) for which the strongest dispersions are found along (1) and (2). The $t - t' - t'' - U$ Hubbard model used to explain the excitation spectrum of LCO predicts – for constant U/t – that the dispersion along (3) scales with $(t'/t)^2$. However, the diagonal hopping t' extracted on LSCO using single-band models is low ($t'/t \sim -0.16$) and decreasing with doping. We therefore invoked a two-orbital ($d_{x^2-y^2}$ and d_{z^2}) model which implies that t' is enhanced and that the Coulomb interaction U is renormalized. Both these effects act to enhance the zone boundary dispersion within the Hubbard model. We thus conclude that hybridization of $d_{x^2-y^2}$ and d_{z^2} states has a significant impact on the zone boundary dispersion in LSCO.

I. INTRODUCTION

Considerable research is being undertaken in the quest to reach consensus on the mechanism of high-temperature superconductivity¹ and the associated pseudogap phase² in copper-oxide materials (cuprates). The energy scales governing the physical properties of these layered materials therefore remain of great interest. It is known that these materials are characterized by a strong super-exchange interaction $J_1 = 4t^2/U$ where t is the nearest-neighbor hopping integral and U is the Coulomb interaction. To first order, this energy scale sets the band-width of the spin-excitation spectrum. Resonant inelastic x-ray scattering (RIXS) experiments³ have demonstrated that this band-width stays roughly unchanged across the entire phase diagram^{4,5} of hole doped cuprates. It has also been demonstrated that the cuprates belong to a regime (of t and U) where the second order exchange-interaction $J_2 = 4t^4/U^3$ contributes to a spin-excitation dispersion along the antiferromagnetic zone boundary (AFZB)⁶⁻⁹. Moreover, it is known from band structure calculations and experiments that the next nearest-neighbor (diagonal) hopping integral t' constitutes a non-negligible fraction of t ¹⁰. Empirically¹¹, the superconducting transition scales with the ratio t'/t whereas Hubbard type models predict the opposite trend^{12,13}. As a resolution, a two-orbital model – in which hybridization of d_{z^2} and $d_{x^2-y^2}$ states suppresses T_c and enhances t' – has been put forward¹⁴.

Here, we address the question as to how t' influences

the spin-excitation spectrum at, and in vicinity to, the antiferromagnetic zone boundary. We have therefore studied – using the RIXS technique – slightly underdoped compounds of $\text{La}_{2-x}\text{Sr}_x\text{CuO}_4$ (LSCO) with $x = 0.12$ and 0.145 . Even though the system is not antiferromagnetically ordered at these dopings, we quantify the zone boundary dispersion $\omega(\vec{q})$ by $E_{ZB} = \omega(1/2,0) - \omega(1/4,1/4)$. In doped LSCO a strongly enhanced zone boundary dispersion is observed. As will also be shown, within the $t - t' - t'' - U$ Hubbard model, one generally expects that the zone boundary dispersion scales with t'/t with a prefactor that depends on U/t . The Fermi surface topology of LSCO, obtained from photoemission spectroscopy and analyzed with a single-band tight binding model, suggests that t' decreases with increasing doping^{10,15}. The Hubbard model is thus within a single-band picture not consistent with the experiment. However, using a two-orbital model, in which hybridization between d_{z^2} and $d_{x^2-y^2}$ states enhances t' ¹⁴ and yields a lower effective Coulomb interaction U . Combined this provides ingredients to a satisfactory description of the zone boundary dispersion. We thus conclude that the two-orbital model¹⁴ is necessary to understand the spin-excitation spectrum of doped LSCO.

II. METHOD

The RIXS experiment was carried out at the Advanced REsonant Spectroscopies (ADRESS) beamline^{17,18} at

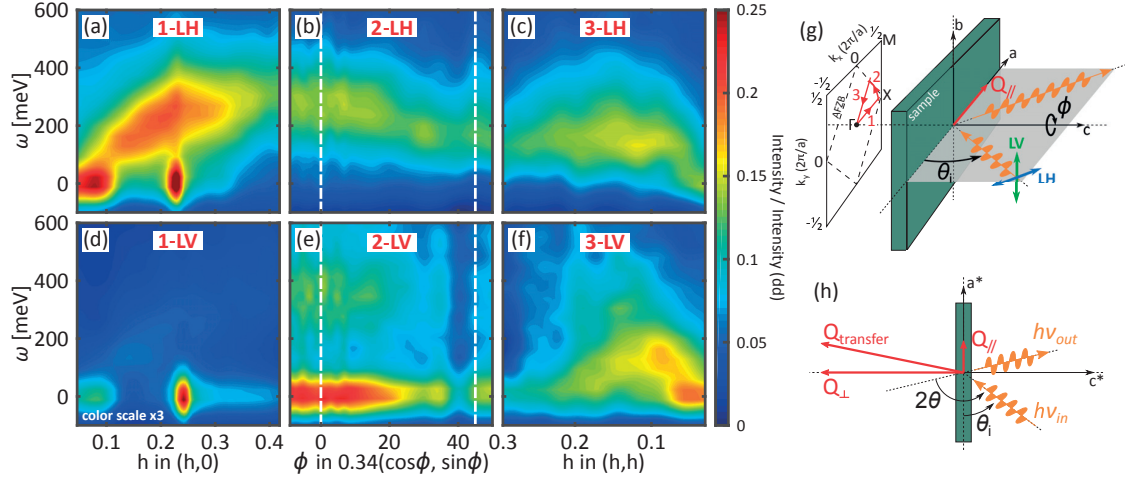


FIG. 1. (Color online) RIXS spectra versus momentum recorded on $\text{La}_{2-x}\text{Sr}_x\text{CuO}_4$ with $x = 0.12$ under grazing exit conditions and displayed in false color scale for different light polarizations. (a,d) RIXS intensity maps along the anti-nodal direction for linear-horizontal and linear-vertical incident light polarizations. (c,f) similar maps but along the nodal direction. (b,e) azimuthal RIXS maps connecting nodal and anti-nodal directions as shown schematically in (g). Consistent with what has previously been shown the spin-excitation matrix element is strongest for the LH polarization. By contrast, the charge-density-wave reflection at $Q_{\text{CDW}} = (\pm\delta_1, \delta_2)$ with $\delta_1 \sim 0.23$ and $\delta_2 \sim 0.01$ is about three times more intense with LV polarization. (g) - (h) displays the scattering geometry (side and top view respectively) where θ_i indicates the incident angle and ϕ is the azimuthal angle. Varying these angles allows to scan the in-plane momentum Q_{\parallel} . In (g) scan directions, with respect to the antiferromagnetic zone boundary are shown.

the Swiss Light Source (SLS) with the geometry shown in Fig. 1(h). The newly installed CARVING RIXS manipulator allowed to probe the full kinematically accessible reciprocal space $\vec{q} = (h, k)$ with a scattering angle of 130° . Incident photons with an energy of 933 eV (at the Cu L_3 -edge resonance) gave an instrumental energy and momentum resolution of 132 meV and 0.01 \AA^{-1} respectively. Both the linear horizontal (LH) and linear vertical (LV) light polarizations were applied to probe high quality single crystals of $\text{La}_{2-x}\text{Sr}_x\text{CuO}_4$ with $x = 0.12$ and 0.145 ($T_c = 27$ and 35 K respectively). These crystals were grown by the traveling floating zone method¹⁹ and previously characterized in neutron^{20–22} and μSR ²³ experiments. Ex-situ pre-alignment of the samples was carried out using a Laue diffractometer. The samples were cleaved in-situ using a standard top-post technique and all data were recorded at $T = 20 \text{ K}$. Although being in the low temperature orthorhombic (LTO) crystal structure, tetragonal notation $a \approx b \approx 3.78 \text{ \AA}$ ($c \approx 13.2 \text{ \AA}$) is adopted to describe the in-plane momentum (h, k) in reciprocal lattice units $2\pi/a$.

III. RESULTS

Fig. 1(a-c) displays grazing exit RIXS spectra of $\text{La}_{1.88}\text{Sr}_{0.12}\text{CuO}_4$ recorded with incident LH light polar-

ization along three trajectories as indicated in (g). Data along the same directions but measured with incident LV polarization are shown in (d-f). Besides the strong elastic scattering found at the specular condition [$Q = (0, 0)$], an elastic charge-density-wave (CDW) reflection is found – consistent with existing literature^{24,25} – along the $(h, 0)$ direction at $Q_{\text{CDW}} = (\delta_1, \delta_2)$ with $\delta_1 = 0.23(3)$ and $\delta_2 \approx 0.01$. The charge order reflection serves as a reference point, demonstrating precise alignment of the crystal.

For grazing exit geometry, it has previously been demonstrated that spin-excitations are enhanced in the LH-channel⁴. In Fig. 2(a,b), selected raw RIXS spectra recorded with LH polarization are shown for momenta near the $(1/2, 0)$ and $(1/4, 1/4)$ points. The low-energy part of the spectrum consists of three components: a weak elastic contribution, a smoothly varying background and a damped spin-excitation. It is immediately clear that the excitations near $(1/4, 1/4)$ are significantly softened compared to those observed around the $(1/2, 0)$ -point (see Fig. 2(a,b)).

For a more quantitative analysis of the magnon dispersion, we modeled the elastic line with a Gaussian for which the standard deviation $\sigma = 56 \text{ meV}$ was set by the instrumental energy resolution. A second order polynomial function is used to mimic the background. Finally, to analyze the spin-excitations we adopted the response

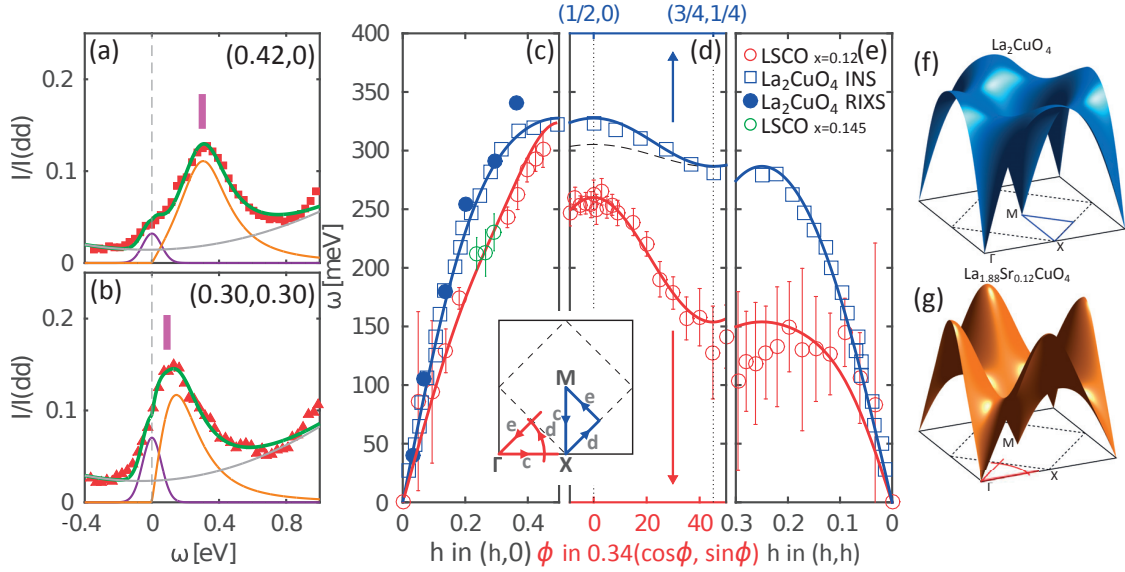


FIG. 2. (Color online) RIXS spectra for anti-nodal (a) and nodal (b) directions with the indicated in-plane momentum. The fit (solid green curve) is composed of three components: elastic line (purple), spin-excitation (orange) modeled by an anti-symmetric Lorentzian function and a quadratic background (grey) – see text for more detailed information. Vertical bars indicate the obtained poles of the Lorentzian function. (c)-(e) dispersion of the magnetic excitations in La_2CuO_4 observed by neutron scattering (open blue squares – Ref. 7) and RIXS (filled blue circles – Ref. 16) and $\text{La}_{2-x}\text{Sr}_x\text{CuO}_4$ with $x = 0.12$ (red circles) measured by RIXS (this work). Green circles in (c) are extracted from $\text{La}_{2-x}\text{Sr}_x\text{CuO}_4$ with $x = 0.145$ data. Within the antiferromagnetic zone scheme (indicated by the dashed line in the insert), red and blue cuts c and e are the equivalent anti-nodal and nodal directions. Solid lines in (c)-(e) are fits using a Heisenberg model, see text for further explanation. In (d) thin dashed line is the corresponding azimuthal scan, for La_2CuO_4 , extracted from the above mentioned model. (f)-(g) schematic illustration of the spin-excitation dispersion in $\text{La}_{2-x}\text{Sr}_x\text{CuO}_4$ with $x = 0$ and $x = 0.12$, as indicated. In the doped compound, the spin-excitation dispersion is strongly renormalized along the diagonal (nodal, Γ -M) direction. Blue and red patterns indicate the experimentally measured high-symmetry directions.

function of a damped harmonic oscillator^{4,26,27}:

$$\chi''(\omega) = \chi_0'' \frac{\gamma\omega}{(\omega^2 - \omega_0^2)^2 + \omega^2\gamma^2} \\ = \frac{\chi_0''}{2\omega_1} \left[\frac{\gamma/2}{(\omega - \omega_1)^2 + (\gamma/2)^2} - \frac{\gamma/2}{(\omega + \omega_1)^2 + (\gamma/2)^2} \right],$$

where the damping coefficient $\gamma/2 = \sqrt{\omega_0^2 - \omega_1^2}$. The RIXS intensities are modeled by $[n_B(\omega) + 1] \cdot \chi''(\omega)$, where $n_B(\omega) = [\exp(\hbar\omega/k_B T) - 1]^{-1}$ is the Bose factor. As shown in Fig. 2(a-b), fitting to this simple model provides a good description of the observed spectra. In this fashion, we extracted the spin-excitation pole dispersion $\omega_1(\vec{q})$ (Fig. 2(c-e)) along the three trajectories shown in the insert. To avoid the influence of CDW ordering on the spin-excitation dispersion²⁸, we analyzed around the charge ordering vector spectra of LSCO $x = 0.145$ where charge order is absent.

The extracted spin-excitation dispersion of LSCO $x = 0.12$ and 0.145 is to be compared with the magnon dispersion of the parent compound La_2CuO_4 ^{6,7,16,29}. Along

the anti-nodal $(1/2, 0)$ -direction comparable dispersions are found. This is consistent with the weak doping dependence reported on LSCO⁵ and the $\text{YBa}_2\text{Cu}_3\text{O}_{7-\delta}$ (YBCO) system⁴. For the nodal $(1/4, 1/4)$ -direction, the dispersion of the doped compound is, however, strongly softened compared to La_2CuO_4 . Whereas this effect has been reported for Bi-based^{30,31} and overdoped LSCO²⁶, we demonstrate directly by an azimuthal scan how exactly this softening appears. Notice that the azimuthal dependence is closely related (but not exactly identical) to the scan along the antiferromagnetic zone boundary.

IV. DISCUSSION

A recent systematic study³² of un-doped cuprate compounds concluded that the zone boundary dispersion scales with the crystal field splitting E_{z^2} of the $d_{x^2-y^2}$ and d_{z^2} states. Exact numerical determination of E_{z^2} is still a matter of debate^{14,33}. For a tetragonal system, E_{z^2} generally depends on the ratio between copper to

apical and planar oxygen distances³⁴. The crystal field splitting E_{z^2} can in principle be accessed by measuring the dd -excitations. For LCO, interpretations of the dd -excitations have consistently placed the d_{z^2} level above (*i.e.* closer to the Fermi level) both the $d_{xz,yz}$ and d_{xy} states^{32,34}. This is also consistent with density functional theory (DFT)¹⁴ and *ab initio*³³ calculations of the electronic band structure that find the d_{z^2} -band above the t_{2g} states. In doped LSCO $x = 0.12$, the spectral weight of the dd -excitations is redistributed and the "center-of-mass" is shifted to lower energies (see Fig. 3). The d_{xy} states are expected to be the least sensitive to crystal field changes³⁴. Therefore, it is conceivable that the $d_{xz,yz}$ and d_{z^2} states are shifting to lower energies. Again from DFT calculations (see Appendix C), we expect the d_{z^2} states to appear above those of $d_{xz,yz}$. Our experimental results thus (Fig. 3) suggest that the crystal field splitting E_{z^2} in doped LSCO $x = 0.12$ is smaller compared to LCO. Yet, the zone boundary dispersion is larger in LSCO $x = 0.12$ (Fig. 2). The present experiment is therefore not lending support for a correlation between the zone boundary dispersion and the crystal field splitting E_{z^2} .

The spin-excitation dispersion of doped LSCO is analyzed using an effective Heisenberg Hamiltonian derived from a $t - t' - t'' - U$ Hubbard model⁷⁻⁹. This discussion has three steps. First, an approximative analytical expression for the zone boundary dispersion is derived. Next, we compare to the experimentally obtained results using the known single-band tight-binding values of t , t' and t'' . It is shown that this approach is leading to unrealistically low values of the Coulomb interaction U . The d_{z^2} band is therefore included. This two-orbital scenario allows to describe the zone boundary dispersion with realistic input parameters, as presented in the last part of the discussion.

The simplest version of the Hubbard model contains only three parameters: the Coulomb interaction U , the band width ($4t$) and a renormalization factor Z – known to have little momentum dependence. To lowest order in $J_1 = 4t^2/U$, no magnon dispersion is expected along the zone boundary. Therefore, to explain the zone boundary dispersion – first observed on La_2CuO_4 – higher order terms $J_2 = 4t^4/U^3$ were included^{6,7} to the model. Later, it has been pointed out that higher order hopping terms t' and t'' can also contribute significantly^{8,9}. Generally, the effective Heisenberg model yields a dispersion^{8,9} $\omega(\vec{q}) = Z\sqrt{A(\vec{q})^2 - B(\vec{q})^2}$ where $A(\vec{q})$ and $B(\vec{q})$ – given in the Appendix A – are depending on U , t , t' and t'' . The zone boundary dispersion can be quantified by $E_{ZB} = \omega(1/2, 0) - \omega(1/4, 1/4)$. Using the single-band Hubbard model with realistic parameters^{8,10,11} ($U/t \sim 8$, $|t'| \leq t/2$ and $t'' = -t'/2$) for hole doped cuprates, we

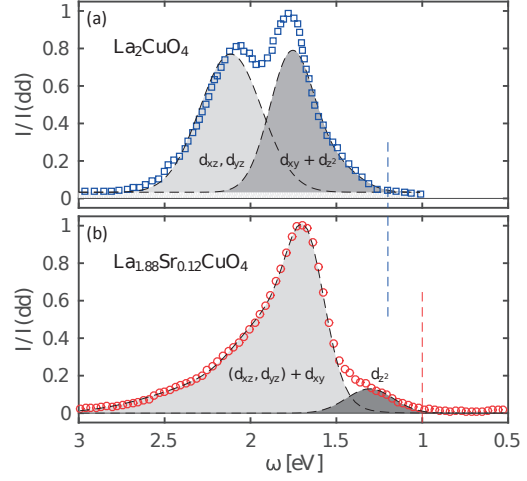


FIG. 3. (Color online) RIXS spectra showing the dd -excitations for La_2CuO_4 (a) (adopted from Ref. 32) and $\text{La}_{1.88}\text{Sr}_{0.12}\text{CuO}_4$ (b) (this work). The grey shaded areas indicate schematically different orbital contributions. Vertical dashed lines display the onset of dd -excitations.

find (see Appendix A):

$$\frac{E_{ZB}}{12ZJ_2} \approx 1 + \frac{1}{12} \left[112 - \left(\frac{U}{t} \right)^2 \right] \left(\frac{t'}{t} \right)^2. \quad (1)$$

A key prediction is thus that E_{ZB} scales as $(t'/t)^2$ with a pre-factor that depends on $(U/t)^2$.

This effective Heisenberg model is in principle not applicable to doped and hence antiferromagnetically disordered cuprates. For an exact description of the data, more sophisticated numerical methods have been developed³⁵. However, in the absence of analytical models, the Heisenberg model serves as a useful effective parametrization tool to describe the damped spin-excitations. Within a single-band tight-binding model, angle resolved photoemission spectroscopy (ARPES) experiments have found that t' decreases slightly with increasing doping^{10,15}. The stronger zone boundary dispersion can thus not be attributed to an increase of t' . Parameterizing the doping dependent zone boundary dispersion would thus imply a strong renormalization of U with increasing doping. For example, if we set $4t = 1720$ meV (obtained from LDA and ARPES^{11,36,37}) and $t'/t = -0.16$ and $t'' = -t'/2$, a fit yields $U/t \sim 4.7$ eV and $Z \sim 0.8$. Although these parameters provide a satisfactory description of the dispersion, the values of U and Z are not physically meaningful.

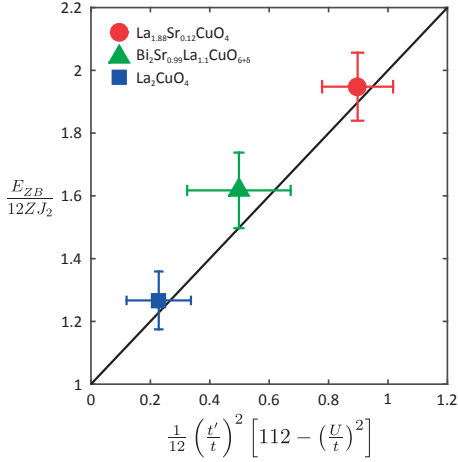


FIG. 4. (Color online) Experimentally obtained zone boundary dispersion E_{ZB} , normalized to $12ZJ_2$ – the expected theoretical value for $t' = t'' = 0$. To obtain J_2 the spin-excitation dispersion is fitted with U/t and t'/t as open parameters while keeping $t = 0.43$ eV, $t'' = -t'/2$ and $Z = 1.219$ fixed. Data points are obtained from fitting data on LSCO presented here (red circle) along with already published spin-excitation dispersions on LCO^{6,7} (blue square) and Bi2201³² (green triangle). Error bars stem from the standard deviations of the fitting parameters U/t and t'/t . The solid line is the predicted dependence of the $t-t'-t''-U$ Hubbard model with $U/t = 8$.

This failure combined with the observation of a reduced level splitting between the d_{z^2} and $d_{x^2-y^2}$ states (Fig. 3) motivates a two-band model. It has been demonstrated that d_{z^2} states contribute to effectively increase the t' hopping parameter¹⁴. Furthermore, with hybridization of d_{z^2} and $d_{x^2-y^2}$ states, a renormalized Coulomb interaction U is expected. Keeping $Z = 1.219$ as in La_2CuO_4 ⁸ and $t'' = -t'/2$, a satisfactory description (solid line in Fig. 2) of the spin-excitation dispersion is obtained for $t'/t = -0.38$ and $U/t = 6.5$. Notice that a similar ratio of t'/t has previously been inferred from the rounded Fermi surface topology of $\text{Ti}_2\text{Ba}_2\text{CuO}_{6+x}$,^{38,39} a material for which the d_{z^2} states are expected to be much less important⁴⁰. It could thus suggest that $t'/t \approx -0.4$ is common to single layer cuprates but masked in LSCO due to the repulsion between the $d_{x^2-y^2}$ and d_{z^2} bands that pushes the van Hove singularity close to the Fermi level and effectively reshapes the Fermi surface topology¹⁴. The more realistic values of U and Z , suggest that – for LSCO – the two-orbital character of this system is an important ingredient to accurately describe the spin-excitation spectrum.

Once having extracted U/t and t'/t by fitting the experimental spin-excitation spectrum, we plot – in Fig. 4 – the normalized zone boundary dispersion $E_{ZB}/(12ZJ_2)$ versus $\frac{1}{12} (t'/t)^2 [112 - (U/t)^2]$.

The same parameters were extracted (see Table I in the Appendix) from published RIXS data on La_2CuO_4 and $\text{Bi}_2\text{Sr}_{0.99}\text{La}_{1.1}\text{CuO}_{6+\delta}$ ³² and plotted in Fig. 4. All three compounds follow approximately the predicted correlation between $E_{ZB}/(12ZJ_2)$ and $\frac{1}{12} (t'/t)^2 [112 - (U/t)^2]$. This suggests that the zone boundary dispersion is controlled by the diagonal hopping t' and the coulomb interaction U . It would be interesting to extend this parametrization to include higher doping concentrations of LSCO. However, from existing RIXS data on overdoped single crystals of LSCO it is not possible to perform the analysis presented here^{26,41}. For LSCO $x = 0.23$, for example, the zone boundary dispersion has not been measured²⁶.

Finally, we notice that recent RIXS experiments on LSCO thin films using SrLaAlO_4 (SLAO) substrates found a much less pronounced softening of the spin-excitation dispersion around the $(1/4, 1/4)$ -point⁴². A possible explanation is that LSCO films on SLAO have a larger c -axis lattice parameter and hence also a larger copper to apical-oxygen distance than what is found in bulk crystals^{43,44}. As a consequence, the d_{z^2} states are less relevant and a larger value of U is expected. This in turn would lead to a less pronounced zone boundary dispersion.

V. CONCLUSIONS

In summary, a comprehensive RIXS study of underdoped LSCO $x = 0.12$ and 0.145 were presented. The spin-excitation dispersion was studied along three high-symmetry directions and a strong zone boundary dispersion is reported. The spin-excitation dispersion was parametrized and discussed using a Heisenberg Hamiltonian derived from a Hubbard model including higher order hopping integrals. Within this model, the zone boundary dispersion scales with next nearest-neighbor hopping integral t'^2 . We argue that hybridization between d_{z^2} and $d_{x^2-y^2}$, which is especially strong in LSCO, leads to an enhanced t' and a renormalization of the Coulomb interaction U . Both these effects – consistent with the observations – lead to a stronger zone boundary dispersion within the $t-t'-t''-U$ Hubbard model.

VI. ACKNOWLEDGMENTS:

We acknowledge support by the Swiss National Science Foundation under grant number BSSG10.155873 and through the SINERGIA network Mott Physics beyond the Heisenberg Model. This work was performed at the ADRESS beamline of the SLS at the Paul Scherrer Institut, Villigen PSI, Switzerland. We thank the ADRESS beamline staff for technical support. M.D. and T.S. have been partially funded by the Swiss National Science Foundation within the D-A-CH pro-

gramme (SNSF Research Grant 200021L 141325). X.L. acknowledges financial support from the European Communitys Seventh Framework Program (FP7/2007–2013)

under grant agreement NO. 290605 (COFUND: PSI-FELLOW). D.M.N. was supported by the Swiss National Science Foundation through the NCCR-MARVEL.

-
- * johan.chang@physik.uzh.ch
- ¹ P. A. Lee, N. Nagaosa, and X.-G. Wen, *Rev. Mod. Phys.* **78**, 17 (2006).
 - ² M. R. Norman, D. Pines, and C. Kallin, *Advances in Physics* **54**, 715 (2005).
 - ³ L. J. P. Ament, M. van Veenendaal, T. P. Devereaux, J. P. Hill, and J. van den Brink, *Rev. Mod. Phys.* **83**, 705 (2011).
 - ⁴ M. L. Tacon, G. Ghiringhelli, J. Chaloupka, M. M. Sala, V. Hinkov, M. W. Haverkort, M. Minola, M. Bakr, K. J. Zhou, S. Blanco-Canosa, C. Monney, Y. T. Song, G. L. Sun, C. T. Lin, G. M. D. Luca, M. Salluzzo, G. Khaliullin, T. Schmitt, L. Braicovich, and B. Keimer, *Nat. Phys.* **7**, 725 (2011).
 - ⁵ M. P. M. Dean, G. Dellea, R. S. Springell, F. Yakhov-Harris, K. Kummer, N. B. Brookes, X. Liu, Y.-J. Sun, J. Strle, T. Schmitt, L. Braicovich, G. Ghiringhelli, I. Božović, and J. P. Hill, *Nat Mater* **12**, 1019 (2013).
 - ⁶ R. Coldea, S. M. Hayden, G. Aeppli, T. G. Perring, C. D. Frost, T. E. Mason, S.-W. Cheong, and Z. Fisk, *Phys. Rev. Lett.* **86**, 5377 (2001).
 - ⁷ N. S. Headings, S. M. Hayden, R. Coldea, and T. G. Perring, *Phys. Rev. Lett.* **105**, 247001 (2010).
 - ⁸ J.-Y. P. Delannoy, M. J. P. Gingras, P. C. W. Holdsworth, and A.-M. S. Tremblay, *Phys. Rev. B* **79**, 235130 (2009).
 - ⁹ B. Dalla Piazza, M. Mourigal, M. Guarise, H. Berger, T. Schmitt, K. J. Zhou, M. Grioni, and H. M. Rønnow, *Phys. Rev. B* **85**, 100508 (2012).
 - ¹⁰ T. Yoshida, X. J. Zhou, K. Tanaka, W. L. Yang, Z. Hus-sain, Z.-X. Shen, A. Fujimori, S. Sahrakorpi, M. Lindroos, R. S. Markiewicz, A. Bansil, S. Komiya, Y. Ando, H. Eisaki, T. Kakeshita, and S. Uchida, *Phys. Rev. B* **74**, 224510 (2006).
 - ¹¹ E. Pavarini, I. Dasgupta, T. Saha-Dasgupta, O. Jepsen, and O. K. Andersen, *Phys. Rev. Lett.* **87**, 047003 (2001).
 - ¹² S. R. White and D. J. Scalapino, *Phys. Rev. B* **60**, R753 (1999).
 - ¹³ T. Maier, M. Jarrell, T. Pruschke, and J. Keller, *Phys. Rev. Lett.* **85**, 1524 (2000).
 - ¹⁴ H. Sakakibara, H. Usui, K. Kuroki, R. Arita, and H. Aoki, *Phys. Rev. Lett.* **105**, 057003 (2010).
 - ¹⁵ J. Chang, M. Shi, S. Pailh  s, M. M  nsson, T. Claesson, O. Tjernberg, A. Bendounan, Y. Sassa, L. Patthey, N. Momono, M. Oda, M. Ido, S. Guerrero, C. Mudry, and J. Mesot, *Phys. Rev. B* **78**, 205103 (2008).
 - ¹⁶ L. Braicovich, J. van den Brink, V. Bisogni, M. M. Sala, L. J. P. Ament, N. B. Brookes, G. M. De Luca, M. Salluzzo, T. Schmitt, V. N. Strocov, and G. Ghiringhelli, *Phys. Rev. Lett.* **104**, 077002 (2010).
 - ¹⁷ G. Ghiringhelli, A. Piazzalunga, C. Dallera, G. Trezzi, L. Braicovich, T. Schmitt, V. N. Strocov, R. Betemps, L. Patthey, X. Wang, and M. Grioni, *Review of Scientific Instruments* **77**, 113108 (2006).
 - ¹⁸ V. N. Strocov, T. Schmitt, U. Flechsig, T. Schmidt, A. Imhof, Q. Chen, J. Raabe, R. Betemps, D. Zimoch, J. Krempasky, X. Wang, M. P. A. Grioni, and L. Patthey, *J. Synchrotron Radiat.* **17**, 631 (2010).
 - ¹⁹ S. Komiya, Y. Ando, X. F. Sun, and A. N. Lavrov, *Phys. Rev. B* **65**, 214535 (2002).
 - ²⁰ J. Chang, N. B. Christensen, C. Niedermayer, K. Lefmann, H. M. R  nnow, D. F. McMorro  , A. Schneidewind, P. Link, A. Hiess, M. Boehm, R. Mottl, S. Pailh  s, N. Momono, M. Oda, M. Ido, and J. Mesot, *Phys. Rev. Lett.* **102**, 177006 (2009).
 - ²¹ A. T. R  mer, J. Chang, N. B. Christensen, B. M. Andersen, K. Lefmann, L. M  hler, J. Gavilano, R. Gilardi, C. Niedermayer, H. M. R  nnow, A. Schneidewind, P. Link, M. Oda, M. Ido, N. Momono, and J. Mesot, *Phys. Rev. B* **87**, 144513 (2013).
 - ²² J. Chang, J. S. White, M. Laver, C. J. Bowell, S. P. Brown, A. T. Holmes, L. Maechler, S. Str  ssle, R. Gilardi, S. Gerber, T. Kurosawa, N. Momono, M. Oda, M. Ido, O. J. Lipscombe, S. M. Hayden, C. D. Dewhurst, R. Vavrin, J. Gavilano, J. Kohlbrecher, E. M. Forgan, and J. Mesot, *Phys. Rev. B* **85**, 134520 (2012).
 - ²³ J. Chang, C. Niedermayer, R. Gilardi, N. B. Christensen, H. M. R  nnow, D. F. McMorro  , M. Ay, J. Stahn, O. Sobolev, A. Hiess, S. Pailh  s, C. Baines, N. Momono, M. Oda, M. Ido, and J. Mesot, *Phys. Rev. B* **78**, 104525 (2008).
 - ²⁴ V. Thampy, M. P. M. Dean, N. B. Christensen, L. Steinke, Z. Islam, M. Oda, M. Ido, N. Momono, S. B. Wilkins, and J. P. Hill, *Phys. Rev. B* **90**, 100510 (2014).
 - ²⁵ T. P. Croft, C. Lester, M. S. Senn, A. Bombardi, and S. M. Hayden, *Phys. Rev. B* **89**, 224513 (2014).
 - ²⁶ C. Monney, T. Schmitt, C. E. Matt, J. Mesot, V. N. Strocov, O. J. Lipscombe, S. M. Hayden, and J. Chang, *Phys. Rev. B* **93**, 075103 (2016).
 - ²⁷ J. Lamsal and W. Montfrooij, *Phys. Rev. B* **93**, 214513 (2016).
 - ²⁸ H. Miao, J. Lorenzana, G. Seibold, Y. Y. Peng, A. Amorese, F. Yakhov-Harris, K. Kummer, N. B. Brookes, R. M. Konik, V. Thampy, G. D. Gu, G. Ghiringhelli, L. Braicovich, and M. P. M. Dean, *arXiv* (2016), 1701.00022.
 - ²⁹ L. Braicovich, L. J. P. Ament, V. Bisogni, F. Forte, C. Aruta, G. Balestrino, N. B. Brookes, G. M. De Luca, P. G. Medaglia, F. M. Granozio, M. Radovic, M. Salluzzo, J. van den Brink, and G. Ghiringhelli, *Phys. Rev. Lett.* **102**, 167401 (2009).
 - ³⁰ M. Guarise, B. D. Piazza, H. Berger, E. Giannini, T. Schmitt, H. M. R  nnow, G. A. Sawatzky, J. van den Brink, D. Altenfeld, I. Eremin, and M. Grioni, *Nat Commun* **5**, 5760 (2014).
 - ³¹ M. P. M. Dean, A. J. A. James, A. C. Walters, V. Bisogni, I. Jarrige, M. H  cker, E. Giannini, M. Fujita, J. Pellicciari, Y. B. Huang, R. M. Konik, T. Schmitt, and J. P. Hill, *Phys. Rev. B* **90**, 220506 (2014).
 - ³² Y. Y. Peng, G. Dellea, M. Minola, M. Conni, A. Amorese, D. Di Castro, G. M. De Luca, K. Kummer, M. Salluzzo, X. Sun, X. J. Zhou, G. Balestrino, M. L. Tacon, B. Keimer, L. Braicovich, N. B. Brookes, and G. Ghiringhelli, *arXiv* (2016), 1609.05405.

- ³³ L. Hozoi, L. Siurakshina, P. Fulde, and J. van den Brink, *Scientific Reports* **1**, 65 EP (2011).
- ³⁴ M. M. Sala, V. Bisogni, C. Aruta, G. Balestrino, H. Berger, N. B. Brookes, G. M. de Luca, D. D. Castro, M. Grioni, M. Guarise, P. G. Medaglia, F. M. Granozio, M. Minola, P. Perna, M. Radovic, M. Salluzzo, T. Schmitt, K. J. Zhou, L. Braicovich, and G. Ghiringhelli, *New Journal of Physics* **13**, 043026 (2011).
- ³⁵ C. J. Jia, E. A. Nowadnick, K. Wohlfeld, Y. F. Kung, C.-C. Chen, S. Johnston, T. Tohyama, B. Moritz, and T. P. Devereaux, *Nature Communications* **5**, 3314 (2014).
- ³⁶ C. G. Fatuzzo, Y. Sassa, M. Månsson, S. Pailhès, O. J. Lipscombe, S. M. Hayden, L. Patthey, M. Shi, M. Grioni, H. M. Rønnow, J. Mesot, O. Tjernberg, and J. Chang, *Phys. Rev. B* **89**, 205104 (2014).
- ³⁷ J. Chang, M. Månsson, S. Pailhès, T. Claesson, O. J. Lipscombe, S. M. Hayden, L. Patthey, O. Tjernberg, and J. Mesot, *Nature Communications* **4**, 2559 (2013).
- ³⁸ M. Platé, J. D. F. Mottershead, I. S. Elfimov, D. C. Peets, R. Liang, D. A. Bonn, W. N. Hardy, S. Chiuazbani, M. Falub, M. Shi, L. Patthey, and A. Damascelli, *Phys. Rev. Lett.* **95**, 077001 (2005).
- ³⁹ D. C. Peets, J. D. F. Mottershead, B. Wu, I. S. Elfimov, R. Liang, W. N. Hardy, D. A. Bonn, M. Raudsepp, N. J. C. Ingle, and A. Damascelli, *New Journal of Physics* **9**, 28 (2007).
- ⁴⁰ H. Sakakibara, H. Usui, K. Kuroki, R. Arita, and H. Aoki, *Phys. Rev. B* **85**, 064501 (2012).
- ⁴¹ S. Wakimoto, K. Ishii, H. Kimura, M. Fujita, G. Dellea, K. Kummer, L. Braicovich, G. Ghiringhelli, L. M. Debeer-Schmitt, and G. E. Granroth, *Phys. Rev. B* **91**, 184513 (2015).
- ⁴² D. Meyers, H. Miao, A. C. Walters, V. Bisogni, R. S. Springell, M. d'Astuto, M. Dantz, J. Pellicciari, H. Huang, J. Okamoto, D. J. Huang, J. P. Hill, X. He, I. Božović, T. Schmitt, and M. P. M. Dean, *arXiv* (2016), 1612.00890.
- ⁴³ J. P. Locquet, J. Perret, J. Fompeyrine, E. Machler, J. W. Seo, and G. Van Tendeloo, *Nature* **394**, 453 (1998).
- ⁴⁴ M. Abrecht, D. Ariosa, D. Cloetta, S. Mitrovic, M. Onellion, X. X. Xi, G. Margaritondo, and D. Pavuna, *Phys. Rev. Lett.* **91**, 057002 (2003).
- ⁴⁵ P. G. Radaelli, D. G. Hinks, A. W. Mitchell, B. A. Hunter, J. L. Wagner, B. Dabrowski, K. G. Vandervoort, H. K. Viswanathan, and J. D. Jorgensen, *Phys. Rev. B* **49**, 4163 (1994).
- ⁴⁶ P. Blaha, K. Schwarz, G. Madsen, D. Kvasnicka, and J. Luitz, Wien2k: An Augmented Plane Wave + Local Orbitals Program for Calculating Crystal Properties (Vienna University of Technology, Vienna, 2001) (2001).
- ⁴⁷ J. P. Perdew, K. Burke, and M. Ernzerhof, *Phys. Rev. Lett.* **77**, 3865 (1996).

VII. APPENDIX A

Here we describe the spin-excitation dispersion of the Heisenberg Hamiltonian derived from the $t - t' - t'' - U$ Hubbard model in two steps. We first consider the simplest model where $t' = t'' = 0$ before including higher order hopping terms.

Generally the dispersion takes the form:

$$\omega(\vec{q}) = Z\sqrt{A(\vec{q})^2 - B(\vec{q})^2}$$

where Z is a renormalization factor and $\vec{q} = (h, k)$. When the Hubbard model contains only the nearest-neighbor hopping integral t , we expand $A(\vec{q})$ and $B(\vec{q})$ to second order in t :

$$A(\vec{q}) = A_0 + A_1 + \dots \quad \& \quad B(\vec{q}) = B_0 + B_1 + \dots \quad (2)$$

To express A_i and B_i , we define: $J_1 = \frac{4t^2}{U}$ and $J_2 = \frac{4t^4}{U^3}$. Moreover we set:

$$P_j(h, k) = \cos jha + \cos jka \quad (3)$$

$$X_j(h, k) = \cos jha \cdot \cos jka \quad (4)$$

$$X_{3a}(h, k) = \cos 3ha \cdot \cos ka + \cos ha \cdot \cos 3ka, \quad (5)$$

where $j = 1, 2, 3$, or 4. With this notation we have:

$$A_0 = 2J_1 \quad \& \quad B_0 = -J_1P_1 \quad (6)$$

and

$$A_1 = J_2(-26 - 8X_1 + P_2) \quad \& \quad B_1 = 16J_2P_1 \quad (7)$$

When the zone boundary dispersion is defined by $E_{ZB} = \omega(1/2, 0) - \omega(1/4, 1/4)$, one finds $E_{ZB} = 12ZJ_2$. Therefore, a zone boundary dispersion is only found when second order terms J_2 are included. Notice also that since $P_1(1/2, 0) = P_1(1/4, 1/4) = 0$, the B -terms are not contributing to the zone boundary dispersion.

Now let us include second-nearest- t' and third-nearest-neighbor t'' hopping integrals. This involves several additional contributions to $A(\vec{q})$ and $B(\vec{q})$:

$$A(\vec{q}) = A_0 + A_1 + A'_0 + A''_0 + A'_c + A'_1 + A''_c + A''_1 \quad (8)$$

$$B(\vec{q}) = B_0 + B_1 + B'_c. \quad (9)$$

To express these new terms, we introduce the following notation $J'_1 = \frac{4t'^2}{U}$, $J'_2 = \frac{4t'^4}{U^3}$, $J''_1 = \frac{4t''^2}{U}$ and $J''_2 = \frac{4t''^4}{U^3}$. Geometrically the following contributions correspond to different hopping path combinations including the cyclic ones.

$$A'_0 = 2J'_1(X_1 - 1) \quad \& \quad A''_0 = J''_1(P_2 - 2) \quad (10)$$

$$A'_c = -\frac{8J_1}{U^2}(-t'^2 + 4t't'' - 2t''^2)(P_2 - 2) \quad (11)$$

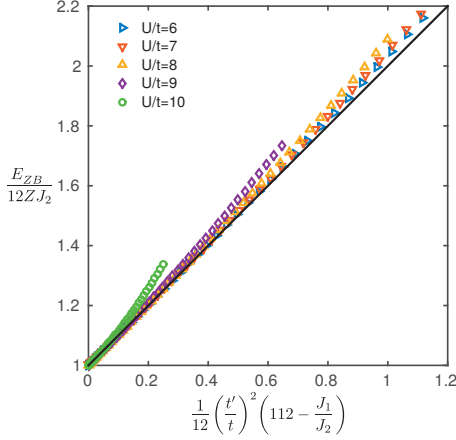


FIG. 5. (Color online) Zone boundary dispersion E_{ZB} normalized to $12ZJ_2$ and plotted versus $\frac{1}{12}(112 - J_1/J_2)(t'/t)^2$. Data points are exact numerical solutions of the Hubbard model for values several of U/t (as indicated) and $t'' = -t'/2$. The solid line is the approximated analytical solution for $U/t = 8$.

$$B'_c = -\frac{4J_1}{U^2} [(6t'^2 - 4t't'')(X_1 - 1) + 3t''^2(P_2 - 2)] P_1 \quad (12)$$

$$A'_1 = 2J'_2(X_2 + 4X_1 - 2P_2 - 1) \quad (13)$$

$$A''_c = \frac{2J'_1J''_1}{U} (-3X_2 + 2X_1 + 5P_2 - X_{3a} - 7) \quad (14)$$

$$A''_1 = J''_2(P_4 - 8X_2 + 4P_2 - 2) \quad (15)$$

As B'_c scales with P_1 , it is again found that $B(\bar{q})$ does not contribute to the zone boundary dispersion. In Fig. 5, we show the numerical evaluation of E_{ZB} for realistic

$\text{La}_{2-x}\text{Sr}_x\text{CuO}_4$	U (eV)	U/t	t'/t	t''/t	Z	Ref.
$x = 0$	2.2	7.4	0	0	1.18	6 and 7
$x = 0$	3.6	8.3	-0.313	0.167	1.219	8
$x = 0$	3.9	9.1	-0.308	0.154	1.219	*
$x = 0.12$	2.8	6.5	-0.389	0.195	1.219	*
Bi2201						
$x = 0$	3.4	8.0	-0.352	0.176	1.219	*

TABLE I. Parametrization – using the Hubbard model – of the spin-excitation dispersion of LCO^{6,7}, LSCO $x = 0.12$ (this work) and Bi2201³². (*) Values obtained from the fit using the same procedure as described in this Appendix, which thus can be directly compared.

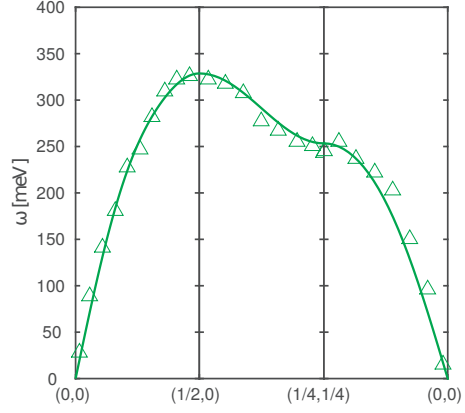


FIG. 6. Spin excitation spectrum of Bi2201 from Ref. 32. The solid line is a fit to the $t - t' - t'' - U$ Hubbard model.

values of U/t , t'/t and with $t'' = -t'/2$. When neglecting terms scaling with J'_2 , J''_2 and $J'_1J''_1$, only Eq. 10 and 11 contribute. Using $P_2(1/2, 0) = 2$, $P_2(1/4, 1/4) = -2$, $X_1(1/2, 0) = -1$ and $X_1(1/4, 1/4) = 0$, we find:

$$\frac{E_{ZB}}{12ZJ_2} \approx 1 + \frac{1}{12} \left(112 - \frac{J_1}{J_2}\right) \left(\frac{t'}{t}\right)^2. \quad (16)$$

This approximation is valid as long as:

$$\frac{U}{t} \geq \sqrt{\frac{28 + 112 \left(\frac{t'}{t}\right)^2}{2 + 3 \left(\frac{t'}{t}\right)^2}}, \quad \text{and} \quad \left|\frac{t'}{t}\right| \lesssim 0.686. \quad (17)$$

As shown in Fig. 5, this analytical expression is a good approximation to the full numerical calculation. Thus it is justified to neglect terms scaling with J'_2 , J''_2 and $J'_1J''_1$ for a realistic cuprate values of U/t and t'/t .

VIII. APPENDIX B

Now, having derived the spin-excitation dispersion within the $t - t' - t'' - U$ Hubbard model, it is possible to fit the experimentally observed dispersion. A final comment goes to the prefactor Z . It is found that, including higher order hopping integrals t' and t'' , Z has a slowly varying momentum dependence. To simplify our analysis we used the mean value obtained⁸ in the first Brillouin zone for the half filled compound La_2CuO_4 . We thus have $Z = 1.219$ constant. From ARPES^{36,37} experiments and LDA calculations¹¹ we have that $t = 0.43$ eV and $t'' = -t'/2$. Our fitting parameters are thus U and t' . In this fashion we obtain a good description of the spin-excitation dispersion of LCO and LSCO $x = 0.12$ (see Fig. 2 in the main text). The obtained values are given in Table I. In Fig. 6 and Table I, we display in

addition our fit and associated fit parameters from the spin-excitation spectrum measured on Bi2201 (Ref. 32). With these values of U and t' , the relation – shown in Fig. 4 – between E_{ZB} and t' is established.

IX. APPENDIX C

To guide our intuition of how the d_{z^2} states evolve as a function of doping, we have carried out DFT calculations of the LSCO band structure as a function of doping. These calculations were performed using the WIEN2K package⁴⁶ in the LTO crystal structure. The doping dependence of the electronic structure for LSCO was approximated by a rigid band shift of all Cu d orbitals in order to obtain the correct d -shell filling. For every calculated doping value, the experimentally derived crystal structure has been used⁴⁵. In the calculation, the Kohn-Sham equation is solved self-consistently by using a full-potential linear augmented plane wave (LAPW) method on a uniform grid of $12 \times 12 \times 12$ k -points in the

Brillouin zone. The exchange-correlation term is treated within the generalized gradient approximation (GGA) in the parametrization of Perdew, Burke and Enzerhof (PBE)⁴⁷. The planewave cutoff condition was set to $RK_{max} = 7$ where R is the radius of the smallest LAPW sphere (*i.e.* 1.63 bohr) and K_{max} denotes the planewave cutoff. Fig. 7 shows the orbital and atomic resolved band structure and density of states (DOS) of LSCO in the tetragonal crystal structure. As shown in panel (a), the d_{z^2} derived band disperses in a binding energy range of $E - E_F = -1.3$ eV close to Γ and $E - E_F = -0.3$ eV at M . The orbital resolved DOS of the d_{z^2} band has a peak at $E - E_F = -0.5$ eV, while closer to E_F the d_{z^2} -DOS is rapidly decaying. This peak originates from the flat shape of the d_{z^2} band close to M . Therefore to track the doping dependence of the d_{z^2} energy level, the position of the band at the M point is plotted as a function of doping x in Fig. 7(c). With increasing doping x the d_{z^2} energy level approaches the Fermi energy. Note that our DFT calculation agrees with recently published results obtained by *ab initio* calculations¹⁴.

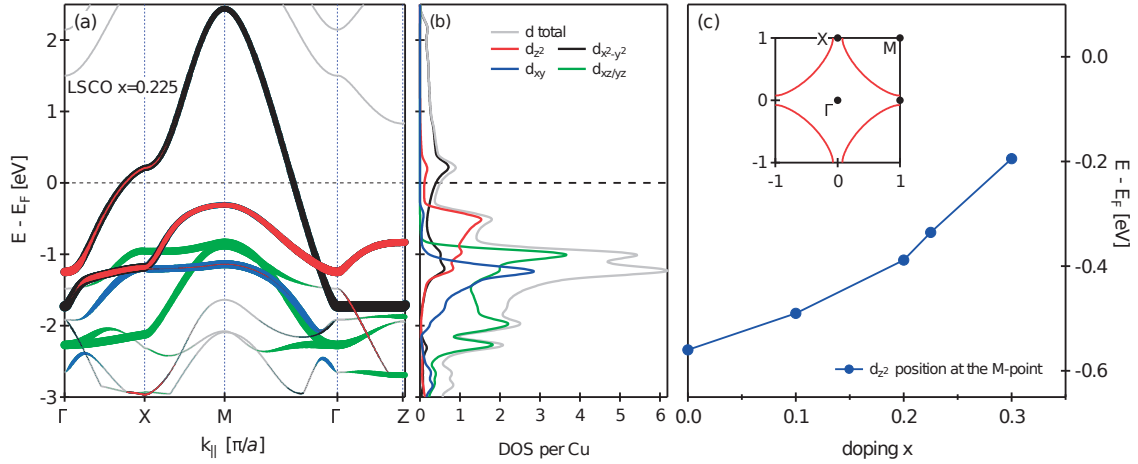


FIG. 7. (Color online) Density functional theory calculations of $\text{La}_{2-x}\text{Sr}_x\text{CuO}_4$. (a) calculated bandstructure along high symmetry directions (see inset of panel(c)) in the tetragonal crystal structure for $x = 0.225$ (Ref. 45). (b) density of states derived by the different Cu $3d$ orbitals. The electronic structure has been shifted such that the overall $3d$ -shell filling reflects the doping x . (c) doping dependence of the d_{z^2} band derived at the M point.

Acknowledgements

‘There’s a lot of things you need
to get across this universe.
Warp drive... wormhole refractors...

You know the thing you need most of all?
You need a hand to hold.’

— Matthew Graham
Doctor Who Season 6, Episode 6

These four years as a PhD student under the supervision of Prof. Johan J. Chang and Prof. Henrik M. Rønnow have been an amazing learning opportunity, so that I wish to express all my gratitude for the guidance and the encouragements that neither has ever spared. They both have been extremely supportive throughout my doctorate. The work environment that they gave me the possibility to experience, at EPFL as well as UZH, has been stimulating and enriching under the professional as well as the personal point of view. For this, I am grateful to all the members of the group, starting from Paul, Bastien and Julian, who have accompanied my first years in Lausanne and feel like they never really left the lab. At the same time, Elahi, Ivica and Minki, who only joined at a later time, feel like they were there all along the way. Which brings me to Peter and Ivan, who were actually there when I arrived and are still present in my life now, that I am leaving. I also wish to thank Alex, Ping, Lyn, Kruno and the most recent acquisitions of the lab, Namrata, Virgile, Tarek and Luc. Thank you for the discussions, the rehearsals, the consultations, the proofreading as well as the house warmings, the *I never, jungle speed*, Eze, Gratallops, movie nights and music explorations. A special thank goes to Caroline and Carmelina, who have always been movingly warm and helpful.

Acknowledgements

A big part of the research performed during my PhD has taken place within Synchrotrons. All experiments were made possible by the collective efforts of all collaborators, starting from the sample growers all the way to the beamline scientists. In these occasions, the help and support of Christian, Yasmine, Martin, Johnny, Stefan, Marcus, Valentina, Oleh, Denys, Simon and Mauro have been particularly precious. While the contribution of Sara F. extends far beyond the professional sphere, I will always cherish the memories of the night shifts, the travels and the conferences we shared.

Beyond the immediate research groups of LQM and LQMR, a special mention goes to Prof. Antonio Vecchione and Dr. Rosalba Fittipaldi, who have provided high quality single crystals of Sr_2RuO_4 and Ca_2RuO_4 and graciously hosted me in multiple occasions. The scientific exchanges have always been extremely useful and I always felt welcome in my visits to Fisciano, also thanks to Veronica and Fiona. Furthermore, Prof. Marco Grioni, Prof. Thorsten Schmitt and Prof. Hugo Dil have all provided precious insights on the theoretical and the experimental aspects of ARPES, RIXS and spin-resolved ARPES. It was a pleasure to collaborate with Fabio, Gianmarco, Luca and Silvan, and I thank Alberto and Edoardo for the discussions on ultrafast physics, as well as the pleasant exchanges during conferences or here in Lausanne. Many other people have contributed to my pleasant stay in EPFL and Lausanne, among which Pau, Cédric, Albano, Πγκα, Zlatco, Romana, Neda, Endre and Arnaud.

I take this opportunity also to thank the president and members of my jury, Prof. Vincenzo Savona, Prof. László Forró, Prof. Claude Monney and Dr. Mario Cuoco, for the valuable discussion and feedback who greatly improved this manuscript.

Ursula, Darja, Vinka and Brit, together with Fernando, Gloria, Diana, Annabela and Andrea P. have all played a major role in the enjoyment and exploration of Lausanne and Switzerland. The friendship and hospitality of Rita, Giovanni, Sara S., Francesco D.A. and Francesco M. have often sustained me in difficult times, as they all have welcomed me in their houses and offered all kinds of help and support, even when not solicited. I am very grateful for the generosity of Francisco, Joël and Yomey, who have introduced me to tango, which considerably helped me survive the writing process. I thank also Katia, Daniel, Yakatia and Amin for the fun times learning and dancing. The months of isolation in the glass cage of the Rolex Learning Center have been bearable only inasmuch as they were shared with Jagoda, whose friendship has exceeded all expectations.

I also want to thank those who have been supporting me from a distance, Nic, Anna, Tyler, Stephane, Leha, Stephen, Sasha, Vincenzo, Júlia, Solmaz, Leandro, Rob and Kelly, as well as Hugo, Alex, Laurent, Jérôme, Anna, Pietro, Laura and many others. It is a blessing to meet, after months or years, and be able to pick it up from exactly where we left off. A similar miracle I experience with Alice, Giorgia, Tiziana, Lucia, Mariachiara, Peppe Dema, Andrea L.R., Carlo and Elisa. Even though we live scattered across Europe, it is amazing how we can depend on each other in the time of need.

Claire, Françoise and Raymond have embraced me in their family and always made me feel

at home, together with Olivier, Karin and the rest of Yannick's family. There was still a lot I could have learned from Yannick, nevertheless he has made me a better person, and a better scientist. I miss you everyday, thank you for every shared moment, I regard each and every one of them as precious gifts.

I owe a great deal to all of my family, who has been always supportive and encouraging. Each member has taught me and contributed in shaping me as the person I am today. I never considered traveling an obstacle, as my father, Fabio, has fostered in me the habit of exploring the world, since I was a small kid. He has provided me with countless opportunities of growth and education, and has always been there for me. My "little" sister, Daniela, knows all my "little" neurosis, and has often endured their outcome - not always pleasant, but never boring! I hold dear the most trivial moments spent together, when we wasted time on each other. I am grateful to all my cousins, the wiser ones and the younger ones, and my aunts and uncles. Alessandra Rachele Adele, Alessandra L.M., Federica, Gaetano, Giuliana, Giuseppina, Mariacarmela, Maria Cristina, Martina, Nicoletta, Nicolò, Roberta, Umberto and Valentina have all taken turns into being mentors, role models, board game buddies, and companions in activities as simple and as rewarding as a stroll to the (Sicilian) beach. Annamaria, Antonella, Filippo, Giovanni, Graziella, Loredana, Maria Teresa, Nicoletta, Nello, Nuccia, Pierluigi, Sergio and Rino have always welcomed me and my sister with open arms, when we were stubborn demanding kids (especially me) and now that we are stubborn assertive women (especially me). They have proved to me over and over again the meaning of family and shelter. No matter how far and for how long I am gone, when I am back it is like I never left. I thank also Giusy, Rachele, Cristina, Dario, Manuela and Miriam, honorary family members, with whom I have shared trips and holidays, inside jokes, meals and celebrations. Your contagious smiles are sprinkled all over my recollection! I would also like to welcome the perspective new members of this big messy noisy (and a bit nosy) warm family, Giovanni, Daniela, Serena and all those who will join us in the future.

I learned how affection is expressed in small gestures from my grandaunt Giovanna. Stefania had a great eye for details and style, and left us way too early. I am grateful for the time spent with them, and my grandaunts Angela and Rosa and uncle Alfio. My mother and my grandmother have been splendid models of strong and caring women, such that I can only wish to be able to live up to their examples.

Lausanne, 20 July 2017

C. G. E.

Bibliography

- [1] S. Maekawa, T. Tohyama, S. E. Barnes, S. Ishihara, W. Koshibae, and G. Khaliullin, *Physics of Transition Metal Oxides*. Springer Berlin Heidelberg, 2004.
- [2] N. F. Mott, “The basis of the electron theory of metals, with special reference to the transition metals,” *Proceedings of the Physical Society. Section A*, vol. 62, no. 7, p. 416, 1949.
- [3] J. Hubbard, “Electron correlations in narrow energy bands,” *Proceedings of the Royal Society of London A: Mathematical, Physical and Engineering Sciences*, vol. 276, no. 1365, pp. 238–257, 1963.
- [4] J. Zaanen, G. A. Sawatzky, and J. W. Allen, “Band gaps and electronic structure of transition-metal compounds,” *Physical Review Letters*, vol. 55, pp. 418–421, Jul 1985.
- [5] J. Orenstein and A. J. Millis, “Advances in the physics of high-temperature superconductivity,” *Science*, vol. 288, no. 5465, pp. 468–474, 2000.
- [6] Y. Tokura and N. Nagaosa, “Orbital physics in transition-metal oxides,” *Science*, vol. 288, no. 5465, pp. 462–468, 2000.
- [7] R. J. Birgeneau and M. A. Kastner, “Frontier physics with correlated electrons,” *Science*, vol. 288, no. 5465, pp. 437–437, 2000.
- [8] T. M. Rice and M. Sigrist, “ Sr_2RuO_4 : an electronic analogue of ^3He ?,” *Journal of Physics: Condensed Matter*, vol. 7, pp. L643–L648, Nov 1995.
- [9] E. Gorelov, M. Karolak, T. O. Wehling, F. Lechermann, A. I. Lichtenstein, and E. Pavarini, “Nature of the mott transition in Ca_2RuO_4 ,” *Physical Review Letters*, vol. 104, p. 226401, Jun 2010.
- [10] A. Liebsch and H. Ishida, “Subband Filling and Mott Transition in $\text{Ca}_{2-x}\text{Sr}_x\text{RuO}_4$,” *Phys. Rev. Lett.*, vol. 98, p. 216403, May 2007.
- [11] V. Anisimov, I. Nekrasov, D. Kondakov, T. Rice, and M. Sigrist, “Orbital-selective Mott-insulator transition in $\text{Ca}_{2-x}\text{Sr}_x\text{RuO}_4$,” *The European Physical Journal B - Condensed Matter and Complex Systems*, vol. 25, no. 2, pp. 191–201, 2002.

Bibliography

- [12] A. Koga, N. Kawakami, T. M. Rice, and M. Sigrist, "Orbital-selective mott transitions in the degenerate hubbard model," *Phys. Rev. Lett.*, vol. 92, p. 216402, May 2004.
- [13] Y. K. Kim, O. Krupin, J. D. Denlinger, A. Bostwick, E. Rotenberg, Q. Zhao, J. F. Mitchell, J. W. Allen, and B. J. Kim, "Fermi arcs in a doped pseudospin-1/2 Heisenberg antiferromagnet," *Science*, vol. 345, no. 6193, pp. 187–190, 2014.
- [14] E. H. da Silva Neto, P. Aynajian, A. Frano, R. Comin, E. Schierle, E. Weschke, A. Gyenis, J. Wen, J. Schneeloch, Z. Xu, S. Ono, G. Gu, M. Le Tacon, and A. Yazdani, "Ubiquitous interplay between charge ordering and high-temperature superconductivity in cuprates," *Science*, vol. 343, no. 6169, pp. 393–396, 2014.
- [15] R. Comin, A. Frano, M. M. Yee, Y. Yoshida, H. Eisaki, E. Schierle, E. Weschke, R. Sutarto, F. He, A. Soumyanarayanan, Y. He, M. Le Tacon, I. S. Elfimov, J. E. Hoffman, G. A. Sawatzky, B. Keimer, and A. Damascelli, "Charge Order Driven by Fermi-Arc Instability in $\text{Bi}_2\text{Sr}_{2-x}\text{La}_x\text{CuO}_{6+\delta}$," *Science*, vol. 343, no. 6169, pp. 390–392, 2014.
- [16] G. Ghiringhelli, M. Le Tacon, M. Minola, S. Blanco-Canosa, C. Mazzoli, N. B. Brookes, G. M. De Luca, A. Frano, D. G. Hawthorn, F. He, T. Loew, M. M. Sala, D. C. Peets, M. Saluzzo, E. Schierle, R. Sutarto, G. A. Sawatzky, E. Weschke, B. Keimer, and L. Braicovich, "Long-Range Incommensurate Charge Fluctuations in $(\text{Y,Nd})\text{Ba}_2\text{Cu}_3\text{O}_{6+x}$," *Science*, vol. 337, no. 6096, pp. 821–825, 2012.
- [17] J. Chang, E. Blackburn, A. T. Holmes, N. B. Christensen, J. Larsen, J. Mesot, R. Liang, D. A. Bonn, W. N. Hardy, A. Watenphul, M. v. Zimmermann, E. M. Forgan, and S. M. Hayden, "Direct observation of competition between superconductivity and charge density wave order in $\text{YBa}_2\text{Cu}_3\text{O}_{6.67}$," *Nature Physics*, vol. 8, pp. 871–876, 2012.
- [18] M. Hücker, M. v. Zimmermann, Z. J. Xu, J. S. Wen, G. D. Gu, and J. M. Tranquada, "Enhanced charge stripe order of superconducting $\text{La}_{2-x}\text{Ba}_x\text{CuO}_4$ in a magnetic field," *Physical Review B*, vol. 87, p. 014501, Jan 2013.
- [19] G. Beamson, D. Briggs, S. F. Davies, I. W. Fletcher, D. T. Clark, J. Howard, U. Gelius, B. Wannberg, and P. Balzer, "Performance and application of the scienta esca300 spectrometer," *Surface and Interface Analysis*, vol. 15, no. 9, pp. 541–549, 1990.
- [20] N. Mårtensson, P. Baltzer, P. Brühwiler, J.-O. Forsell, A. Nilsson, A. Stenborg, and B. Wannberg, "A very high resolution electron spectrometer," *Journal of Electron Spectroscopy and Related Phenomena*, vol. 70, no. 2, pp. 117 – 128, 1994.
- [21] G. Ghiringhelli, A. Piazzalunga, C. Dallera, G. Trezzi, L. Braicovich, T. Schmitt, V. N. Strocov, R. Betemps, L. Patthey, X. Wang, and M. Grioni, "Saxes, a high resolution spectrometer for resonant x-ray emission in the 400-1600ev energy range," *Review of Scientific Instruments*, vol. 77, no. 11, p. 113108, 2006.
- [22] A. Damascelli, Z. Hussain, and Z.-X. Shen, "Angle-resolved photoemission studies of the cuprate superconductors," *Reviews of Modern Physics*, vol. 75, pp. 473–541, Apr 2003.

-
- [23] S. Hüfner, *Photoelectron Spectroscopy: Principles and Applications*. Springer Science & Business Media, 1996.
- [24] S. Kevan, *Angle-Resolved Photoemission, Theory and Current Applications*. Elsevier Science, 1992.
- [25] L. J. P. Ament, M. van Veenendaal, T. P. Devereaux, J. P. Hill, and J. van den Brink, “Resonant inelastic x-ray scattering studies of elementary excitations,” *Reviews of Modern Physics*, vol. 83, pp. 705–767, Jun 2011.
- [26] A. Kotani and S. Shin, “Resonant inelastic x-ray scattering spectra for electrons in solids,” *Reviews of Modern Physics*, vol. 73, pp. 203–246, Feb 2001.
- [27] W. Schülke, *Electron dynamics by inelastic X-ray scattering*. Series: Oxford series on synchrotron radiation ; 7, Oxford : Oxford University Press, 2007.
- [28] E.-E. Koch, G. V. Marr, G. Brown, D. Moncton, S. Ebashi, M. Koch, and E. Rubenstein, *Handbook on synchrotron radiation*. Elsevier Science, Amsterdam, 1991.
- [29] H. Hertz, “Ueber einen einfluss des ultravioletten lichtes auf die electrische entladung,” *Annalen der Physik*, vol. 267, no. 8, pp. 983–1000, 1887.
- [30] A. Einstein, “Über einen die Erzeugung und Verwandlung des Lichtes betreffenden heuristischen Gesichtspunkt,” *Annual Annalen der Physik*, vol. 17, pp. 132–148, 1905.
- [31] C. E. Matt, *Electron correlation in copper and iron-based high temperature superconductors - An angle-resolved photoemission spectroscopy perspective*. PhD thesis, ETH ZURICH, 2016.
- [32] J. Wen, Q. Jie, Q. Li, M. Hücker, M. v. Zimmermann, S. J. Han, Z. Xu, D. K. Singh, R. M. Konik, L. Zhang, G. Gu, and J. M. Tranquada, “Uniaxial linear resistivity of superconducting $\text{La}_{1.905}\text{Ba}_{0.095}\text{CuO}_4$ induced by an external magnetic field,” *Physical Review B*, vol. 85, p. 134513, Apr 2012.
- [33] M. P. Seah and W. A. Dench, “Quantitative electron spectroscopy of surfaces: A standard data base for electron inelastic mean free paths in solids,” *Surface and Interface Analysis*, vol. 1, no. 1, pp. 2–11, 1979.
- [34] U. Flechsig, L. Patthey, and T. Schmidt, “Performance measurements at the sls spectroscopy beamline,” *AIP Conference Proceedings*, vol. 705, p. 316, 2004.
- [35] M. Månsson, T. Claesson, U. O. Karlsson, O. Tjernberg, S. Pailh  s, J. Chang, J. Mesot, M. Shi, L. Patthey, N. Momono, M. Oda, and M. Ido, “On-board sample cleaver,” *Review of Scientific Instruments*, vol. 78, no. 7, pp. –, 2007.
- [36] V. Bisogni, *Local and collective excitations in cuprates investigated by high resolution Resonant Inelastic X-ray Scattering*. PhD thesis, Politecnico di Milano, 2010.

Bibliography

- [37] F. de Groot, "High-resolution x-ray emission and x-ray absorption spectroscopy," *Chemical Reviews*, vol. 101, no. 6, pp. 1779–1808, 2001. PMID: 11709999.
- [38] F. de Groot and A. Kotani, *Core Level Spectroscopy of Solids*. Advances in Condensed Matter Science, Volume 6, Boca Raton, FL : CRC Presst, 2008.
- [39] C. S. Schnohr and M. C. Ridgway, *Introduction to X-Ray Absorption Spectroscopy*. Berlin, Heidelberg: Springer Berlin Heidelberg, 2015.
- [40] F. de Groot, "Multiplet effects in x-ray spectroscopy," *Coordination Chemistry Reviews*, vol. 249, no. 1 - 2, pp. 31 – 63, 2005. Synchrotron Radiation in Inorganic and Bioinorganic Chemistry.
- [41] N. Wolchover, "The phase diagram of hole-doped cuprates," *Quanta Magazine*, 2016.
- [42] R. Comin and A. Damascelli, "Resonant x-ray scattering studies of charge order in cuprates," *Annual Review of Condensed Matter Physics*, vol. 7, no. 1, pp. 369–405, 2016.
- [43] S. E. Sebastian and C. Proust, "Quantum oscillations in hole-doped cuprates," *Annual Review of Condensed Matter Physics*, vol. 6, no. 1, pp. 411–430, 2015.
- [44] R. J. Birgeneau, C. Stock, J. M. Tranquada, and K. Yamada, "Magnetic neutron scattering in hole-doped cuprate superconductors," *Journal of the Physical Society of Japan*, vol. 75, no. 11, p. 111003, 2006.
- [45] C. Kittel, *Introduction to solid state physics*. Wiley, 1971.
- [46] B. Sapoval and C. Hermann, *Physique des semi-conducteurs*. Ellipses, 1988.
- [47] P. M. C. Rourke, A. F. Bangura, T. M. Benseman, M. Matusiak, J. R. Cooper, A. Carrington, and N. E. Hussey, "A detailed de Haas-van Alphen effect study of the overdoped cuprate $\text{Ti}_2\text{Ba}_2\text{CuO}_{6+\delta}$," *New Journal of Physics*, vol. 12, no. 10, p. 105009, 2010.
- [48] C. G. Fatuzzo, Y. Sassa, M. Månsson, S. Pailhès, O. J. Lipscombe, S. M. Hayden, L. Patthey, M. Shi, M. Grioni, H. M. Rønnow, J. Mesot, O. Tjernberg, and J. Chang, "Nodal Landau Fermi-liquid quasiparticles in overdoped $\text{La}_{1.77}\text{Sr}_{0.23}\text{CuO}_4$," *Physical Review B*, vol. 89, p. 205104, May 2014.
- [49] A. C. Jacko, J. O. Fjaerestad, and B. J. Powell, "A unified explanation of the kadowaki-woods ratio in strongly correlated metals," *Nature Physics*, vol. 5, pp. 422 – 425, 2009.
- [50] J. Mravlje, M. Aichhorn, T. Miyake, K. Haule, G. Kotliar, and A. Georges, "Coherence-Incoherence Crossover and the Mass-Renormalization Puzzles in Sr_2RuO_4 ," *Physical Review Letters*, vol. 106, p. 096401, Mar 2011.
- [51] X. Deng, J. Mravlje, R. Žitko, M. Ferrero, G. Kotliar, and A. Georges, "How bad metals turn good: Spectroscopic signatures of resilient quasiparticles," *Physical Review Letters*, vol. 110, p. 086401, Feb 2013.

- [52] A. A. Kordyuk, S. V. Borisenko, A. Koitzsch, J. Fink, M. Knupfer, and H. Berger, “Bare electron dispersion from experiment: Self-consistent self-energy analysis of photoemission data,” *Physical Review B*, vol. 71, p. 214513, Jun 2005.
- [53] J. Chang, M. Månsson, S. Pailh  s, T. Claesson, O. J. Lipscombe, S. M. Hayden, L. Patthey, O. Tjernberg, and J. Mesot, “Anisotropic breakdown of Fermi liquid quasiparticle excitations in overdoped $\text{La}_{2-x}\text{Sr}_x\text{CuO}_4$,” *Nature Communications*, vol. 4, pp. –, Oct. 2013.
- [54] G.-H. Gweon, B. S. Shastry, and G. D. Gu, “Extremely correlated fermi-liquid description of normal-state arpes in cuprates,” *Physical Review Letters*, vol. 107, p. 056404, Jul 2011.
- [55] X. J. Zhou, T. Yoshida, A. Lanzara, P. V. Bogdanov, S. A. Kellar, K. M. Shen, W. L. Yang, F. Ronning, T. Sasagawa, T. Kakeshita, T. Noda, H. Eisaki, S. Uchida, C. T. Lin, F. Zhou, J. W. Xiong, W. X. Ti, Z. X. Zhao, A. Fujimori, Z. Hussain, and Z.-X. Shen, “High-temperature superconductors: Universal nodal fermi velocity,” *Nature*, vol. 423, p. 398, 2003.
- [56] T. Yoshida, X. J. Zhou, D. H. Lu, S. Komiya, Y. Ando, H. Eisaki, T. Kakeshita, S. Uchida, Z. Hussain, Z.-X. Shen, and A. Fujimori, “Low-energy electronic structure of the high- T_c cuprates $\text{La}_{2-x}\text{Sr}_x\text{CuO}_4$ studied by angle-resolved photoemission spectroscopy,” *Journal of Physics: Condensed Matter*, vol. 19, no. 12, p. 125209, 2007.
- [57] J. Chang, C. Niedermayer, R. Gilardi, N. B. Christensen, H. M. R  nnow, D. F. McMorro  , M. Ay, J. Stahn, O. Sobolev, A. Hiess, S. Pailhes, C. Baines, N. Momono, M. Oda, M. Ido, and J. Mesot, “Tuning competing orders in $\text{La}_{2-x}\text{Sr}_x\text{CuO}_4$ cuprate superconductors by the application of an external magnetic field,” *Physical Review B*, vol. 78, p. 104525, Sep 2008.
- [58] E. Abrahams and C. M. Varma, “What angle-resolved photoemission experiments tell about the microscopic theory for high-temperature superconductors,” *PNAS*, vol. 97, pp. 5714–5716, 2000.
- [59] A. Mourachkine, *Room-temperature Superconductivity*. Cambridge International Science Publishing Ltd., 2004.
- [60] C. Varma, Z. Nussinov, and W. van Saarloos, “Singular or non-fermi liquids,” *Physics Reports*, vol. 361, no. 5-6, pp. 267 – 417, 2002.
- [61] E. Pavarini, I. Dasgupta, T. Saha-Dasgupta, O. Jepsen, and O. K. Andersen, “Band-structure trend in hole-doped cuprates and correlation with t_{cmax} ,” *Physical Review Letters*, vol. 87, p. 047003, Jul 2001.
- [62] A. Lanzara, P. V. Bogdanov, X. J. Zhou, S. A. Kellar, D. L. Feng, E. D. Lu, T. Yoshida, H. Eisaki, A. Fujimori, K. Kishio, J. I. Shimoyama, S. U. T. Noda, Z. Hussain, and Z. X. Shen, “Evidence for ubiquitous electron-phonon coupling in high temperature superconductors.,” *Nature*, vol. 412, p. 510, 2001.

Bibliography

- [63] J. D. Rameau, H.-B. Yang, G. D. Gu, and P. D. Johnson, “Coupling of low-energy electrons in the optimally doped $\text{Bi}_2\text{Sr}_2\text{CaCu}_2\text{O}_{8+\delta}$ superconductor to an optical phonon mode,” *Physical Review B*, vol. 80, p. 184513, Nov 2009.
- [64] N. C. Plumb, T. J. Reber, J. D. Koralek, Z. Sun, J. F. Douglas, Y. Aiura, K. Oka, H. Eisaki, and D. S. Dessau, “Low-Energy (< 10 meV) Feature in the Nodal Electron Self-Energy and Strong Temperature Dependence of the Fermi Velocity in $\text{Bi}_2\text{Sr}_2\text{CaCu}_2\text{O}_{8+\delta}$,” *Physical Review Letters*, vol. 105, p. 046402, Jul 2010.
- [65] I. M. Vishik, W. S. Lee, F. Schmitt, B. Moritz, T. Sasagawa, S. Uchida, K. Fujita, S. Ishida, C. Zhang, T. P. Devereaux, and Z. X. Shen, “Doping-Dependent Nodal Fermi Velocity of the High-Temperature Superconductor $\text{Bi}_2\text{Sr}_2\text{CaCu}_2\text{O}_{8+\delta}$ Revealed Using High-Resolution Angle-Resolved Photoemission Spectroscopy,” *Physical Review Letters*, vol. 104, p. 207002, May 2010.
- [66] T. Valla, A. V. Fedorov, J. Lee, J. C. Davis, and G. D. Gu, “The ground state of the pseudogap in cuprate superconductors,” *Science*, vol. 314, no. 5807, pp. 1914–1916, 2006.
- [67] C. E. Matt, C. G. Fatuzzo, Y. Sassa, M. Månsson, S. Fatale, V. Bitetta, X. Shi, S. Pailhès, M. H. Berntsen, T. Kurosawa, M. Oda, N. Momono, O. J. Lipscombe, S. M. Hayden, J.-Q. Yan, J.-S. Zhou, J. B. Goodenough, S. Pyon, T. Takayama, H. Takagi, L. Patthey, A. Bendounan, E. Razzoli, M. Shi, N. C. Plumb, M. Radovic, M. Grioni, J. Mesot, O. Tjernberg, and J. Chang, “Electron scattering, charge order, and pseudogap physics in $\text{La}_{1.6-x}\text{Nd}_{0.4}\text{Sr}_x\text{CuO}_4$: An angle-resolved photoemission spectroscopy study,” *Physical Review B*, vol. 92, p. 134524, Oct 2015.
- [68] T. Wu, H. Mayaffre, S. Krämer, M. Horvatic, C. Berthier, W. N. Hardy, R. Liang, D. A. Bonn, and M.-H. Julien, “Magnetic-field-induced charge-stripe order in the high-temperature superconductor $\text{YBa}_2\text{Cu}_3\text{O}_y$,” *Nature*, vol. 477, p. 191, 2011.
- [69] J. G. Bednorz and K. A. Müller, “Perovskite-type oxides—The new approach to high- T_c superconductivity,” *Reviews of Modern Physics*, vol. 60, pp. 585–600, Jul 1988.
- [70] M. R. Norman, H. Ding, M. Randeria, J. C. Campuzano, T. Yokoya, T. Takeuchi, T. Takahashi, T. Mochiku, K. Kadowaki, P. Guptasarma, and D. G. Hinks, “Destruction of the fermi surface in underdoped high- T_c superconductors,” *Nature*, vol. 392, pp. 157–160, 1998.
- [71] J. M. Tranquada, B. J. Sternlieb, J. D. Axe, Y. Nakamura, and S. Uchida, “Evidence for stripe correlations of spins and holes in copper oxide superconductors,” *Nature*, vol. 375, pp. 561–563, 1995.
- [72] M. R. Norman, D. Pines, and C. Kallin, “The pseudogap: friend or foe of high T_c ?,” *Advances in Physics*, vol. 54, no. 8, pp. 715–733, 2005.

- [73] A. A. Kordyuk, “Pseudogap from ARPES experiment: Three gaps in cuprates and topological superconductivity (Review Article) ,” *Low Temperature Physics*, vol. 41, p. 319, 2015.
- [74] R. Daou, N. Doiron-Leyraud, D. LeBoeuf, S. Y. Li, F. Laliberté, O. Cyr-Choinière, Y. J. Jo, L. Balicas, J.-Q. Yan, J.-S. Zhou, J. B. Goodenough, and L. Taillefer, “Linear temperature dependence of resistivity and change in the fermi surface at the pseudogap critical point of a high- t_c superconductor,” *Nature Physics*, vol. 5, pp. 31–34, 2009.
- [75] S. Wakimoto, R. J. Birgeneau, Y. Fujimaki, N. Ichikawa, T. Kasuga, Y. J. Kim, K. M. Kojima, S.-H. Lee, H. Niko, J. M. Tranquada, S. Uchida, and M. v. Zimmermann, “Effect of a magnetic field on the spin- and charge-density-wave order in $\text{La}_{1.45}\text{Nd}_{0.4}\text{Sr}_{0.15}\text{CuO}_4$,” *Physical Review B*, vol. 67, p. 184419, May 2003.
- [76] J. Fink, V. Soltwisch, J. Geck, E. Schierle, E. Weschke, and B. Büchner, “Phase diagram of charge order in $\text{La}_{1.8-x}\text{Eu}_{0.2}\text{Sr}_x\text{CuO}_4$ from resonant soft x-ray diffraction,” *Physical Review B*, vol. 83, p. 092503, Mar 2011.
- [77] N. B. Christensen, H. M. Rønnow, J. Mesot, R. A. Ewings, N. Momono, M. Oda, M. Ido, M. Enderle, D. F. McMorrow, and A. T. Boothroyd, “Nature of the Magnetic Order in the Charge-Ordered Cuprate $\text{La}_{1.48}\text{Nd}_{0.4}\text{Sr}_{0.12}\text{CuO}_4$,” *Physical Review Letters*, vol. 98, p. 197003, May 2007.
- [78] S. B. Wilkins, M. P. M. Dean, J. Fink, M. Hücker, J. Geck, V. Soltwisch, E. Schierle, E. Weschke, G. Gu, S. Uchida, N. Ichikawa, J. M. Tranquada, and J. P. Hill, “Comparison of stripe modulations in $\text{La}_{1.875}\text{Ba}_{0.125}\text{CuO}_4$ and $\text{La}_{1.48}\text{Nd}_{0.4}\text{Sr}_{0.12}\text{CuO}_4$,” *Physical Review B*, vol. 84, p. 195101, Nov 2011.
- [79] B. Nachumi, Y. Fudamoto, A. Keren, K. M. Kojima, M. Larkin, G. M. Luke, J. Merrin, O. Tchernyshyov, Y. J. Uemura, N. Ichikawa, M. Goto, H. Takagi, S. Uchida, M. K. Crawford, E. M. McCarron, D. E. MacLaughlin, and R. H. Heffner, “Muon spin relaxation study of the stripe phase order in $\text{La}_{1.6-x}\text{Nd}_{0.4}\text{Sr}_x\text{CuO}_4$ and related 214 cuprates,” *Physical Review B*, vol. 58, pp. 8760–8772, Oct 1998.
- [80] J. M. Tranquada, J. D. Axe, N. Ichikawa, Y. Nakamura, S. Uchida, and B. Nachumi, “Neutron-scattering study of stripe-phase order of holes and spins in $\text{La}_{1.48}\text{Nd}_{0.4}\text{Sr}_{0.12}\text{CuO}_4$,” *Physical Review B*, vol. 54, pp. 7489–7499, Sep 1996.
- [81] M. Fujita, H. Goka, K. Yamada, J. M. Tranquada, and L. P. Regnault, “Stripe order, depinning, and fluctuations in $\text{La}_{1.875}\text{Ba}_{0.125}\text{CuO}_4$ and $\text{La}_{1.875}\text{Ba}_{0.075}\text{Sr}_{0.050}\text{CuO}_4$,” *Physical Review B*, vol. 70, p. 104517, Sep 2004.
- [82] J. Chang, Y. Sassa, S. Guerrero, M. Månsson, M. Shi, S. Pailhès, A. Bendounan, R. Mottl, T. Claesson, O. Tjernberg, L. Patthey, M. Ido, M. Oda, N. Momono, C. Mudry, and J. Mesot, “Electronic structure near the $1/8$ -anomaly in La -based cuprates,” *New Journal of Physics*, vol. 10, p. 103016, 2008.

Bibliography

- [83] T. Yoshida, X. J. Zhou, K. Tanaka, W. L. Yang, Z. Hussain, Z.-X. Shen, A. Fujimori, S. Sahrakorpi, M. Lindroos, R. S. Markiewicz, A. Bansil, S. Komiya, Y. Ando, H. Eisaki, T. Kakeshita, and S. Uchida, “Systematic doping evolution of the underlying Fermi surface of $\text{La}_{2-x}\text{Sr}_x\text{CuO}_4$,” *Physical Review B*, vol. 74, p. 224510, Dec 2006.
- [84] E. Razzoli, Y. Sassa, G. Drachuck, M. Månsson, A. Keren, M. Shay, M. H. Berntsen, O. Tjernberg, M. Radovic, J. Chang, S. Pailhès, N. Momono, M. Oda, M. Ido, O. J. Lipscombe, S. M. Hayden, L. Patthey, J. Mesot, and M. Shi, “The fermi surface and band folding in $\text{La}_{2-x}\text{Sr}_x\text{CuO}_4$, probed by angle-resolved photoemission,” *New Journal of Physics*, vol. 12, no. 12, p. 125003, 2010.
- [85] T. L. Miller, W. Zhang, H. Eisaki, and A. Lanzara, “Particle-hole asymmetry in the cuprate pseudogap measured with time-resolved spectroscopy,” *Physical Review Letters*, vol. 118, p. 097001, Feb 2017.
- [86] M. Hashimoto, R.-H. He, K. Tanaka, J.-P. Testaud, W. Meevasana, R. G. Moore, D. Lu, H. Yao, Y. Yoshida, H. Eisaki, T. P. Devereaux, Z. Hussain, and Z.-X. Shen, “Particle-hole symmetry breaking in the pseudogap state of Bi2201 ,” *Nature Physics*, vol. 6, pp. 414–418, 2010.
- [87] A. V. Chubukov, M. R. Norman, A. J. Millis, and E. Abrahams, “Gapless pairing and the fermi arc in the cuprates,” *Physical Review B*, vol. 76, p. 180501, Nov 2007.
- [88] M. Franz and A. J. Millis, “Phase fluctuations and spectral properties of underdoped cuprates,” *Physical Review B*, vol. 58, pp. 14572–14580, Dec 1998.
- [89] A. Kanigel, M. R. Norman, M. Randeria, U. Chatterjee, S. Souma, A. Kaminski, H. M. Fretwell, S. Rosenkranz, M. Shi, T. Sato, T. Takahashi, Z. Z. Li, H. Raffy, K. Kadowaki, D. Hinks, L. Ozyuzer, and J. C. Campuzano, “Evolution of the pseudogap from fermi arcs to the nodal liquid,” *Nature Physics*, vol. 2, pp. 447–451, July 2006.
- [90] M. Shi, J. Chang, S. Pailhès, M. R. Norman, J. C. Campuzano, M. Månsson, T. Claesson, O. Tjernberg, A. Bendounan, L. Patthey, N. Momono, M. Oda, M. Ido, C. Mudry, and J. Mesot, “Coherent d -Wave Superconducting Gap in Underdoped $\text{La}_{2-x}\text{Sr}_x\text{CuO}_4$ by Angle-Resolved Photoemission Spectroscopy,” *Physical Review Letters*, vol. 101, p. 047002, Jul 2008.
- [91] M. Shi, A. Bendounan, E. Razzoli, S. Rosenkranz, M. R. Norman, J. C. Campuzano, J. Chang, M. Månsson, Y. Sassa, T. Claesson, O. Tjernberg, L. Patthey, N. Momono, M. Oda, M. Ido, S. Guerrero, C. Mudry, and J. Mesot, “Spectroscopic evidence for pre-formed cooper pairs in the pseudogap phase of cuprates,” *EPL (Europhysics Letters)*, vol. 88, no. 2, p. 27008, 2009.
- [92] J. Lee, K. Fujita, A. R. Schmidt, C. K. Kim, H. Eisaki, S. Uchida, and J. C. Davis, “Spectroscopic Fingerprint of Phase-Incoherent Superconductivity in the Underdoped $\text{Bi}_2\text{Sr}_2\text{CaCu}_2\text{O}_{8+d}$,” *Science*, vol. 325, p. 1099, 2009.

- [93] J. Chang, M. Shi, S. Pailh  s, M. M  nsson, T. Claesson, O. Tjernberg, A. Bendounan, Y. Sassa, L. Patthey, N. Momono, M. Oda, M. Ido, S. Guerrero, C. Mudry, and J. Mesot, “Anisotropic quasiparticle scattering rates in slightly underdoped to optimally doped high-temperature $\text{La}_{2-x}\text{Sr}_x\text{CuO}_4$ superconductors,” *Physical Review B*, vol. 78, p. 205103, Nov 2008.
- [94] J. Chang, A. P. Schnyder, R. Gilardi, H. M. R  nnow, S. Pailhes, N. B. Christensen, C. Niedermayer, D. F. McMorrow, A. Hiess, A. Stunault, M. Enderle, B. Lake, O. Sobolev, N. Momono, M. Oda, M. Ido, C. Mudry, and J. Mesot, “Magnetic-Field-Induced Spin Excitations and Renormalized Spin Gap of the Underdoped $\text{La}_{1.895}\text{Sr}_{0.105}\text{CuO}_4$ Superconductor,” *Physical Review Letters*, vol. 98, p. 077004, Feb 2007.
- [95] J. Chang, J. S. White, M. Laver, C. J. Howell, S. P. Brown, A. T. Holmes, L. Maechler, S. Str  ssle, R. Gilardi, S. Gerber, T. Kurosawa, N. Momono, M. Oda, M. Ido, O. J. Lipscombe, S. M. Hayden, C. D. Dewhurst, R. Vavrin, J. Gavilano, J. Kohlbrecher, E. M. Forgan, and J. Mesot, “Spin density wave induced disordering of the vortex lattice in superconducting $\text{La}_{2-x}\text{Sr}_x\text{CuO}_4$,” *Physical Review B*, vol. 85, p. 134520, Apr 2012.
- [96] U. Chatterjee, M. Shi, D. Ai, J. Zhao, A. Kanigel, S. Rosenkranz, H. Raffy, Z. Z. Li, K. Kadowaki, D. G. Hinks, Z. J. Xu, J. S. Wen, G. Gu, C. T. Lin, H. Claus, M. R. Norman, M. Randeria, and J. C. Campuzano, “Observation of a d-wave nodal liquid in highly underdoped $\text{Bi}_2\text{Sr}_2\text{CaCu}_2\text{O}_{8+d}$,” *Nature Physics*, vol. 6, pp. 99–103, 2010.
- [97] T. Kondo, R. Khasanov, T. Takeuchi, J. Schmalian, and A. Kaminski, “Competition between the pseudogap and superconductivity in the high- T_c copper oxides,” *Nature*, vol. 457, pp. 296–300, 2009.
- [98] T. Valla, A. V. Fedorov, P. D. Johnson, Q. Li, G. D. Gu, and N. Koshizuka, “Temperature Dependent Scattering Rates at the Fermi Surface of Optimally Doped $\text{Bi}_2\text{Sr}_2\text{CaCu}_2\text{O}_{8+\delta}$,” *Physical Review Letters*, vol. 85, pp. 828–831, Jul 2000.
- [99] G. Gr  ner, “The dynamics of charge-density waves,” *Reviews of Modern Physics*, vol. 60, pp. 1129–1181, Oct 1988.
- [100] M. Vojta, “Lattice symmetry breaking in cuprate superconductors: stripes, nematics, and superconductivity,” *Advances in Physics*, vol. 58, no. 6, pp. 699–820, 2009.
- [101] J. Chang, R. Daou, C. Proust, D. LeBoeuf, N. Doiron-Leyraud, F. Lalibert  , B. Pngault, B. J. Ramshaw, R. Liang, D. A. Bonn, W. N. Hardy, H. Takagi, A. B. Antunes, I. Sheikin, K. Behnia, and L. Taillefer, “Nernst and seebeck coefficients of the cuprate superconductor $\text{YBa}_2\text{Cu}_3\text{O}_{6.67}$: A study of fermi surface reconstruction,” *Physical Review Letters*, vol. 104, p. 057005, Feb 2010.
- [102] Q. Li, M. H  cker, G. D. Gu, A. M. Tsvelik, and J. M. Tranquada, “Two-Dimensional Superconducting Fluctuations in Stripe-Ordered $\text{La}_{1.875}\text{Ba}_{0.125}\text{CuO}_4$,” *Physical Review Letters*, vol. 99, p. 067001, Aug 2007.

Bibliography

- [103] M. Fujita, K. Yamada, H. Hiraka, P. M. Gehring, S. H. Lee, S. Wakimoto, and G. Shirane, “Static magnetic correlations near the insulating-superconducting phase boundary in $\text{La}_{2-x}\text{Sr}_x\text{CuO}_4$,” *Physical Review B*, vol. 65, p. 064505, Jan 2002.
- [104] S. Wakimoto, S. Ueki, Y. Endoh, and K. Yamada, “Systematic study of short-range anti-ferromagnetic order and the spin-glass state in lightly doped $\text{La}_{2-x}\text{Sr}_x\text{CuO}_4$,” *Physical Review B*, vol. 62, pp. 3547–3553, Aug 2000.
- [105] D. Sénéchal and A.-M. S. Tremblay, “Hot spots and pseudogaps for hole- and electron-doped high-temperature superconductors,” *Physical Review Letters*, vol. 92, p. 126401, Mar 2004.
- [106] E. Gull, O. Parcollet, and A. J. Millis, “Superconductivity and the pseudogap in the two-dimensional hubbard model,” *Physical Review Letters*, vol. 110, p. 216405, May 2013.
- [107] G. Sordi, P. Sémon, K. Haule, and A.-M. S. Tremblay, “*c*-axis resistivity, pseudogap, superconductivity, and widom line in doped mott insulators,” *Physical Review B*, vol. 87, p. 041101, Jan 2013.
- [108] M. Ferrero, P. S. Cornaglia, L. D. Leo, O. Parcollet, G. Kotliar, and A. Georges, “Valence bond dynamical mean-field theory of doped mott insulators with nodal/antinodal differentiation,” *EPL (Europhysics Letters)*, vol. 85, no. 5, p. 57009, 2009.
- [109] H. Alloul, “What is the simplest model that captures the basic experimental facts of the physics of underdoped cuprates?,” *Comptes Rendus de Physique*, vol. 15, no. 6, p. 519, 2014.
- [110] P. A. Lee, “Amperean pairing and the pseudogap phase of cuprate superconductors,” *Physical Review X*, vol. 4, p. 031017, Jul 2014.
- [111] I. M. Vishik, M. Hashimoto, R.-H. He, W.-S. Lee, F. Schmitt, D. Lu, R. G. Moore, C. Zhang, W. Meevasana, T. Sasagawa, S. Uchida, K. Fujita, S. Ishida, M. Ishikado, Y. Yoshida, H. Eisaki, Z. Hussain, T. P. Devereaux, and Z.-X. Shen, “Phase competition in trisected superconducting dome,” *Proceedings of the National Academy of Sciences*, vol. 109, no. 45, pp. 18332–18337, 2012.
- [112] E. G. Moon and S. Sachdev, “Quantum critical point shifts under superconductivity: Pnictides and cuprates,” *Physical Review B*, vol. 82, p. 104516, Sep 2010.
- [113] M. Hashimoto, I. M. Vishik, R.-H. He, T. P. Devereaux, and Z.-X. Shen, “Energy gaps in high-transition-temperature cuprate superconductors,” *Nature Physics*, vol. 10, pp. 483–495, 2014.
- [114] A. Greco, “Evidence for two competing order parameters in underdoped cuprate superconductors from a model analysis of fermi-arc effects,” *Physical Review Letters*, vol. 103, p. 217001, Nov 2009.

- [115] A. Greco and M. Bejas, "Short-ranged and short-lived charge-density-wave order and pseudogap features in underdoped cuprate superconductors," *Physical Review B*, vol. 83, p. 212503, Jun 2011.
- [116] U. Chatterjee, J. Zhao, M. Iavarone, R. Di Capua, J. Castellan, G. Karapetrov, C. Malliakas, M. Kanatzidis, H. Claus, J. Ruff, F. Weber, J. vanWezel, J. Campuzano, R. Osborn, M. Randeria, N. Trivedi, M. Norman, and S. Rosenkranz, "Emergence of coherence in the charge-density wave state of 2H-NbSe_2 ," *Nature Communications*, vol. 6, p. 6313, 2015.
- [117] D. S. Inosov, D. V. Evtushinsky, V. B. Zabolotnyy, A. A. Kordyuk, B. Büchner, R. Follath, H. Berger, and S. V. Borisenko, "Temperature-dependent fermi surface of 2H-tase_2 driven by competing density wave order fluctuations," *Physical Review B*, vol. 79, p. 125112, Mar 2009.
- [118] C. Monney, G. Monney, P. Aebi, and H. Beck, "Electron-hole fluctuation phase in 1t-tise_2 ," *Physical Review B*, vol. 85, p. 235150, Jun 2012.
- [119] R.-H. He, X. J. Zhou, M. Hashimoto, T. Yoshida, K. Tanaka, S.-K. Mo, T. Sasagawa, N. Maniella, W. Meevasana, H. Yao, M. Fujita, T. Adachi, S. Komiyama, S. Uchida, Y. Ando, F. Zhou, Z. X. Zhao, A. Fujimori, Y. Koike, K. Yamada, Z. Hussain, and Z.-X. Shen, "Doping dependence of the (π, π) shadow band in La -based cuprates studied by angle-resolved photoemission spectroscopy," *New Journal of Physics*, vol. 13, no. 1, p. 013031, 2011.
- [120] V. B. Zabolotnyy, A. A. Kordyuk, D. S. Inosov, D. V. Evtushinsky, R. Schuster, B. Büchner, N. Wizen, G. Behr, S. Pyon, T. Takayama, H. Takagi, R. Follath, and S. V. Borisenko, "Evidence for Fermi surface reconstruction in the static stripe phase of $\text{La}_{1.8-x}\text{Eu}_{0.2}\text{Sr}_x\text{CuO}_4$, $x=1/8$," *EPL (Europhysics Letters)*, vol. 86, no. 4, p. 47005, 2009.
- [121] T. Kondo, T. Takeuchi, A. Kaminski, S. Tsuda, and S. Shin, "Evidence for Two Energy Scales in the Superconducting State of Optimally Doped $(\text{Bi, Pb})_2(\text{Sr, La})_2\text{CuO}_{6+\delta}$," *Physical Review Letters*, vol. 98, p. 267004, Jun 2007.
- [122] S. Hfner, M. A. Hossain, A. Damascelli, and G. A. Sawatzky, "Two gaps make a high-temperature superconductor?," *Reports on Progress in Physics*, vol. 71, no. 6, p. 062501, 2008.
- [123] J.-H. Ma, Z.-H. Pan, F. C. Niestemski, M. Neupane, Y.-M. Xu, P. Richard, K. Nakayama, T. Sato, T. Takahashi, H.-Q. Luo, L. Fang, H.-H. Wen, Z. Wang, H. Ding, and V. Madhavan, "Coexistence of Competing Orders with Two Energy Gaps in Real and Momentum Space in the High Temperature Superconductor $\text{Bi}_2\text{Sr}_{2-x}\text{La}_x\text{CuO}_{6+\delta}$," *Physical Review Letters*, vol. 101, p. 207002, Nov 2008.
- [124] M. Hashimoto, E. A. Nowadnick, R.-H. He, I. M. Vishik, B. Moritz, Y. He, K. Tanaka, R. G. Moore, D. Lu, Y. Yoshida, M. Ishikado, T. Sasagawa, K. Fujita, S. Ishida, S. Uchida, H. Eisaki, Z. Hussain, T. P. Devereaux, and Z.-X. Shen, "Direct spectroscopic evidence for

- phase competition between the pseudogap and superconductivity in $\text{Bi}_2\text{Sr}_2\text{CaCu}_2\text{O}_{8+\delta}$,” *Nature Materials*, vol. 14, pp. 37–42, Jan. 2015.
- [125] E. Dagotto, “Complexity in strongly correlated electronic systems,” *Science*, vol. 309, no. 5732, pp. 257–262, 2005.
- [126] Y. Maeno, H. Hashimoto, K. Yoshida, S. Nishizaki, T. Fujita, J. G. Bednorz, and F. Lichtenberg, “Superconductivity in a layered perovskite without copper,” *Nature*, vol. 372, pp. 532 – 534, 1994.
- [127] P. L. Alireza, F. Nakamura, S. K. Goh, Y. Maeno, S. Nakatsuji, Y. T. C. Ko, M. Sutherland, S. Julian, and G. G. Lonzarich, “Evidence of superconductivity on the border of quasi-2D ferromagnetism in Ca_2RuO_4 at high pressure,” *Journal of Physics: Condensed Matter*, vol. 22, no. 5, p. 052202, 2010.
- [128] H.-J. Noh, S.-J. Oh, B.-G. Park, J.-H. Park, J.-Y. Kim, H.-D. Kim, T. Mizokawa, L. H. Tjeng, H.-J. Lin, C. T. Chen, S. Schuppler, S. Nakatsuji, H. Fukazawa, and Y. Maeno, “Electronic structure and evolution of the orbital state in metallic $\text{Ca}_{2-x}\text{Sr}_x\text{RuO}_4$,” *Physical Review B*, vol. 72, p. 052411, Aug 2005.
- [129] C. T. Chen, F. Sette, Y. Ma, M. S. Hybertsen, E. B. Stechel, W. M. C. Foulkes, M. Schuler, S.-W. Cheong, A. S. Cooper, L. W. Rupp, B. Batlogg, Y. L. Soo, Z. H. Ming, A. Krol, and Y. H. Kao, “Electronic states in $\text{La}_{2-x}\text{Sr}_x\text{CuO}_{4+\delta}$ probed by soft-x-ray absorption,” *Physical Review Letters*, vol. 66, pp. 104–107, Jan 1991.
- [130] M. Schmidt, T. R. Cummins, M. Bürk, D. H. Lu, N. Nücker, S. Schuppler, and F. Lichtenberg, “Nature of the electronic states in the layered perovskite noncuprate superconductor Sr_2RuO_4 ,” *Physical Review B*, vol. 53, pp. R14761–R14764, Jun 1996.
- [131] J.-H. Park, T. Kimura, and Y. Tokura, “Competition between lattice distortion and charge dynamics for the charge carriers of double-layered manganites,” *Physical Review B*, vol. 58, pp. R13330–R13333, Nov 1998.
- [132] M. Moretti Sala, M. Rossi, S. Boseggia, J. Akimitsu, N. B. Brookes, M. Isobe, M. Minola, H. Okabe, H. M. Rønnow, L. Simonelli, D. F. McMorrow, and G. Monaco, “Orbital occupancies and the putative $j_{\text{eff}} = \frac{1}{2}$ ground state in Ba_2IrO_4 : A combined oxygen k -edge xas and rixs study,” *Physical Review B*, vol. 89, p. 121101, Mar 2014.
- [133] T. Mizokawa, L. H. Tjeng, G. A. Sawatzky, G. Ghiringhelli, O. Tjernberg, N. B. Brookes, H. Fukazawa, S. Nakatsuji, and Y. Maeno, “Spin-Orbit Coupling in the Mott Insulator Ca_2RuO_4 ,” *Physical Review Letters*, vol. 87, p. 077202, Jul 2001.
- [134] M. Malvestuto, E. Carleschi, R. Fittipaldi, E. Gorelov, E. Pavarini, M. Cuoco, Y. Maeno, F. Parmigiani, and A. Vecchione, “Electronic structure trends in the $\text{Sr}_{n+1}\text{Ru}_n\text{O}_{3n+1}$ family ($n = 1, 2, 3$),” *Physical Review B*, vol. 83, p. 165121, Apr 2011.

-
- [135] M. Malvestuto, V. Capogrosso, E. Carleschi, L. Galli, E. Gorelov, E. Pavarini, R. Fittipaldi, F. Forte, M. Cuoco, A. Vecchione, and F. Parmigiani, “Nature of the apical and planar oxygen bonds in the $\text{Sr}_{n+1}\text{Ru}_n\text{O}_{3n+1}$ family ($n = 1, 2, 3$),” *Physical Review B*, vol. 88, p. 195143, Nov 2013.
 - [136] S. J. Moon, M. W. Kim, K. W. Kim, Y. S. Lee, J.-Y. Kim, J.-H. Park, B. J. Kim, S.-J. Oh, S. Nakatsuji, Y. Maeno, I. Nagai, S. I. Ikeda, G. Cao, and T. W. Noh, “Electronic structures of layered perovskite Sr_2MO_4 ($M = \text{Ru, Rh, and Ir}$),” *Physical Review B*, vol. 74, p. 113104, Sep 2006.
 - [137] M. Braden, G. André, S. Nakatsuji, and Y. Maeno, “Crystal and magnetic structure of Ca_2RuO_4 : magnetoelastic coupling and the metal-insulator transition,” *Physical Review B*, vol. 58, pp. 847–861, Jul 1998.
 - [138] W. A. Harrison, *Electronic Structure and the Properties of Solids: The Physics of the Chemical Bond*. W. H. Freeman and Company, 1980.
 - [139] M. Braden, A. Moudden, S. Nishizaki, Y. Maeno, and T. Fujita, “Structural analysis of Sr_2RuO_4 ,” *Physica C: Superconductivity*, vol. 273, no. 3, pp. 248 – 254, 1997.
 - [140] M. M. Sala, V. Bisogni, C. Aruta, G. Balestrino, H. Berger, N. B. Brookes, G. M. de Luca, D. D. Castro, M. Grioni, M. Guarise, P. G. Medaglia, F. M. Granozio, M. Minola, P. Perna, M. Radovic, M. Salluzzo, T. Schmitt, K. J. Zhou, L. Braicovich, and G. Ghiringhelli, “Energy and symmetry of dd excitations in undoped layered cuprates measured by Cu L_{3} resonant inelastic x-ray scattering,” *New Journal of Physics*, vol. 13, no. 4, p. 043026, 2011.
 - [141] Y. Harada, K. Okada, R. Eguchi, A. Kotani, H. Takagi, T. Takeuchi, and S. Shin, “Unique identification of zhang-rice singlet excitation in $\text{Sr}_2\text{CuO}_2\text{Cl}_2$ mediated by the $\text{O } 1s$ core hole: Symmetry-selective resonant soft x-ray raman scattering study,” *Physical Review B*, vol. 66, p. 165104, Oct 2002.
 - [142] M. W. Haverkort, I. S. Elfimov, L. H. Tjeng, G. A. Sawatzky, and A. Damascelli, “Strong spin-orbit coupling effects on the fermi surface of Sr_2RuO_4 and Sr_2RhO_4 ,” *Physical Review Letters*, vol. 101, p. 026406, Jul 2008.
 - [143] C. N. Veenstra, Z.-H. Zhu, M. Raichle, B. M. Ludbrook, A. Nicolaou, B. Slomski, G. Landolt, S. Kittaka, Y. Maeno, J. H. Dil, I. S. Elfimov, M. W. Haverkort, and A. Damascelli, “Spin-orbital entanglement and the breakdown of singlets and triplets in Sr_2RuO_4 revealed by spin- and angle-resolved photoemission spectroscopy,” *Physical Review Letters*, vol. 112, p. 127002, Mar 2014.
 - [144] G.-Q. Liu, “Spin-orbit coupling induced mott transition in $\text{Ca}_{2-x}\text{Sr}_x\text{RuO}_4$ ($0 < x < 0.2$),” *Physical Review B*, vol. 84, p. 235136, Dec 2011.
 - [145] G.-Q. Liu, “Competition between spin-orbit coupling and magnetic exchange splitting in Ca_2RuO_4 ,” *Physical Review B*, vol. 88, p. 104428, Sep 2013.

Bibliography

- [146] M. Moretti Sala, S. Boseggia, D. F. McMorrow, and G. Monaco, “Resonant x-ray scattering and the $j_{\text{eff}}=1/2$ electronic ground state in iridate perovskites,” *Physical Review Letters*, vol. 112, p. 026403, Jan 2014.
- [147] X. Liu, V. M. Katukuri, L. Hozoi, W.-G. Yin, M. P. M. Dean, M. H. Upton, J. Kim, D. Casa, A. Said, T. Gog, T. F. Qi, G. Cao, A. M. Tsvelik, J. van den Brink, and J. P. Hill, “Testing the Validity of the Strong Spin-Orbit-Coupling Limit for Octahedrally Coordinated Iridate Compounds in a Model System $\text{Sr}_3\text{CuIrO}_6$,” *Physical Review Letters*, vol. 109, p. 157401, Oct 2012.
- [148] A. Georges, L. deMedici, and J. Mravlje, “Strong correlations from hunds coupling,” *Annual Review of Condensed Matter Physics*, vol. 4, pp. 137–178, April 2013.
- [149] D. Sutter, C. G. Fatuzzo, S. Moser, M. Kim, R. Fittipaldi, A. Vecchione, V. Granata, Y. Sassa, F. Cossalter, G. Gatti, M. Grioni, H. M. Rønnow, N. C. Plumb, C. E. Matt, M. Shi, M. Hoesch, T. K. Kim, T.-R. Chang, H.-T. Jeng, C. Jozwiak, A. Bostwick, E. Rotenberg, A. Georges, T. Neupert, and J. Chang, “Hallmarks of Hunds coupling in the Mott insulator Ca_2RuO_4 ,” *Nature Communications*, vol. 8, p. 15176, 2017.
- [150] B. J. Kim, H. Jin, S. J. Moon, J.-Y. Kim, B.-G. Park, C. S. Leem, J. Yu, T. W. Noh, C. Kim, S.-J. Oh, J.-H. Park, V. Durairaj, G. Cao, and E. Rotenberg, “Novel $J_{\text{eff}} = 1/2$ mott state induced by relativistic spin-orbit coupling in Sr_2IrO_4 ,” *Physical Review Letters*, vol. 101, p. 076402, Aug 2008.
- [151] J. Kim, M. Daghofer, A. H. Said, T. Gog, J. van den Brink, G. Khaliullin, and B. J. Kim, “Excitonic quasiparticles in a spin-orbit mott insulator,” *Nature Communications*, vol. 5, p. 4453, July 2014.
- [152] C. G. Fatuzzo, M. Dantz, S. Fatale, P. Olalde-Velasco, N. E. Shaik, B. Dalla Piazza, S. Toth, J. Pelliciari, R. Fittipaldi, A. Vecchione, N. Kikugawa, J. S. Brooks, H. M. Rønnow, M. Grioni, C. Rüegg, T. Schmitt, and J. Chang, “Spin-orbit-induced orbital excitations in Sr_2RuO_4 and Ca_2RuO_4 : A resonant inelastic x-ray scattering study,” *Physical Review B*, vol. 91, p. 155104, Apr 2015.
- [153] Y. K. Kim, N. H. Sung, J. D. Denlinger, and B. J. Kim, “Observation of a d-wave gap in electron-doped Sr_2IrO_4 ,” *Nature Physics*, vol. 12, pp. 37–41, 2016.

**Claudia Giuseppina Fatuzzo****PERSONAL INFORMATION**

Av. De Valmont 16, CH1010 Lausanne - Switzerland
 +41767856005 (CH) claudia.fatuzzo@epfl.ch Skype claudia.fatuzzo
 Date of birth 09/12/1985 Nationality Italian Sex female Civil status single
 Licence Swiss driving licence B Hobbies cooking, running, yoga, Puerto Rican salsa, tango
 Languages Italian (mother tongue); English (fluent, C2); French (intermediate, B1)
 English exam TOEFL iBT registration n°0000000017870377; evaluation: 111/120 (2013)

EDUCATION

- Jun 2013 – now** Doctoral School of Physics
Spectroscopy studies of the electronic structures in layered cuprates and ruthenates
 Supervisors: Prof. J.Chang, Prof. H. Rønnow

 Laboratory of Quantum Magnetism, EPFL (CH)
 Laboratory for Quantum Matter Research, UZH (CH)
 Topic: **strongly correlated electron systems**, with focus on the physics of **cuprates** and **ruthenates**.
 Experimental techniques: **XAS, RIXS, ARPES, Spin-Resolved ARPES** (within synchrotrons).
 Data analysis software: **Matlab**.
 Courses: “*Thermodynamics of HTS Superconductors*” Dr. J. Tallon; “*Quantum Magnetism at Extreme Conditions*” Prof. Ch. Rüegg; “*Solid State Physics IV*” Prof. H.M. Rønnow; “*Functional Oxides*” Prof. N. Spaldin; “*Water mysteries reveled by X-ray experiments*” Prof. A. Nilsson.
 Schools: “*Materials - structure and magnetism*”, 2013 PSI Summer School on Condensed Matter Research; “*Shedding light on correlated electrons*” 2015 MaNEP Winter School on Condensed Matter Research.
 Others: sample preparation, LaTeX.
- Oct 2009 – Nov 2012** Graduate in Physics (master level degree) 110/110 cum laude
 University of Catania (IT)
- Feb 2011 – Sep 2011** Erasmus Master Project at Imperial College London (7 months)
Broadband Plasmonics for Improved Photovoltaics
 Supervisors: Prof. F. Priolo, Prof. S.A. Maier, Dr. N. Hylton
 Experimental Solid State Physics Department, Imperial College London (UK)
 Project: Fundamental research on plasmonics, with approach both theoretical and experimental.
 Techniques: commercial simulation software *lumerical*, Fourier-transform IR spectroscopy.
- Oct 2004 – Jul 2009** Graduate in Physics (bachelor degree) 110/110 cum laude
 University of Catania (IT)
- Sep 1999 – Jul 2004** Scientific Baccalauréat (A levels) 100/100
 Scientific High School “P. Umberto di Savoia”, Catania (IT)

EMPLOYMENT HISTORY AND TEACHING ACTIVITIES

- Jun 2013 – now** Doctoral Assistant (Supervisors: Prof. J.Chang, Prof. H. Rønnow) Sector Education
 Laboratory for Quantum Magnetism, Institute of Physics, EPFL (CH)
 Assistant to exercise classes for the courses *Solid State Physics IV* (Prof. H.M. Rønnow),
Physique Générale III (Prof. H.M. Rønnow; Prof. P. Leiman), *Physique Générale IV* (Prof. M. Grioni);
Course coordinator for the course *Physique Générale III* (Prof. H.M. Rønnow).

- Mar 2006 – May 2013** – Private Tutor (individuals and small groups) Sector Education
Self-study assistance in Physics, Mathematics, and Geometry to middle school, high school and bachelor students.
- Jan 2012 – Jun 2012** – Tutor (50 hours distributed in 6 months) Sector Education
Department of Physics and Astrophysics, University of Catania (IT)
Assistant to practical classes on mechanics and thermodynamics;
appointed through competitive selection, mostly based on grades.

ACTIVE MEMBERSHIPS

- Jun 2013 – now** – Associate member of MaNEP Switzerland Network.

PRIZES, AWARDS, FELLOWSHIPS

- May 2017** – Early Postdoc.Mobility fellowship, program of the Swiss National Science Foundation.
- July 2014** – “2014 - Josep Askenazi Award” to oral contributions of young scientists, *Superstripes 2014*. Value: 200 €.
- Dec 2011** – Tutor Activity Collaboration for the Physics department of University of Catania. Value: 475 €.
- Feb 2010** – Erasmus Scholarship from the University of Catania. Value: 1 552 €.

SCIENTIFIC PUBLICATIONS

D. Sutter*, **C.G. Fatuzzo***, S. Moser, M. Kim, R. Fittipaldi, A. Vecchione, V. Granata, Y. Sassa, F. Cossalter, G. Gatti, M. Grioni, H.M. Ronnow, N.C. Plumb, C.E. Matt, M. Shi, M. Hoesch, T.K. Kim, T.R. Chang, H.T. Jeng, C. Jozwiak, A. Bostwick, E. Rotenberg, A. Georges, T. Neupert and J. Chang;
“*Hallmarks of Hund’s coupling in the Mott insulator Ca_2RuO_4* ”;
Nature Communications, **8**, 15176 (2017);
*contributed equally.

O. Ivashko, N. E. Shaik, X. Lu, **C. G. Fatuzzo**, M. Dantz, P. G. Freeman, D. E. McNally, D. Destraz, N. B. Christensen, T. Kurosawa, N. Momono, M. Oda, C. Monney, H. M. Rønnow, T. Schmitt, J. Chang;
“*Damped spin-excitations in a doped cuprate superconductor with orbital hybridization*”;
Accepted for publication in Physical Review B;
arXiv:1702.02782v2 (2017).

C.G. Fatuzzo, M. Dantz, S. Fatale, P. Olalde-Velasco, N.E. Shaik, B. Dalla Piazza, S. Toth, J. Pellicciari, R. Fittipaldi, A. Vecchione, N. Kikugawa, J.S. Brooks, H.M. Rønnow, M. Grioni, Ch. Rüegg, T. Schmitt, and J. Chang;
“*Spin-orbit coupling and orbital excitations in Sr_2RuO_4 and Ca_2RuO_4* ”;
Physical Review B **91**, 155104 (2015).

C.E. Matt, **C.G. Fatuzzo**, Y. Sassa, M. Månsson, S. Fatale, V. Bitetta, X. Shi, S. Pailhès, M.H. Berntsen, T. Kurosawa, M. Oda, N. Momono, O.J. Lipscombe, S. M. Hayden, J.-Q. Yan, J.-S. Zhou, J.B. Goodenough, S. Pyon, T. Takayama, H. Takagi, L. Patthey, A. Bendounan, E. Razzoli, M. Shi, N.C. Plumb, M. Radovic, M. Grioni, J. Mesot, O. Tjernberg and J. Chang;
“*Electron scattering, charge order, and pseudogap physics in $\text{La}_{1.6-x}\text{Nd}_{0.4}\text{Sr}_x\text{CuO}_4$: An angle-resolved photoemission spectroscopy study*”;
Physical Review B **92**, 134524 (2015).

This work was highlighted in the **MaNEP Switzerland Network Newsletter** n°32 (December 2015).
<http://www.manep.ch/fingerprints-of-pseudogap-and-charge-ordering-a-photoemission-spectroscopy-investigation/>

C.G. Fatuzzo, Y. Sassa, M. Maansson, S. Pailhes, O.J. Lipscombe, S.M. Hayden, L. Patthey, M. Shi, M. Grioni, H. M. Rønnow, J. Mesot, O. Tjernberg, J. Chang;
"Nodal Landau Fermi-liquid quasiparticles in overdoped $La_{1.77}Sr_{0.23}CuO_4$ ";
 Physical Review B **89**, 205104 (2014).

S. Fatale, **C.G. Fatuzzo**, P. Babkevich, N. E. Shaik, J. Pellicciari, A. Kikkawa, Y. Taguchi, Y. Tokura, T. Schmitt, H.M. Rønnow, and M. Grioni;
"Electronic and magnetic excitations in the half-stuffed Cu-O planes of $Ba_2Cu_3O_4Cl_2$ measured by resonant inelastic x-ray scattering";
 In preparation.

CONFERENCE CONTRIBUTIONS AND SEMINARS

Chaired sessions

- Session 26 of the international conference *Superstripes 2015*, Ischia (IT) 15 June 2015.

Invited talks

- *"Novel Synchrotron spectroscopic experiments on ruthenates"*, at the international conference *Superstripes 2016*, Ischia (IT) 23-29 June 2016.
- *"A XAS and RIXS combined study of spin-orbit coupling and orbital excitations in Sr/Ca_2RuO_4 "*, at the international conference *Superstripes 2015*, Ischia (IT) 13-18 June 2015.

Seminars

- *"Synchrotron spectroscopic experiments on ruthenates"*, visit to the T-REX lab of Prof. Parmigiani at the FERMI lab in Trieste (IT) 18 November 2016.
- *"A XAS and RIXS combined study of spin-orbit coupling and orbital excitations in Sr/Ca_2RuO_4 "*, visit to the SPIN CNR Institute – Salerno, Fisciano (IT) 11 June 2015.

Contributed talks

- *"Synchrotron spectroscopic experiments on ruthenates"*, at the Swiss conference *SPS 2016* (CH) 23 - 25 August 2016.
- *"Synchrotron spectroscopic experiments on ruthenates"*, at the international workshop *UFOX*, Fisciano (IT) 7-8 July 2016.
- *"A XAS and RIXS combined study of spin-orbit coupling and orbital excitations in Sr/Ca_2RuO_4 "*, at the international conference *NGSCES 2015*, Trogir (HR) 14-18 September 2015.
- *"A XAS and RIXS combined study of spin-orbit coupling and orbital excitations in Sr/Ca_2RuO_4 "*, at the international conference *ICM 2015*, Barcellona (SP) 5-10 July 2015.
- *"Disentanglement of pseudogap and charge stripe order in Nd-LSCO"*, at the international conference *Superstripes 2014*, Erice (IT) 25-31 July 2014;
 honoured by the **"2014 - Josep Askenazi Award"**.
<http://actu.epfl.ch/news/claudia-fatuzzo-winner-of-the-2014-josep-askenaz-2/>

Posters

- *"Spectroscopy evidences for true Landau Fermi quasiparticles in LSCO"*, at the international conference *SCES 2014*, Grenoble (FR) 7-11 July 2014.
- *"Spectroscopy evidences for true Landau Fermi quasiparticles in LSCO"*, at the Swiss conference *SPS 2014*, Fribourg (CH) 30 June-2 July 2014.

‘What the caterpillar calls
 the end of the world,
the rest of the world calls
 a butterfly.’
— Anonymous

